MICROBIOLOGICALLY INFLUENCED CORROSION OF 1018 PLAIN CARBON STEEL IN BIODIESELS

A THESIS SUBMITTED TO THE GRADUATE DIVISION OF THE UNIVERSITY OF HAWAIʻI AT MĀNOA IN PARTIAL FULFILLMENT OF THE REQUIREMENTS FOR THE DEGREE OF

MASTER OF SCIENCE

IN

MECHANICAL ENGINEERING

December 2012

By

Corey Kaneshiro

Thesis Committee:
Lloyd H. Hihara, Chairperson
Scott F. Miller
Weilin Qu

Acknowledgements

I would like to acknowledge my advisor, Dr. Lloyd H. Hihara, for giving me the opportunity to work on this thesis. His expertise and guidance throughout this entire process was critical to the success of this thesis. I would also like to thank my committee members, Dr. Scott F. Miller and Dr. Weilin Qu.

Mr. Ryan Sugamoto and other Hawaii Corrosion Lab members have also helped me tremendously within the lab regarding experiments, equipment use, and consultation, and for that, I am very grateful. I am also thankful for Mr. Benjamin Respicio and Mr. Brian Kodama from the college of engineering machine shop for their countless assistance in the fabrication of metal coupon samples.

This research was funded by the Hawaii Natural Energy Institute at the University of Hawaii at Manoa, and by the Office of Naval Research. Financial assistance from these agencies is greatly acknowledged.

Lastly, I would like to thank my parents, Owen and Ann Kaneshiro, and my brother, Tyler Kaneshiro, for their love and support throughout this critical period in my life. They have always believed in me and pushed me to achieve my goals.

Abstract

This research focuses on the microbiological effects of corrosion on 1018 plain carbon steel immersed in biodiesels. Corrosion of steel immersed in sterilized ultra-pure water (18.2 MΩ·cm) contaminated biodiesels of 100% (B100) and 20% (B20) concentration along with ultra-low sulfur diesel (ULSD) was initiated under three environmental conditions: anaerobic, aerobic, and selective (sterile) aerobic. Three time exposures of 1 month, 6 months and 1 year were conducted. Corrosion products were identified via Raman spectroscopy, x-ray diffraction, and scanning electron microscopy equipped with an energy dispersive x-ray system. Corrosion rates were calculated based on mass loss data obtained at the end of the 6 month and 1 year exposure periods. Microorganism contamination was identified based on molecular biology techniques such as colony polymerase chain reaction and DNA sequencing. pH, total acid number, and dissolved oxygen were also measured in the fuel and water layers of the ultra-pure water-fuel mixtures.

Raman and x-ray diffraction revealed lepidocrocite, goethite, magnetite, and iron formate hydrate as the dominant corrosion products found on the 1018 steel coupon samples. Corrosion rates were highest among steel coupon samples exposed in ultra-low sulfur diesel in comparison to samples exposed in B100 and B20 fuels.

As far as microbiological contamination within samples, two different microorganisms, a fungus, *Paecilomyces variotti*, and the bacteria *Ralstonia solanacearum* were successfully cultured and isolated from the fuel-water interface and water layer of the B20 and ULSD fuel-water mixtures in the experiment. Microbiological effects in the form of sludge was observed only on 1018 steel coupons exposed in the B20 fuel-water mixtures set in an aerobic environment.

Contents

List of Figures

List of Tables

Chapter 1

Introduction

The production of biodiesel fuels has emerged as an alternative fuel of petroleum diesel worldwide. Cleaner emissions and availability are known advantages of using biodiesels. Biodiesels are essentially ester-based fuels derived from vegetable oils or animal fats through a transesterification process [1]. Few studies have taken into consideration the biological nature of biodiesels and their corrosive effects in the pipeline transportation and long-term storage sectors.

Corrosion is defined as the deterioration of metals which is caused by electrochemical processes in which electrons are transferred to an external electron acceptor causing the release of the metal ions into the surrounding medium [2]. Literature has shown that microbiologically influenced corrosion (MIC) enhances or accelerates corrosion. MIC is also caused by electrochemical processes where microorganisms accelerate the corrosion of metals [3]. The microorganisms of primary interest in this research are bacteria.

1.1 Objectives of this Study

This project is a comprehensive study to elucidate the effects of biodiesel on MIC of 1018 plain-carbon steel that are typically used for pipelines, storage tanks, and fuel tanks. Corrosion testing and microbial analysis will encompass a biodiesel-freshwater system.

Chapter 2

Literature Review

2.1 Introduction

Microbiologically influenced corrosion (MIC) is an electrochemical process where microorganisms initiate, facilitate, or accelerate a corrosion reaction on a metal surface [3]. There are three types of microorganisms. These include bacteria, fungi, and algae. Bacteria will be the focus in this project. Bacteria are ubiquitous single-celled prokaryotic organisms. They vary in size and shape, each having its own characteristics. Some bacteria are pathogenic, but the majority is beneficial to us and the environment.

In MIC, sulfur-reducing bacteria (SRB) are the most notable and have been shown to accelerate corrosion [2]. These types of bacteria are anaerobic and produce hydrogen sulfide which acidifies the environment. They are also responsible for catalyzing the penetration of hydrogen into steels, a phenomenon known as sulfide-induced stress cracking. One theory suggests SRBs utilize molecular hydrogen resulting from the following anodic and cathodic reactions shown below.

$$Fe \rightarrow Fe^{2+} + 2e^{-} \text{ (Anodic)}$$

$$2H^{+} + 2e^{-} \rightarrow H_2 \text{ (Cathodic)}$$

or

$$2H_2S + 2e^{-} \rightarrow 2HS^{-} + H_2 \text{ (Cathodic)}$$

This removal of hydrogen is termed cathodic depolarization as it facilitates the electrochemical cathodic reaction which is considered the controlling step in the overall corrosion process [4]. A second theory suggests that SRBs stimulate corrosion by anodic depolarization [4]. This is

possible by the localized acidification at the anode which results from the formation of iron sulfide corrosion products as depicted by the reaction below.

$$Fe^{2+} + HS^- \rightarrow FeS + H^+$$

Both theories result in the production of sulfide which results in the precipitation of ferrous sulfide corrosion products within the anoxic regions of the biofilm. Both reduced ferrous and sulfide ions are subject to oxidation across the biofilm interface which in turn generates further corrosion products of the form ferric oxide and or hydroxide and elemental sulfur as shown by the reaction below [4].

$$S + H_2O + 2e^- \rightarrow HS^- + OH^-$$

Corrosion products ferric oxide and or hydroxide and elemental sulfur are often indicative of active SRB corrosion [4]. SRBs are just one type of bacteria which have been shown to accelerate corrosion. Others include sulfur-oxidizing bacteria, iron-oxidizing/reducing bacteria, manganese-oxidizing bacteria, and bacteria secreting organic acids and slime [2].

The organic nature of biodiesels makes it a prime target for microbial contamination mainly in the form of bacteria. Bacteria are able to survive in these fuels whenever there is the presence of water. Microorganisms generally flourish in the water phase, but feed on fuel at the water-fuel phase boundary [5]. Contamination of fuel by microorganisms can cause biofouling. Whenever biofouling occurs, an extracellular polymeric substance is formed at the fuel-water interface. This is more commonly known as the biofilm. The term biofilm refers to the development of microbial communities on submerged surfaces in aqueous environments [6]. Thus, a bacterial consortium is formed and corrosion is accelerated due to the variety of bacteria present.

2.2 Biodiesels

Biodiesel can be used in its pure form (B100) or blended with petroleum diesel as another source of renewable energy. Biodiesel, in comparison to petroleum fuel, has the advantage of being biodegradable and non-toxic, having higher flash point, and causing reduced emissions. However, the major cons of biodiesel include its oxidative instability, poorer low-temperature properties, slightly lower power and torque generation, and higher fuel consumption [7].

Biodiesel is synthesized from vegetable oils and or animal fats which mainly contain triglyceride molecules. Unfortunately, glycerides cause the natural oils to thicken and become sticky; hence the natural oils are converted from triglycerides into three mono-alkyl esters via transesterification. The glycerol is removed as a by-product and the esters that remain comprise the biodiesel. Hence, biodiesel can be synthesized from many different types of natural oils and as a result many acronyms are used to describe their origins: For example, they are soybean methyl ester (SME), rapeseed methyl ester (RME), fatty acid methyl ester (FAME), and palm oil methyl ester (POME) to name a few. A study has shown that the fatty acid profiles of biodiesels differ based on the source. Biodiesel from coconut oil, palm oil, and tallow contained more saturated acids; whereas, biodiesel from soybean, sunflower, rapeseed, calona, etc. contained more unsaturated fatty acids [7]. Therefore, it can be expected that coconut or palm oil based biodiesels are less prone to oxidation than biodiesels based on sources that contain higher amounts of unsaturated acids.

A number of studies have also been conducted to assess biodiesel compatibility with different materials. In one study, petroleum diesel, a soybean-derived biodiesel, and a sunflower-derived biodiesel were tested for material compatibility against structural carbon steel (ASTM A36) and high density polyethylene (HDPE) [8]. Weight loss data for the samples over a 60 and

115 day immersion revealed that time is a relevant factor in diesel-fuel action on the carbon steel, which experienced a fourfold weight loss between the two time periods. The soybean-derived biodiesel was also found to be more compatible with carbon steel than the petroleum diesel and sunflower biodiesel. Immersion experiments regarding the HDPE revealed a significant weight gain instead of a mass loss. The HDPE immersed in petroleum diesel showed the highest weight gain, while those immersed in the other two biodiesels show minimum weight gain. In terms of fuel ageing, Fourier transform infrared spectroscopy (FTIR) was used to monitor the different fuels before and after their immersion experiments. Surprisingly, ageing was shown to take place only in the biodiesels which had very little effect on the degradation of the carbon steel and HDPE. The petroleum diesel, which did not age, was the most aggressive towards the steel and HDPE.

In 2007, a study on the corrosion rates of a piston metal and piston liner metal immersed in biodiesel originating from various seed oils (*Pongamia glabra*, *Salvadora oleoides*, *Madhuca Indica*, and *Jatropha curcas*) revealed that the biodiesel comprised of Salvadora oil was the most aggressive leading to the corrosion rate for the piston metal and piston liner metal of 0.1236 and 0.1329 mpy respectively [9]. Interestingly, petroleum diesel showed low corrosivity and was tied with biodiesel comprised of Pongamia and Madhuca oil as having the lowest corrosion rates for piston metal and piston liner metal of 0.0058 and 0.0065 mpy, respectively. Kaul et al [9] attributed the higher corrosivity of the biodiesel comprised of Salvadora oil to the higher percentage of sulphur content.

Another study in 2008 tested the corrosive effects of biodiesel derived from rice husk on aluminum, mild steel (Q235A), brass (H62), and austenite stainless steel (SS321, 1Cr18Ni9Ti) [10]. Three bio-oil-diesel emulsions were used which were 100% biodiesel, 30% biodiesel, and

10% biodiesel. Capped 50 mL glass bottles were used to hold the metal samples whereupon the coupons were immersed in their respective fuel emulsions. The bottles were then placed at room temperature (25°C), 50°C, and 70°C with weight loss data of the coupons taken at intervals of 6, 12, 24, 48, 72, and 120 h. It was reported that the most significant weight loss was observed for mild steel, followed by aluminum, while brass exhibited only slight weight loss. Also, for elevated temperatures, the weight loss rates were found to greatly increase. Stainless steel was not affected under any of the conditions. The 100% biodiesel fuel was found to be the most corrosive followed by the emulsions with 30% biodiesel and 10% biodiesel. Qiang et al [10] attributed this to the fact that the 10% and 30% emulsions of bio-oil with diesel have a limited contact area between the metal surfaces since the diesel is the continuous phase in the emulsions.

In 2010, Haseeb et al [11] investigated the corrosion behavior of copper and bronze in diesel and palm biodiesel. Static immersions of test coupons were conducted at two different temperatures, room temperature (25 - 30°C) and 60°C. At room temperature, the fuels tested were diesel, 50% palm biodiesel, and 100% palm biodiesel for an exposure time of 2640 h. At 60°C, diesel, 100% palm biodiesel and 100% oxidized palm biodiesel were tested for an exposure time of 840 h. Copper was shown to have higher corrosion rates in comparison to leaded bronze. A corrosion rate of 0.042 compared to 0.018 mpy for 100% palm biodiesel at room temperature and 0.053 versus 0.023 mpy for 100% palm biodiesel at 60°C. It is believed that the improved corrosion resistance of bronze is due to the presence of alloying elements such as tin (Sn) [9]. Kaul et al [9] also noted that biodiesel exposed to different metals showed significant degradation, as evidenced by an increased TAN (total acid number), oxidation product rate, along with free water content with increasing concentration of biodiesel in blends. The permissible TAN as stated by ASTM standard D6751 is 0.8 mg KOH/g. It was found that

the TAN values of diesel when exposed to copper and bronze for 2640 h remained relatively constant at a value of approximately 0.25. When copper and bronze were exposed to 50% and 100% palm biodiesel, there was an increase in TAN after the exposure. This was especially true for 100% palm biodiesel, where the TAN increased from an initial 0.5 to approximately 1.1. As stated before, the permissible TAN as stated by ASTM standard D6751 is 0.8 mg KOH/g which was clearly exceeded in the case of the copper and bronze coupons exposed in the 100% palm biodiesel for only 2640 h. Thus, it can be seen that increased TAN indicate the oxidation of biodiesel [9].

In 2010, Fazal et al [12] performed an investigation on the corrosion behavior of copper (99.99% pure), aluminum (99% pure), and stainless steel (316) in diesel and palm biodiesel. Test coupons were immersed in both diesel and palm biodiesel (continually stirred at 250 rpm) at 80°C for 1200 h. The results revealed that copper had the highest corrosion rate of 0.586 mpy followed by aluminum with 0.202 mpy and stainless steel having the lowest at 0.015 mpy. Copper again was shown to have the highest TAN which suggests that copper acts as a strong catalyst to oxidize the biodiesel. Also, it was noted that the difference in TAN between stainless steel and copper exposed biodiesel was very small, but the difference in their respective corrosion rates varied greatly. This suggests that the corrosiveness of the fuel is the same, but the copper is less resistant compared to the stainless steel. There is no strong correlation between the change in the acid number and the degree of corrosion on the exposed metal. Similarly in 2012, Fazal et al [13] set out to investigate the degradation mechanism of different automotive materials such as copper, brass, aluminum, and cast iron by characterizing the corrosion products. The corrosion effects of palm biodiesel and diesel at room temperature (25 - 27°C) for an exposure time of 2880 h was investigated. The corrosion rates were found to be the following for

copper, brass, aluminum, and cast iron: 0.39278, 0.209898, 0.173055, and 0.112232 mpy respectively for palm biodiesel. In the case of diesel, the rates were the following for copper, brass, aluminum, and cast iron: 0.158296, 0.120122, 0.084055, and 0.77402 mpy respectively. Thus, it was shown that palm biodiesel was more corrosive than diesel, and that copper showed the most severe corrosion.

Biodiesel has a higher affinity toward moisture content in comparison to petroleum diesel, and the water retaining capacity of biodiesel is much higher than diesel [14]. The hygroscopic fatty acid methyl ester (FAME) compounds are the primary reason for biodiesel being much more hydrophilic than diesel. Although the maximum water content allowed by ASTM standard D6751 is 500 $mg \cdot kg^{-1}$, water contamination often occurs in storage, where temperature and humidity greatly affect the amount of excess water absorbed within the surrounding environment. Water contamination within biodiesel also poses a serious problem as it harbors and facilitates the growth of microorganisms which could then lead to the corrosion of metals, and the formation of sludge and slime, thereby constricting fuel filters and fuel lines. [5, 14]. Water at high temperatures has also been shown to hydrolyze esters as well as triglycerides and produce different types of fatty acids which are more corrosive [11].

Therefore, a study in 2012 was carried out to determine the water absorbance of samples of biodiesel and biodiesel-diesel fuel blends by evaluating the temperature and blend ratio parameters [14]. Diesel and Brazilian biodiesel and subsequent blends in the form of 5%, 10%, 20%, 40%, 60%, 80%, and 100% biodiesel were the fuels tested. The methods employed to measure water content consisted of the Karl Fischer measurement, moisture absorption, turbidity measurements (clear and bright test), and high-temperature simulated distillation gas chromatography. The results revealed that the water absorption capacity of 100% biodiesel and

diesel oil rapidly decrease if the temperature drops. At a temperature of 293.15 and 323.15 K, 100% biodiesel absorbed 15 and 10 times more water respectively than diesel. Fregolente et al [14] ultimately concluded that the soluble water content of biodiesel, diesel, and blends depends strongly on the temperature and blend ratio. Blending creates a mixture with a lower capacity for water absorption, while the addition of biodiesel in diesel increases the water holding capacity of the blend. Also it was found that under a relative humidity of 79% and 66%, there was an increase of 51% and 23% respectively, of water content for 100% biodiesel and an increase of only 8% and 7% respectively, of water content for diesel samples.

Due to the inherent nature of biodiesel to absorb water, microbial contamination is a serious problem as the presence of such organisms enhances corrosion via biocorrosion or MIC.

2.3 Biocorrosion/MIC

Biocorrosion, is a result of interactions, which are often synergistic, between the metal surface, abiotic corrosion products, and bacterial cells and their metabolites [2]. A unifying electron-transfer hypothesis offers MIC of ferrous metals as a model system for the study of metal-microbe interactions. It states that biocorrosion is a process in which metabolic activities of microorganisms associated with metallic materials supply insoluble products which are able to accept electrons from the base metal. This sequence of biotic and abiotic reactions produces a kinetically favored pathway of electron flow from the metal anode to the universal electron acceptor, oxygen [4]. However, the hypothesis does not take into account the possibility that the organic component of the biofilm matrix itself can facilitate electron transfer from the metal to an electron acceptor such as oxygen. For example, enzymes active within the biofilm matrix and metal ions bound by bacterial extracellular polymeric substances can catalyze cathodic reactions [2]. Thus, it is important to take a closer look at the biofilm to understand its role in biocorrosion.

2.4 Biofilm

The development of the biofilm is facilitated by the production of extracellular polymeric substances (EPS) comprising macromolecules such as proteins, polysaccharides, nucleic acids and lipids [2]. Growth of the biofilm is considered to be the result of complex processes involving the transport of organic and inorganic molecules and microbial cells to the surface, adsorption of molecules to the surface, and initial attachment of microbial cells followed by their irreversible adhesion facilitated by production of EPS, often referred to as the glycocalyx or slime [15]. It has also been documented that degradation of metal surfaces occurs when the contact between microbial cells, or products of their metabolism such as EPS, and the surface is established [16].

The EPS plays an important role in attachment to metal surfaces. It also has the ability to complex with metal ions [16]. This is important since for all bacteria to grow, metal ions are required. The availability and type of ions are likely to have an effect on the colonization of a metal surface [16].

2.5 Case Studies

The coupling of microorganisms to corrosion usually gives the adverse effect of accelerated corrosion. MIC has posed to be a serious problem in biodiesel usage, storage, and transportation. Here is a summary of notable studies documenting the extent of biocorrosion damage to storage tanks and pipeline steel.

In 2010, Aktas et al [17] exposed biodiesel to anaerobic microorganisms from fresh water and marine environments with differing histories of exposure to hydrocarbons, biodiesel, and oxygen. Gas chromatography was used to measure biodegradation of biodiesel, while electrochemical and imaging techniques was used to monitor corrosion of carbon steel over a 60

day period. A soy-based biodiesel was used in their experiments. A total of five different anaerobic inocula were used as the microbial contaminant. The experiment was performed in triplicate with environmental conditions stated as seawater immersion, seawater/biodiesel interface, and biodiesel immersion. Two common features of the five diverse anaerobic inocula were that they could reduce sulfate or produce methane in less than or equal to one month in biodiesel-amended incubations, well in excess of biodiesel-free or sterile negative controls, and that all inocula metabolized biodiesel, regardless of their freshwater or marine origins or prior history to biodiesel, over a very short time period, from weeks to one month.

Another study performed in the same year designed experiments to evaluate the nature and extent of microbial contamination and the potential for MIC in alternative fuels, i.e., biodiesel, ULSD, and blends of the two. The main objectives of this work was to characterize the corrosion and electrochemical behavior of storage and fuel tank alloys in the presence of alternative fuels over time, and to determine the microflora and chemistry of as-received fuels as a function of biodiesel content and storage time [18]. ULSD, L100, B100, B5, and B20 were the selected fuels for this experiment. Microorganisms were identified via denaturing gradient gel electrophoresis, DGGE, and by 16S rRNA for bacteria and 28S rRNA for fungi. The selected materials to represent fuel tank alloys were the following: carbon steel UNS C10200, stainless steel UNS S30403, and aluminum alloy UNS A95052. To ensure microbial contamination within the experiments, an inoculum was used from the sludge layer in a tank containing L100. After a two week period, the water layer was separated from the sludge using a separation funnel. 20 mL of this contaminated water was then added to each experimental fuel/water mixture which would be exposed for a total duration of six months. Lee et al [18] found that for each fuel/water combination, microorganism species diversity generally decreased over the six months. Stainless

steel exhibited no visual signs of corrosion. Visual and microscopic analyses revealed an absence of corrosion on C1020 in the presence of biodiesel, even in the lowest concentration. Lee et al [18] hypothesized that biodiesel has a passivating effect on C1020. In the case of aluminum, pitting was visually observed in all AA5052 fuel/water exposures. Overall, Lee et al [18] concluded that C1020 exhibited general active corrosion in ULSD and L100, and passive behavior in B100 and biodiesel/ULSD blends. SS304L remained passive in all exposures, and AA5052 was susceptible to subsurface pitting in the water and fuel layers, in addition to the fuel/water interface.

Chapter 3

Materials and Methods

3.1. Introduction

This section describes the materials and methods used for the biodiesel experiments.

3.2. Materials Used

Plain carbon 1018 steel was chosen as the material to be investigated based on its similar chemical compositions to that of ASTM A36 steel and API Spec 5L X60, which are often used for fuel tank storage and pipelines, respectively. Table 1 tabulates the chemical compositions of these specifications and 1018 grade steel.

Table 1. Chemical composition of selected specifications and 1018 steel.

Material Specifications	Chemical Composition			
	C, max. %	Mn, max. %	P, max. %	S, max. %
ASTM A36	0.25	-	0.04	0.05
API Spec 5L X60	0.28	1.40	0.03	0.03

Material	Chemical Composition			
	C, %	Mn, %	P, max. %	S, max. %
1018 Steel	0.15 - 0.20	0.60 - 0.90	0.035	0.04

The types of fuel that was chosen for this experiment were 100% biodiesel (B100), 20% biodiesel (B20), and ultra-low sulfur diesel (ULSD) for control. These fuels were obtained locally from gas stations (i.e., 76 and Aloha Petroleum gas stations). To further investigate the effects of biodiesel on corrosion, a second set consisting of sterilized versions of the aforementioned fuels were used. Sterility of the B100, B20, and ULSD fuels were achieved via vacuum filter sterilization by a 0.22 μm Millipore membrane filter.

3.3. Experimental Setup

The 1018 steel coupons were machined to the following dimensions: 2.25 in. x 1 in. x 0.125 in. A BenchMark 320 marking system was used to pin stamp the coupons for identification. The coupons were then acetone washed to remove any oil residue and weighed to obtain an initial mass. To prevent oxidation of the steel, the coupons were kept in a dry box (< 1% relative humidity) prior to the experiment.

Nanopure water was added to facilitate contamination within the fuels. This fuel-water mixture (40 mL fuel, 40 mL water) was stored in 100 mL glass Pyrex media bottles. The 1018 steel coupon samples were placed in these fuel-water mixtures at an approximate angle of 45° with respect to the horizon. Figure 1 depicts this setup.

Figure 1. Experimental setup of fuel-water mixtures with 1018 steel coupons immersed. Left to right: B100/water mixture, B20/water mixture, and ULSD/water mixture.

Triplicates of each fuel-water mixture and 1018 steel coupon were exposed outdoors under the three following environmental conditions: anaerobic, aerobic, and selective aerobic. UV exposure from the sun and rain water contamination was kept to a minimum by encasing

samples in boxes under a protective alcove. The following figure depicts the environmental systems.

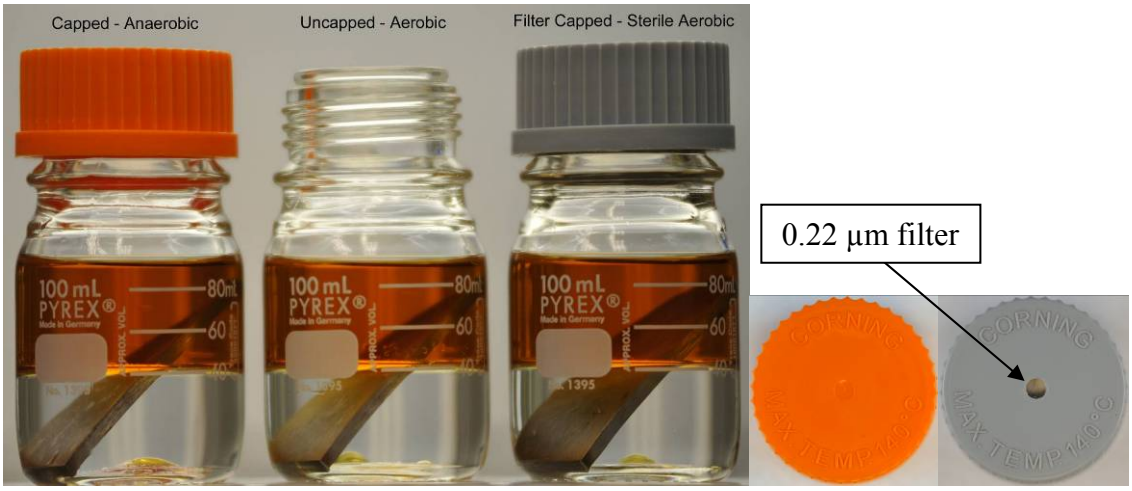

Figure 2. B100/water fuel mixture depicting anaerobic, aerobic, and selective aerobic environments. Anaerobic cap and selective aerobic cap depicted.

Bottles with an orange cap are sealed air-tight to simulate an anaerobic environment. Uncapped bottles simulate an aerobic environment, while bottles with a gray cap simulate a "sterile" aerobic environment. The gray cap is fitted with a 0.22 µm filter at the top to allow only air to be exchanged into and out of the bottle. Contamination from the outside environment will not be able to enter the bottle.

An exposure time of 6 months and 1 year were chosen for this experiment to compare and contrast the corrosion of the steel samples.

The following table summarizes the entire experimental design.

Table 2. Experimental design.

Fuel	Environment	Exposure Time
B100	Anaerobic	6 Months
B20	Aerobic	1 Year
ULSD	Selective Aerobic	
Sterile B100		
Sterile B20		
Sterile ULSD		

Therefore, since the experiment was run in triplicate, a total of 108 samples were exposed under these conditions. The following figure depicts the entire experimental setup and deployment.

Figure 3. 108 samples loaded in boxes to be exposed outdoors for six months and one year.

3.4. pH Measurements

pH measurements were taken of both water and fuel layers within samples. The pH was determined using a Thermo Scientific Orion gel-filled pH/ATC triode with epoxy body electrode connected to a Thermo Scientific Orion 4-star pH/RDO portable meter as depicted by Figure 4. Prior to taking measurements, a two buffer calibration procedure was performed to ensure accuracy. Since the predicted pH measurements were assumed to be more acidic than alkaline, buffers of pH 4 and 7 were used in this calibration process.

Figure 4. pH measurement setup.

3.5. Dissolved Oxygen (DO) Measurements

DO measurements were taken to determine how quickly oxygen was depleted from the three environmental conditions. DO readings were taken every 5 minutes for a duration of 1 hour using a Thermo Scientific field RDO probe connected to a Thermo Scientific Orion 4-star pH/RDO portable meter as depicted by Figure 5.

Figure 5. DO experimental setup.

3.6. Total Acid Number Measurements

TAN is essentially defined as the number of milligrams of KOH required to neutralize the acidity in one gram of oil [19]. Therefore, oil with high TAN values, approximately > 0.5, are less desirable since they have been known to cause problems with respect to corrosion and refinery processes [19].

Individual Dexsil Titra-Lube TAN kits as depicted by Figure 6 were used to determine the change in TAN of the fuels. These readings were taken upon receiving the fuels and upon completion of both exposure time periods of 6 months and 1 year.

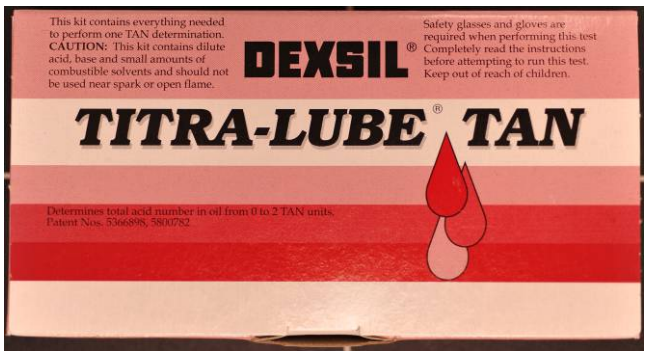

Figure 6. Dexsil TAN kit.

3.7. Microbial Contamination

A preliminary 1 month experiment was conducted to assess microbial contamination within B100 fuels. Blood agar plates which consist of tryptic soy agar with an addition of 5% defibrinated sheep blood was used as the microbial media to culture microorganisms within the B100 fuel. Blood agar plates are a general purpose media used to encourage growth of more fastidious microorganisms [20]. 100 µl samples of B100 fuels were pipetted onto blood agar plates and incubated aerobically for a maximum of 1 week at 35°C. Unfortunately, no microorganisms could be cultured directly from the fuel. Literature suggests that microorganism

contamination only occurs with the introduction of water into the fuel [5]. Therefore, a B100 fuel-water mixture consisting of 10 mL of B100 fuel and 10 mL of deionized water was exposed outdoors aerobically for 1 month in 100 mL Pyrex media bottles. After the 1 month exposure, 100 µl of the water layer in the B100 fuel-water mixture was plated on blood agar plates and incubated as described previously. The following figures depict the isolated bacteria colonies cultured in the laboratory from this preliminary experiment along with their species specific molecular identification.

Figure 7. Bacteria sample, 16S rRNA sequencing yields a 65% match to the bacterial species *Bacillus licheniformis*.

Figure 8. Bacteria sample, 16S rRNA sequencing yields a 98% match to the bacterial species *Aeromicrobium tamlense*.

Figure 9. Bacteria sample, 16S rRNA sequencing yields a 98% match to the bacterial species *Bacillus horikoshi*.

Figure 10. Bacteria sample, 16S rRNA sequencing yields a 93% match to the bacterial species *Bacillus novalis*.

Upon isolation of these microorganisms, colony polymerase chain reaction (PCR) was carried out according to Suzuki et al [21] using a thermal cycler depicted by Figure 11. The products of the PCR were sent to be sequenced at Greenwood Molecular Biology Facility located on the University of Hawaii at Manoa campus. Upon successful sequencing of the PCR products, species specific bacteria identification was possible using a BLAST search database.

All fuel samples used in this experiment underwent similar microbial screening for contamination. Existing microorganisms within fuels were determined by plating 100 µl samples of fuels on blood agar and tryptic soy agar plates. Tryptic soy agar plates were used since it is considered a standard media in microbiology [20]. Plates were incubated in an aerobic incubator set to 26°C and monitored for 1 week.

Upon sample retrieval of the 6 month exposure and 1 year exposure times, another sampling of fuels, fuel-water layer interface, and water were carried out. Again, 100 µl of fuel, fuel-water layer, and water from samples were plated on blood agar, tryptic soy agar, and an

additional type of media, R2A. Samples were incubated for 1 week in an aerobic and anaerobic incubator for 1 week at a temperature of 26°C.

Microbial contamination was then down-processed via molecular biology techniques such as polymerase chain reaction and genetic sequencing to identify up to the species level of microorganisms as previously performed in the preliminary microbial contamination experiment.

Figure 11. Eppendorf thermo cycler.

3.8. Corrosion Product Characterization – Raman Spectroscopy

Characterization of corrosion product via Raman spectroscopy was performed similarly to Li et al [22]. A Nicolet Almega XR dispersive Raman Spectrometer (Thermo Scientific Corp.) equipped with multiple Olympus objectives and a Peltier-cold charge-coupled device (CCD) detector was used for the experiments. An objective with magnification of 50× with estimated

spatial resolutions of 1.6 μm was used. The instrument was operated with laser sources of a green Nd:YAG laser with 532 nm wavelength excitation and an infrared diode laser with 780 nm wavelength excitation.

The maximum spectra resolution was up to 2.2 – 2.6 cm-1 using a 25 μm pinhole or slit, which requires longer acquisition time and produces more noise. To reduce the collecting time, an aperture of 100 μm pinhole was used, giving an estimated resolution in the range of 8.4 – 10.2 cm-1. The accumulation time was 120 seconds.

Figure 12. Raman spectroscopy setup.

3.9. Corrosion Product Characterization – Scanning Electron Microscope (SEM)

A Hitachi S-3400N SEM equipped with an Oxford Instruments energy dispersive X-ray analyzer system was used to characterize the 1018 steel coupons. Quantitative elemental analysis (fixed-point) was conducted on corroded regions on sample steel coupons.

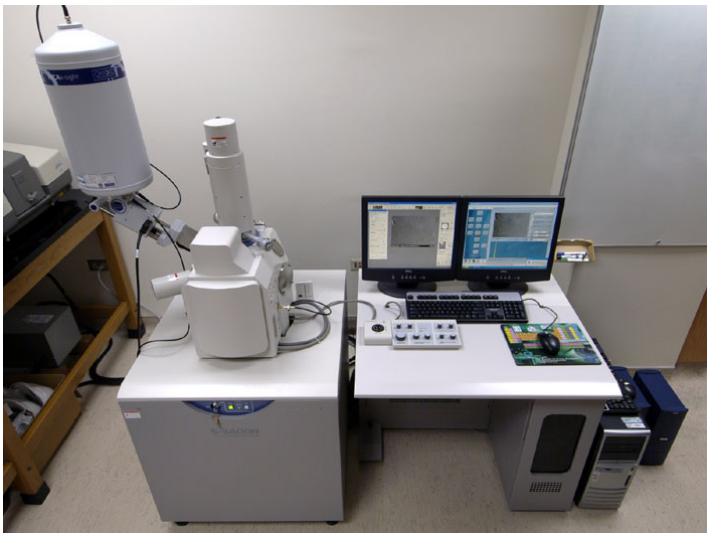

Figure 13. SEM/EDXA setup.

3.10. Corrosion Product Characterization – X-Ray Diffraction (XRD)

A Rigaku MiniFlex™ II benchtop XRD system equipped with a Cu (Kα) radiation was used for XRD measurements. X-ray diffraction spectra were obtained directly on the corroded steel coupon surfaces. The scans were done in the range of 3 – 90° (2(θ)). A scan speed of 1° (2θ)/min was used.

Figure 14. XRD analysis setup.

3.11. Weight Loss Technique

The penetration rate (mm/year) was calculated for each steel coupon based on the total mass loss. The following equation was used to calculate the penetration rate for steel coupon samples:

$$Penetration\ Rate = \frac{\Delta m}{A \cdot t} x \frac{1}{\rho}$$

where Δm is the change in mass in grams, A the area of the sample in mm^2, t the time in years, and ρ the density of the 1018 steel in g/mm^3.

To obtain the total mass loss, the steel coupons were cleaned with an acid wash to remove any corrosion product. The acid wash procedure followed ISO 8407 – "Removal of corrosion products from corrosion test specimens." After acid washing and air drying, the steel coupons were weighed and compared to their respective initial mass values to obtain the total mass loss.

Chapter 4

Thermodynamics of Iron

To determine thermodynamically whether iron will have the tendency to corrode in an aerated fuel-water solution of pH (0, 1, 2, 3, 4, 5, 6, and 7) at 30ºC, the following calculations were made.

The following represent the anodic reaction or the oxidation of iron, and the cathodic reaction or the reduction of oxygen. Their respective standard potentials, Φ°, are given, measured in volts with respective to the standard hydrogen electrode.

$$Fe \rightarrow Fe^{2+} + 2e^- \qquad (\Phi^\circ = -0.440 \text{ VSHE})$$

$$O_2 + 2H_2O + 4e^- \rightarrow 4OH^- \qquad (\Phi^\circ = 0.401 \text{ VSHE})$$

Balancing these two reactions yields the following overall reaction:

$$2Fe \rightarrow 2Fe^{2+} + 4e^-$$
$$O_2 + 2H_2O + 4e^- \rightarrow 4OH^-$$

$$2Fe + O_2 + 2H_2O \rightarrow 2Fe^{2+} + 4OH^-$$

The overall electrochemical cell potential of the cell is defined by the following equation below:

$$E_{cell} = \phi_{O_2/OH^-} - \phi_{Fe^{2+}/Fe}$$

where ϕ_{O_2/OH^-} is the equilibrium or reversible potential for the cathodic reaction, and $\phi_{Fe^{2+}/Fe}$ is the equilibrium or reversible potential for the anodic reaction. ϕ_{O_2/OH^-} can also be re-written in the form of the Nernst Equation which follows below:

$$\phi_{O_2/OH^-} = \phi^\circ_{O_2/OH^-} - \frac{2.303RT}{nF}\log\frac{(a_{OH^-})^4}{(a_{O_2})(a_{H_2O})^2}$$

where $\phi^\circ_{O_2/OH^-}$ is defined as the equilibrium or reversible standard state potential, R the universal gas constant, 8.314 *J/K•mol*, T, the temperature in *K*, n, the number of electrons, F, Faraday's constant, 96,487 *C/mol*, and a_{OH^-}, a_{O_2}, a_{H_2O}, the respective activities. The activities are calculated as follows below:

$$a_{OH^-} \times a_{H^+} = 10^{-14}$$
$$a_{H^+} = 10^{-pH}$$
$$a_{OH^-} = \frac{10^{-14}}{10^{-pH}}$$

For the activity a_{OH^-}, it can be shown from above that a_{OH^-} is related to the pH. In the case for activity a_{O_2}, as shown below, the activity is related to the partial pressure of oxygen which accounts for roughly 20% of air.

$$a_{O_2} = \frac{P_{O_2}}{1\ atm}$$
$$a_{O_2} = \frac{0.2\ atm}{1\ atm} = 0.2$$

Lastly, the activity a_{H_2O} is simply equal to 1 since water is a one component heterogeneous phase.

$$a_{H_2O} = 1$$

Thus, the following table tabulates the equilibrium potential $\phi^\circ_{O_2/OH^-}$ for varying pH values.

Table 3. Equilibrium potential of $\phi°_{O_2/OH^-}$ for various pH values.

pH	ϕ_{O_2/OH^-} (V_{SHE})
0	1.2323
1	1.1722
2	1.1120
3	1.0519
4	0.9918
5	0.9316
6	0.8715
7	0.8114

Similarly, the equilibrium or reversible potential for the anodic reaction, $\phi_{Fe^{2+}/Fe}$, can also be re-written in the form of the Nernst Equation which follows below:

$$\phi_{Fe^{2+}/Fe} = \phi°_{Fe^{2+}/Fe} - \frac{2.303RT}{nF}\log\frac{(a_{Fe})^2}{(a_{Fe^{2+}})^2}$$

Again, $\phi°_{Fe^{2+}/Fe}$ is defined as the equilibrium or reversible standard state potential, R the universal gas constant, 8.314 *J/K•mol*, T, the temperature in K, n, the number of electrons, F, Faraday's constant, 96,487 *C/mol*, and a_{Fe}, $a_{Fe^{2+}}$, the respective activities. The activities are calculated as follows below:

$$a_{Fe} = 1$$

The activity a_{Fe} shown above is equal to 1 since iron is a one component heterogeneous phase. For the activity $a_{Fe^{2+}}$, more detailed calculations are required as depicted below.

$$a_{Fe^{2+}} = \frac{K_{sp}}{(a_{OH^-})^2}$$

For iron(II) hydroxide, $Fe(OH)_2$, the reaction and solubility product, K_{sp}, is given below.

$$Fe(OH)_2 \rightarrow Fe^{2+} + 2OH^-$$
$$K_{sp} = 8\times10^{-16}$$

Therefore the activity $a_{Fe^{2+}}$ can be solved by the following:

$$a_{Fe^{2+}} \times (a_{OH^-})^2 = 8 \times 10^{-16}$$

where the activity a_{OH^-}, is calculated as before.

$$a_{OH^-} = \frac{10^{-14}}{10^{-pH}}$$

Hence, the following table tabulates the equilibrium potential $\phi°_{Fe^{2+}/Fe}$ for varying pH values.

Table 4. Equilibrium potential of $\phi°_{Fe^{2+}/Fe}$ for various pH values.

pH	$\phi_{Fe^{2+}/Fe}$ (V_{SHE})
0	-0.0521
1	-0.1122
2	-0.1723
3	-0.2325
4	-0.2926
5	-0.3527
6	-0.4128
7	-0.4730

Now the overall electrochemical cell potential can be calculated.

$$E_{cell} = \phi_{O_2/OH^-} - \phi_{Fe^{2+}/Fe}$$

The table below tabulates the overall electrochemical cell potential.

Table 5. Overall electrochemical cell potential for various pH values.

pH	ϕ_{O_2/OH^-} (V_{SHE})	$\phi_{Fe^{2+}/Fe}$ (V_{SHE})	E_{cell} (V)
0	1.2323	-0.0521	1.2844
1	1.1722	-0.1122	1.2844
2	1.1120	-0.1723	1.2843
3	1.0519	-0.2325	1.2844
4	0.9918	-0.2926	1.2844
5	0.9316	-0.3527	1.2843
6	0.8715	-0.4128	1.2843
7	0.8114	-0.4730	1.2844

Therefore, since $E_{cell} > 0$ in all cases, the reaction is spontaneous to the right and iron has the tendency to corrode in the system.

Similarly, to determine thermodynamically whether iron will have the tendency to corrode in a deaerated fuel-water solution of pH (0, 1, 2, 3, 4, 5, 6, and 7) at 30ºC, the following calculations were carried out below.

The following represent the anodic reaction or the oxidation of iron, and the cathodic reaction or the evolution of hydrogen. Their respective standard potentials, Φ° , are given, measured in volts with respective to the standard hydrogen electrode.

$$Fe \rightarrow Fe^{2+} + 2e^- \qquad (\Phi° = -0.440\ V_{SHE})$$

$$2H^+ + 2e^- \rightarrow H_2 \qquad (\Phi° = 0\ V_{SHE})$$

Balancing these two reactions yields the following overall reaction:

$$Fe \rightarrow Fe^{2+} + 2e^-$$
$$2H^+ + 2e^- \rightarrow H_2$$

$$Fe + 2H^+ \rightarrow Fe^{2+} + H_2$$

The overall electrochemical cell potential of the cell is defined by the following equation below:

$$E_{cell} = \phi_{H^+/H_2} - \phi_{Fe^{2+}/Fe}$$

where ϕ_{H^+/H_2} is the equilibrium or reversible potential for the cathodic reaction, and $\phi_{Fe^{2+}/Fe}$ is the equilibrium or reversible potential for the anodic reaction. ϕ_{H^+/H_2} can also be re-written in the form of the Nernst Equation which follows below:

$$\phi_{H^+/H_2} = \phi°_{H^+/H_2} - \frac{2.303RT}{nF}\log\frac{a_{H_2}}{(a_{H^+})^2}$$

where ϕ_{H^+/H_2} is defined as the equilibrium or reversible standard state potential, *R* the universal gas constant, 8.314 *J/K•mol*, *T*, the temperature in *K*, *n*, the number of electrons, *F*, Faraday's

constant, 96,487 *C/mol*, and a_{H_2}, a_{H^+}, the respective activities. The activities are calculated as follows below:

$$a_{H_2} = \frac{P_{H_2}}{1\ atm}$$
$$a_{H_2} = \frac{10^{-6}\ atm}{1\ atm}$$
$$a_{H_2} = 10^{-6}$$

For the activity a_{H_2}, it can be shown from above that a_{H_2} is related to the partial pressure of hydrogen which accounts for roughly 0.6 ppm of air. In the case for activity a_{H^+}, as shown below, the activity is related to pH.

$$a_{H^+} = 10^{-pH}$$

Thus, the following table tabulates the equilibrium potential ϕ_{H^+/H_2} for varying pH values.

Table 6. Equilibrium potential of ϕ_{H^+/H_2} for various pH values.

pH	ϕ_{H^+/H_2} (V_{SHE})
0	0.1804
1	0.1203
2	0.0601
3	0.0000
4	-0.0601
5	-0.1203
6	-0.1804
7	-0.2405

Similarly, the equilibrium or reversible potential for the anodic reaction, $\phi_{Fe^{2+}/Fe}$, can also be re-written in the form of the Nernst Equation which follows below:

$$\phi_{Fe^{2+}/Fe} = \phi^{\circ}_{Fe^{2+}/Fe} - \frac{2.303RT}{nF}\log\frac{a_{Fe}}{a_{Fe^{2+}}}$$

Again, $\phi°_{Fe^{2+}/Fe}$ is defined as the equilibrium or reversible standard state potential, R the universal gas constant, 8.314 *J/K•mol*, T, the temperature in K, n, the number of electrons, F, Faraday's constant, 96,487 *C/mol*, and a_{Fe} , $a_{Fe^{2+}}$, the respective activities. The activities are calculated in the same way as in the aerated case above. Hence, the following table tabulates the equilibrium potential $\phi°_{Fe^{2+}/Fe}$ for varying pH values.

Table 7. Equilibrium potential of $\phi°_{Fe^{2+}/Fe}$ for various pH values.

pH	$\phi_{Fe^{2+}/Fe}$ (V_{SHE})
0	-0.0521
1	-0.1122
2	-0.1723
3	-0.2325
4	-0.2926
5	-0.3527
6	-0.4128
7	-0.4730

Now the overall electrochemical cell potential can be calculated.

$$E_{cell} = \phi_{H^+/H_2} - \phi_{Fe^{2+}/Fe}$$

The table below tabulates the overall electrochemical cell potential.

Table 8. Overall electrochemical cell potential for various pH values.

pH	ϕ_{H^+/H_2} (V_{SHE})	$\phi_{Fe^{2+}/Fe}$ (V_{SHE})	E_{cell} (V)
0	0.1804	-0.0521	0.2325
1	0.1203	-0.1122	0.2325
2	0.0601	-0.1723	0.2324
3	0.0000	-0.2325	0.2325
4	-0.0601	-0.2926	0.2325
5	-0.1203	-0.3527	0.2324
6	-0.1804	-0.4128	0.2324
7	-0.2405	-0.4730	0.2325

Similar to the aerated case, since $E_{cell} > 0$ in all cases, the reaction is spontaneous to the right and iron has the tendency to corrode in the system.

These calculations serve to verify that iron will have the tendency to corrode regardless of oxygen levels within the environment since the environmental conditions of the experiment will consist of both anaerobic and aerobic settings.

Chapter 5

Corrosion Product Characterization

5.1. Introduction

This section summarizes the characterization of corrosion product found on sample steel coupons. Techniques such as Raman spectroscopy, XRD, and SEM/EDXA were used to characterize and determine any trends found in corrosion product.

5.2. Corrosion Product Morphology

A Nikon D700 DSLR camera equipped with AF Micro-NIKKOR 60mm f/2.8D was used to obtain images of sample coupons. The figures below depict the 6 month and 1 year steel coupons retrieved from specified environments. All steel coupons immersed in filtered and unfiltered B100 and B20 fuels were lightly acetone washed to remove oil residue prior to digital imaging. Steel coupons immersed in filtered and unfiltered ULSD did not have to be acetone washed as very little oil residue remained upon retrieval of coupons.

6 Month Steel Coupon Samples Exposed in Anaerobic Environment

B100 Unfiltered

B100 Filtered

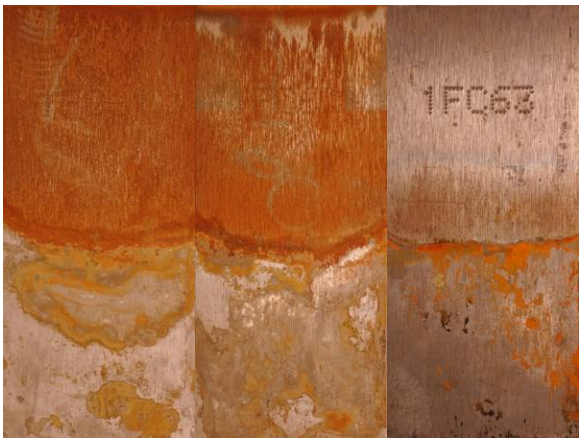

B20 Unfiltered

B20 Filtered

ULSD Unfiltered

ULSD Filtered

Figure 15. 6 month steel coupon samples exposed in an anaerobic environment segregated by type of fuel.

6 Month Steel Coupon Samples Exposed in Aerobic Environment

B100 Unfiltered

B100 Filtered

B20 Unfiltered

B20 Filtered

ULSD Unfiltered

ULSD Filtered

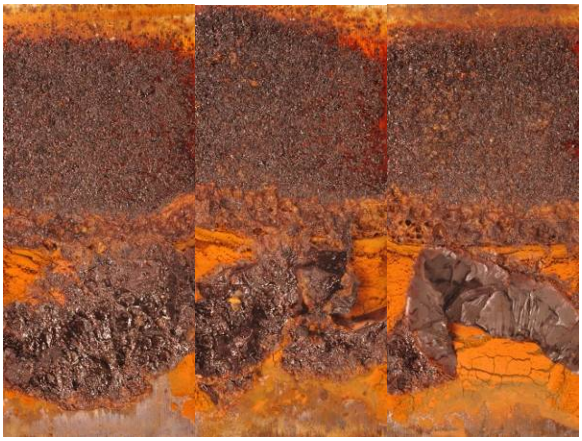

Figure 16. 6 month steel coupon samples exposed in an aerobic environment segregated by type of fuel.

6 Month Steel Coupon Samples Exposed in Selective Aerobic Environment

B100 Unfiltered

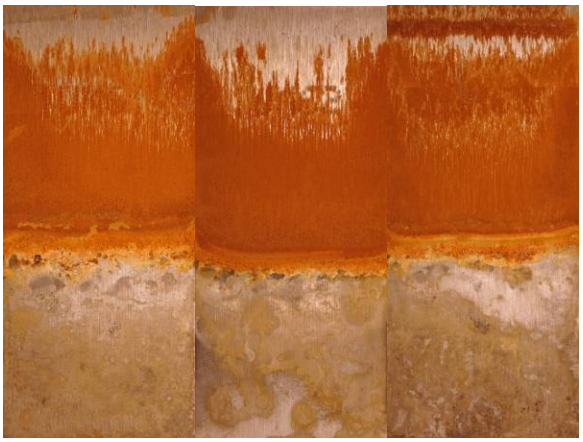

B100 Filtered

B20 Unfiltered

B20 Filtered

ULSD Unfiltered

ULSD Filtered

Figure 17. 6 month steel coupon samples exposed in a selective aerobic environment segregated by type of fuel.

1 Year Steel Coupon Samples Exposed in Anaerobic Environment

B100 Unfiltered

B100 Filtered

B20 Unfiltered

B20 Filtered

ULSD Unfiltered

ULSD Filtered

Figure 18. 1 year steel coupon samples exposed in an anaerobic environment segregated by type of fuel.

1 Year Steel Coupon Samples Exposed in Aerobic Environment

B100 Unfiltered

B100 Filtered

B20 Unfiltered

B20 Filtered

ULSD Unfiltered

ULSD Filtered

Figure 19. 1 year steel coupon samples exposed in an aerobic environment segregated by type of fuel.

1 Year Steel Coupon Samples Exposed in Selective Aerobic Environment

B100 Unfiltered

B100 Filtered

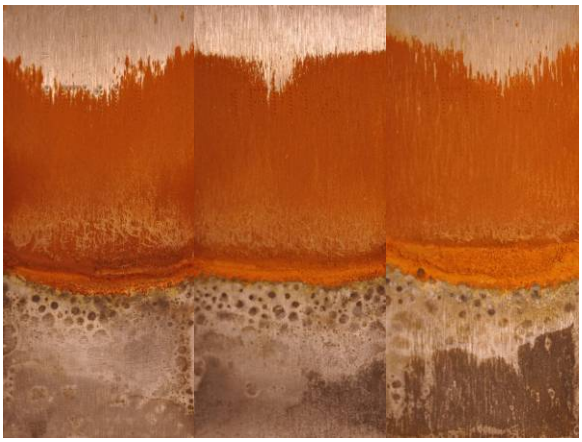

B20 Unfiltered

B20 Filtered

ULSD Unfiltered

ULSD Filtered

Figure 20. 1 year steel coupon samples exposed in a selective aerobic environment segregated by type of fuel.

These figures reveal trends on corrosion product deposition specific to location. For example, 6 month exposure steel coupons exposed in filtered and unfiltered B100 fuel-water mixtures exhibited corrosion product on the top part, or fuel layer, and interface of the coupon as depicted by Figures 15, 16, and 17. Corrosion product on the lower part, or water layer, of the coupons are non-existent or very sparse with the exception of some such as the steel coupons immersed in filtered B100 fuel-water mixtures exposed in a selective aerobic environment as depicted by Figure 17. In contrast, steel coupons exposed in B20 or ULSD fuel-water mixtures exhibit corrosion product primarily on the lower part, or water layer, of the coupon as depicted by Figures 15, 16, and 17. For the case of steel coupons immersed in filtered and unfiltered B20 fuel-water mixtures exposed in an aerobic environment, virtually no corrosion product was found as depicted by Figure 16. The steel coupons immersed in the filtered and unfiltered ULSD fuel-water mixtures exposed in an aerobic environment visually exhibited the worst corrosion as both top and bottom parts of the steel coupons were corroded as depicted by Figure 16.

For the 1 year exposure time period, steel coupons exposed in filtered and unfiltered B100 and B20 fuel-water mixtures exhibited very little corrosion product, with most, if any, located on the top part of the coupons as depicted by Figures 18, 19, and 20. Steel coupons immersed in filtered and unfiltered ULSD fuel-water mixtures followed the same trends as their 6 month exposure steel coupon counterparts as depicted by Figures 18, 19, and 20.

Microbial evidence was revealed only on steel coupons exposed to both filtered and unfiltered B20 fuel-water mixtures exposed in an aerobic environment. This was true for both 6 month and 1 year exposures.

Figure 21. Microbial contamination in the form of sludge on 1018 steel coupon exposed in filtered/unfiltered B20 fuel-water mixture in aerobic environment.

The sludge layer of the steel coupon as depicted by Figure 21 is visual evidence of microbial activity as suggested by literature [5, 14, 18].

5.3. Raman Spectroscopy

The following figures depict the results obtained via Raman spectroscopy for the 6 month exposure time period. The y-axis for all Raman results is an arbitrary intensity value, whereas the x-axis is the more important Raman shift in cm^{-1} which reveals the band locations of corrosion products.

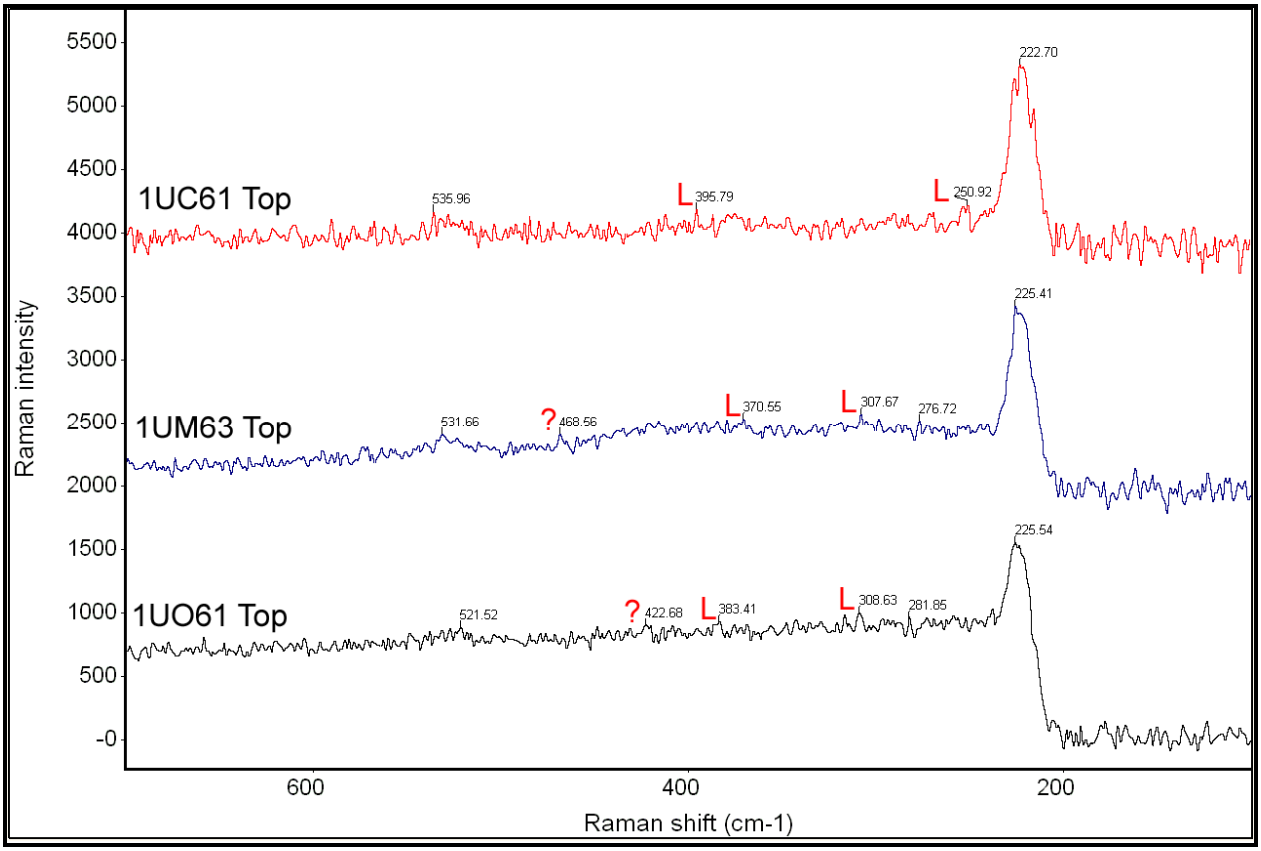

Figure 22. Raman spectroscopy of 6 months 1018 steel coupons exposed in unfiltered B100 fuel samples in anaerobic (1UC61), selective aerobic (1UM63), and aerobic (1UO61) environments.

Characteristic bands of lepidocrocite (250.92, 395.79, 307.67, 370.55, 308.63, and 383.41 cm^{-1}) [22] were observed for all steel coupons in Figure 22. Other bands (222.70, 535.96, 225.41, 276.72, 531.66, 225.54, 281.85, and 521.52 cm^{-1}) [22] in the figure are ghost bands obtained using the 780 nm laser system. Unfortunately, bands 468.56 and 422.68 cm^{-1} could not be

identified. In further analysis via XRD, corrosion product of iron formate hydrate is found. Thus, perhaps these bands belong to that corrosion product. Literature reveals no information regarding Raman band locations of this type of corrosion product.

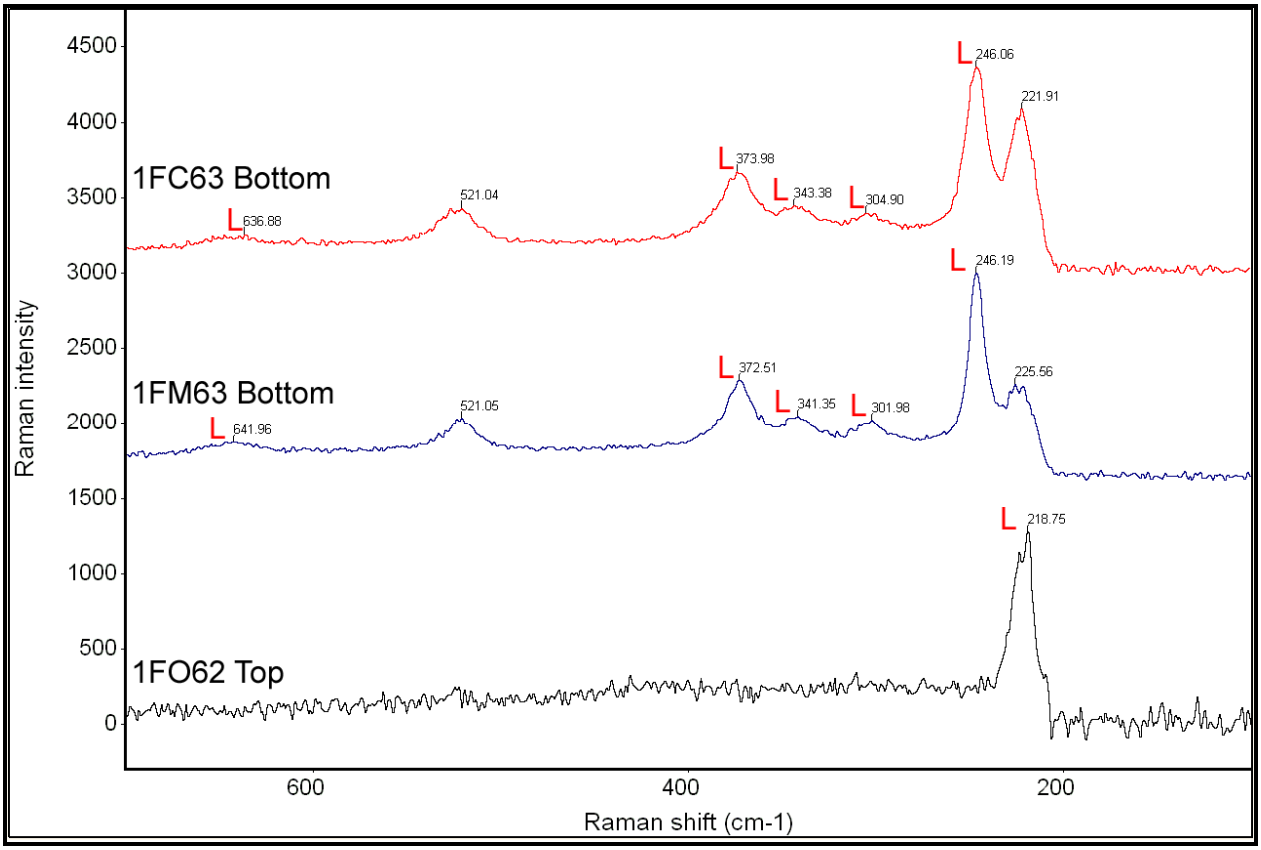

Figure 23. Raman spectroscopy of 6 months 1018 steel coupons exposed in filtered B100 fuel samples in anaerobic (1FC63), selective aerobic (1FM63), and aerobic (1FO62) environments.

Characteristic bands of lepidocrocite (246.06, 304.90, 343.38, 373.98, 636.88, 246.19, 301.98, 341.35, 372.51, 641.96, and 218.75 cm^{-1}) [22] were observed for all steel coupons in Figure 23. Again, the remaining bands (221.91, 521.04, 225.56, and 521.05 cm^{-1}) [22] are ghost bands.

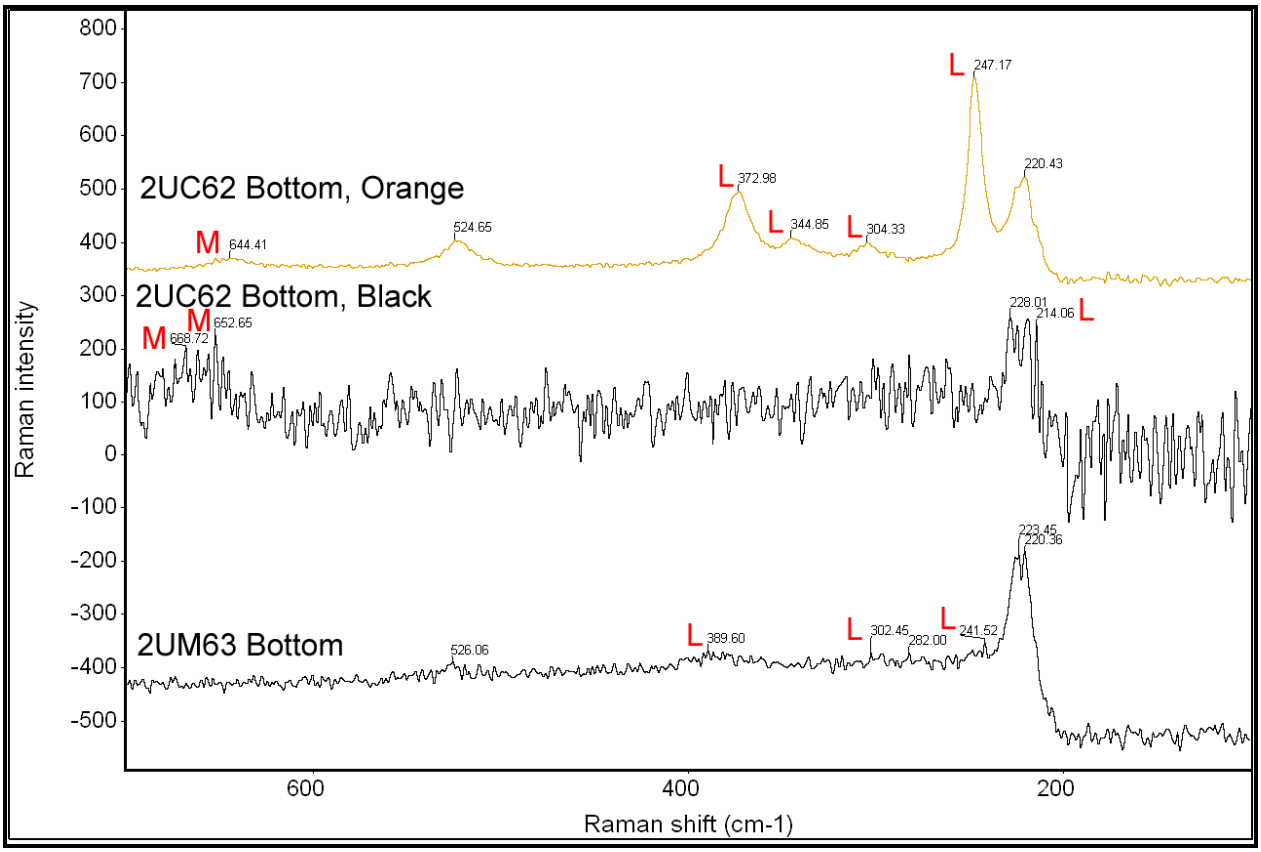

Figure 24. Raman spectroscopy of 6 months 1018 steel coupons exposed in unfiltered B20 fuel samples in anaerobic (2UC62) and selective aerobic (2UM63) environments.

1018 steel coupon 2UC62 has two spectrum obtained via Raman due to different corrosion product morphology sites (orange and black) on the coupon. Characteristic bands of lepidocrocite (247.17, 304.33, 344.85, 372.98, 214.06, 241.52, 302.45, and 389.60 cm^{-1}) [22] and magnetite (644.41, 652.65, and 668.72 cm^{-1}) [22] were observed as depicted in Figure 24. Remaining bands (220.43, 524.65, 228.01, 220.36, 223.45, 282.00, and 526.06 cm^{-1}) [22] were identified as ghost bands. Although Raman measurements were taken at two different sites on steel coupon 2UC62, both corrosion products of lepidocrocite and magnetite were observed. This is due to the observation that lepidocrocite seems to form over magnetite and vice versa. Hence, as the laser penetrates the sample, both corrosion products are detected. Lepidocrocite was the only corrosion product found on steel coupon 2UM63. Raman data is missing for steel coupons

exposed in unfiltered B20 fuel-water mixtures placed in aerobic environments since no corrosion product was detected upon acetone washing the sludge layer off the coupons.

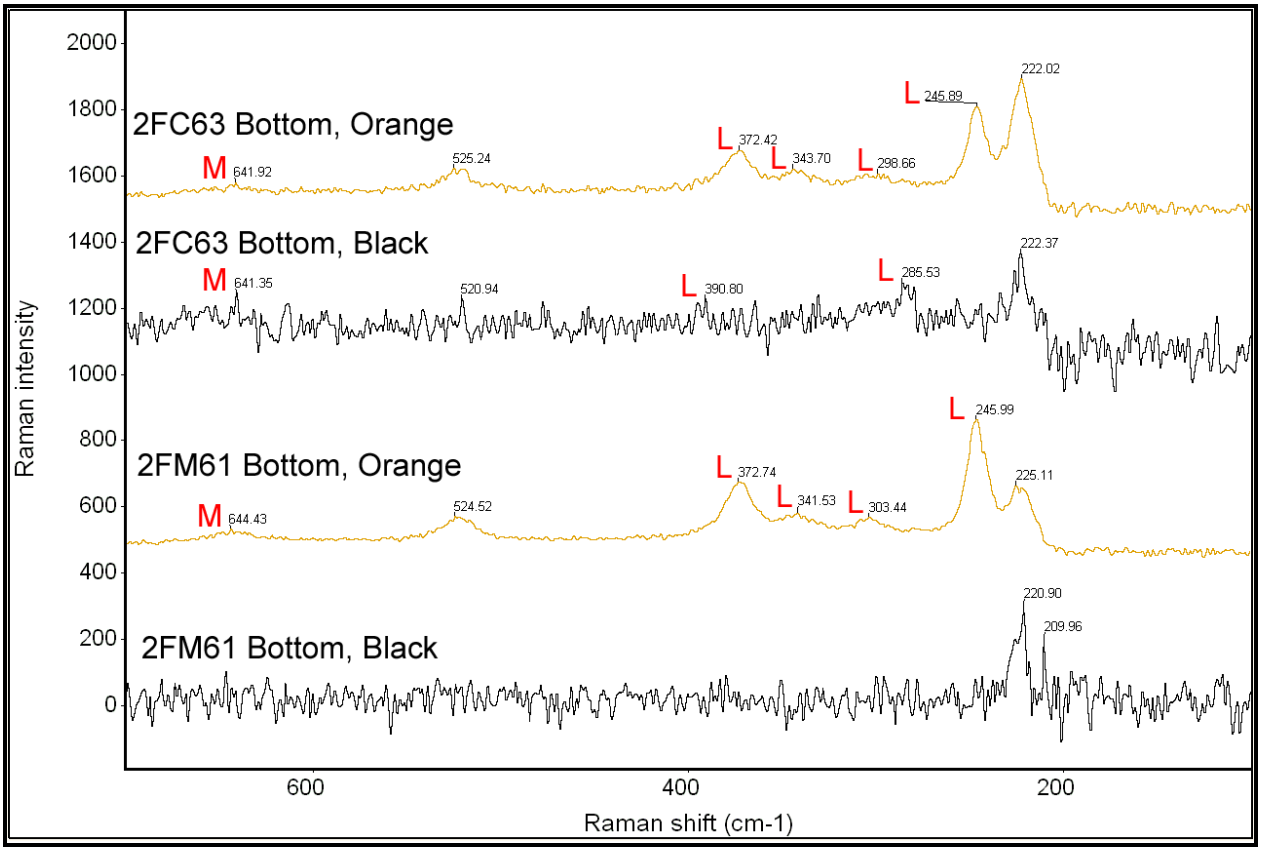

Figure 25. Raman spectroscopy of 6 months 1018 steel coupons exposed in filtered B20 fuel samples in anaerobic (2FC63) and selective aerobic (2FM61) environments.

Similar to the 1018 steel coupons exposed in unfiltered B20 fuel-water mixtures of Figure 24, lepidocrocite (245.89, 298.66, 343.70, 372.42, 285.53, 390.80, 245.99, 303.44, 341.53, and 372.74 cm^{-1}) [22] and magnetite (641.92, 641.35, and 644.43 cm^{-1}) [22] corrosion product bands were observed as depicted by Figure 25. Other bands (220.02, 525.24, 222.37, 520.94, 225.11, 524.52, 209.96, and 220.90 cm^{-1}) [22] are ghost bands. Steel coupons 2FC63 and 2FM61 exhibited similar corrosion product morphology as steel coupon 2UC62 from Figure 24. Analysis from XRD reveals that steel coupon 2FM61 black should have magnetite corrosion product present, but, magnetite bands were missing from the Raman spectra. Again, Raman data is missing for steel coupons exposed in filtered B20 fuel-water mixtures placed in aerobic

environments since no corrosion product was detected upon acetone washing the sludge layer off the coupons.

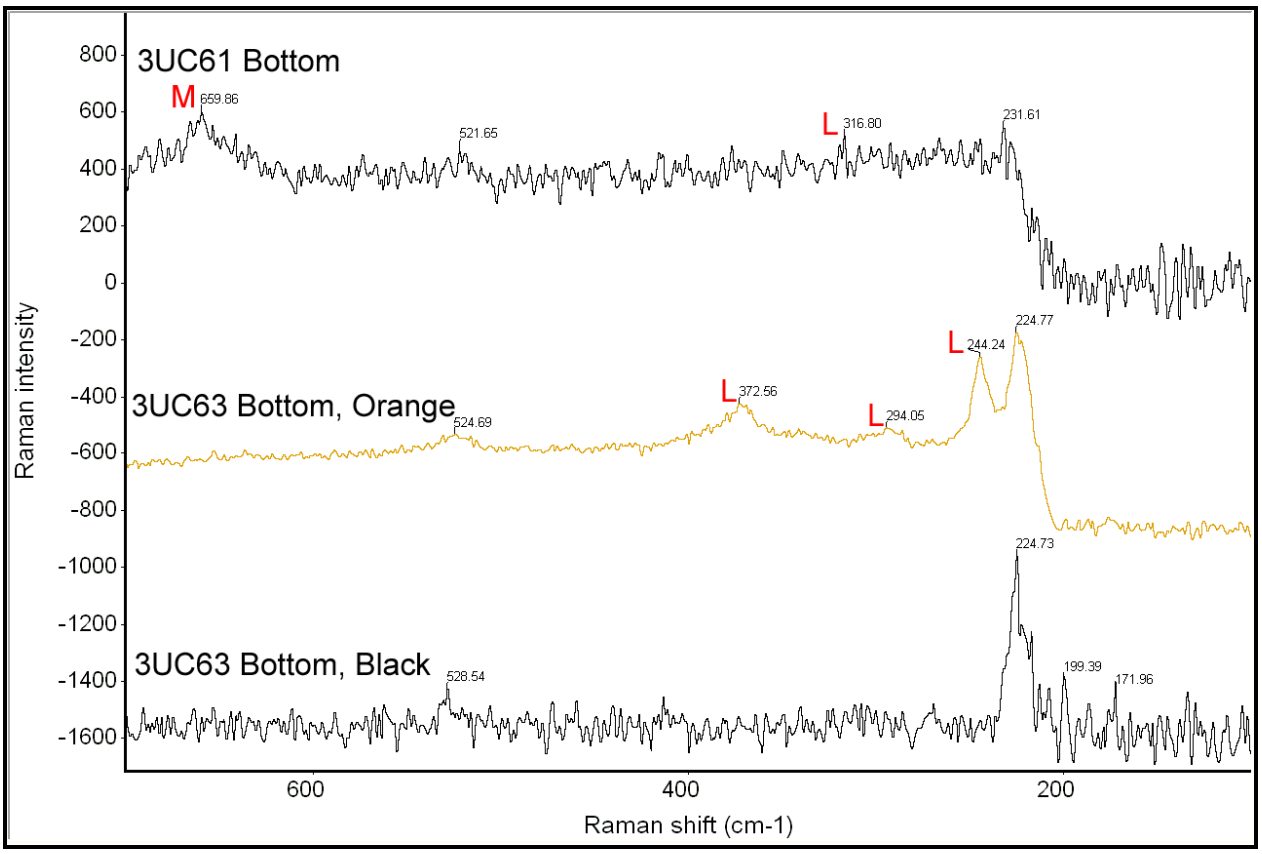

Figure 26. Raman spectroscopy of 6 months 1018 steel coupons exposed in unfiltered ULSD fuel samples in anaerobic (3UC61 and 3UC63) environments.

Characteristic bands of lepidocrocite (316.80, 244.24, 294.05, and 372.56 cm^{-1}) [22] and magnetite (659.86 cm^{-1}) [22] were observed as depicted by Figure 26. The remaining bands (231.61, 521.65, 224.77, 524.69, 171.96, 199.39, 224.73, and 528.54 cm^{-1}) [22] are ghost bands. Two different corrosion product morphologies were observed on 1018 steel coupons exposed in unfiltered ULSD fuel-water mixtures placed in anaerobic environments. The first, 3UC61, appeared to exhibit only the corrosion product magnetite, while the other coupon, 3UC63, depicted corrosion product morphologies similar to the B20 fuel-water mixture steel coupons 2UC62, 2FC63, and 2FM61 of Figure 25. Steel coupon 3UC61 revealed both lepidocrocite and

magnetite as corrosion products whereas steel coupons 3UC63 orange and 3UC63 black revealed only lepidocrocite and no corrosion product, respectively.

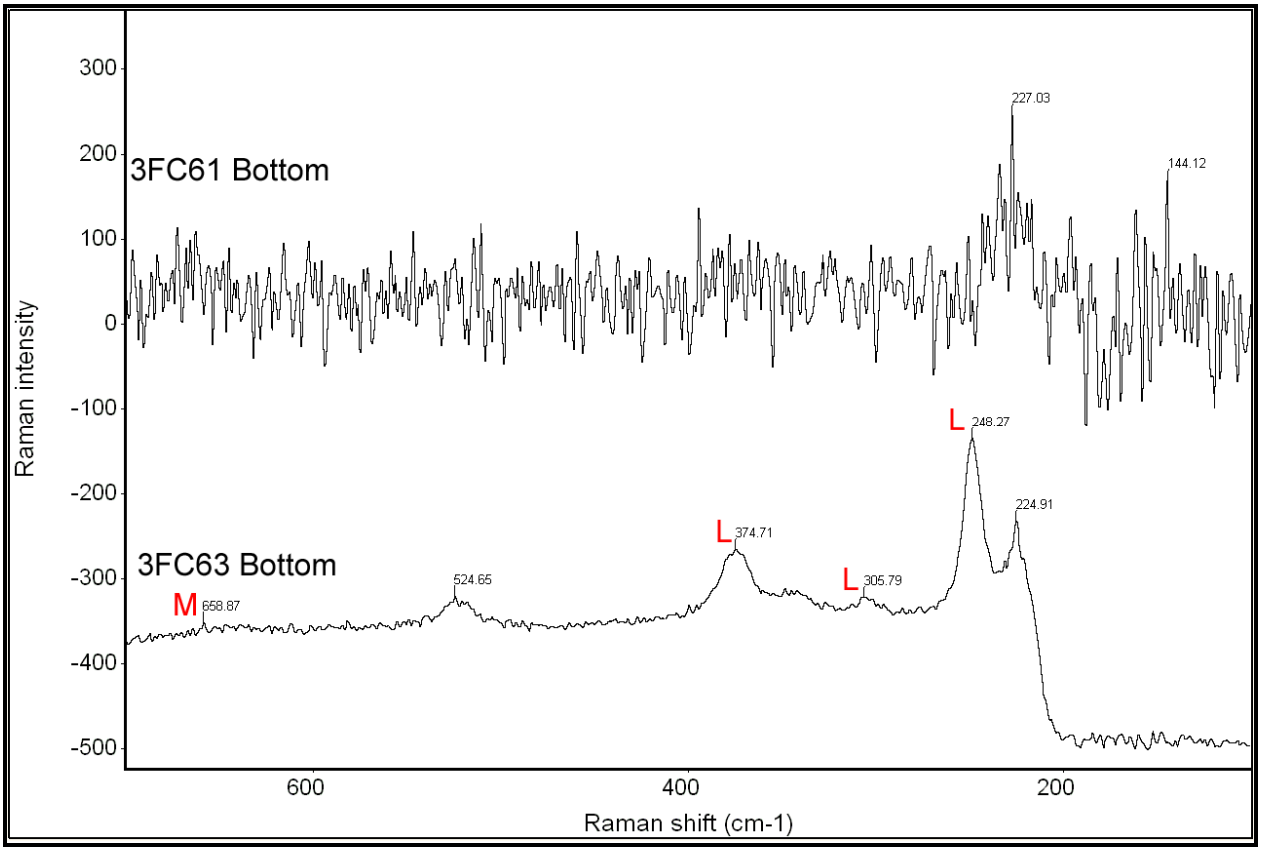

Figure 27. Raman spectroscopy of 6 months 1018 steel coupons exposed in filtered ULSD fuel samples in anaerobic (3FC61 and 3FC63) environments.

Characteristic bands of lepidocrocite (248.27, 305.79, and 374.71 cm^{-1}) [22] and magnetite (658.87 cm^{-1}) [22] were observed as depicted by Figure 27. The remaining bands (144.12, 227.03, 224.91 and 524.65 cm^{-1}) [22] are ghost bands. Again, two different corrosion product morphologies were observed on 1018 steel coupons exposed this time in filtered ULSD fuel-water mixtures placed in anaerobic environments. The first, 3FC61 appeared to exhibit only the corrosion product magnetite while the other coupon, 3FC63 depicted corrosion product morphologies similar to the B20 fuel-water mixture steel samples 2UC62, 2FC63, 2FM61 and ULSD fuel-water mixture sample coupon 3UC63 of Figures 24 and 26 respectively. However, Raman measurements detected no corrosion product spectrum for the 3FC61 coupon with only

two ghost bands detected. Again, magnetite is the suspect corrosion product, but the Raman was unable to detect its presence. Steel coupon 3FC63 exhibited both lepidocrocite and magnetite as corrosion products.

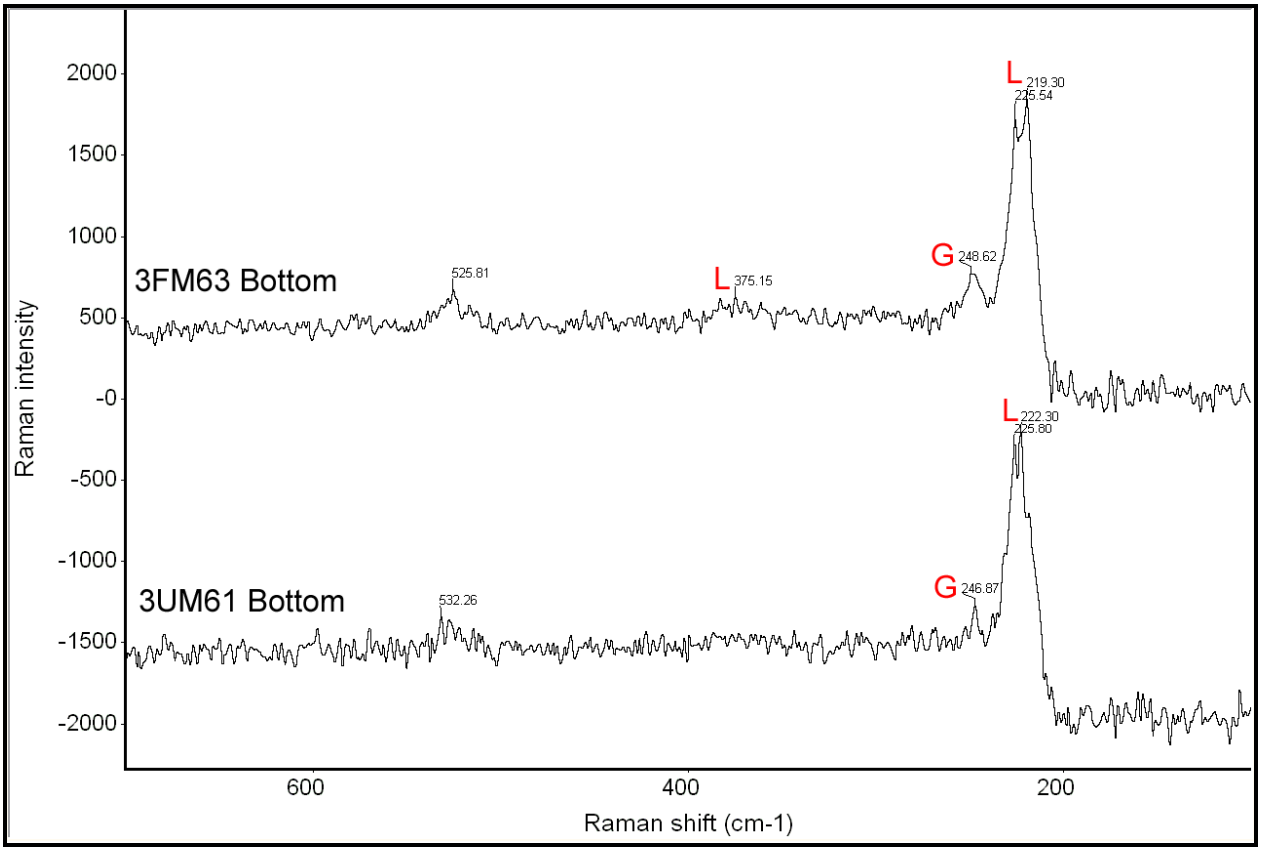

Figure 28. Raman spectroscopy of 6 months 1018 steel coupons exposed in filtered and unfiltered ULSD fuel samples in selective aerobic (3FM63 and 3UM61) environments.

Characteristic bands of lepidocrocite (219.30, 375.15, and 222.30 cm^{-1}) [22] and goethite (248.62 and 246.87 cm^{-1}) [22] were observed for all steel coupons in Figure 28. The remaining bands (225.54, 525.81, 225.80, and 532.26 cm^{-1}) [22] are ghost bands.

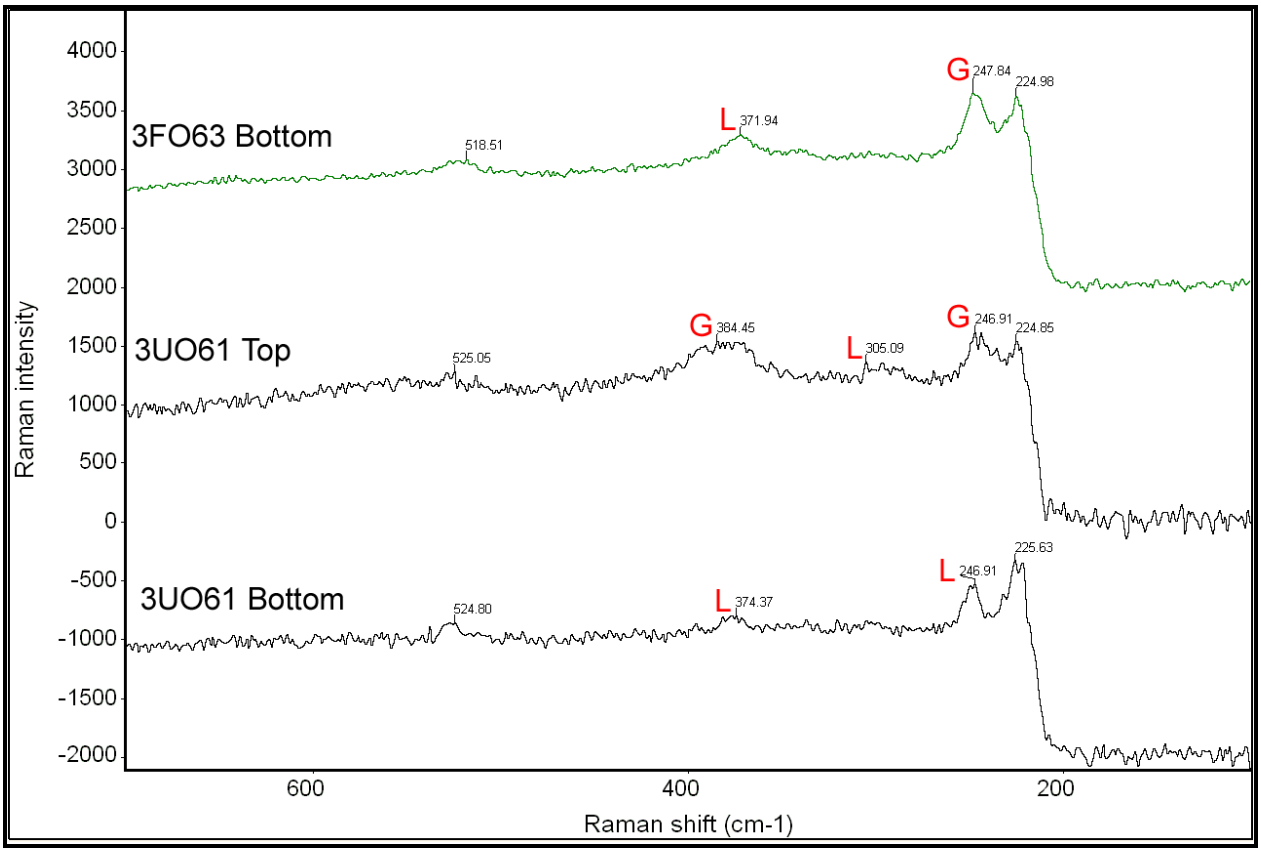

Figure 29. Raman spectroscopy of 6 months 1018 steel coupons exposed in filtered and unfiltered ULSD fuel samples in aerobic (3FO63 and 3UO61) environments.

Similarly, for the case of 1018 steel coupons immersed in ULSD fuel-water mixtures exposed in an aerobic environment, characteristic bands of lepidocrocite (371.94, 305.09, 246.91, and 374.37 cm^{-1}) [22] and goethite (247.84, 246.91, and 384.45 cm^{-1}) [22] were observed as depicted by Figure 29. The remaining bands (224.98, 518.51, 224.85, 525.05, 225.63, and 524.80 cm^{-1}) [22] are ghost bands. For steel coupon 3UO61, two different corrosion product morphologies were observed. The top part of the coupon exhibited both lepidocrocite and goethite whereas the bottom part revealed only lepidocrocite. This is quite different when compared to its filtered counterpart, steel coupon 3FO63 which exhibited both lepidocrocite and goethite on the bottom part of the coupon.

Similarly, the following figures depict the results obtained via Raman spectroscopy for the 1 year exposure time period.

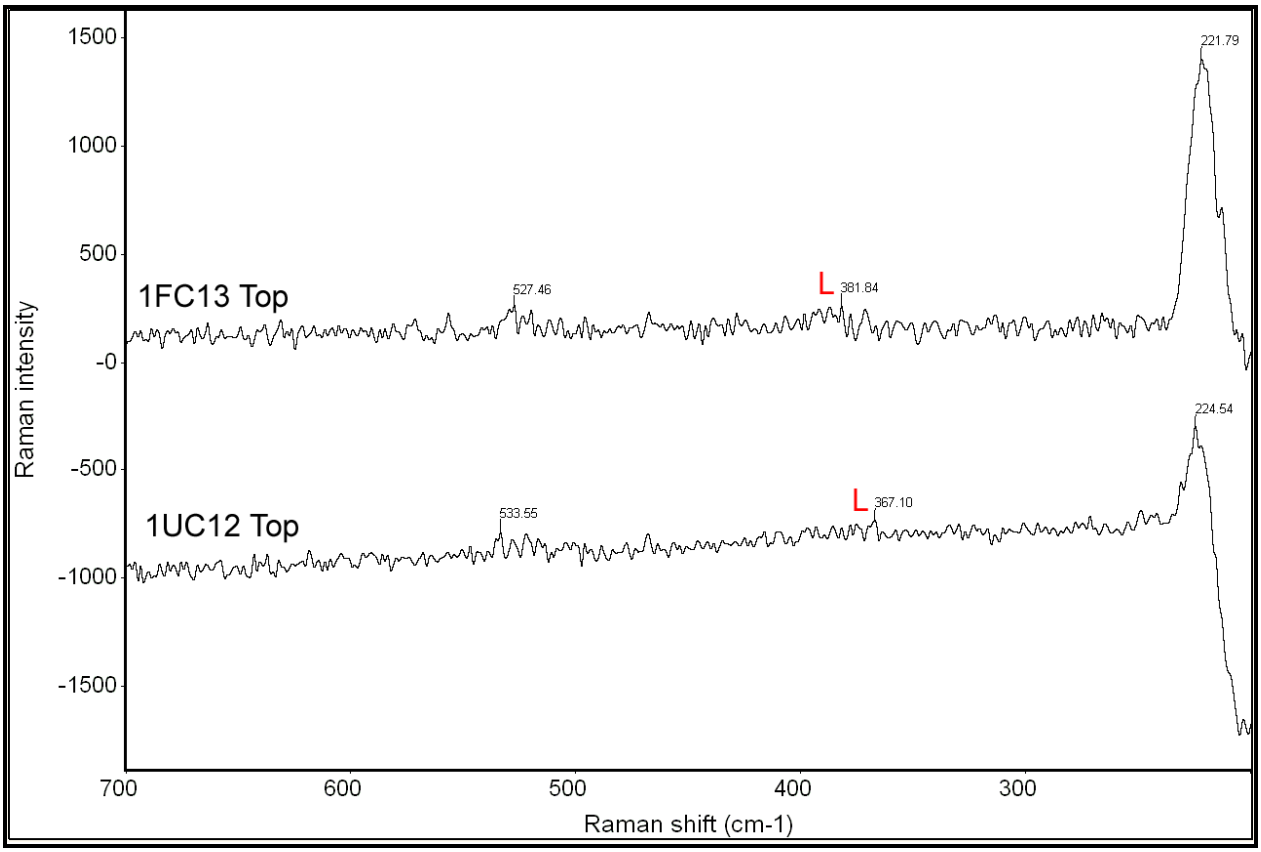

Figure 30. Raman spectroscopy of 1 year 1018 steel coupons exposed in filtered and unfiltered B100 fuel samples in anaerobic (1FC13 and 1UC12) environments.

Very faint bands, characteristic of lepidocrocite (381.84 and 367.10 cm^{-1}) [22] were observed for both steel coupons in Figure 30. The remaining bands (221.79, 527.46, 224.54, and 533.55 cm^{-1}) [22] are ghost bands.

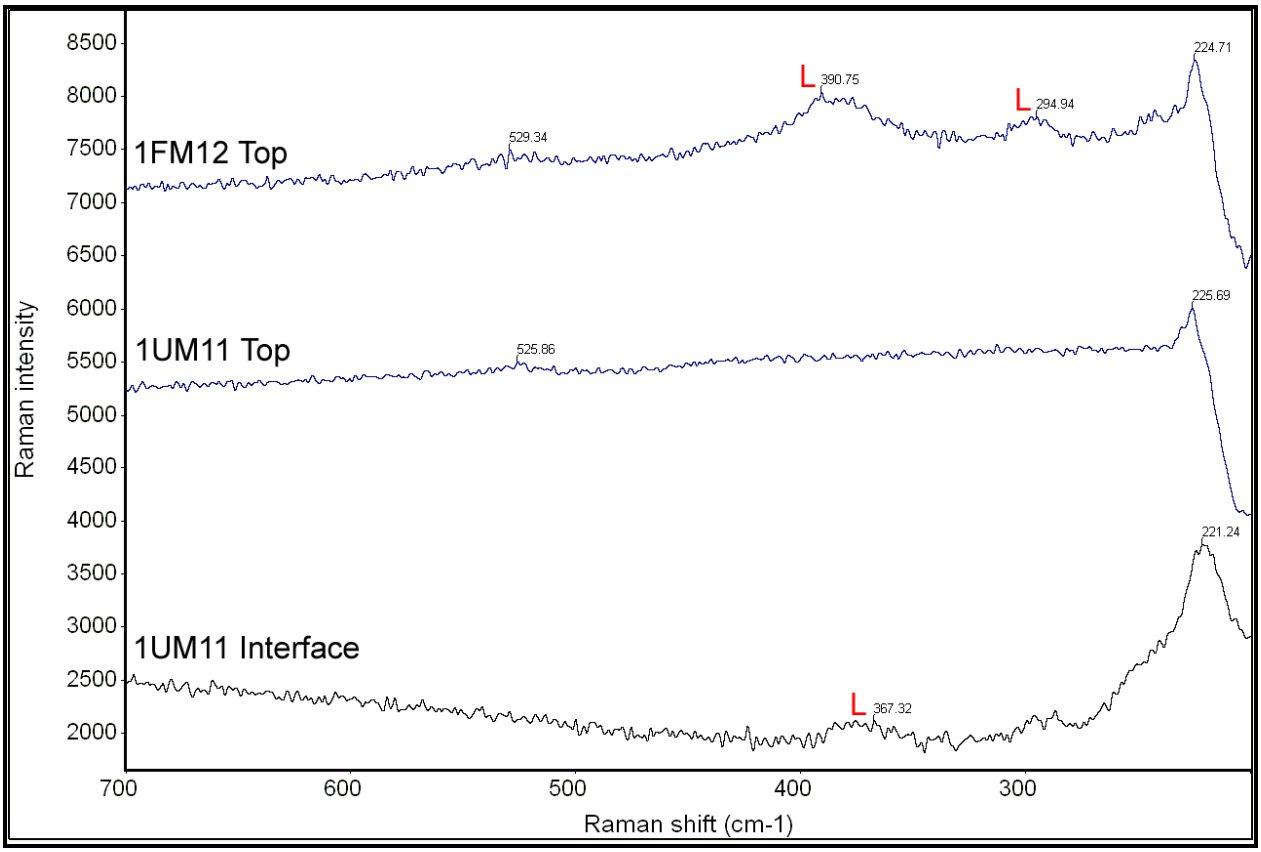

Figure 31. Raman spectroscopy of 1 year 1018 steel coupons exposed in filtered and unfiltered B100 fuel samples in selective aerobic (1FM12 and 1UM11) environments.

Characteristic bands of lepidocrocite (294.94, 390.75, and 367.32 cm^{-1}) [22] were observed as depicted by Figure 31. Remaining bands (224.71, 529.34, 225.69, 525.86, and 221.24 cm^{-1}) [22] are ghost bands. Corrosion product was especially sparse on steel coupon 1UM11 which is why the Raman could not detect any bands.

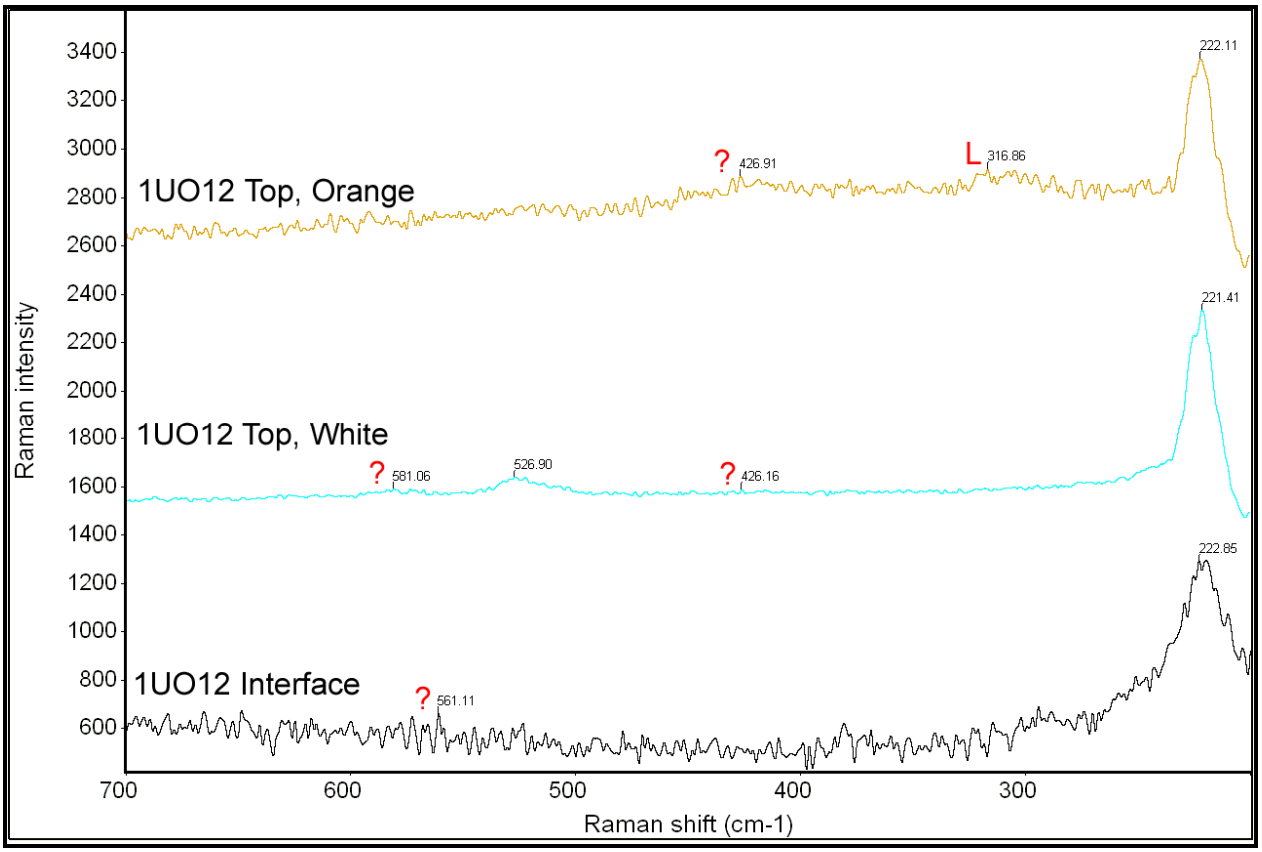

Figure 32. Raman spectroscopy of 1 year 1018 steel coupons exposed in unfiltered B100 fuel samples in an aerobic (1UO12) environment.

One band characteristic of lepidocrocite (316.86 cm^{-1}) [22] was observed on the 1UO12 orange steel coupon. Other bands (222.11, 221.41, 526.90, and 222.85 cm^{-1}) [22] are ghost bands. Bands at 426.91, 426.16, 581.06, and 561.11 cm^{-1} unfortunately could not be identified. Similar to the case of Raman results for the 6 month time period exposure of Figure 22, these unidentified bands may belong to the corrosion product iron formate hydrate as XRD analysis confirms this type of product on the steel coupons.

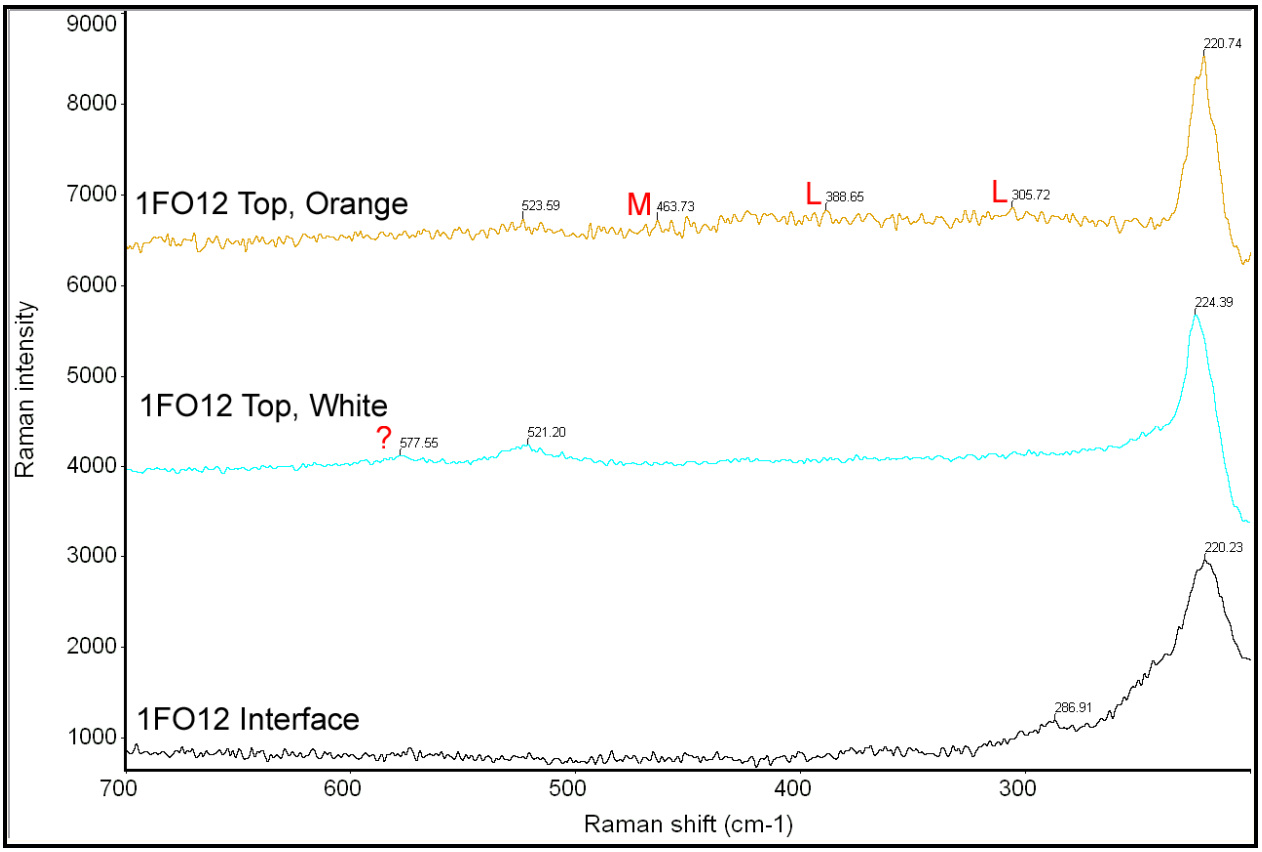

Figure 33. Raman spectroscopy of 1 year 1018 steel coupons exposed in filtered B100 fuel samples in an aerobic (1FO12) environment.

Characteristic bands of lepidocrocite (305.72 and 388.65 cm^{-1}) [22] and maghemite (463.73 cm^{-1}) [22] were observed as depicted by Figure 33. Remaining bands (220.74, 523.59, 224.39, 521.20, 220.23, and 286.91 cm^{-1}) [22] are ghost bands. Band 577.55 cm^{-1} could again not be identified. Steel coupon 1FO12 orange revealed lepidocrocite and maghemite, which has the same structure of magnetite, as corrosion products. No spectrum was detected at the interface region of steel coupon 1FO12. This is likely due to the very little corrosion product observed in that area.

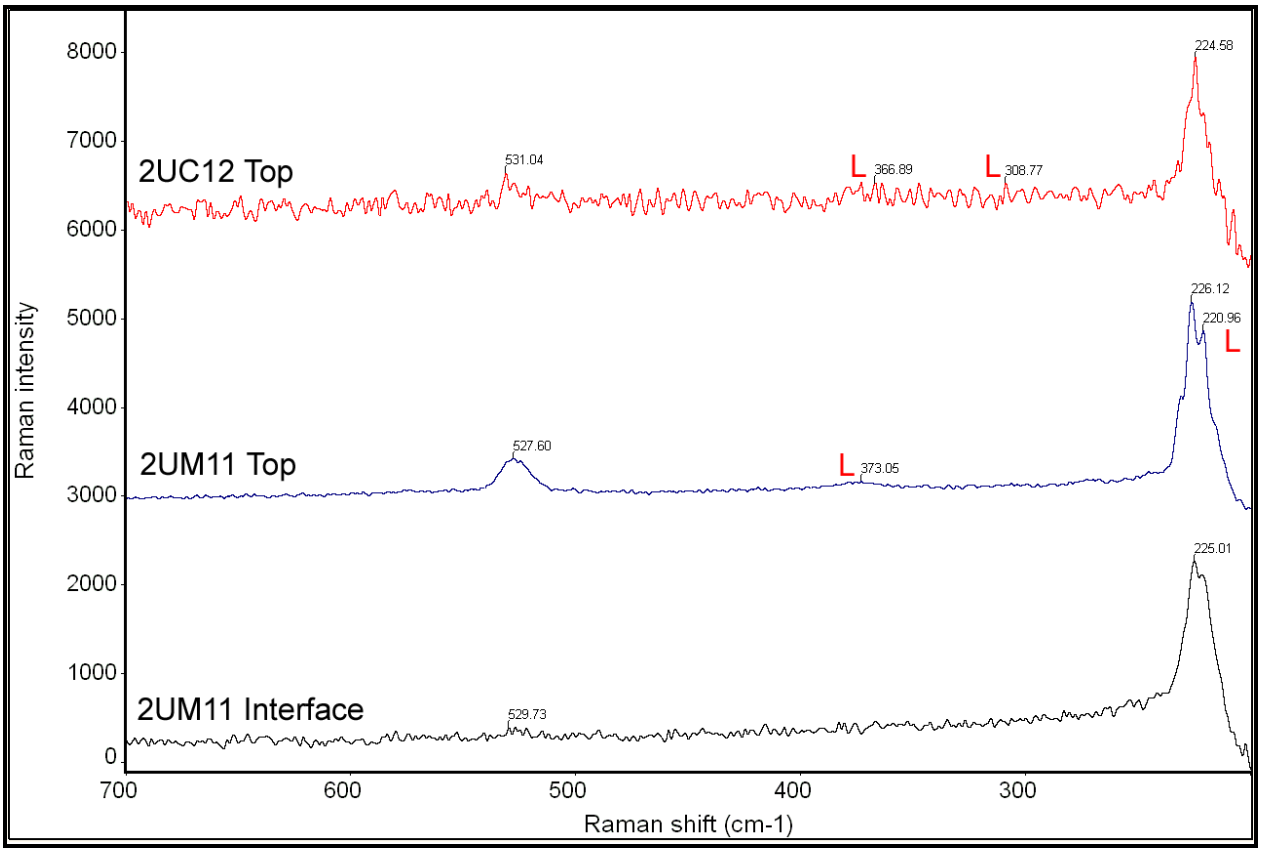

Figure 34. Raman spectroscopy of 1 year 1018 steel coupons exposed in unfiltered B20 fuel samples in anaerobic (2UC12) and selective aerobic (2UM11) environments.

Characteristic bands of lepidocrocite (308.77, 366.89, 220.96, and 373.05 cm^{-1}) [22] were observed as depicted by Figure 34. Remaining bands (224.58, 531.04, 226.12, 527.60, 225.01, and 529.73 cm^{-1}) [22] are ghost bands. Steel coupons 2UC12 and 2UM11 both revealed lepidocrocite as the corrosion product. Again, the interface for steel coupon 2UM11 had very little corrosion product and therefore no Raman spectrum could be obtained. Similar to the 6 month steel coupon samples exposed in an aerobic environment, Raman data is missing since no corrosion product was detected upon acetone washing the sludge layer off the coupons.

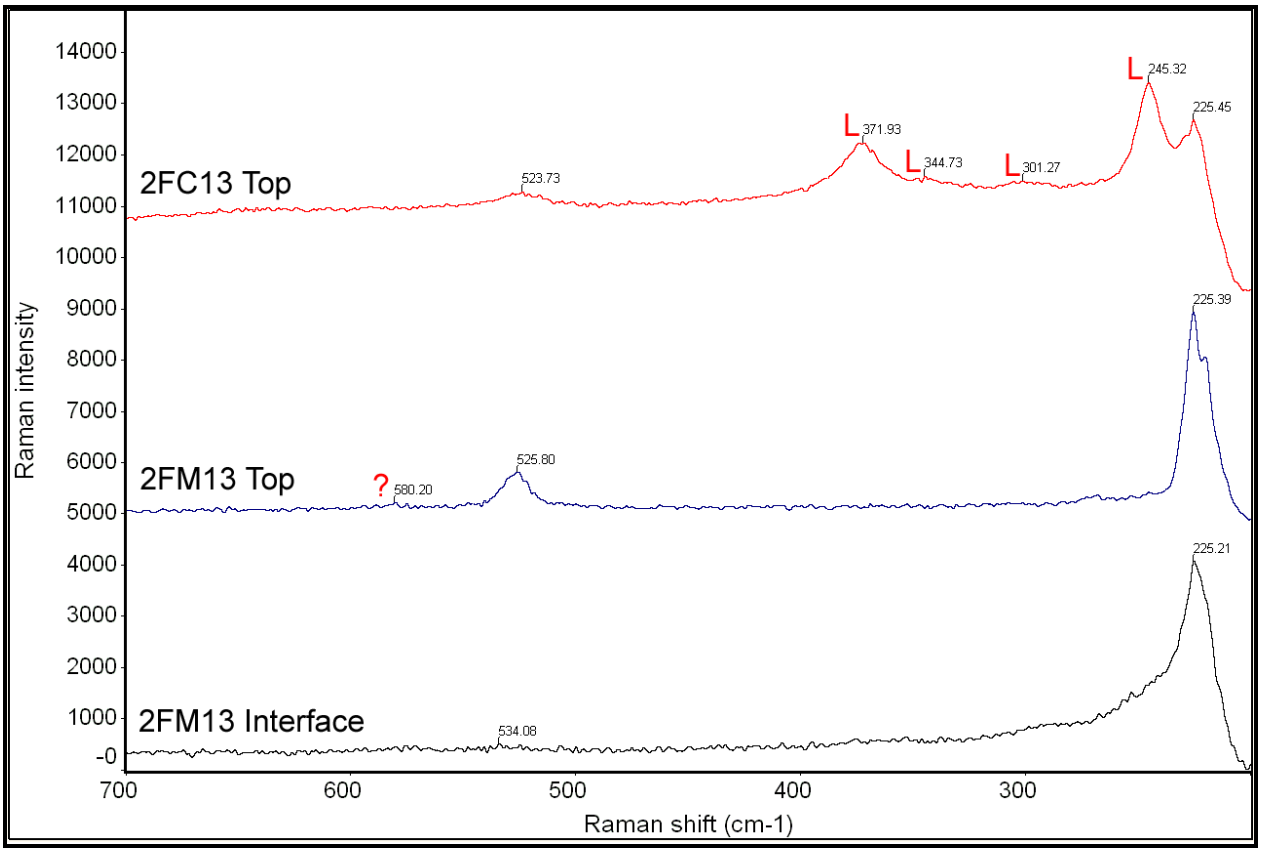

Figure 35. Raman spectroscopy of 1 year 1018 steel coupons exposed in filtered B20 fuel samples in anaerobic (2FC13) and selective aerobic (2FM13) environments.

Lepidocrocite bands (245.32, 301.27, 344.73, and 371.93 cm^{-1}) [22] were observed on steel coupon sample 2FC13. Other bands (225.45, 523.73, 225.39, 525.80, 225.21, and 534.08 cm^{-1}) [22] were identified as ghost bands. Band 580.20 cm^{-1} on steel coupon sample 2FM13 could not be identified. The interface for steel coupon 2FM13 had very little corrosion product and therefore no Raman spectrum could be obtained. Again, Raman data is missing for steel coupons exposed in the filtered B20 fuel-water mixtures placed in aerobic environments since no corrosion product was detected upon acetone washing the sludge layer off the coupons.

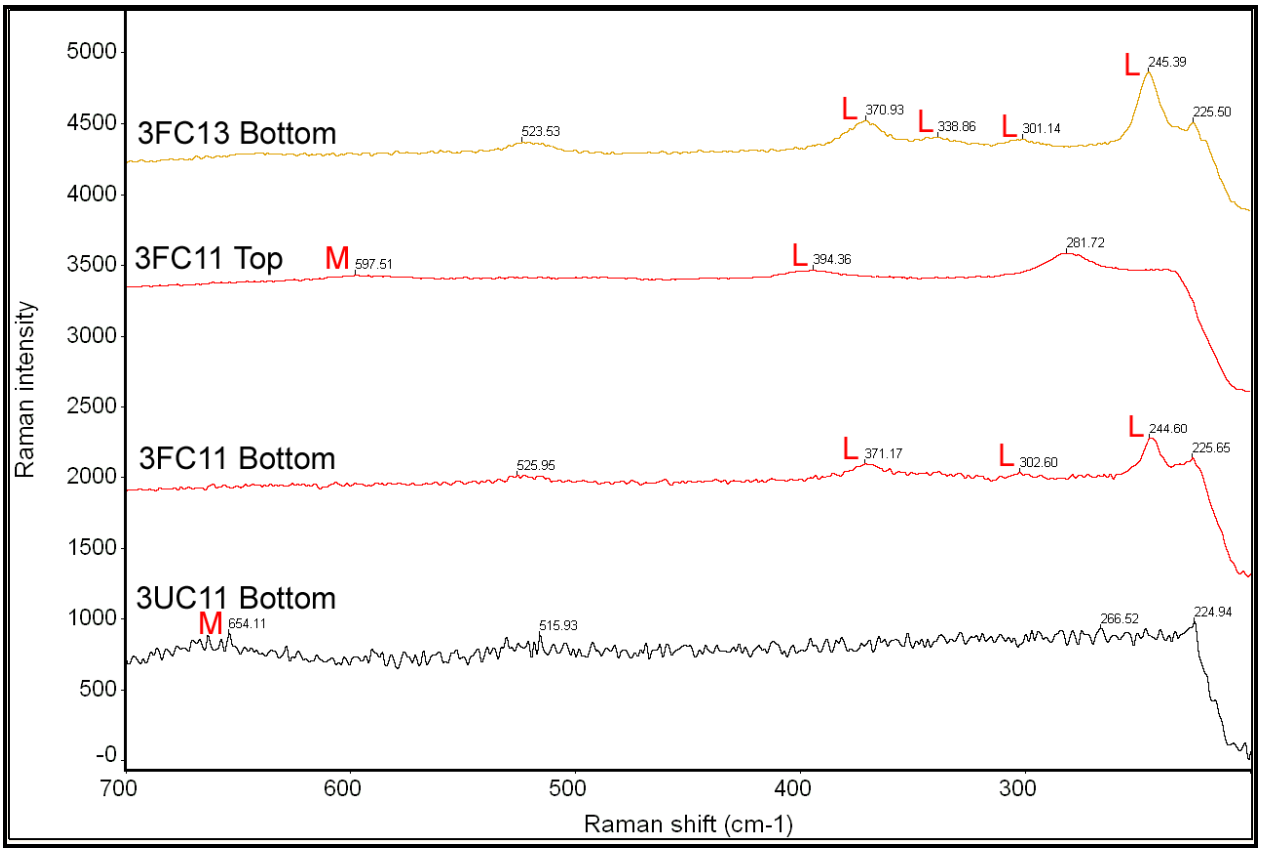

Figure 36. Raman spectroscopy of 1 year 1018 steel coupons exposed in filtered and unfiltered ULSD fuel samples in anaerobic (3FC13, 3FC11, and 3UC11) environments.

Characteristic bands of lepidocrocite (245.39, 301.14, 338.86, 370.93, 394.36, 244.60, 302.60, and 371.17 cm^{-1}) [22] and magnetite (597.51 and 654.11 cm^{-1}) [22] were observed as depicted by Figure 36. Remaining bands (225.50, 523.53, 281.72, 225.65, 525.95, 224.94, 266.52, and 515.93 cm^{-1}) [22] were identified as ghost bands. Lepidocrocite was found only on steel coupons 3FC13 and 3FC11. Magnetite was found only on the top part of steel coupon 3FC11 and the bottom of 3UC11.

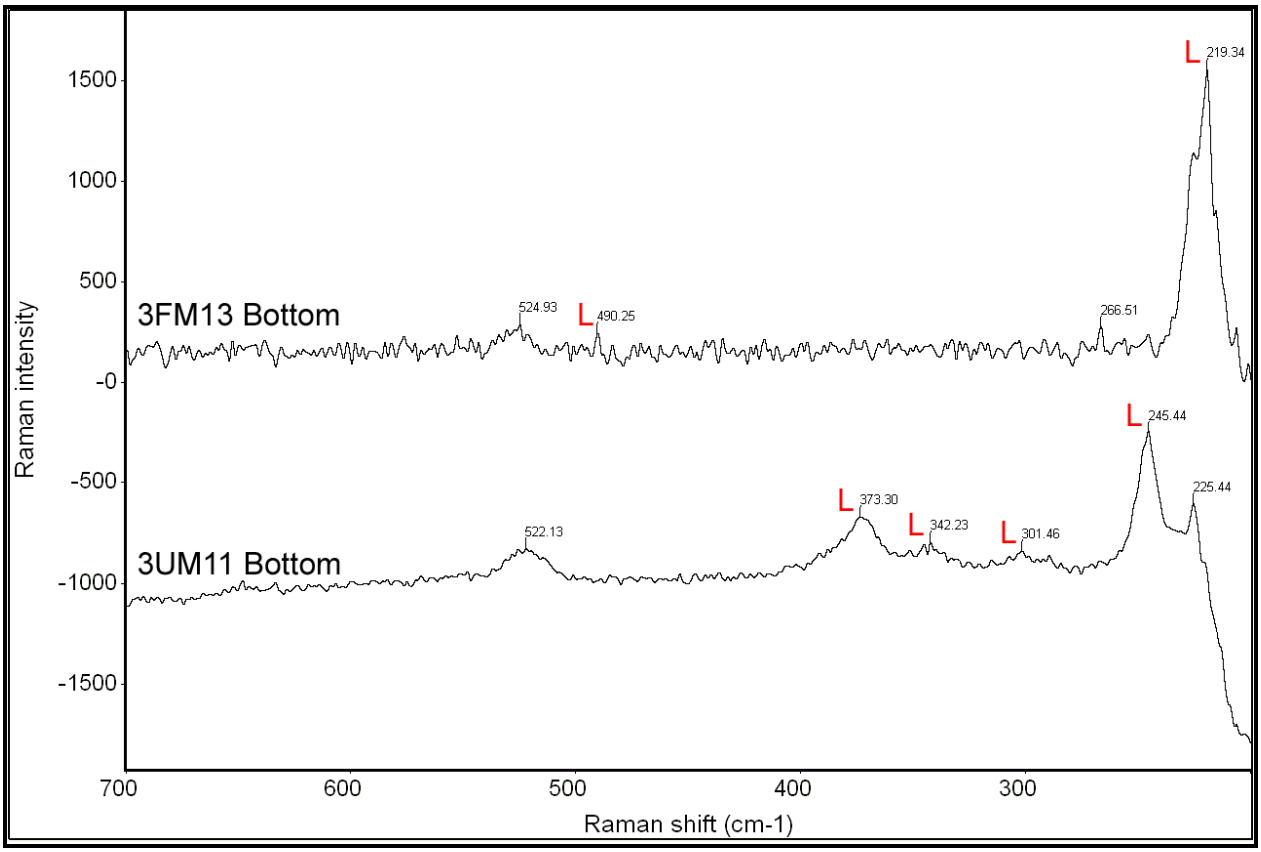

Figure 37. Raman spectroscopy of 1 year 1018 steel coupons exposed in filtered and unfiltered ULSD fuel samples in selective aerobic (3FM13 and 3UM11) environments.

Characteristic bands of lepidocrocite (219.34, 490.25, 245.44, 301.46, 342.23, and 373.30 cm^{-1}) [22] were observed in both steel coupons 3FM13 and 3UM11 as depicted by Figure 37. The other remaining bands (266.51, 524.93, 225.44, and 522.13 cm^{-1}) [22] are ghost bands.

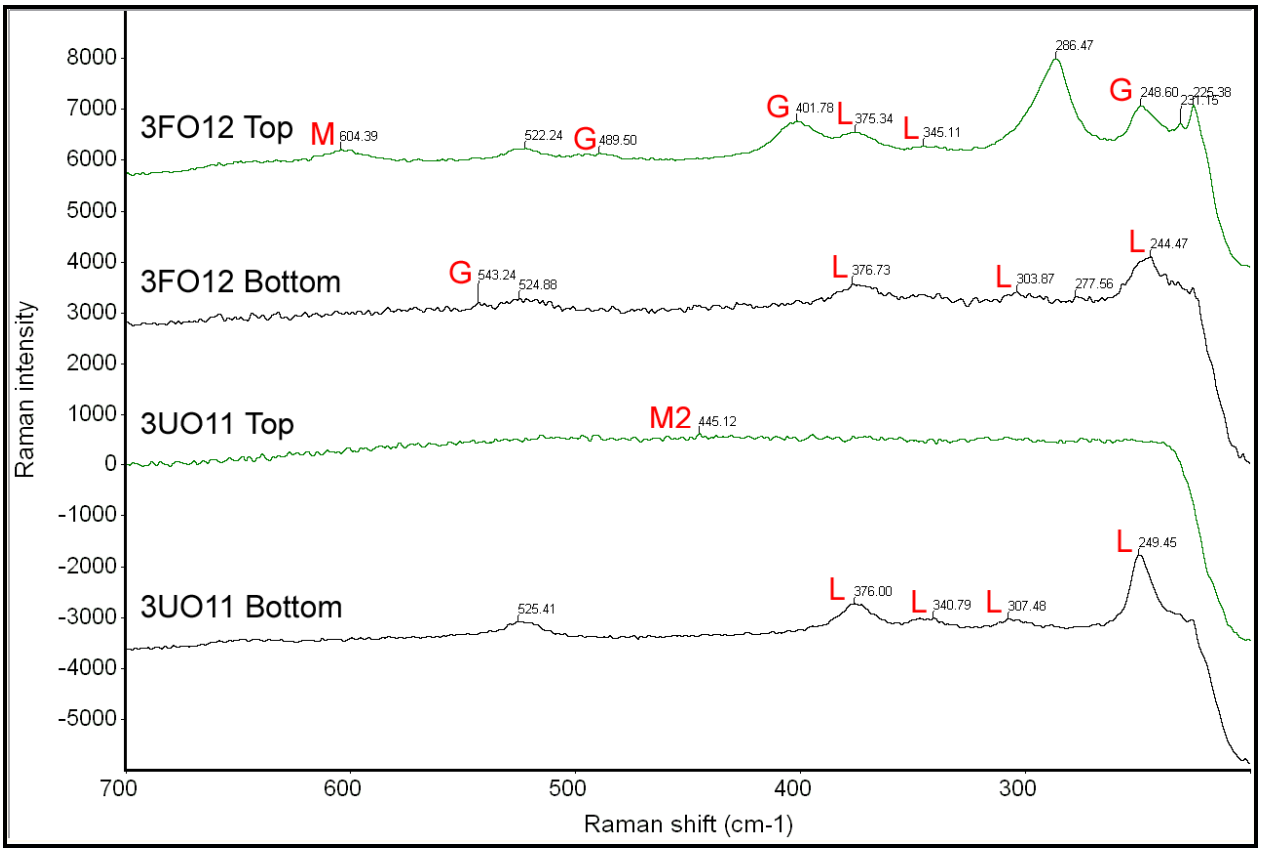

Figure 38. Raman spectroscopy of 1 year 1018 steel coupons exposed in filtered and unfiltered ULSD fuel samples in aerobic (3FO12 and 3UO11) environments.

Characteristic bands of lepidocrocite (345.11, 375.34, 244.47, 303.87, 376.73, 249.45, 307.48, 340.79, and 376.00 cm^{-1}) [22], goethite (248.60, 401.78, 489.50, and 543.24 cm^{-1}) [22], magnetite (604.39 cm^{-1}) [22], and maghemite (445.12 cm^{-1}) [22] were observed as depicted by Figure 38. Remaining bands (225.38, 231.15, 286.47, 522.24, 277.56, 524.88, and 525.41 cm^{-1}) [22] were identified as ghost bands. Lepidocrocite was found on steel coupon 3FO12 and the bottom part of steel coupon 3UO11. Goethite was found throughout steel coupon 3FO12. Magnetite was found on the top part of steel coupon 3FO12, and maghemite was found on the bottom part of steel coupon 3FO12.

5.4. XRD

The following figures depict the results obtained via XRD for the 6 month exposure time period.

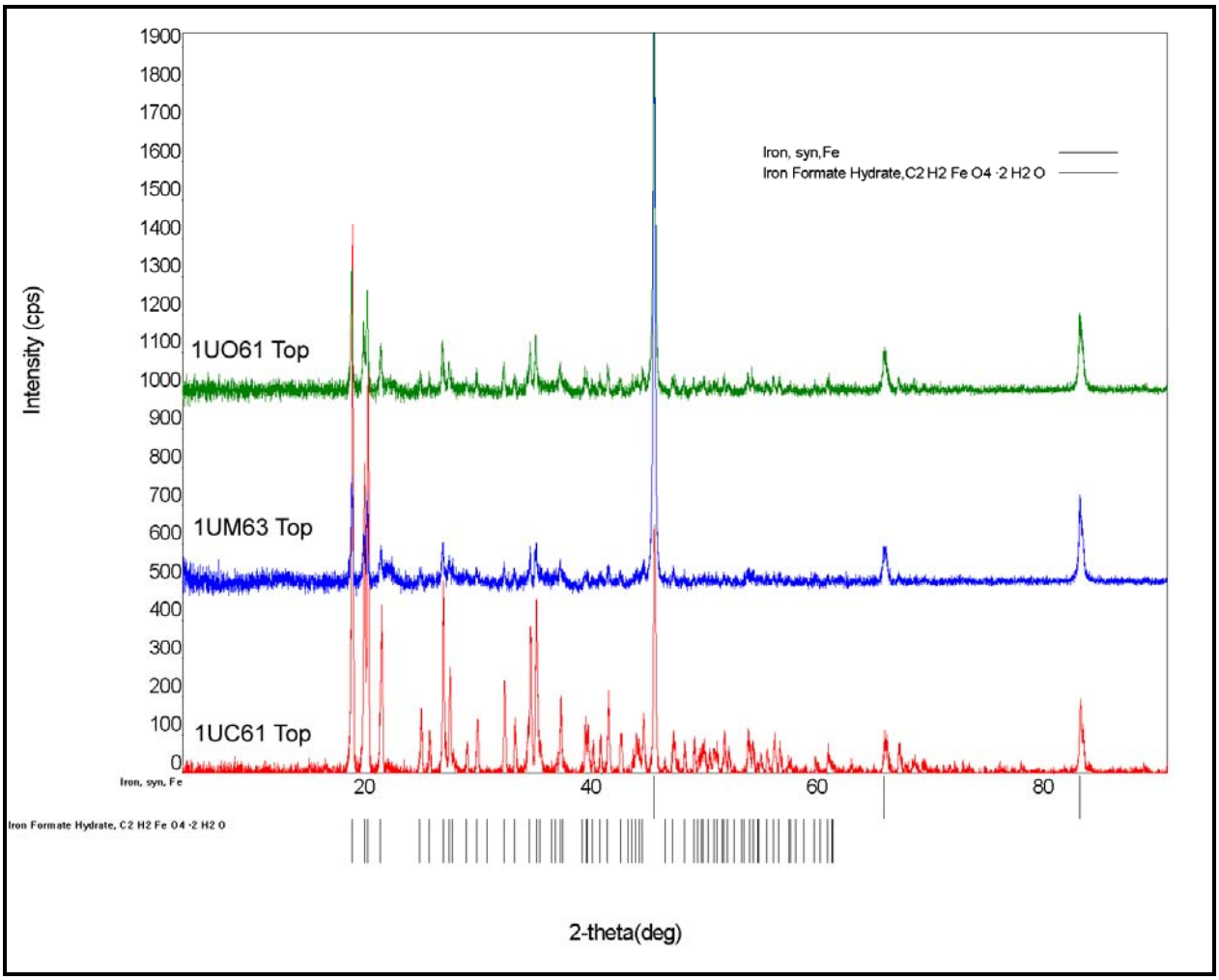

Figure 39. XRD of 6 months 1018 steel coupons exposed in unfiltered B100 fuel samples in anaerobic (1UC61), selective aerobic (1UM63), and aerobic (1UO61) environments.

XRD results of Figure 39 reveal iron formate hydrate as the main corrosion product on 1018 steel coupons immersed in unfiltered B100 fuel-water mixtures exposed in all environmental conditions. Raman analysis from Figure 22 agrees with XRD results and revealed

bands characteristic of lepidocrocite and two unknown bands that could possibly belong to iron formate hydrate.

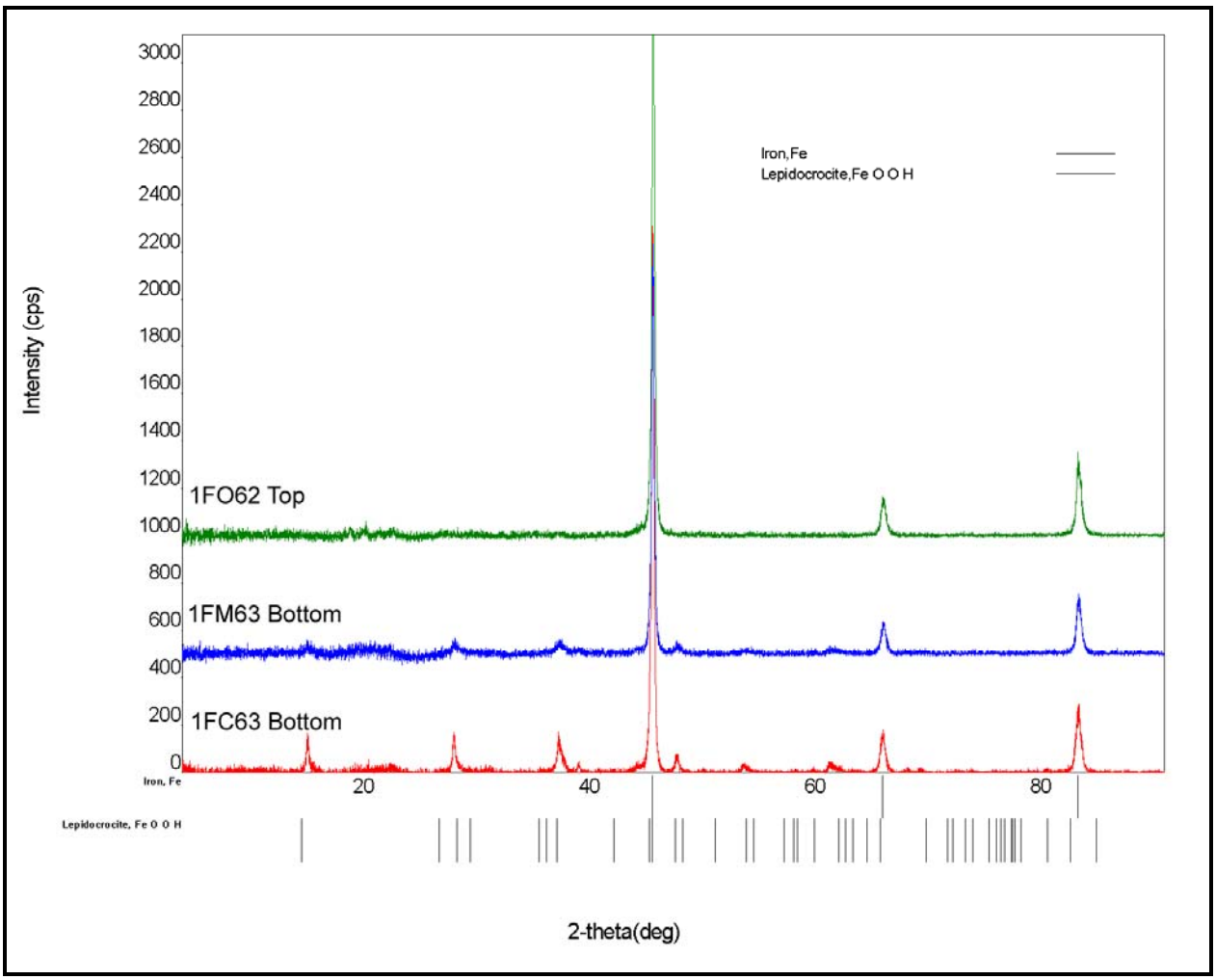

Figure 40. XRD of 6 months 1018 steel coupons exposed in filtered B100 fuel samples in anaerobic (1FC63), selective aerobic (1FM63), and aerobic (1FO62) environments.

Lepidocrocite was identified by XRD analysis on steel coupons 1FC63 and 1FM63 as depicted by Figure 40. No corrosion product was detected on steel coupon 1FO62. This correlates well with Raman analysis of Figure 23, as lepidocrocite was identified as the primary corrosion product on these steel coupons.

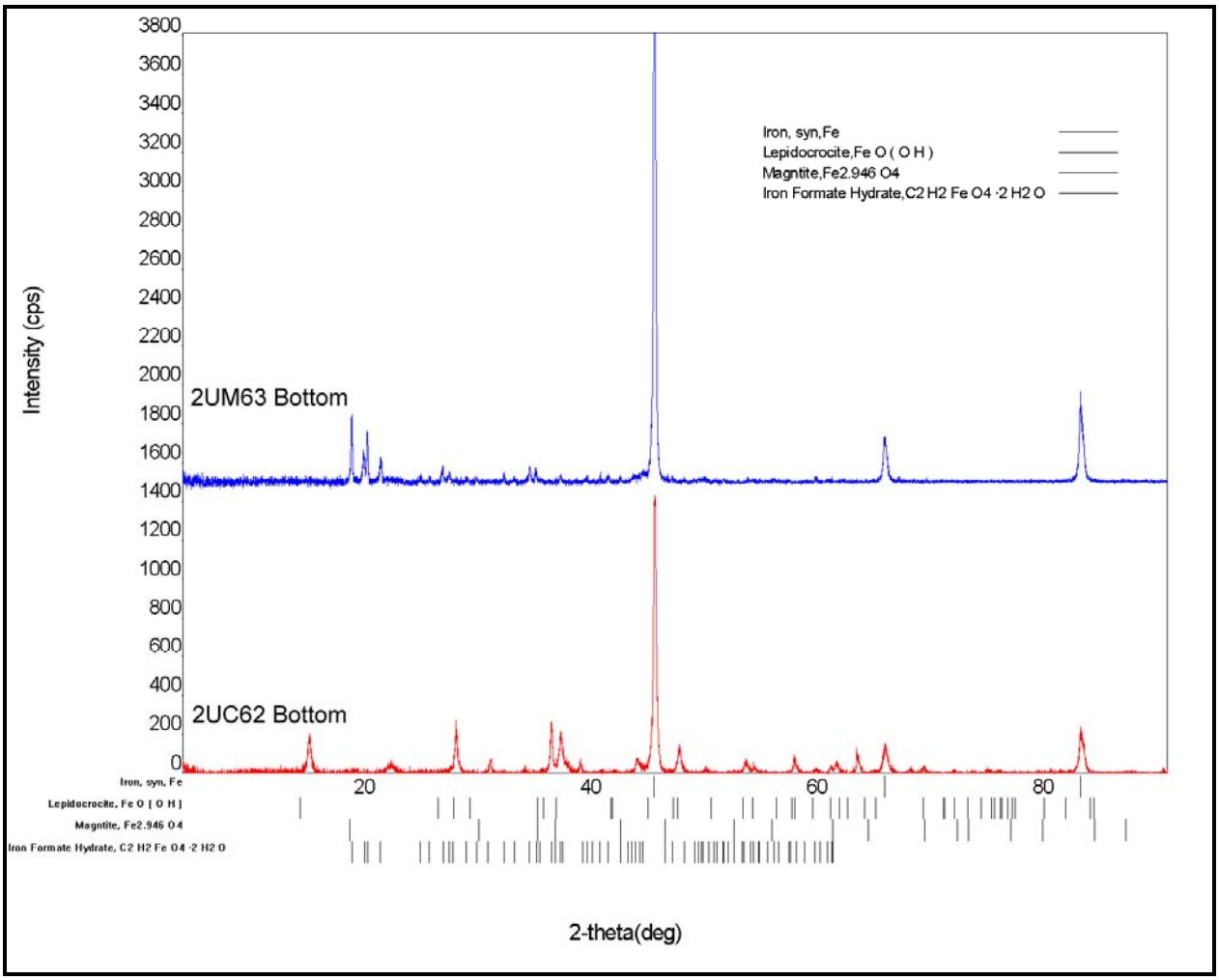

Figure 41. XRD of 6 months 1018 steel coupons exposed in unfiltered B20 fuel samples in anaerobic (2UC62) and selective aerobic (2UM63) environments.

Lepidocrocite and magnetite was found on steel coupon 2UC62 whereas iron formate hydrate was found on steel coupon 2UM63 as depicted by Figure 41. Raman analysis from Figure 24 correlates well with steel coupon 2UC62 as both lepidocrocite and magnetite bands were observed. In the case of steel coupon 2UM63, Raman analysis revealed lepidocrocite bands. As for the case of the previous analysis performed with Raman, there is no XRD data for the steel coupon samples exposed in the aerobic environement since no corrosion product was detected upon acetone washing the sludge layer off the coupons.

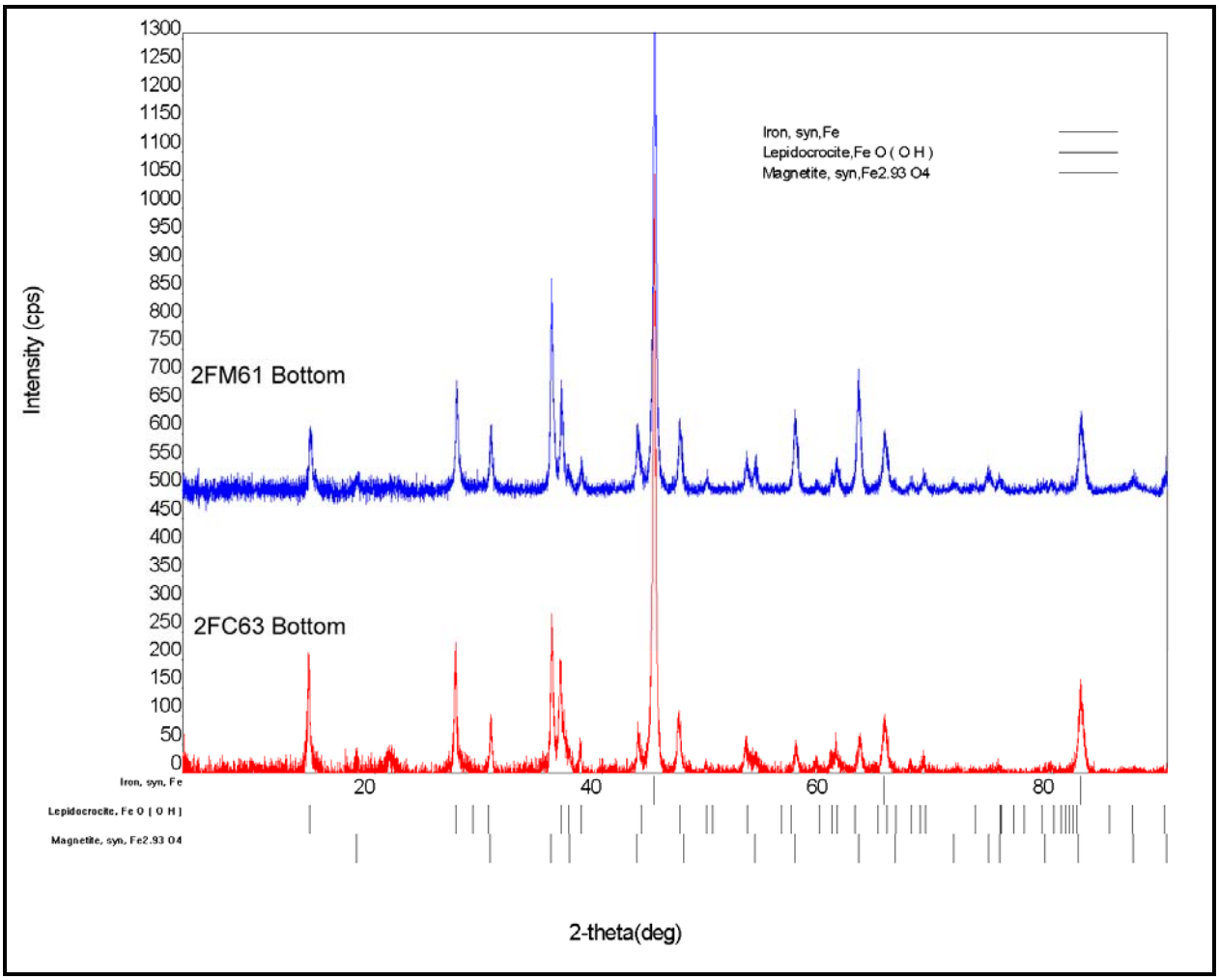

Figure 42. XRD of 6 months 1018 steel coupons exposed in filtered B20 fuel samples in anaerobic (2FC63) and selective aerobic (2FM61) environments.

Lepidocrocite and magnetite were found on both steel coupon samples 2FC63 and 2FM61 as depicted by Figure 42. Again, this correlates very well with Raman analysis shown in Figure 25 as both these corrosion product bands were detected on both steel coupon samples. Similarly, there is no XRD data for the steel coupon samples exposed in the aerobic environment since no corrosion product was detected upon acetone washing the sludge layer off the coupons.

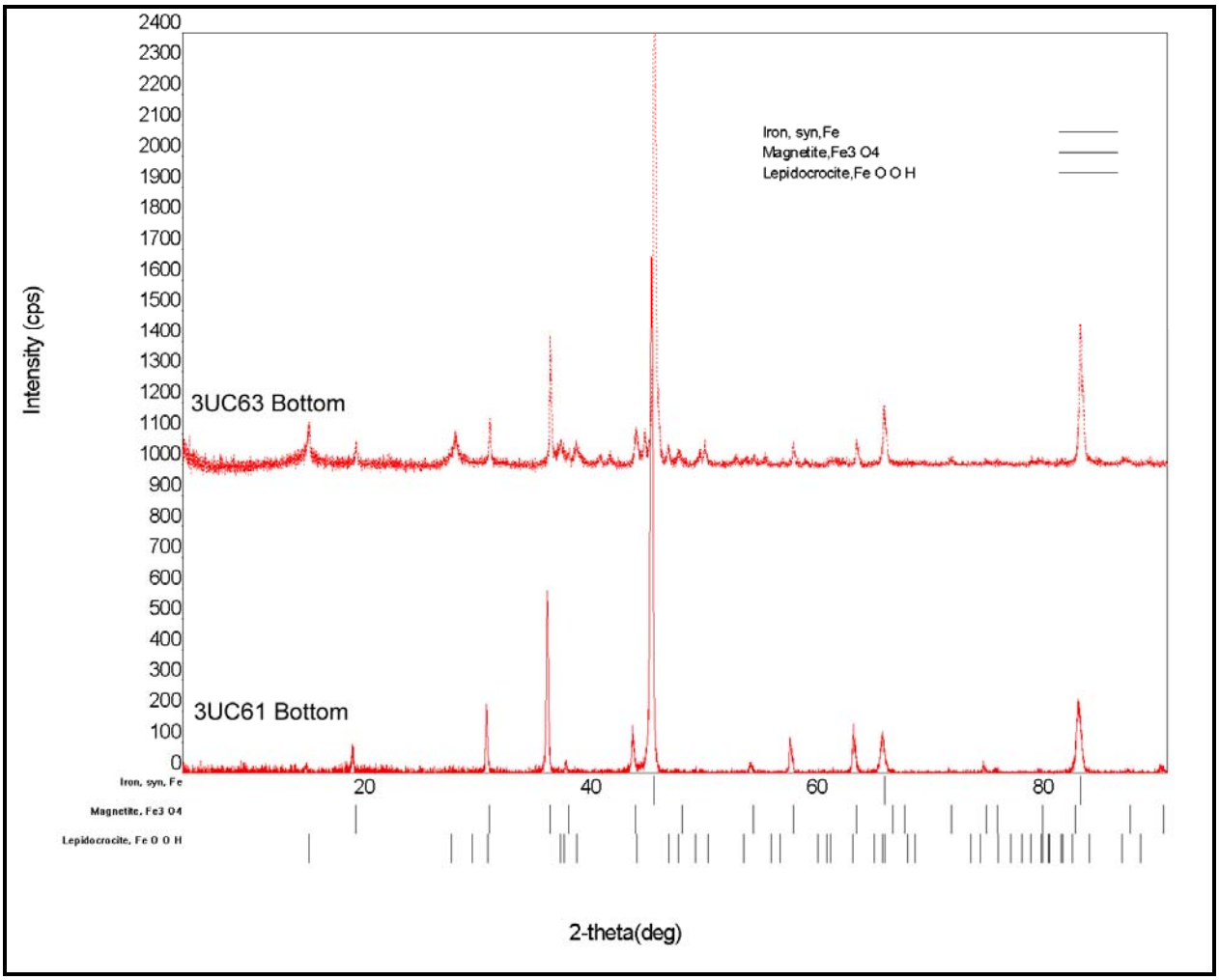

Figure 43. XRD of 6 months 1018 steel coupons exposed in unfiltered ULSD fuel samples in an anaerobic (3UC61 and 3UC63) environment.

Lepidocrocite and magnetite was detected as the corrosion products on steel coupon 3UC63 whereas magnetite was the only corrosion product detected on steel coupon 3UC61 as depicted by Figure 43. Raman analysis from Figure 26 differs slightly from these XRD results. Raman detected bands characteristic of lepidocrocite and magnetite on sample 3UC61, while lepidocrocite was the only corrosion product found on steel coupon 3UC63.

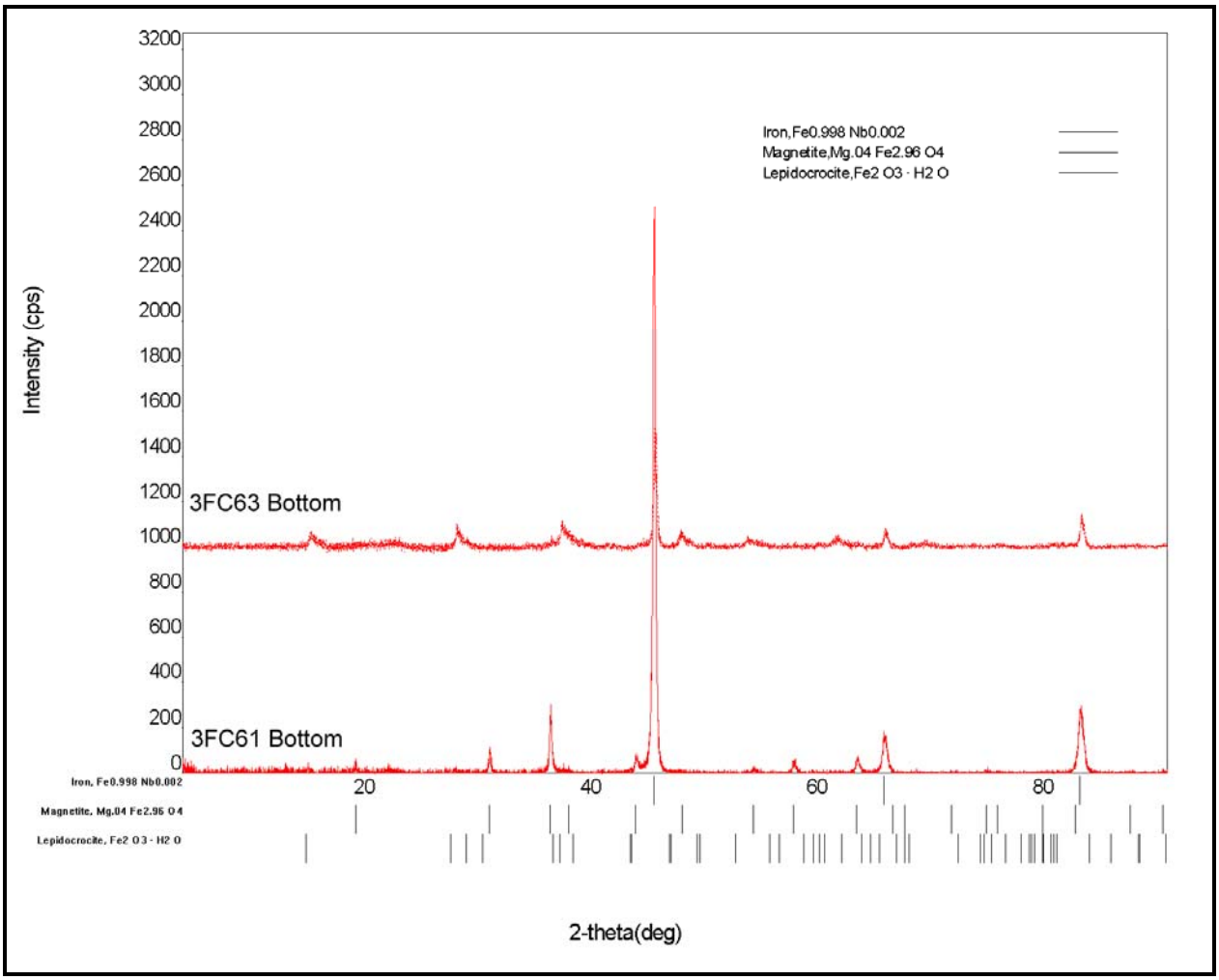

Figure 44. XRD of 6 months 1018 steel coupons exposed in filtered ULSD fuel samples in an anaerobic (3FC61 and 3FC63) environment.

Similar to steel coupon 3UC63 of Figure 43, Lepidocrocite and magnetite were the corrosion products identified by XRD on steel coupon 3FC63 as depicted by Figure 44. On steel coupon 3FC61, magnetite was the only corrosion product identified. Raman results from Figure 27 correlate well with steel coupon 3FC63, but in the case of steel coupon 3FC61, no corrosion product bands could be detected. As explained before, the Raman could not detect any bands due to the very little corrosion product on the steel coupon, but fortunately in the case of XRD analysis, corrosion product could be detected in the form of magnetite.

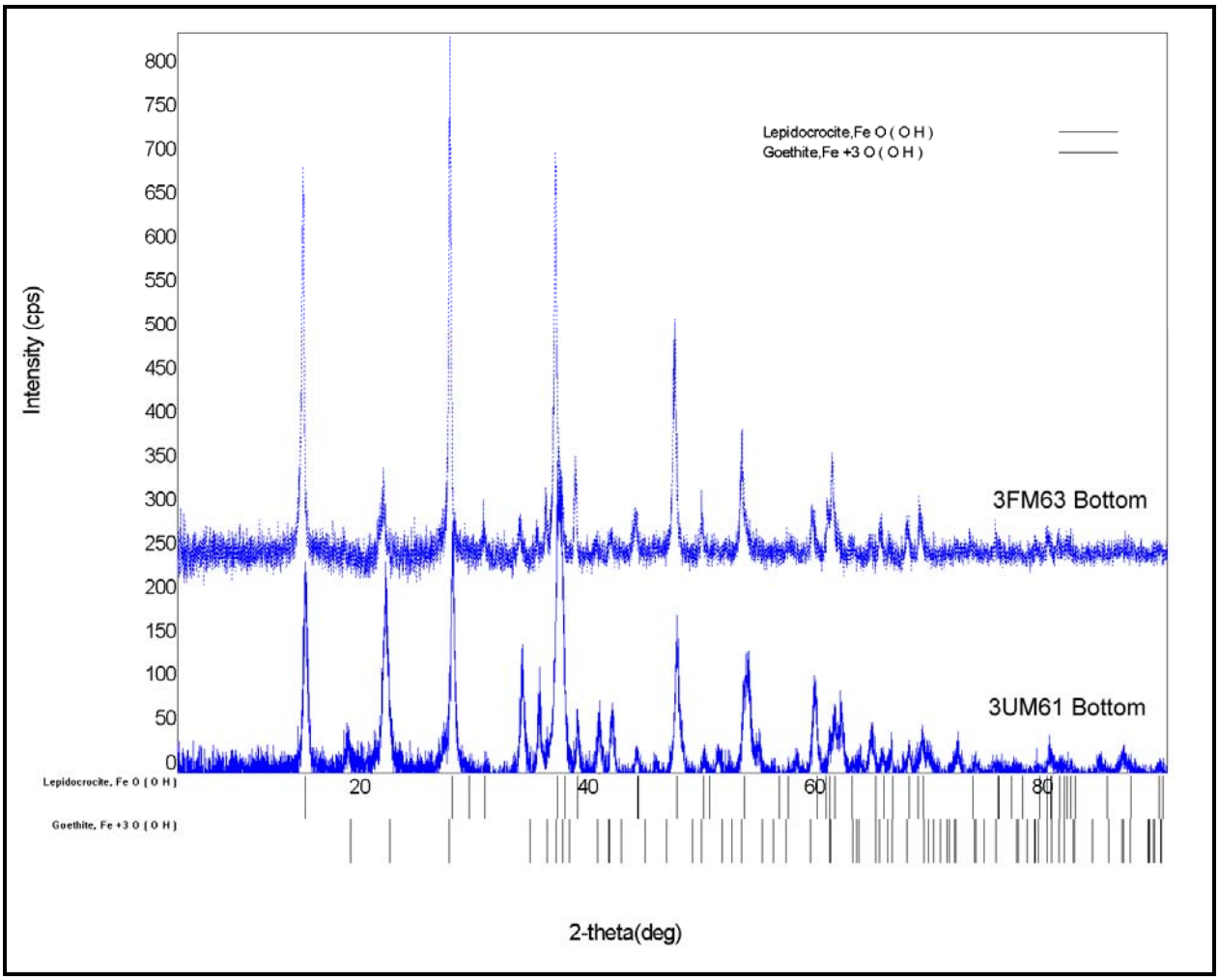

Figure 45. XRD of 6 months 1018 steel coupons exposed in filtered and unfiltered ULSD fuel samples in a selective aerobic (3FM63 and 3UM61) environment.

Lepidocrocite and goethite were the two corrosion products found on both steel samples 3FM63 and 3UM61 as depicted by Figure 45. These two corrosion products were also revealed by Raman analysis of Figure 28.

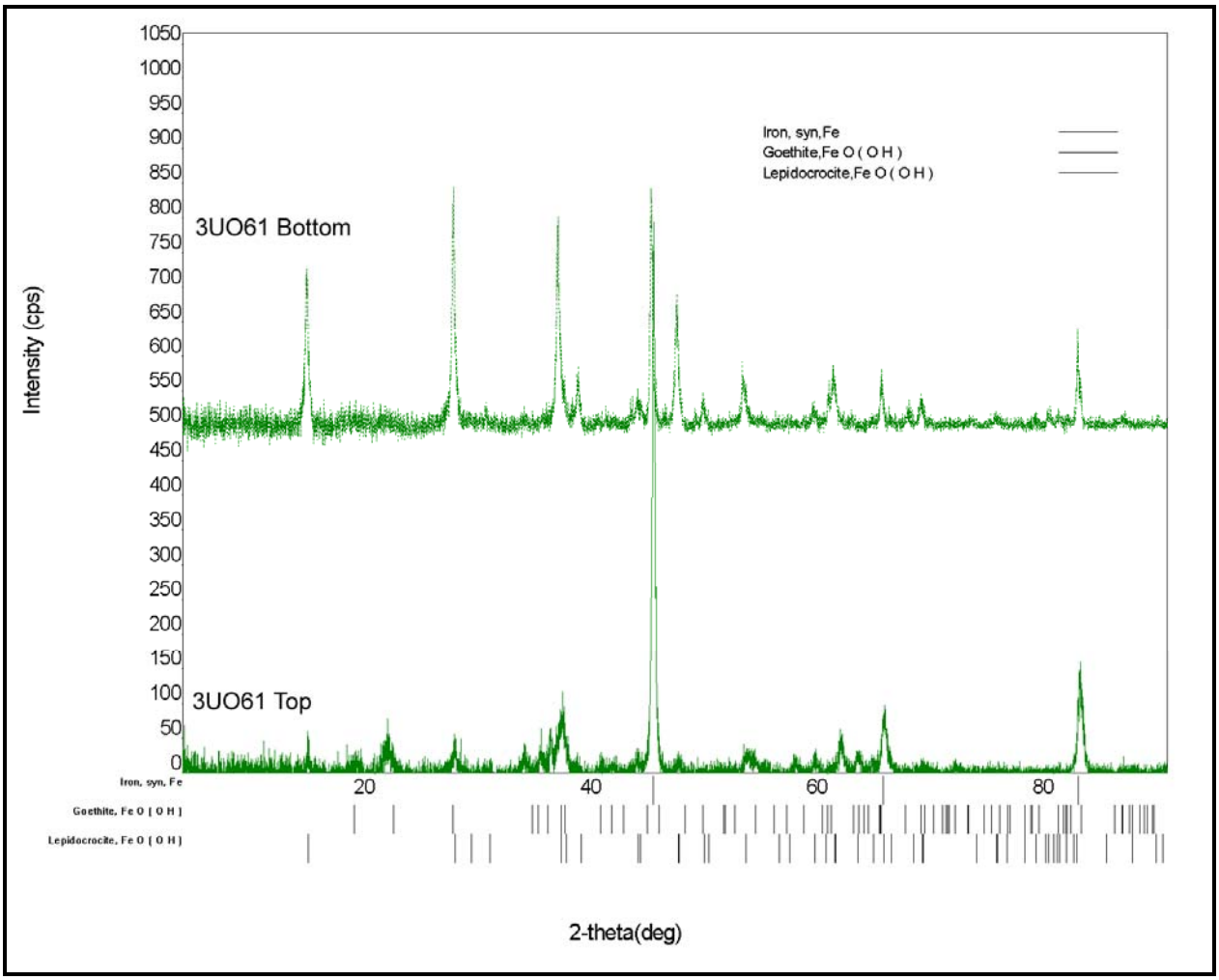

Figure 46. XRD of 6 months 1018 steel coupons exposed in unfiltered ULSD fuel samples in an aerobic (3UO61) environment.

Figure 46 depicts lepidocrocite and goethite as the corrosion products identified on the top part of steel coupon 3UO61 whereas only lepidocrocite was identified as the only corrosion product on the bottom of steel coupon 3UO61. Again, these results correlate well with Raman results of Figure 29.

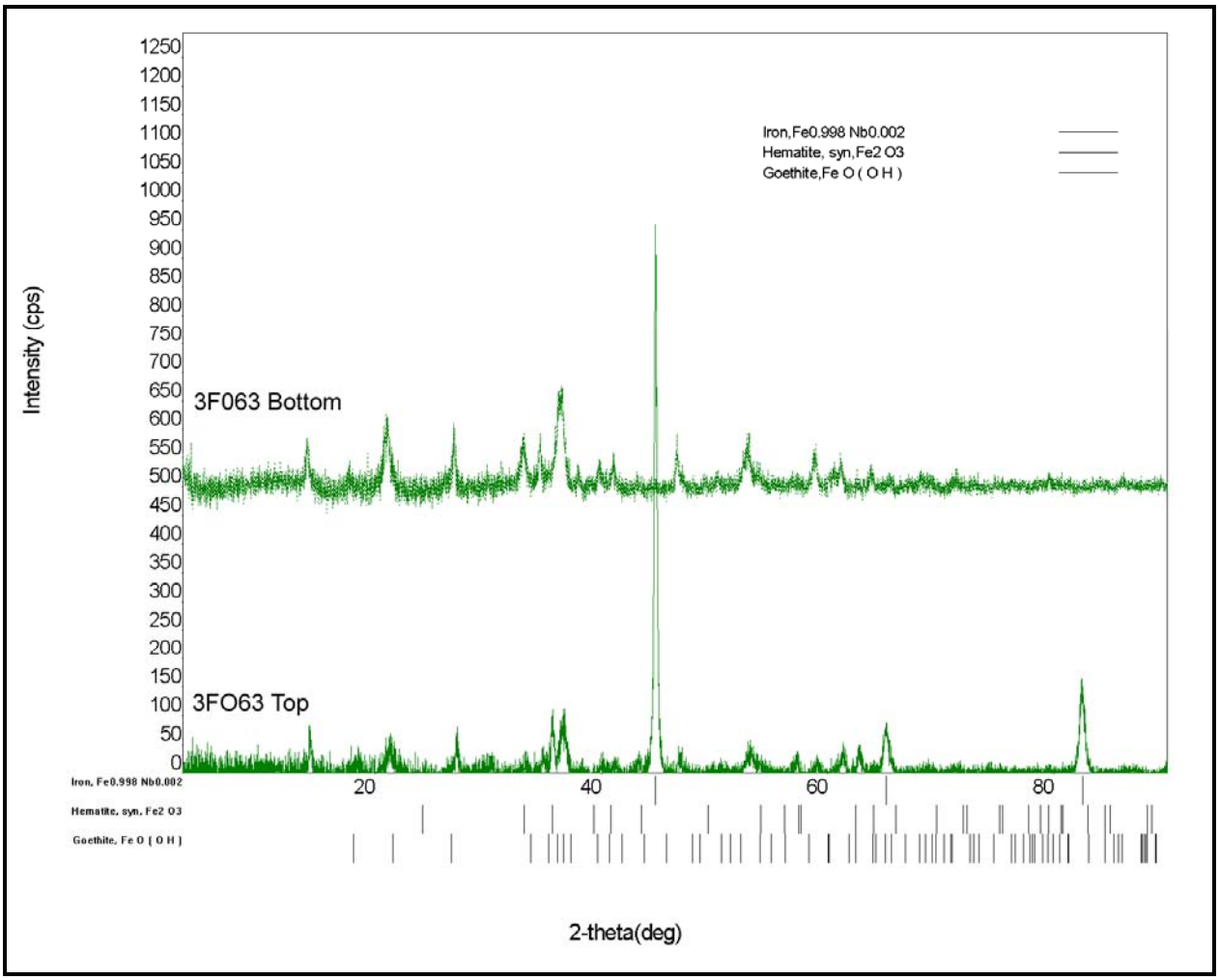

Figure 47. XRD of 6 months 1018 steel coupons exposed in filtered ULSD fuel samples in an aerobic (3FO63) environment.

Lepidocrocite and hematite were detected as corrosion products on both the top and bottom parts of steel coupon 3FO63 as depicted by Figure 47. Raman analysis of Figure 30 reveals lepidocrocite and a slightly different iron oxide, goethite, as the two corrosion products for steel coupon 3FO63. Hematite was not detected by the Raman.

Similarly, the following figures depict the results obtained via XRD for the 1 year exposure time period.

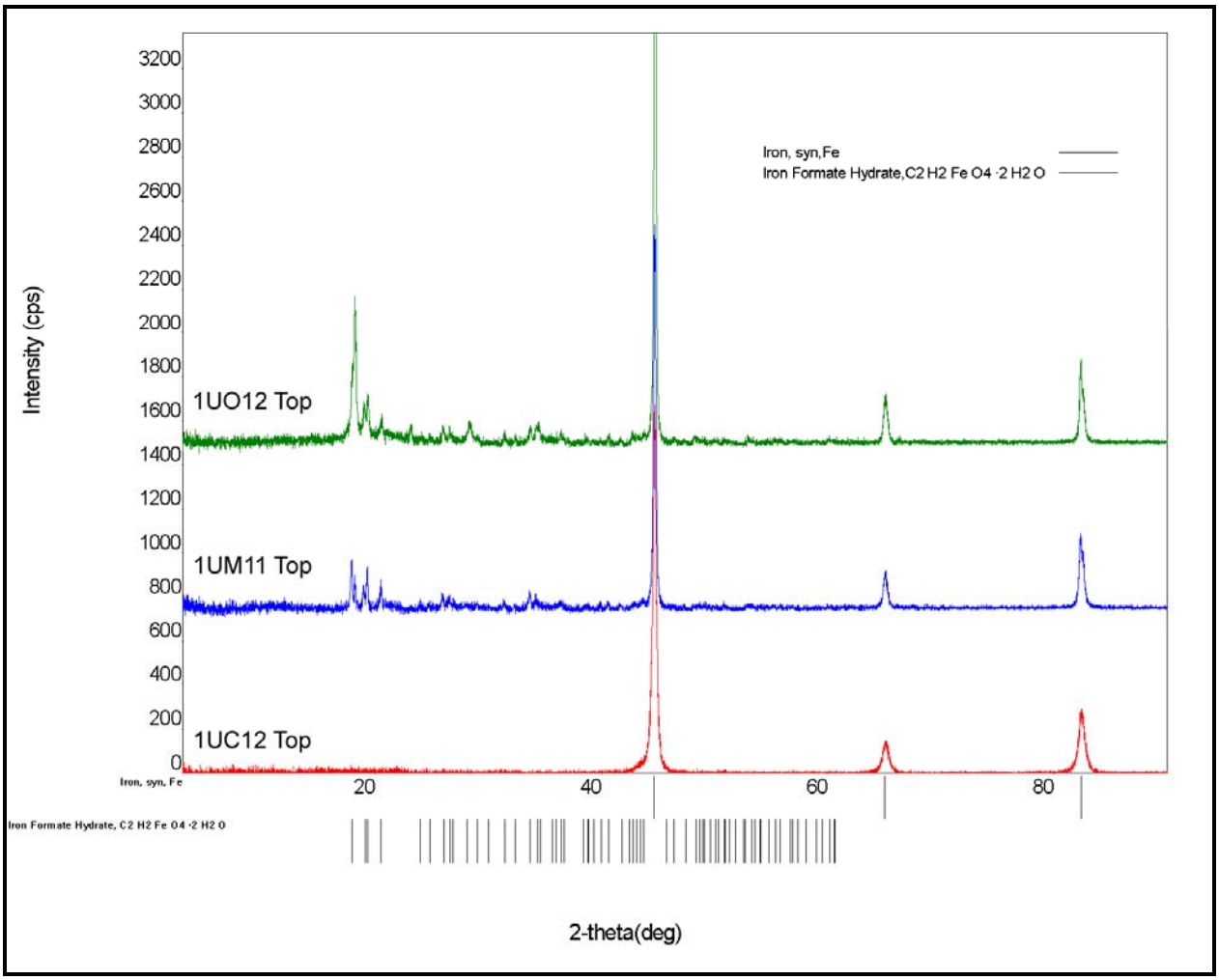

Figure 48. XRD of 1 year 1018 steel coupons exposed in unfiltered B100 fuel samples in an anaerobic (1UC12), selective aerobic (1UM11), and aerobic (1UO12) environments.

Similar to the 6 month exposure of Figure 39, XRD results depicted by Figure 48, revealed iron formate hydrate as the main corrosion product on 1018 steel coupons 1UM11 and 1UO12. As for steel coupon 1UC12, no corrosion product could be detected by XRD. Raman analysis from Figures 30, 31, and 32 revealed bands characteristic of lepidocrocite and an unknown band which could possibly be iron formate hydrate for steel coupons 1UC12 and 1UO12. Raman was unable to determine corrosion product on sample 1UM11.

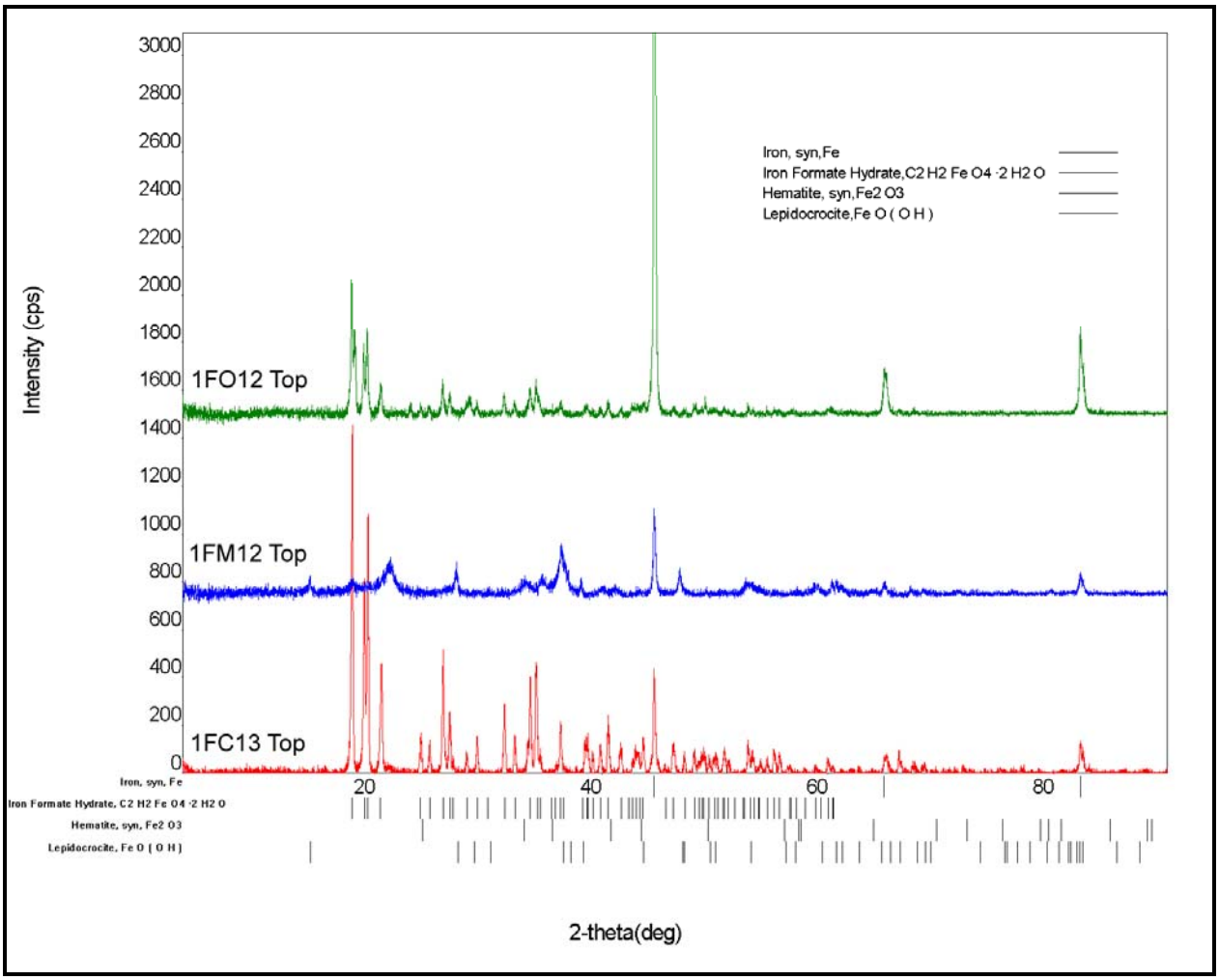

Figure 49. XRD of 1 year 1018 steel coupons exposed in filtered B100 fuel samples in an anaerobic (1FC13), selective aerobic (1FM12), and aerobic (1FO12) environments.

XRD analysis reveals iron formate hydrate for steel coupons 1FC13 and 1FO12 whereas steel coupon 1FM12 showed hematite and lepidocrocite as corrosion products as depicted by Figure 49. In contrast to the XRD results obtained, Raman results of Figures 30, 31, and 33 revealed lepidocrocite as the corrosion products for steel coupons 1FC13, 1FM12, and 1FO12. In addition, maghemite was also found on steel coupon 1FO12.

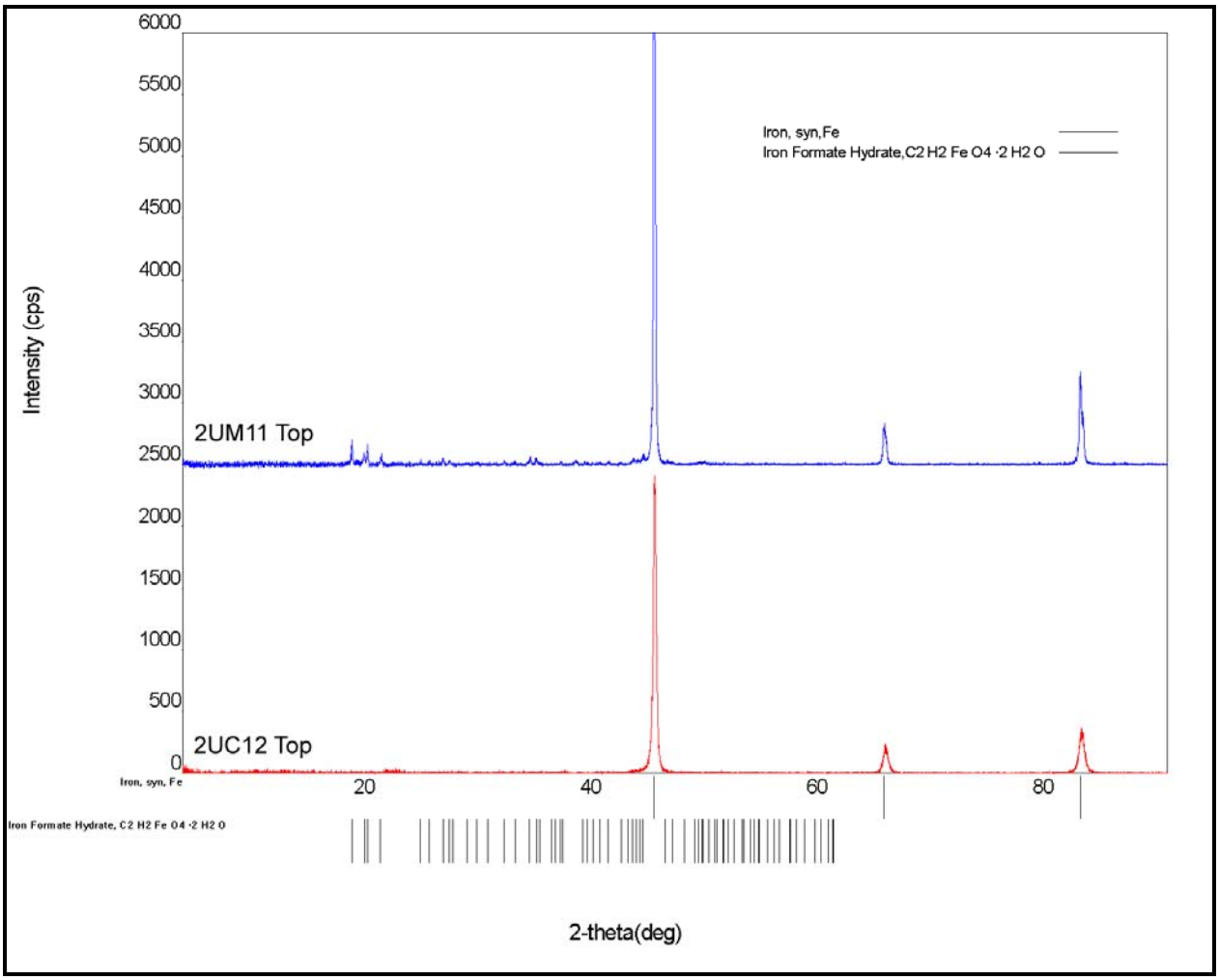

Figure 50. XRD of 1 year 1018 steel coupons exposed in unfiltered B20 fuel samples in an anaerobic (2UC12) and selective aerobic (2UM11) environment.

Iron formate hydrate was the corrosion product observed on steel coupon 2UM11 as depicted by Figure 50. There was too little corrosion product for XRD analysis on steel coupon 2UC12. Raman analysis of Figure 34 revealed different results as both steel coupon samples showed bands characteristic of lepidocrocite as the corrosion product. As for the case of the previous analysis performed with Raman, there is no XRD data for the steel coupon samples exposed in the aerobic environment since no corrosion product was detected upon acetone washing the sludge layer off the coupons.

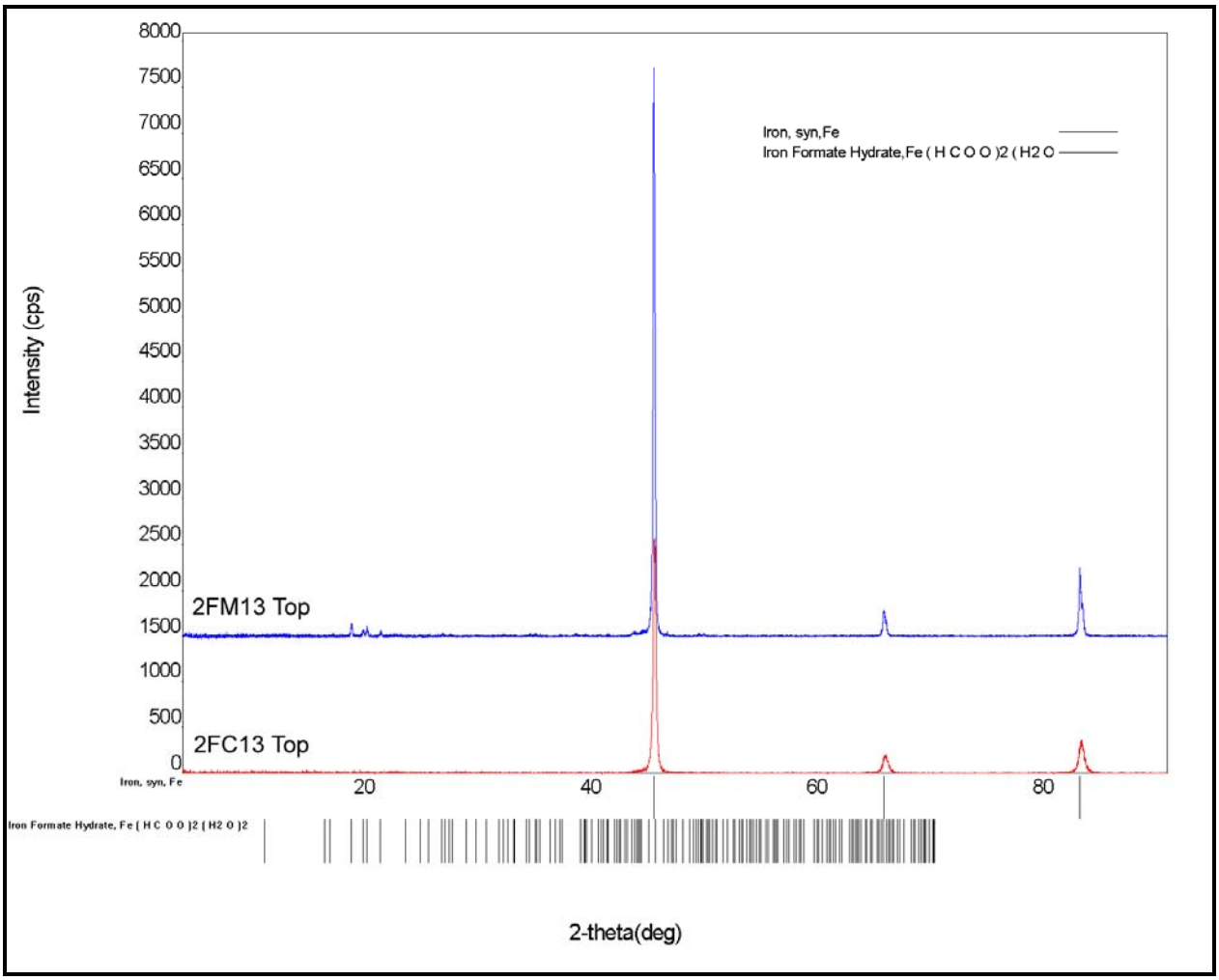

Figure 51. XRD of 1 year 1018 steel coupons exposed in filtered B20 fuel samples in an anaerobic (2UC12) and selective aerobic (2UM11) environment.

Faint iron formate hydrate peaks were found on sample 2FM13 as depicted by Figure 51. Again, there was too little corrosion product for XRD analysis on steel coupon 2FC13. Characteristic bands of lepidocrocite was revealed in Raman analysis for both coupon samples as depicted by Figure 35. Also on steel coupon 2FM13, an unknown band was detected which as stated previously could possibly belong to iron formate hydrate. Similarly, there is no XRD data for the steel coupon samples exposed in the aerobic environment since no corrosion product was detected upon acetone washing the sludge layer off the coupons.

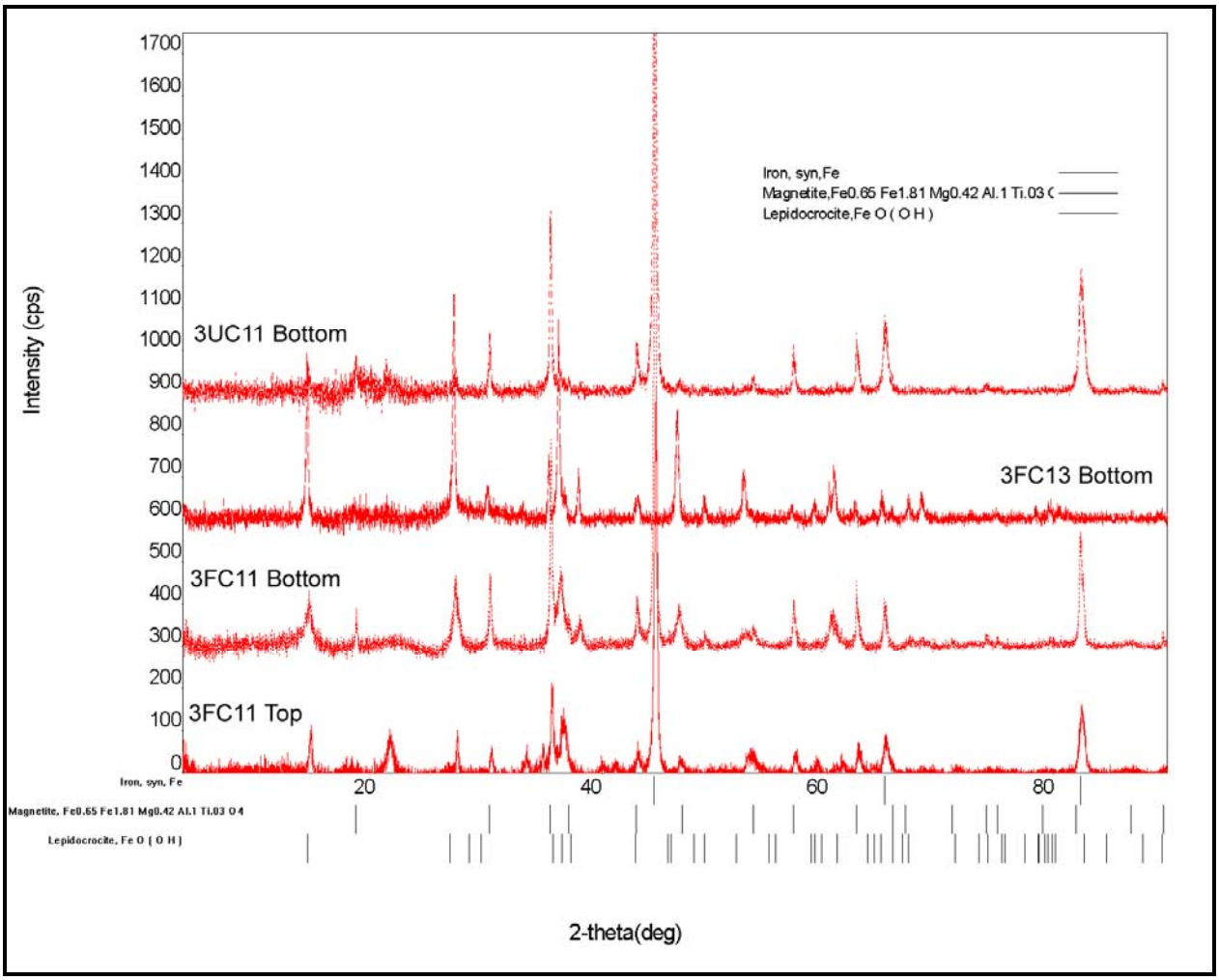

Figure 52. XRD of 1 year 1018 steel coupons exposed in filtered and unfiltered ULSD fuel samples in an anaerobic (3FC11, 3FC13, and 3UC11) environment.

XRD analysis revealed lepidocrocite and magnetite as the corrosion products found in all steel coupon samples as depicted by Figure 52. Raman results of Figure 36 are also in agree with XRD analysis as bands characteristic of lepidocrocite and magnetite were detected.

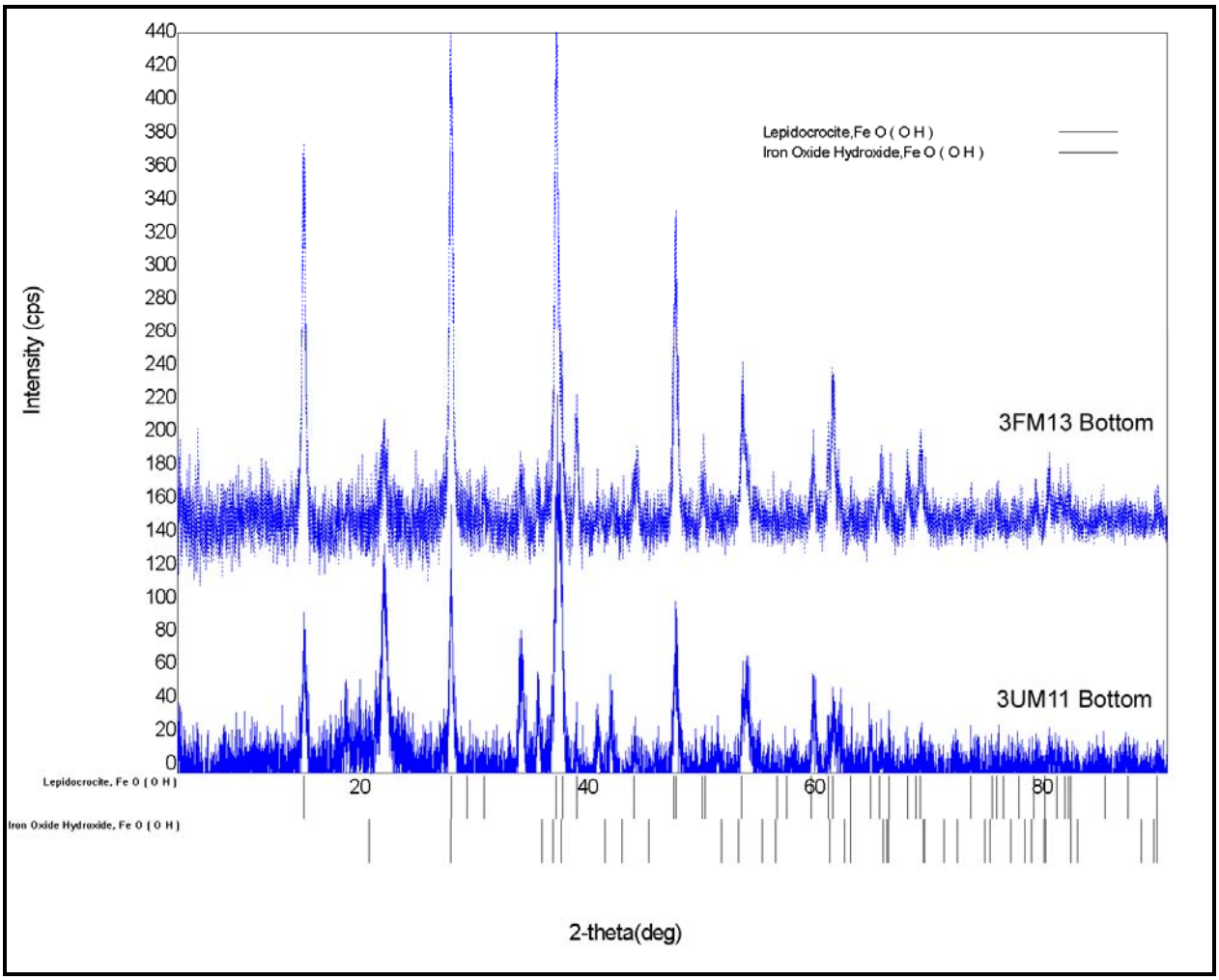

Figure 53. XRD of 1 year 1018 steel coupons exposed in filtered and unfiltered ULSD fuel samples in a selective aerobic (3UM11 and 3FM13) environment.

XRD results reveal lepidocrocite and iron oxide hydroxide as the corrosion products for both steel samples as depicted by Figure 53. Raman results of Figure 37 only detected characteristic bands pertaining to lepidocrocite for both samples. The additional iron oxide hydroxide was not detected by Raman.

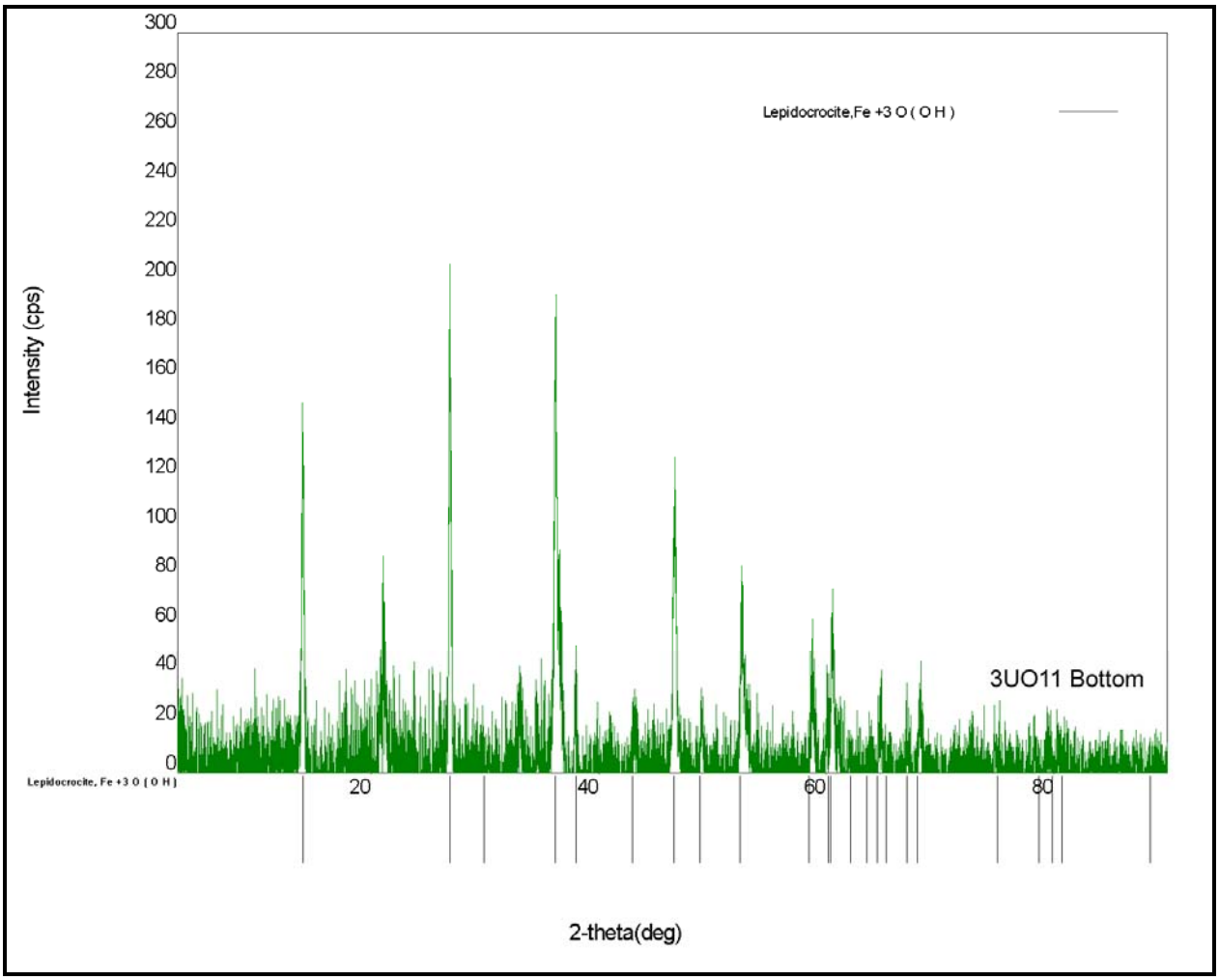

Figure 54. XRD of 1 year 1018 steel coupon exposed in unfiltered ULSD fuel samples in an aerobic (3UO11) environment.

XRD analysis revealed lepidocrocite as the corrosion product on the bottom portion of steel coupon 3UO11 as depicted by Figure 54. Unfortunately, for the top portion of 3UO11, XRD was unable to detect any reasonable corrosion product. The Raman results of Figure 38 also agree with XRD analysis and was able to detect a slight band characteristic of maghemite for the top portion of steel coupon 3UO11.

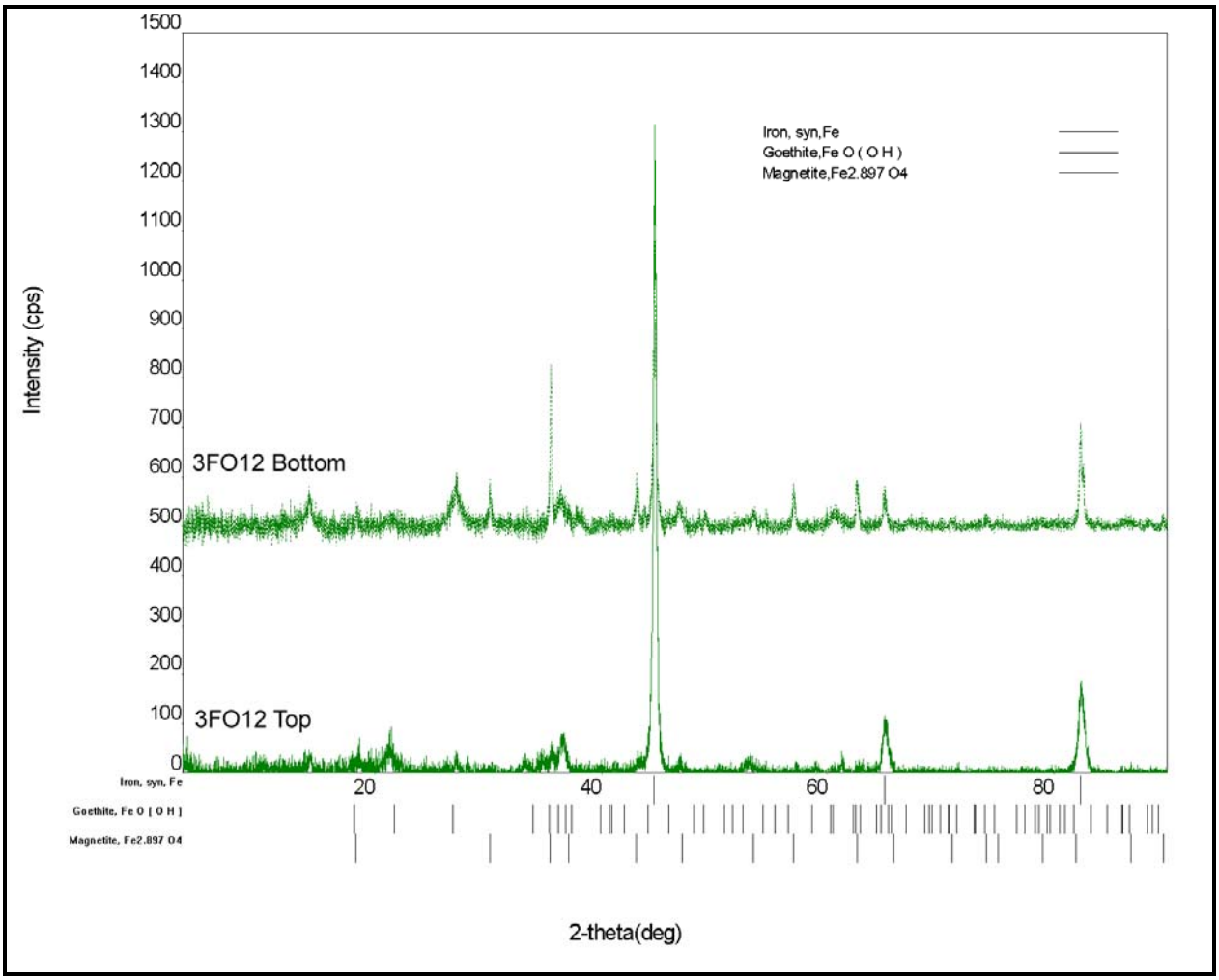

Figure 55. XRD of 1 year 1018 steel coupon exposed in filtered ULSD fuel samples in an aerobic (3FO12) environment.

Goethite and magnetite were the two corrosion products detected by XRD analysis in both steel coupons as depicted by Figure 55. Raman results of Figure 38 also agree and compliment these results.

5.5. SEM/EDXA

The SEM/EDXA analysis of this section is viewed more as supplementary to the Raman and XRD analysis. The corrosion product form listed in the SEM/EDXA analysis serves only as a hypothesis as to the types of products found, and are not definitive as in the case of the Raman and XRD. This form column was added based on SEM/EDXA analysis involving the atomic percentages of elements found. Therefore, corrosion products are listed based on these atomic percentages but are in no way definitive or representative in the actual corrosion products on the 1018 steel coupons. Hence, SEM/EDXA analysis is here to compliment the corrosion product findings of both Raman and XRD analyses.

Due to the vast amount of data obtained through SEM/EDXA analysis, only data of importance is presented in this section. The remaining SEM/EDXA data can be found in the appendix. The following figures depict the results obtained via SEM/EDXA for the 6 month exposure time period.

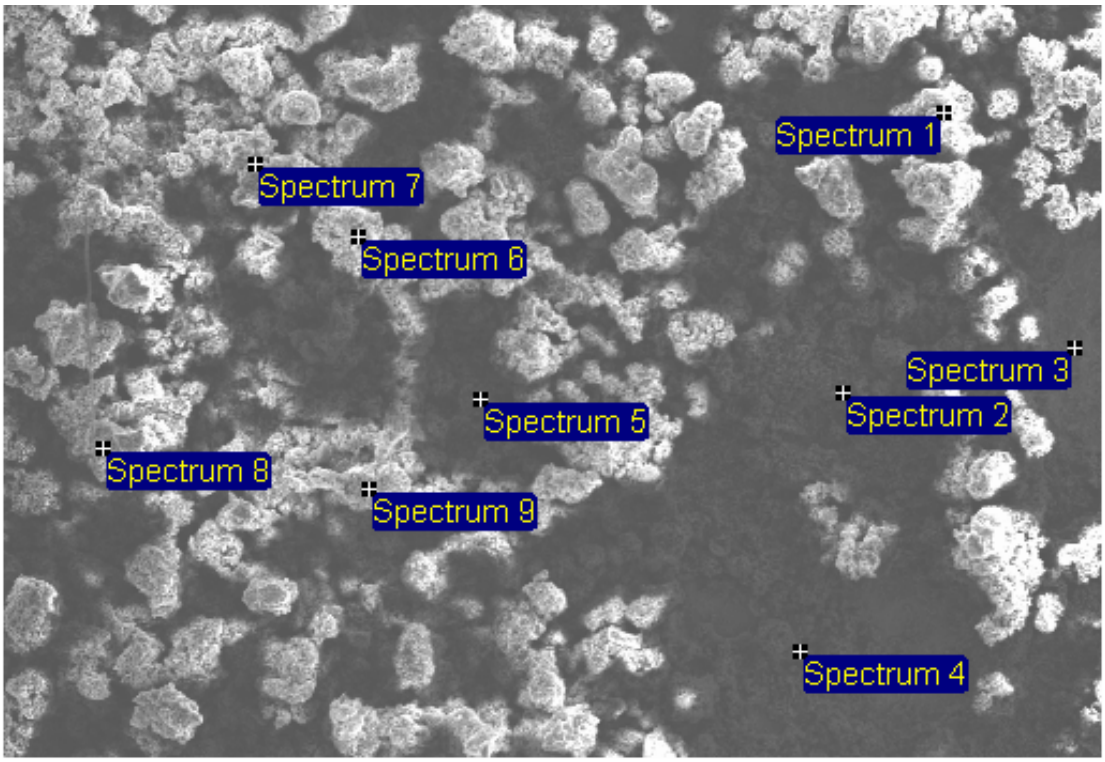

Processing option : All elements analysed

Spectrum	In stats.	C	O	Mn	Fe	Form*
Spectrum 1	Yes	38.69	33.78		27.53	Fe_3O_4
Spectrum 2	Yes	31.00	52.92	0.15	15.93	$Fe(OH)_3$
Spectrum 3	Yes	41.58			58.42	Fe_3O_4
Spectrum 4	Yes	27.81	41.68		30.52	Fe_3O_4
Spectrum 5	Yes	34.09	50.69		15.22	$Fe(OH)_3$
Spectrum 6	Yes	28.01	64.98		7.01	
Spectrum 7	Yes	37.30	53.24		9.46	
Spectrum 8	Yes	34.61	57.32		8.07	
Spectrum 9	Yes	27.63	66.01		6.36	
Max.		41.58	66.01	0.15	58.42	
Min.		27.63	33.78	0.15	6.36	

All results in atomic%
*Based on the ratios of iron oxides and hydroxides.

Figure 56. SEM analysis of 1018 steel coupon (1UC61) exposed in unfiltered B100 fuel-water mixture exposed in an anaerobic environment.

For the SEM/EDXA analysis depicted by Figure 56, EDXA spectra reveals possible corrosion product high in iron and oxygen, which is indicative of possible iron oxides and

hydroxides of the form Fe_3O_4 and $Fe(OH)_3$. Carbon is also found which is indicative of fuel that may have remained on the sample.

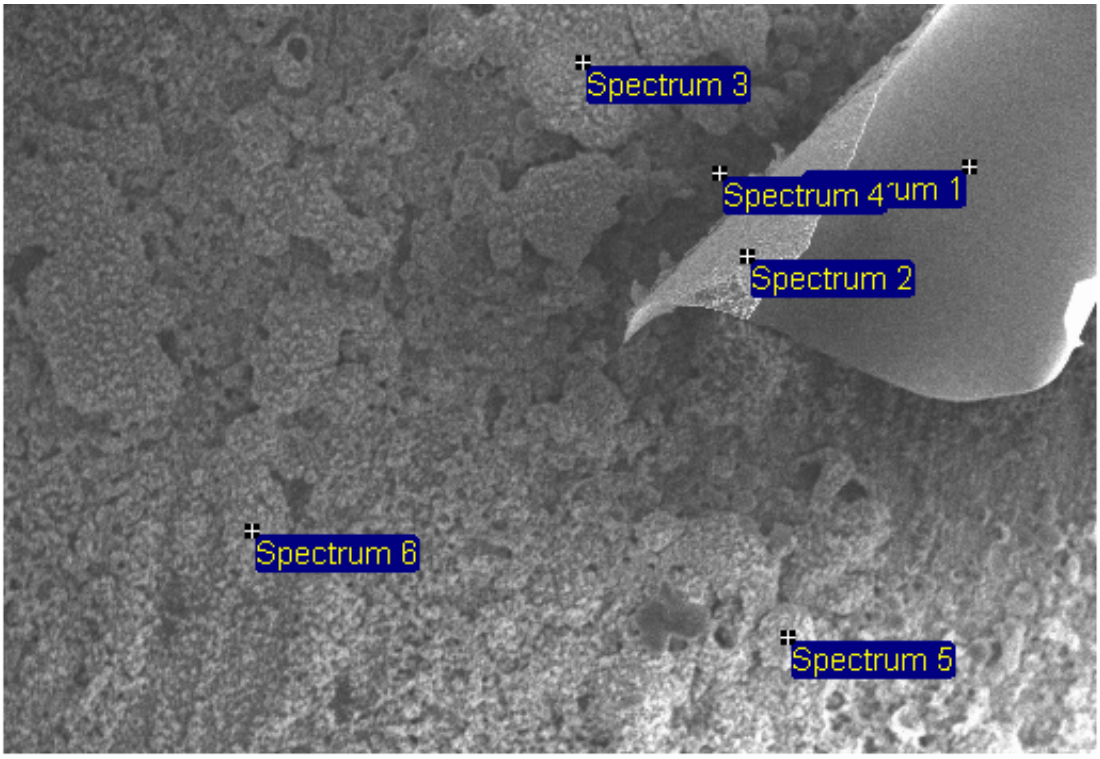

Processing option : All elements analysed

Spectrum	In stats.	C	O	Fe	Form*
Spectrum 1	Yes	30.94	56.12	12.93	
Spectrum 2	Yes	43.32	49.79	6.89	
Spectrum 3	Yes	35.01	47.05	17.94	$Fe(OH)_3$
Spectrum 4	Yes		11.82	88.18	
Spectrum 5	Yes	33.30	38.85	27.85	Fe_3O_4
Spectrum 6	Yes	26.91	54.60	18.50	$Fe(OH)_3$
Max.		43.32	56.12	88.18	
Min.		26.91	11.82	6.89	

All results in atomic%
*Based on the ratios of iron oxides and hydroxides.

Figure 57. SEM analysis of 1018 steel coupon (2FC63) exposed in filtered B20 fuel-water mixture exposed in an anaerobic environment.

For the SEM/EDXA analysis depicted by Figure 57, EDXA spectra reveals possible corrosion product high in iron and oxygen, which is indicative of possible iron oxide and

hydroxide in the form of Fe_3O_4 and $Fe(OH)_3$. Carbon was again found which is indicative of fuel that may have remained on the sample.

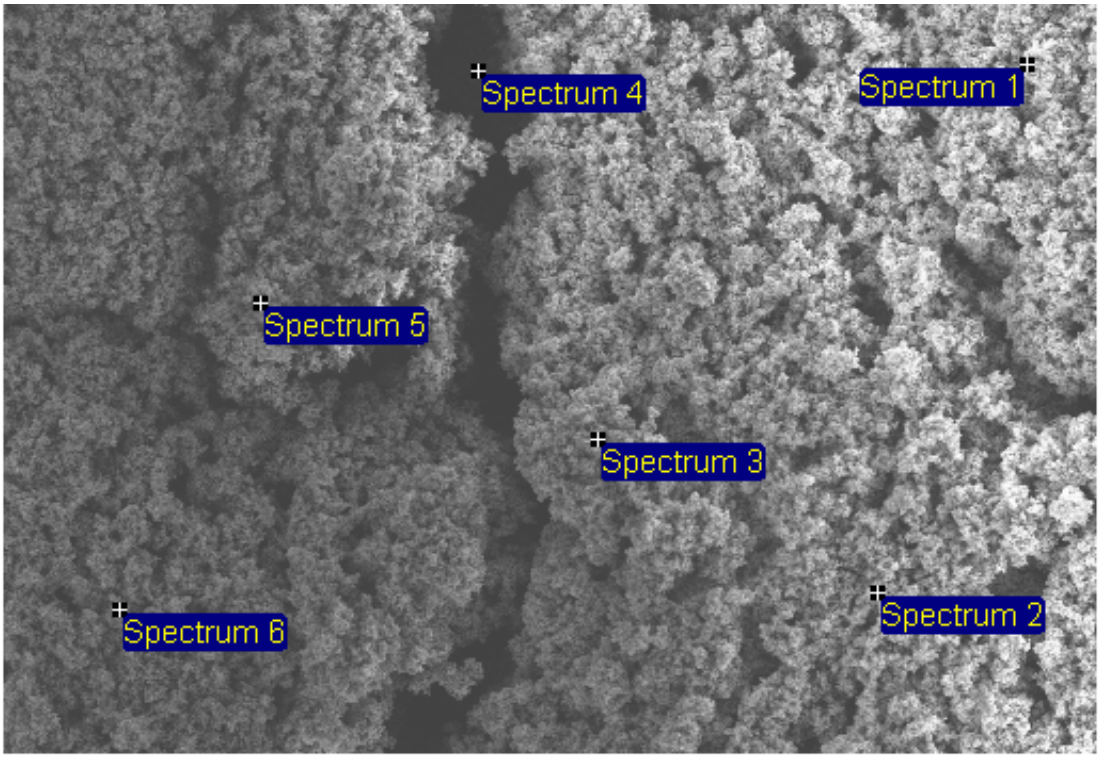

Processing option : All elements analysed

Spectrum	In stats.	C	O	Fe	Form*
Spectrum 1	Yes	37.81	33.42	28.77	
Spectrum 2	Yes	34.43	52.10	13.47	
Spectrum 3	Yes	37.76	43.85	18.39	
Spectrum 4	Yes	39.03	49.86	11.11	
Spectrum 5	Yes	35.14	42.96	21.90	FeO(OH)
Spectrum 6	Yes	35.16	56.20	8.64	
Max.		39.03	56.20	28.77	
Min.		34.43	33.42	8.64	

All results in atomic%
*Based on the ratios of iron oxides and hydroxides.

Figure 58. SEM analysis of 1018 steel coupon (3UO61) exposed in unfiltered ULSD fuel-water mixture exposed in an aerobic environment.

For the SEM/EDXA analysis depicted by Figure 58, EDXA spectra reveals possible corrosion product high in iron and oxygen, which is indicative of possible iron oxide-hydroxide

of the form FeO(OH). The Carbon is again indicative of fuel that may have remained on the sample.

Similarly, the following figures depict the results obtained via SEM/EDXA for the 1 year exposure time period.

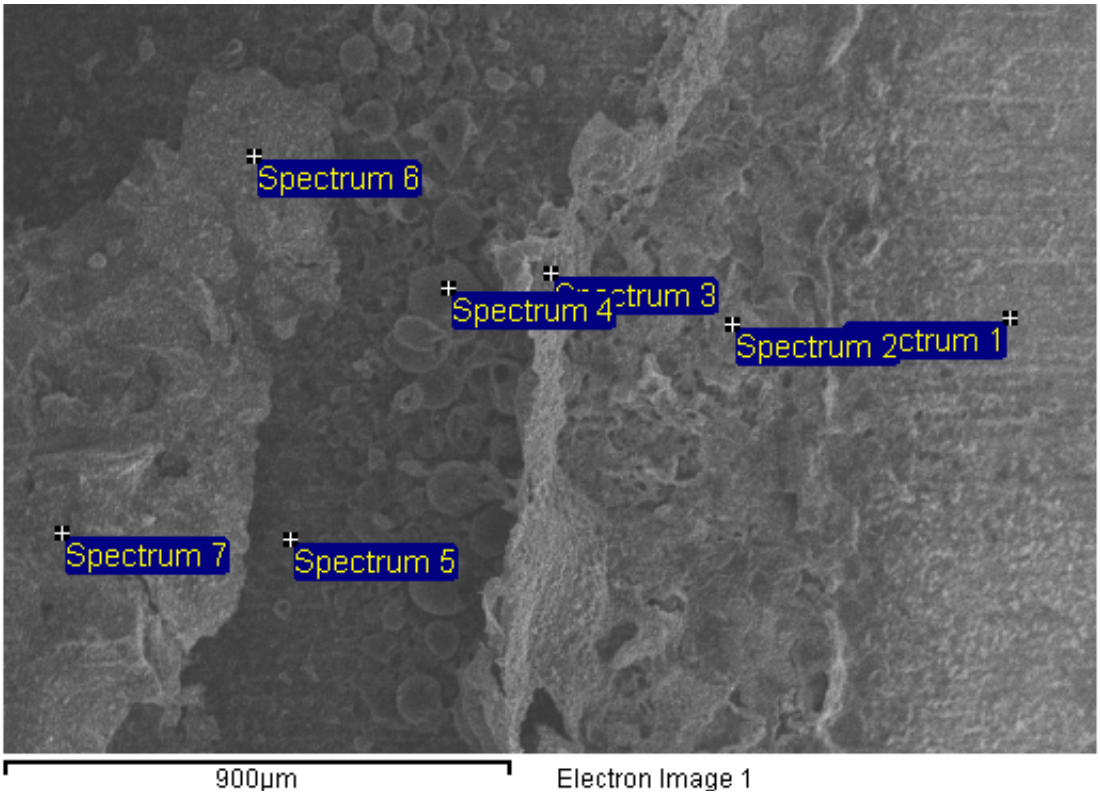

Processing option : All elements analysed

Spectrum	In stats.	C	O	Fe	Form*
Spectrum 1	Yes	54.09	27.33	18.58	Fe_2O_3
Spectrum 2	Yes	45.75	33.63	20.62	Fe_2O_3
Spectrum 3	Yes	75.06	15.73	9.22	Fe_2O_3
Spectrum 4	Yes	36.15	51.37	12.48	
Spectrum 5	Yes	53.00	35.29	11.71	$Fe(OH)_3$
Spectrum 6	Yes	49.56	36.05	14.39	$Fe(OH)_3$
Spectrum 7	Yes	40.31	43.37	16.32	$Fe(OH)_3$
Max.		75.06	51.37	20.62	
Min.		36.15	15.73	9.22	

All results in atomic%
*Based on the ratios of iron oxides and hydroxides.

Figure 59. SEM analysis of 1018 steel coupon (3UC11) exposed in unfiltered ULSD fuel-water mixture exposed in an anaerobic environment.

For the SEM/EDXA analysis depicted by Figure 59, EDXA spectra reveals possible corrosion product high in iron and oxygen, which is indicative of possible iron oxides and hydroxides of the form Fe_2O_3 and $Fe(OH)_3$. Carbon is also found which is indicative of fuel that may have remained on the sample.

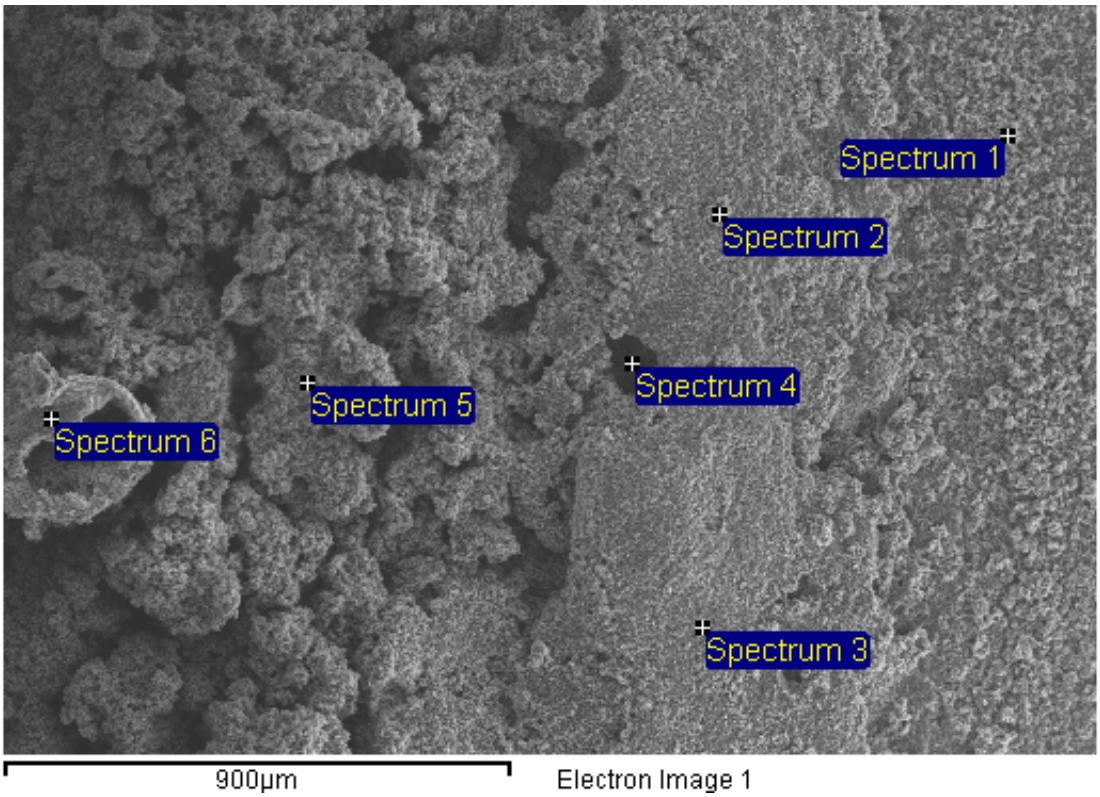

Processing option : All elements analysed

Spectrum	In stats.	C	O	Fe	Form*
Spectrum 1	Yes	39.61	55.79	4.59	
Spectrum 2	Yes	28.18	63.82	7.99	
Spectrum 3	Yes	37.83	55.10	7.07	
Spectrum 4	Yes			100.00	
Spectrum 5	Yes	35.58	55.53	8.89	
Spectrum 6	Yes	36.33	47.20	16.47	$Fe(OH)_3$
Max.		39.61	63.82	100.00	
Min.		28.18	47.20	4.59	

All results in atomic%
*Based on the ratios of iron oxides and hydroxides.

Figure 60. SEM analysis of 1018 steel coupon (1UO12) exposed in unfiltered B100 fuel-water mixture exposed in an aerobic environment.

For the SEM/EDXA analysis depicted by Figure 60, EDXA spectra reveals possible corrosion product high in iron and oxygen, which is indicative of possible iron hydroxide of the form $Fe(OH)_3$. Carbon is also found which is indicative of fuel that may have remained on the sample.

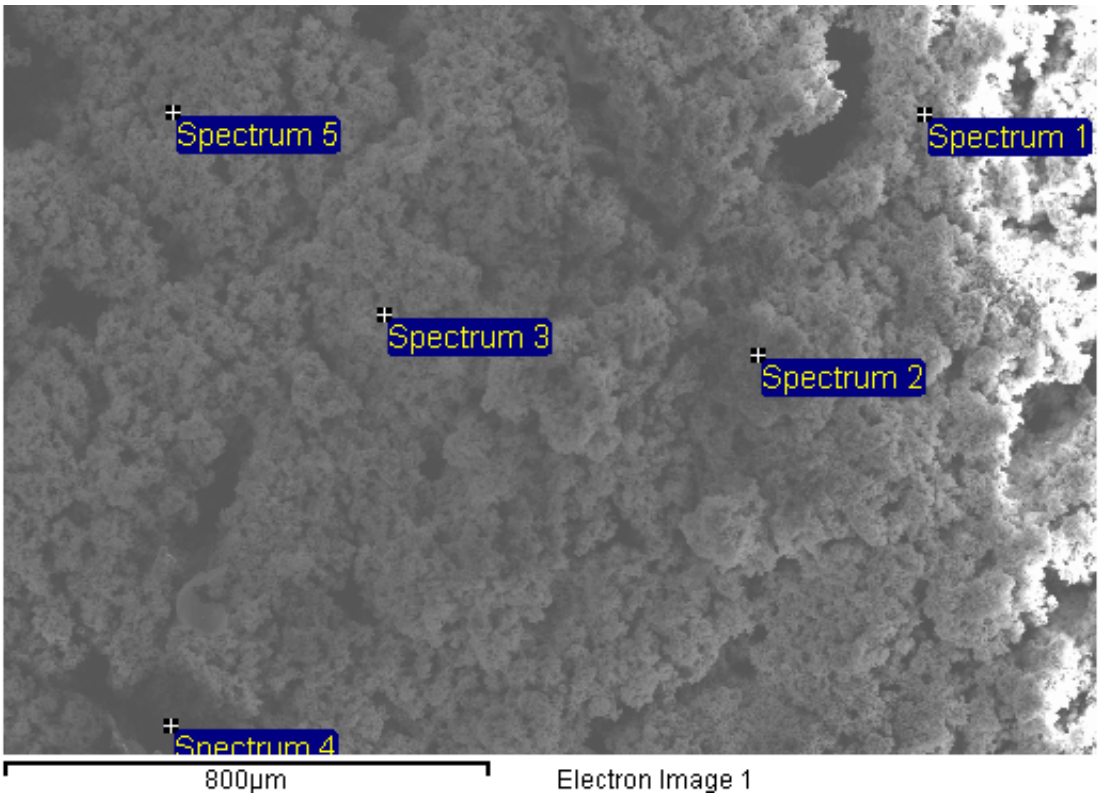

Processing option : All elements analysed

Spectrum	In stats.	C	O	Fe	Form*
Spectrum 1	Yes	51.02	40.89	8.09	
Spectrum 2	Yes	52.81	27.17	20.02	Fe_3O_4
Spectrum 3	Yes	41.00	26.42	32.58	
Spectrum 4	Yes	14.29	4.34	81.37	
Spectrum 5	Yes	56.99	34.73	8.28	
Max.		56.99	40.89	81.37	
Min.		14.29	4.34	8.09	

All results in atomic%
*Based on the ratios of iron oxides and hydroxides.

Figure 61. SEM analysis of 1018 steel coupon (3FO12) exposed in filtered ULSD fuel-water mixture exposed in an aerobic environment.

For the SEM/EDXA analysis depicted by Figure 61, EDXA spectra reveals possible corrosion product high in iron and oxygen, which is indicative of possible iron oxide of the form Fe3O4. The Carbon is again indicative of fuel that may have remained on the sample.

Chapter 6

pH, TAN, DO and Mass Loss

6.1. pH

The following tables depict the pH readings for the 6 month experimental exposures.

Table 9. pH results for 6 month steel coupon samples exposed in an anaerobic environment.

Fuel Type	Fuel	Water
B100	5.26	4.39
B100F	5.19	4.46
B20	4.81	5.22
B20F	4.10	5.15
ULSD	3.66	5.77
ULSDF	3.98	5.76

Table 10. pH results for 6 month steel coupon samples exposed in an aerobic environment.

Fuel Type	Fuel	Water
B100	5.09	4.54
B100F	4.26	3.98
B20	3.74	4.11
B20F	3.98	4.20
ULSD	3.90	5.32
ULSDF	3.25	5.47

Table 11. pH results for 6 month steel coupon samples exposed in a selective aerobic environment.

Fuel Type	Fuel	Water
B100	4.67	3.90
B100F	3.99	3.91
B20	3.94	4.54
B20F	3.94	4.69
ULSD	3.34	5.26
ULSDF	3.39	5.24

Table 12. pH results for B100, B20, and ULSD as received straight from the pump.

Fuel Type	Fuel
B100	4.18
B20	4.65
ULSD	4.49

The following trends were observed from the pH results. Filtered and unfiltered B20 and ULSD fuel-water mixtures revealed lower pH values in the fuel layer with respect to the water layer as depicted by Tables 9, 10, and 11. Filtered and unfiltered B100 fuel-water mixtures revealed the exact opposite trend with lower pH values observed in the water layer with respect to the fuel layer as depicted by Tables 9, 10, and 11. Initial pH values of Table 12 also reveal that B100 fuel-water mixtures increased in alkalinity as time progressed whereas B20 and ULSD fuel-water mixtures increased in acidity as time progressed. Differences in pH values between filtered and unfiltered fuels were negligible. B20 and ULSD fuel-water mixtures appeared to follow similar trends probably due to the fact that B20 fuel contains 80% ULSD in its composition.

Similarly, the following tables depict the pH readings for the 1 year experimental exposures.

Table 13. pH results for 1 year steel coupon samples exposed in an anaerobic environment.

Fuel Type	Fuel	Water
B100	3.80	4.47
B100F	3.70	4.09
B20	3.78	4.23
B20F	3.42	4.79
ULSD	4.01	4.80
ULSDF	3.58	4.53

Table 14. pH results for 1 year steel coupon samples exposed in an aerobic environment.

Fuel Type	Fuel	Water
B100	4.37	4.86
B100F	4.28	4.74
B20	3.45	4.22
B20F	3.90	4.36
ULSD	3.15	4.02
ULSDF	3.14	3.99

Table 15. pH results for 1 year steel coupon samples exposed in a selective aerobic environment.

Fuel Type	Fuel	Water
B100	3.95	4.27
B100F	3.41	3.75
B20	2.87	4.05
B20F	3.81	4.39
ULSD	3.23	4.01
ULSDF	3.18	4.41

Table 16. pH results for 1 year old B100, B20, and ULSD fuels.

Fuel Type	Fuel
B100	5.61
B20	4.24
ULSD	4.40

The 1 year pH results differed from the 6 month results as all fuel types revealed a decrease in pH value in the fuel layer with respect to the water layer. The 1 year old pH results of Table 16 also revealed that all fuels increased with acidity as time progressed.

6.2. TAN

The following table depicts the TAN readings for the 6 month experimental exposures. The figures that accompany the table are a plot of respective pH values from Tables 9 to 11 with corresponding TAN values.

Table 17. 6 month TAN results for fuels in an anaerobic, aerobic, and selective aerobic environment.

Fuel Type	TAN (Anaerobic)	TAN (Aerobic)	TAN (Sel. Aerobic)
B100	2.00	2.00	2.00
B100F	1.03	2.00	1.97
B20	0.00	2.00	1.00
B20F	0.00	2.00	0.80
ULSD	0.00	0.40	0.03
ULSDF	0.00	0.17	0.00

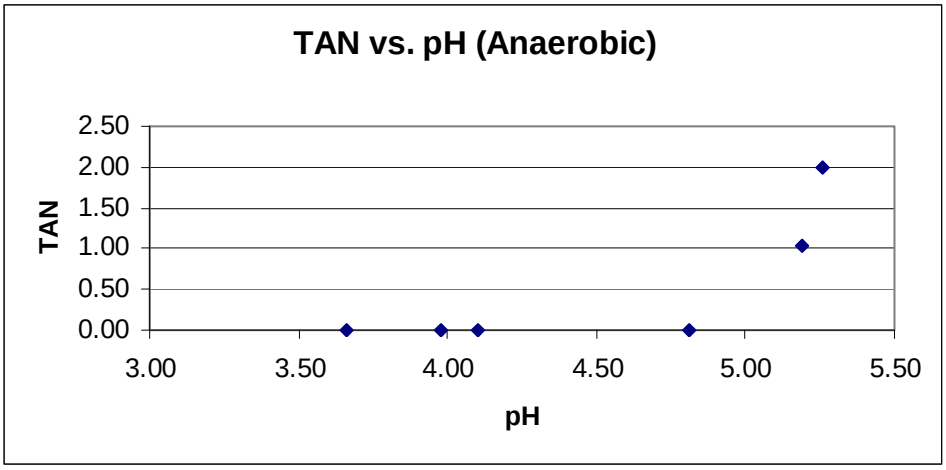

Figure 62. 6 month plot of TAN vs. pH of fuels in an anaerobic environment.

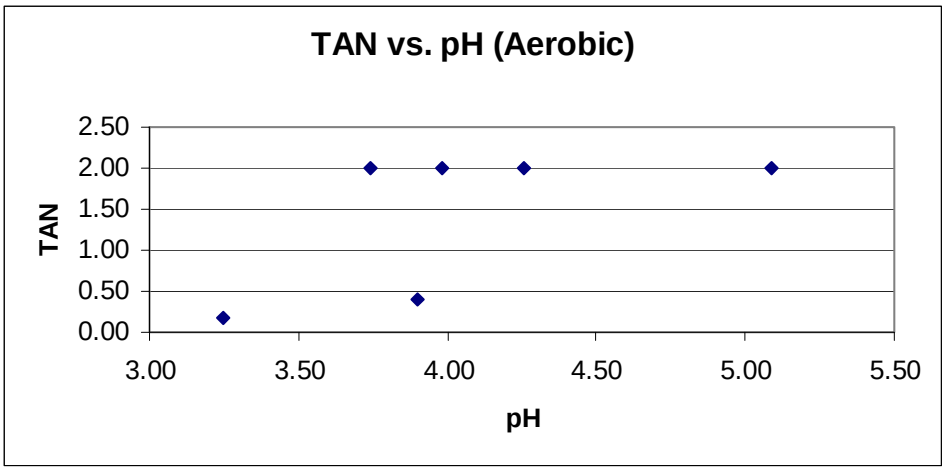

Figure 63. 6 month plot of TAN vs. pH of fuels in an aerobic environment.

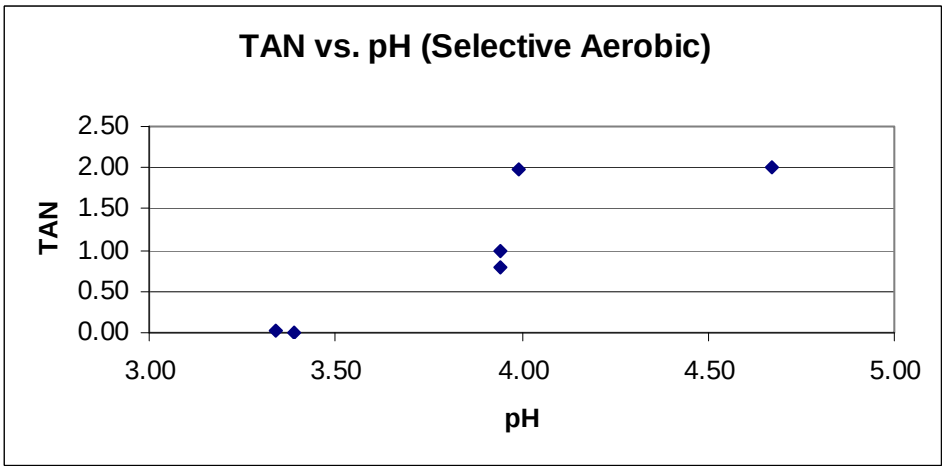

Figure 64. 6 month plot of TAN vs. pH of fuels in a selective aerobic environment.

These TAN vs. pH plots of Figures 62 to 64 reveal the trend that TAN increases as pH values increase (become more alkaline). As mentioned earlier, TAN is essentially defined as the number of milligrams of KOH required to neutralize the acidity in one gram of oil [19]. Therefore, oil with high TAN values, approximately > 0.5, are less desirable since they have been known to cause problems with respect to corrosion and refinery processes [19].

Similarly, the following table depicts the TAN readings for the 1 year experimental exposures. The figures that accompany the table are a plot of respective pH values from Tables 13 to 15 with corresponding TAN values.

Table 18. 1 year TAN results for fuels in an anaerobic, aerobic, and selective aerobic environment.

Fuel Type	TAN (Anaerobic)	TAN (Aerobic)	TAN (Sel. Aerobic)
B100	0.10	2.00	2.00
B100F	0.83	2.00	2.00
B20	0.00	2.00	2.00
B20F	0.00	2.00	2.00
ULSD	0.00	0.87	0.30
ULSDF	0.10	0.83	0.33

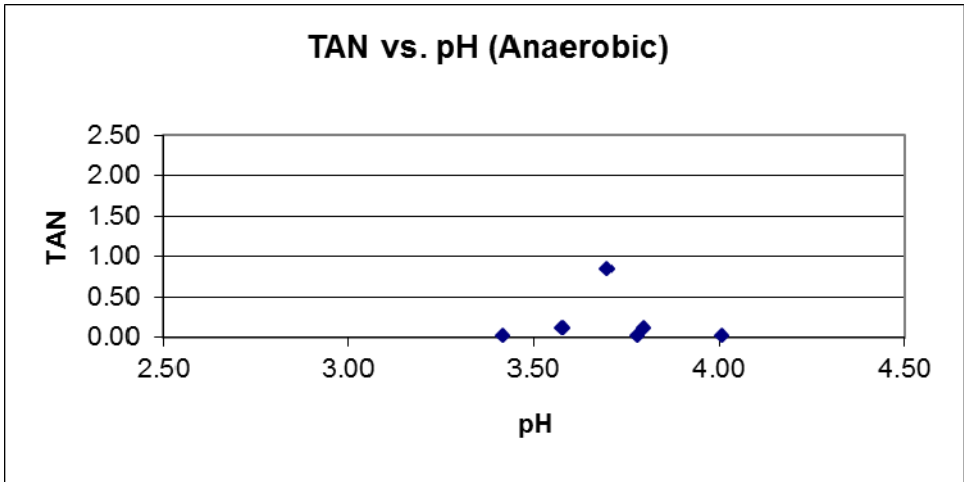

Figure 65. 1 year plot of TAN vs. pH of fuels in an anaerobic environment.

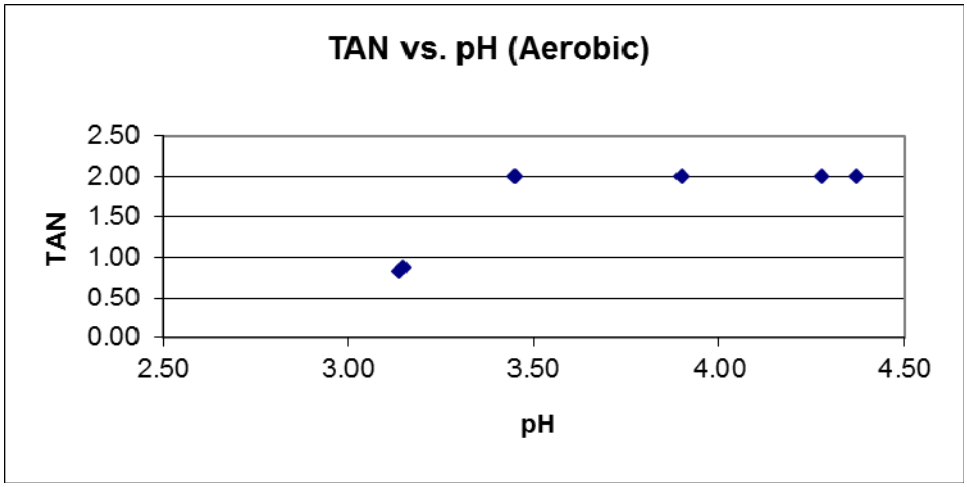

Figure 66. 1 year plot of TAN vs. pH of fuels in an aerobic environment.

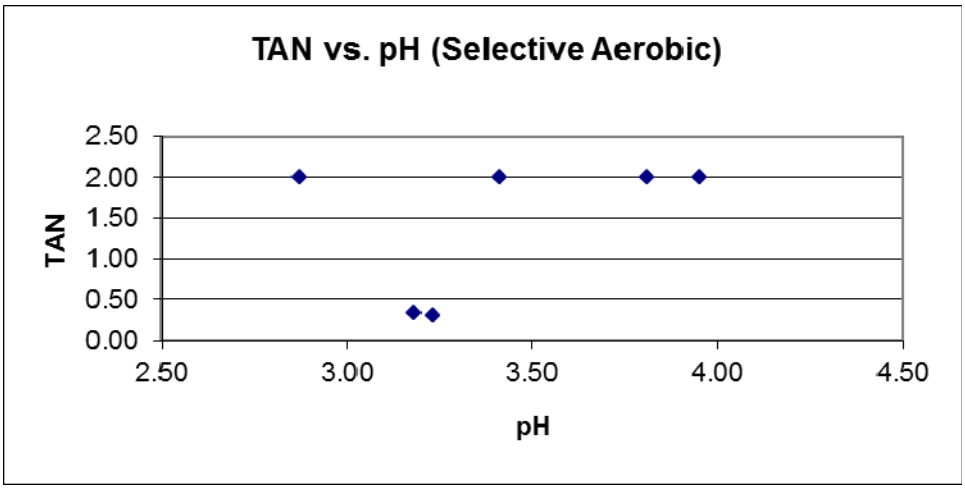

Figure 67. 1 year plot of TAN vs. pH of fuels in a selective aerobic environment.

Again, for the most part, these TAN vs. pH plots of Figures 65 to 67 reveal the trend that TAN increases as pH values increase (become more alkaline). There are some slight deviations with respect to the anaerobic and selective aerobic environment of Figures 65 and 67. In the anaerobic setting of Figure 65, the TAN values virtually remain the same at a value of 0, whereas in the selective aerobic setting of Figure 67, the exact opposite is seen where the majority TAN values are seen at a maximum value of 2.

To fully understand the relationships between pH and TAN values, a graph of both values were plotted. The following plots are for the 6 month time exposure period.

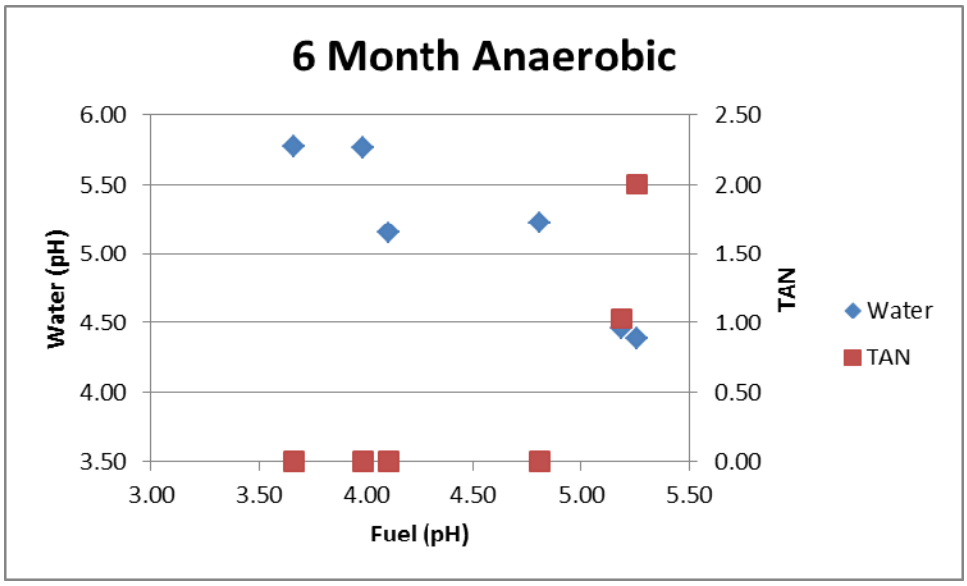

Figure 68. Plot of pH and TAN values for 6 month anaerobic environment.

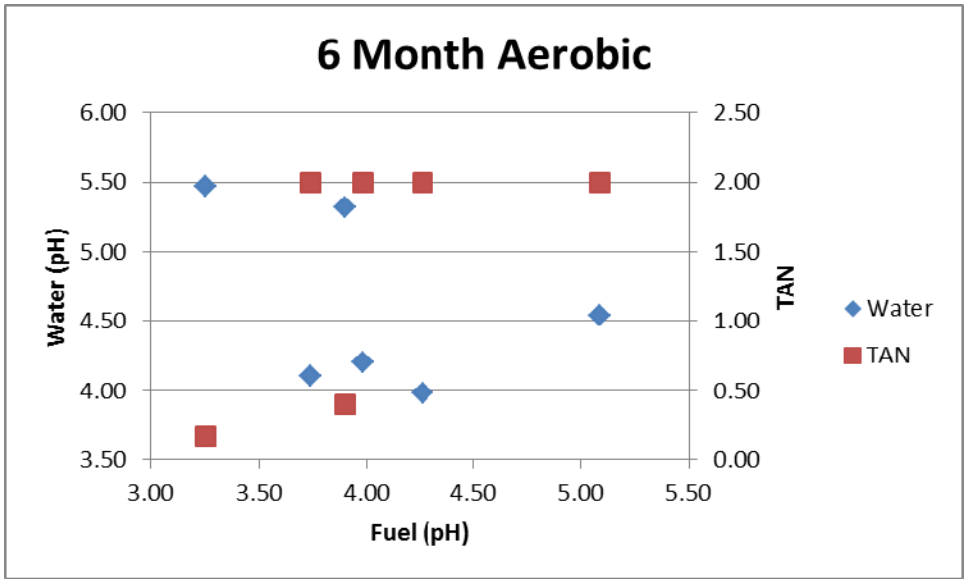

Figure 69. Plot of pH and TAN values for 6 month aerobic environment.

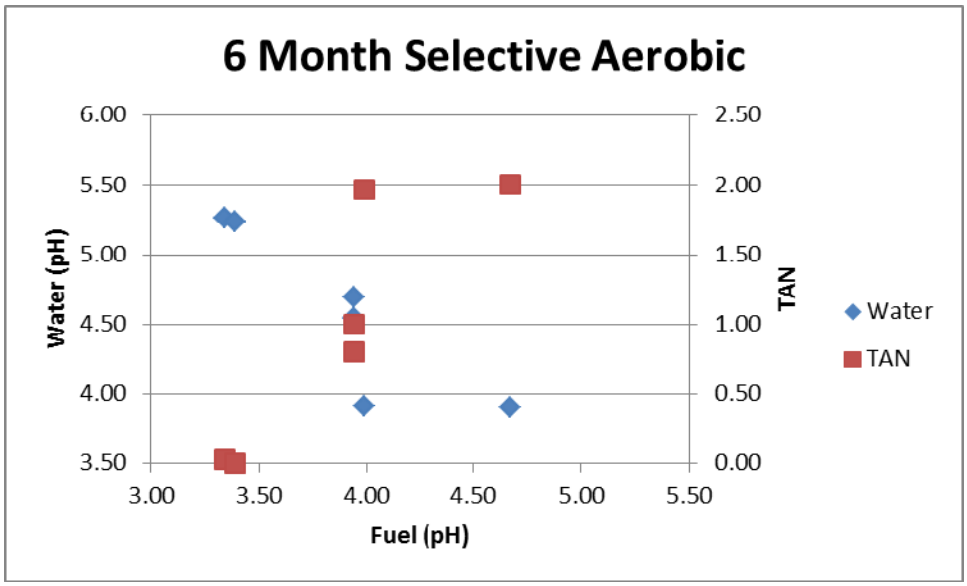

Figure 70. Plot of pH and TAN values for 6 month selective aerobic environment.

Trends seen from Figures 68 to 70 reveal that as the pH of fuel increases (becomes more alkaline) corresponding water pH values decrease (become more acidic) and corresponding TAN values increase.

Similarly, the following plots are for the 1 year time exposure period.

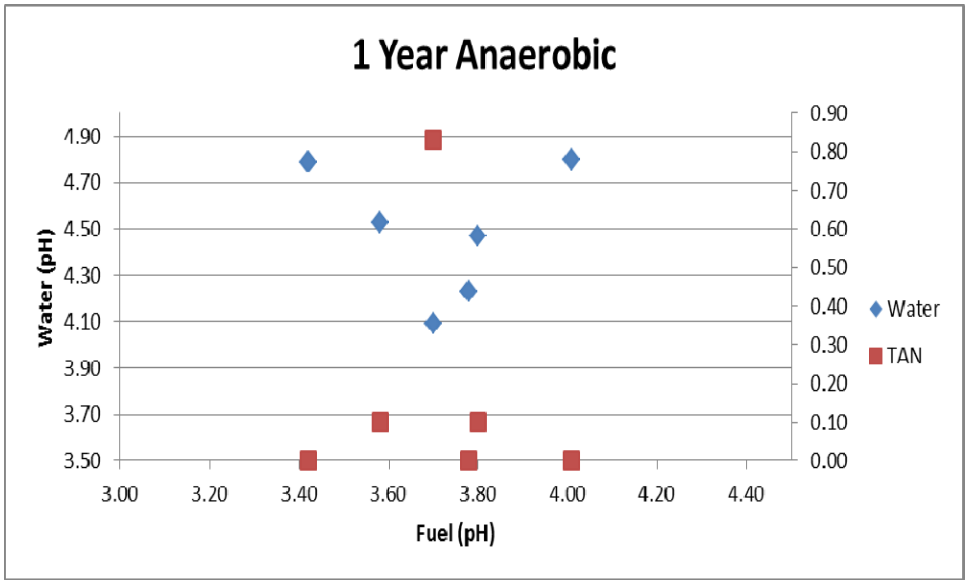

Figure 71. Plot of pH and TAN values for 1 year anaerobic environment.

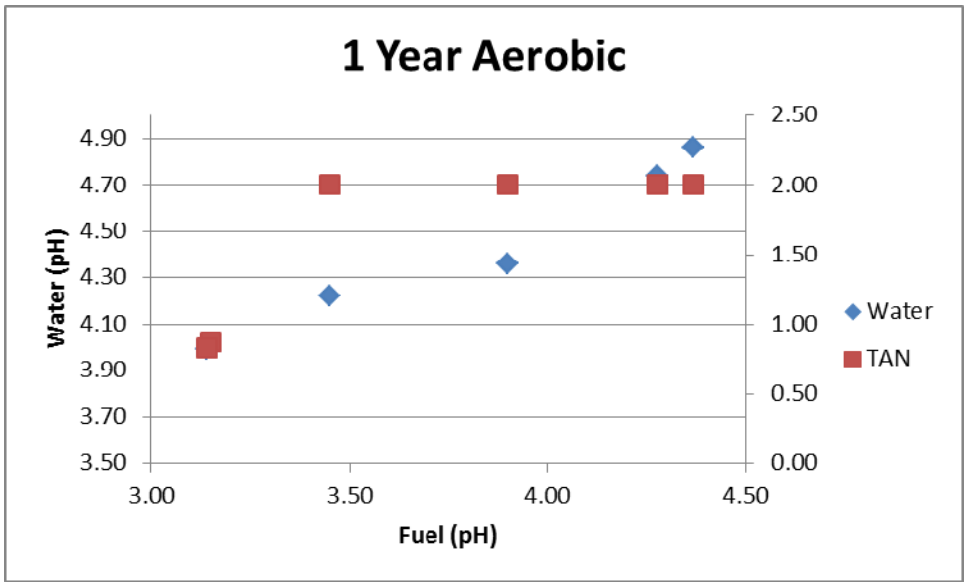

Figure 72. Plot of pH and TAN values for 1 year aerobic environment.

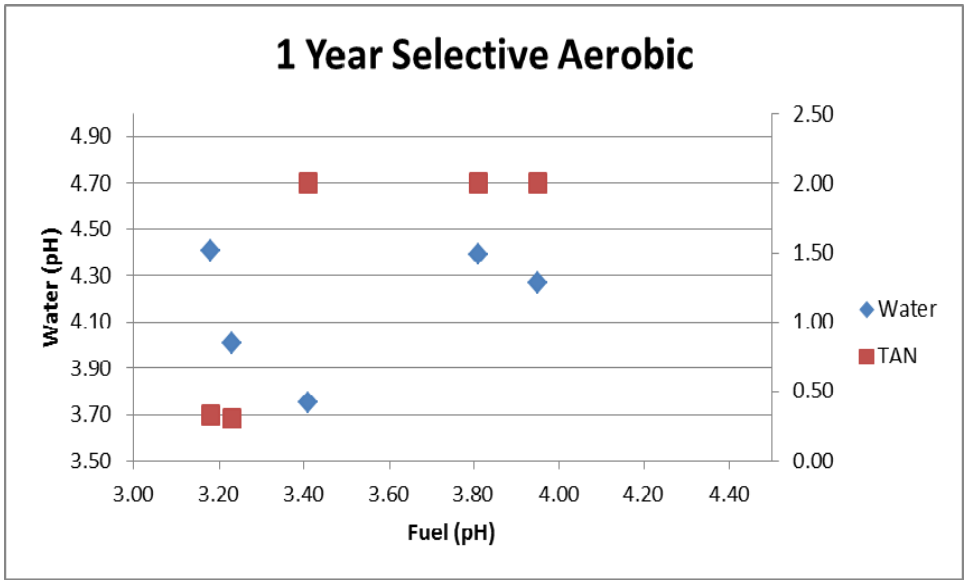

Figure 73. Plot of pH and TAN values for 1 year selective aerobic environment.

Trends from Figures 71 to 73 are more difficult to see in comparison to the 6 month counterparts of Figures 68 to 70. For the case of aerobic and selective aerobic environments of Figures 72 and 73, as fuel pH values increase (become more alkaline), corresponding TAN values increase. Water pH values of the aerobic environment from Figure 72 also show an increase in value (become more alkaline) as fuel pH values increase (become more alkaline). Trends for the anaerobic environment of Figure 71 are hard to see.

It is important to note that the disparity between pH and TAN values seen in the data is not atypical. pH is known to be an apparent representation on how corrosive the fuel may be, but does not indicate the acidic or alkaline constituents [23]. TAN measures the acidic or alkaline constituents but gives less of a representation on how corrosive the fuel may be [23]. In comparison to pH, TAN has a better ability to detect weak acids, which do not readily dissociate in water [23]. Thus, pH and TAN measure different aspects of the fuel's acidic or alkaline character.

6.3. DO

The following tables are the DO results obtained for B100, B20, and ULSD fuel-water mixtures exposed in their respective environments (aerobic, selective aerobic, and anaerobic) for an equilibrium duration period of 1 hour. DO measurements were taken in the water layer of the fuel-water mixtures as depicted by Figure 5.

Table 19. DO results for B100 fuel-water mixture in an aerobic, selective aerobic, and anaerobic environment.

Aerobic		Selective Aerobic		Anaerobic	
Time (min.)	DO (ppm)	Time (min.)	DO (ppm)	Time (min.)	DO (ppm)
0	7.14	0	6.67	0	6.54
5	6.90	5	6.67	5	6.55
10	6.73	10	6.67	10	6.55
15	6.57	15	6.68	15	6.54
20	6.60	20	6.67	20	6.52
25	6.61	25	6.66	25	6.49
30	6.63	30	6.65	30	6.45
35	6.65	35	6.64	35	6.41
40	6.66	40	6.62	40	6.39
45	6.67	45	6.61	45	6.37
50	6.68	50	6.60	50	6.37
55	6.69	55	6.58	55	6.37
60	6.69	60	6.57	60	6.36

Table 20. DO results for B20 fuel fuel-water mixture in an aerobic, selective aerobic, and anaerobic environment.

Aerobic		Selective Aerobic		Anaerobic	
Time (min.)	DO (ppm)	Time (min.)	DO (ppm)	Time (min.)	DO (ppm)
0	6.84	0	6.98	0	7.06
5	6.84	5	6.99	5	7.06
10	6.84	10	6.99	10	7.07
15	6.81	15	6.99	15	7.10
20	6.78	20	7.00	20	7.11
25	6.79	25	7.02	25	7.11
30	6.83	30	7.02	30	7.12
35	6.86	35	7.02	35	7.13
40	6.90	40	7.02	40	7.15
45	6.93	45	7.04	45	7.15
50	6.96	50	7.05	50	7.16
55	6.97	55	7.06	55	7.18
60	6.98	60	7.06	60	7.19

Table 21. DO results for ULSD fuel fuel-water mixture in an aerobic, selective aerobic, and anaerobic environment.

Aerobic		Selective Aerobic		Anaerobic	
Time (min.)	DO (ppm)	Time (min.)	DO (ppm)	Time (min.)	DO (ppm)
0	8.31	0	7.93	0	7.66
5	8.26	5	7.91	5	7.67
10	8.25	10	7.89	10	7.67
15	8.23	15	7.86	15	7.69
20	8.23	20	7.81	20	7.70
25	8.21	25	7.78	25	7.69
30	8.15	30	7.74	30	7.68
35	8.09	35	7.72	35	7.67
40	8.06	40	7.70	40	7.68
45	8.04	45	7.68	45	7.72
50	8.01	50	7.68	50	7.76
55	7.98	55	7.68	55	7.78
60	7.96	60	7.66	60	7.78

The results for most of the fuel-water mixtures as depicted by Tables 19 to 21, the aerobic environment setting had the highest concentration of DO with the anaerobic having the lowest concentration of DO. Therefore, more importantly, these results indicate that even in

anaerobic environments, there is still DO present within the water layer of the fuel-water mixture.

6.4. Mass Loss

The following tables depict the mass loss results for the 6 month exposure period.

Table 22. Mass loss results for 1018 steel coupons exposed for 6 months in unfiltered fuels in an aerobic, selective aerobic, and anaerobic environment.

Sample	Total Mass Loss Avg (g)	STDEV (+/-)	PR (mm/year)
B100 Anaerobic	0.3719	0.0167	0.1199
B100 Aerobic	0.1987	0.0115	0.0641
B100 Sel. Aerobic	0.2142	0.0382	0.0691
B20 Anaerobic	0.0347	0.0455	0.0112
B20 Aerobic	0.2074	0.0060	0.0669
B20 Sel. Aerobic	0.0735	0.1152	0.0237
ULSD Anaerobic	0.1654	0.1645	0.0533
ULSD Aerobic	0.2734	0.0182	0.0881
ULSD Sel. Aerobic	0.3256	0.0098	0.1050

Table 23. Mass loss results for 1018 steel coupons exposed for 6 months in filtered fuels in an aerobic, selective aerobic, and anaerobic environment.

Sample	Total Mass Loss Avg (g)	STDEV (+/-)	PR (mm/year)
B100F Anaerobic	0.0715	0.0350	0.0231
B100F Aerobic	0.1474	0.0104	0.0475
B100F Sel. Aerobic	0.0642	0.0048	0.0207
B20F Anaerobic	0.0261	0.0175	0.0084
B20F Aerobic	0.1835	0.0027	0.0592
B20F Sel. Aerobic	0.1358	0.1155	0.0438
ULSDF Anaerobic	0.1123	0.1264	0.0362
ULSDF Aerobic	0.2241	0.0055	0.0723
ULSDF Sel. Aerobic	0.2659	0.0192	0.0857

These mass loss results reveal that filtered fuel-water mixtures suffer less corrosion damage and have lower penetration rates when compared to their counterpart unfiltered fuel-water mixtures as seen in Tables 22 and 23. In terms of environment condition, there are some trends that can be seen. For example, in the case of 1018 steel coupons immersed in both filtered and unfiltered B20 fuel-water mixtures, the aerobic environment showed the greatest mass loss with anaerobic environment the least amount of mass loss. Similarly, for 1018 steel coupons immersed in both filtered and unfiltered ULSD fuel-water mixtures, the selective aerobic

environment showed the greatest mass loss with anaerobic environment the least amount of mass loss. For the B100 fuel-water mixtures, the highest corrosion rate was observed in the unfiltered anaerobic samples. In general, the corrosion rates were higher in the unfiltered B100 fuel-water mixtures compared to the filtered B100 fuel-water mixtures.

Similarly, the following tables depict the mass loss results for the 1 year exposure period.

Table 24. Mass loss results for 1018 steel coupons exposed for 1 year in unfiltered fuels in an aerobic, selective aerobic, and anaerobic environment.

Sample	Total Mass Loss Avg (g)	STDEV (+/-)	PR (mm/year)
B100 Anaerobic	0.0224	0.0110	0.0072
B100 Aerobic	0.2587	0.0065	0.0834
B100 Sel. Aerobic	0.3489	0.0108	0.1125
B20 Anaerobic	0.0107	0.0008	0.0034
B20 Aerobic	0.3543	0.0127	0.1142
B20 Sel. Aerobic	0.2323	0.0569	0.0749
ULSD Anaerobic	0.0285	0.0185	0.0092
ULSD Aerobic	0.4141	0.0279	0.1335
ULSD Sel. Aerobic	0.6083	0.0256	0.1961

Table 25. Mass loss results for 1018 steel coupons exposed for 1 year in filtered fuels in an aerobic, selective aerobic, and anaerobic environment.

Sample	Total Mass Loss Avg (g)	STDEV (+/-)	PR (mm/year)
B100F Anaerobic	0.2120	0.2993	0.0684
B100F Aerobic	0.2680	0.0215	0.0864
B100F Sel. Aerobic	0.2585	0.0383	0.0833
B20F Anaerobic	0.0090	0.0007	0.0029
B20F Aerobic	0.3200	0.0203	0.1032
B20F Sel. Aerobic	0.2129	0.0726	0.0687
ULSDF Anaerobic	0.4088	0.1847	0.1318
ULSDF Aerobic	0.3608	0.0260	0.1163
ULSDF Sel. Aerobic	0.5086	0.0132	0.1640

Again, similar trends can be seen with the 1 year exposure mass loss results of Tables 24 and 25. Most of the results reveal again that filtered fuel-water mixtures suffer less corrosion damage and less penetration rates in comparison to their unfiltered fuel-water mixture counterparts. In terms of specific environmental trends, the 1 year mass loss data almost matches trends seen in the 6 month mass loss data. For 1018 steel coupons exposed in filtered and unfiltered ULSD fuel-water mixtures, the selective aerobic environment showed the highest mass loss with the anaerobic environment the least for unfiltered ULSD fuel-water mixture and

aerobic least for filtered ULSD fuel-water mixture. Again, for 1018 steel coupons exposed in filtered and unfiltered B20 fuel-water mixtures, the aerobic environment showed the highest mass loss with the anaerobic environment the least. For the B100 fuel-water mixtures, no significant difference in trends was observed comparing the filtered and unfiltered fuel-water mixtures, however, the corrosion rate in both fuel-water mixtures were higher in the aerobic and selective aerobic conditions.

Chapter 7

Microbial Contamination

No microbial contamination was found solely in the fuel layer of the fuel-water mixtures of the experiment. Microbial contamination was only found to an extent within the water and interface regions of the fuel-water mixtures. For the case of the 6 month exposure part of the experiment, a fungi was successfully isolated and identified. This particular fungi was found only within the water/interface regions of the 1018 steel coupons exposed in unfiltered B20 fuel-water mixtures set in a anaerobic environment (2UC63) and selective aerobic environment (2UM62).

Figure 74. Fungi culture, 18S rRNA sequencing yields a 99% match to the fungi *Paecilomyces saturatus*.

Figure 74 depicts the isolated fungus cultured on specialized fungi media sab dex agar. With the help of Dr. Stuart Donachie's lab from the department of microbiology at University of Hawaii at Manoa, and his graduate student, Mark Chaplin, successful identification of this fungi was possible through 18S rRNA sequencing. The following depicts the sequences obtained for the forward primers (18sF) and reverse primers (18sR) of the fungi:

18sF:

TGCATGTCTAAGTATAAGCAATCTATACGGTGAAACTGCGAATGGCTCATTAAATCA
GTTATCGTTTATTTGATAGTACCTTGCTACATGGATACCTGTGGTAATTCTAGAGCTA
ATACATGCTGAAAACCTCGACTTCGGAAGGGGTGTATTTATTAGATAAAAAACCAAT
GCCCTTCGGGGCTCCTTGGTGATTCATAATAACTTAACGAATCGCATGGCCTTGCGC
CGGCGATGGTTCATTCAAATTTCTGCCCTATCAACTTTCGATGGTAGGATAGTGGCC
TACCATGGTGGCAACGGGTAACGGGGAATTAGGGTTCGATTCCGGAGAGGGAGCCT
GAGAAACGGCTACCACATCCAAGGAAGGCAGCAGGCGCGCAAATTACCCAATCCCG
ACACGGGGAGGTAGTGACAATAAATACTGATACAGGGCTCTTTTGGGTCTTGTAATC
GGAATGAGTACAATCTAAATCCCTTAACGAGGAACAATTGGAGGGCAAGTCTGGTG
CCAGCAGCCGCGGTAATTCCAGCTCCAATAGCGTATATTAAAGTTGTTGCAGTTAAA
AAGCTCGTAGTTGAACCTTGGGTCTGGCTGGCCGGTCCGCCTCACCGCGAGTACTGG
TCCGGCTGGACCTTTCCTTCTGGGGAACCCCATGGCCTTCACTGGCCGTGGCGGGGA
ACCAGGACTTTTACTGTGAAAAAATTAGAGTGTTCAAAGCAGGCCTTTGCTCGAATA
CATTAGCATGGAATAATAGAATAGG

18sR:

ACTTCCTCTAAATGACCAAGTTTGACCAACTTTCCGGCTCTGGGCGGTCGTTGCCAA
CCCCCCTGAGCCAGTCCGAAGGCCTCACTGAGCCATTCAATCGGTAGTAGCGACGG
GCGGTGTGTACAAAGGGCAGGGACGTAATCGGCACGAGCTGATGACTCGTGCCTAC
TAGGCATTCCTCGTTGAAGAGCAATAATTGCAATGCTCTATCCCCAGCACGACAGGG
TTTAACAAGATTACCCAGACCTCTCGGCCAAGGTGATGTACTCGCTGGCCCTGTCAG
TGTAGCGCGCGTGCGGCCCAGAACATCTAAGGGCATCACAGACCTGTTATTGCCGC
GCACTTCCATCGGCTTGAGCCGATAGTCCCCCTAAGAAGCCAGCGGCCCGCAAACG
CGGACCGGGCTATTTAAGGGCCGAGGTCTCGTTCGTTATCGCAATTAAGCAGACAAA
TCACTCCACCAACTAAGAACGGCCATGCACCACCATCCAAAAGATCAAGAAAGAGC
TCTCAATCTGTCAATCCTTATTTTGTCTGGACCTGGTGAGTTTCCCCGTGTTGAGTCA
AATTAAGCCGCAGGCTCCACGCCTTGTGGTGCCCTTCCGTCAATTTCTTTAAGTTTCA
GCCTTGCGACCATACTCCCCCCAGAACCCAAAAACTTTGATTTCTCGTAAGGTGCCG
AACGGGTCATCATAGAACACCGTCCGATCCCTAGTCGGCATAGTTTATGGTTAAGAC
TACGACGGTATCTGATCGTCTTCGATCCCCTAACTTTCGTTCCCTGATTAATGAAAAC
ATCCTTGGCGAATGCTTTCGCAGTAGTTAGTCNTCAGCAAATCCAAGAATTTCACCT
CTGACAGCTGAATACTGACGCCCCCGACTATCCCTA

Thus, with these sequences, a BLAST database search was performed to identify the specific species of fungi cultured. The BLAST results obtained revealed a 99% match identity to the fungi *Paecilomyces saturatus*.

According to literature, *Paecilomyces variotti*, which closely resembles *Paecilomyces saturatus*, is the most commonly occuring species within this genus and is often found in foods, soil, indoor air, and wood [24]. *Paecilomyces* strains are also often heat resistant and may produce mycotoxins in contaminated pasteurised foods [25].

For the case of the 1 year exposure experiment, the same fungi was isolated and cultured from the water/interface regions of the 1018 steel coupons exposed in unfiltered B20 fuel-water mixtures set in an anaerobic environment (2UC13). However this time, no fungi was found in the B20 fuel-water mixtures set in a selective aerobic environment as was the case in the 6 month exposure. There was an additional bacteria isolate from the 1 year exposure. This bacteria was successfully isolated and identified from the water/interface regions of the 1018 steel coupons exposed in unfiltered ULSD fuel-water mixtures set in an anaerobic environment.

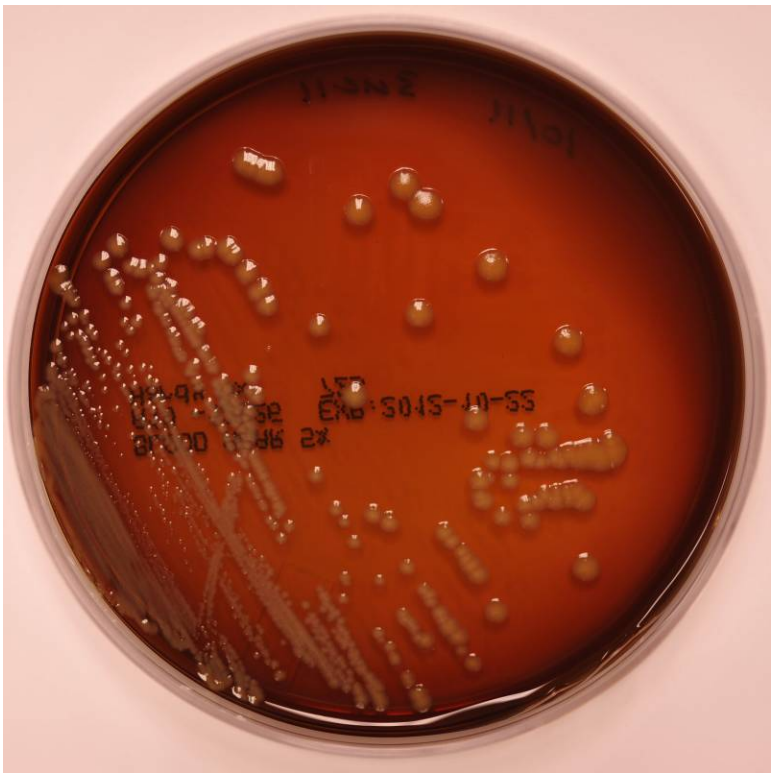

Figure 75. Bacteria isolate, 16S rRNA sequencing yields a 97% match to the bacteria *Ralstonia solanacearum*.

Figure 75 depicts the isolated bacteria cultured on blood agar media. Following the colony PCR procedure [21], successful identification of the bacteria was possible through the use of 16S rRNA sequencing. To verify the size of the PCR products being amplified, a gel electrophoresis was performed.

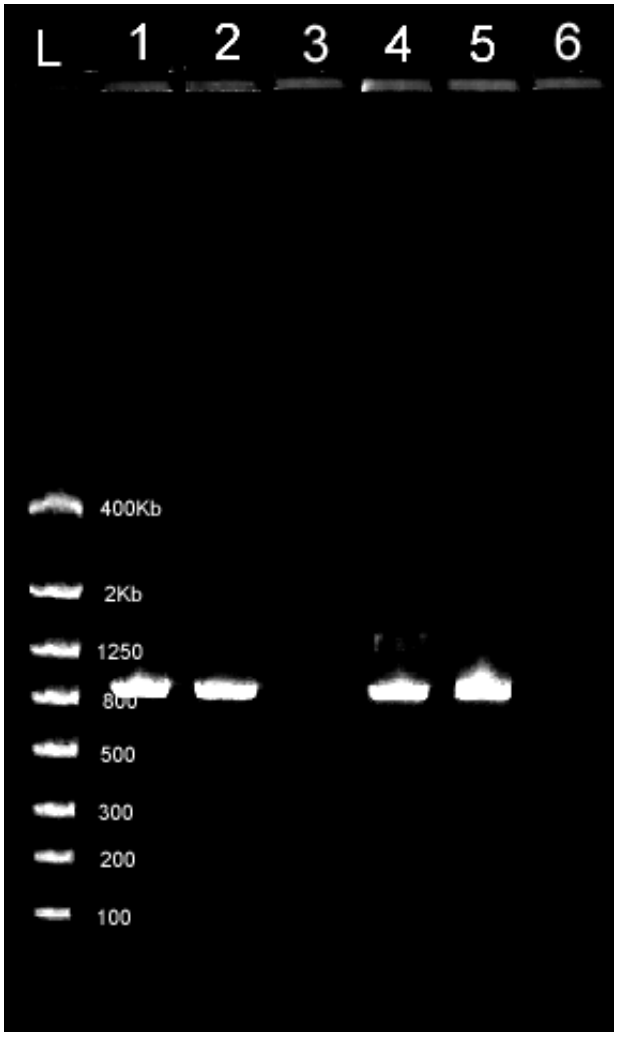

Figure 76. Gel electrophoresis of colony PCR products from bacteria isolate.

The gel electrophoresis depicted by Figure 76 clearly shows that the PCR products amplified fall within the range of approximately 800 base pairs. This is determined by the first column marked L which designates the DNA ladder in units of base pair. Columns 1 through 6 are the individual bacterial samples with column 3 and 6 as negative controls, hence no product was seen in those columns. Columns 1 and 2 utilized forward and reverse primers of concentration 0.5 μM whereas column 4 and 5 utilized forward and reverse primer concentrations of 1 μM. Thus, primer concentration did not make any difference in the success of the colony PCR performed.

The following depicts the sequences obtained for the forward primers (519F) and reverse primers (1406R) of the bacteria:

519F:

TTACTTACAGACGCTGGGCGTAAGCGTGCGCAGGCGGTTGTGCAAGACCGATGTGA
AATCCCCGGGCTTAACCTGGGAATTGCATTGGTGACTGCACGGCTAGAGTGTGTCAG
AGGGGGGTAGAATTCCACGTGTAGCATTGAAATGCGTACAGATGTGGAGGTCCCCC
ATGTTCCCTTCAT

1406R:

GCCAATCAACGAGCATGCGTGATCCGCGATTACTAGCGATTCCAGCTTCACGTAGTC
GAGTTGCAGACTACGATCCGGACTACGATGCATTTTCTGGGATTAGCTCCACCTCGC
GGCTTGGCAACCCTCTGTATGCACCATTGTATGACGTGTGAAGCCCTACCCATAAGG
GCCATGAGGACTTGACGTCATCCCCACCTTCCTCCGGTTTGTCACCGGCAGTCTCTCT
AGAGTGCCCTTTCGTAGCAACTAGAGACAAGGGTTGCGCTCGTTGCGGGACTTAACC
CAACATCTCACGACACGAGCTGACGACAGCCATGCAGCACCTGTGTCCACTTTCTCT
TTCGAGCACCTAATGCATCTCTGCTTCGTTAGTGGCATGTCAAGGGTAGGTAAGGTT
TT

Thus, with these sequences, a BLAST database search was performed again to identify the specific species of bacteria isolated. The BLAST results obtained revealed a 97% match identity to the bacteria *Ralstonia solanacearum*.

According to literature, *Ralstonia solanacearum* is a soilborne gram-negative bacterium that causes bacterial wilt in many crops [26]. This particular strain of bacteria has also been found to be well adjusted to hydrocarbons, as a study performed in 2010 reveals that this bacteria among others dominate the microorganism popluation within hydrocarbon contaminated soils with respect to soils with no hydrocarbon contamination [27]. Hence it's presence within the 1018 steel coupons exposed in unfiltered ULSD fuel-water mixtures set in an anaerobic environment is no surprise.

The fungi and bacteria were the only two types of microorganisms that were isolated from both 6 year exposures and 1 year exposures. Little is known whether or not they play a role in corrosion.

Chapter 8

Summary

No microorganisms were detected in any part of the fuel layer of the fuel-water mixtures used in these experiments. This agrees well with literature as microorganisms are only capable of growth when fuels have been contaminated with water [5]. Microbial contamination was only observed in a few fuel samples such as the ULSD fuel-water mixtures and B20 fuel-water mixtures. As mentioned earlier, all microbial contamination was found within the fuel-water layer interface or within the water layer itself. Although no direct evidence of bacteria was found in the B100 fuels, the formation of sediments in the fuel within approximately 1 week of dispensing fuel from the pump indicated microbial activity. In addition, filtered B100 fuel did not form sediments and remained lucid for over one year.

Contrary to the preliminary 1 month exposure experiment which revealed many different types of microbial contamination, the 6 month and 1 year exposure experiments were only able to identify a single fungi and bacteria species. The length of duration for the time the samples were exposed most likely decreased the amount of "culturable" microorganisms [28]. The preliminary 1 month experiment exposed a B100 fuel-water mixture for 1 month; whereas, the main experiment exposed fuel-water mixtures for 6 months and 1 year. According to literature, bacteria seldom experience environmental conditions that allow prolonged continuous growth [29]. On contrary, due to their fast exponential growth cycles, bacteria often consume required nutrients efficiently and because of this, are nutritionally starved most of the time [29]. Bacteria that are nutritionally starved then enter a stationary phase in which metabolic activities begin to slow down until nutrients are again available [29]. Some bacteria however are unable to survive

such extended periods of starvation and die off [29]. In most cases, bacteria are known to enter a viable but nonculturable (VBNC) state [28]. Bacteria in this state fail to grow on routine bacteriological media on which they would normally grow and develop into colonies, but are alive and capable of renewed metabolic activity [28]. Thus, in the case of the 6 month and 1 year experiments, a hypothesis can be made that the majority of microorganisms died off and/or entered into the VBNC state; whereas, the preliminary 1 month exposure experiment had adequate nutritional levels enough to sustain bacterial growth.

Microorganisms isolated from the 1 month exposure experiment revealed 4 different types of bacterial species isolated from the B100 fuel-water mixture. The specific bacterial species (Figures 7 through 10) are typical of the types of microorganisms found within fuels [30]. The two microorganisms isolated from the 6 month and 1 year exposures (depicted by Figures 74 and 75) are also typical of common microorganisms found within fuels [30, 31].

Although few microorganisms were successfully cultured in the lab, their effects on corrosion of 1018 steel can still be noted. Strong evidence for this can be found on the 1018 steel coupons exposed to the B100-water mixture for the 6 month period. The corrosion rate in unfiltered B100-water mixture in the anaerobic environment was more than 5 times higher than in the anaerobic filtered B100-water mixture. The corrosion rate in the anaerobic unfiltered B100-water mixture was also almost 2 times higher than the aerobic unfiltered B100-water mixture. In the case of the filtered B100-water mixtures, corrosion rates were higher in the aerated environments. Interestingly, for the 1 year exposure period, the unfiltered and filtered B100-water mixtures shared similar trends in the corrosion behavior, where the corrosion rates in the anaerobic environment was significantly lower than the aerated environments. This was likely caused by dead or dormant bacteria in the unfiltered B100 fuel. The 1 year exposure

experiments were started approximately 1 month after the 6 month exposure experiments using the same B100 fuel from the same lot. It is plausible that the population of active bacteria dwindled during this 1 month period. Other evidence of microbial activity was observed in both filtered and unfiltered B20 fuel-water mixtures exposed in aerobic conditions. As shown previously in Figure 21, these steel coupons taken from the 6 month and 1 year exposure times all revealed a thick sludge layer characteristic of microbial contamination in the form of biofouling [5, 14, 18]. Figure 77 below depicts a before and after image of the steel coupon upon acetone washing. Clearly, little to very little corrosion products remain upon acetone washing which indicates that the corrosion products was embedded within the sludge layer.

Figure 77. Before and after acetone wash image of 1018 steel coupon exposed in B20 fuel-water mixture exposed in an aerobic environment.

Although numerous attempts of culturing microorganisms from the sludge failed, the sludge formation is indicative of microbiological activity. Mass loss data also supports this hypothesis as steel coupons exposed in the aerobic environment observed mass loss greater than 7 times that of the respective selective aerobic environments as depicted in Tables 22 to 25.

Corrosion product analysis via Raman, XRD, and SEM/EDXA were successful in characterizing the different forms of rust observed on 1018 steel coupons. Although the severity of corrosion damage to coupons cannot be directly correlated to the presence of microorganisms, the majority of the coupons experienced corrosion that occurred within the fuel-water interface and water layers where microorganisms if any are able to survive. It was observed that for most steel coupons, the fuel layer of the fuel-water mixtures served as a protective layer from corrosion and MIC. Trends on the type of dominant corrosion product found on 1018 steel coupons exposed to different fuel-water mixtures and environments were also revealed from these experiments. The corrosion products lepidocrocite and iron formate hydrate are the dominant corrosion products observed on 1018 steel coupons exposed in filtered/unfiltered B100 fuel-water mixtures exposed in all environmental conditions (Table 26). Table 26 also reveals corrosion products lepidocrocite and magnetite as the dominant corrosion products observed on 1018 steel coupons exposed in filtered/unfiltered B20 fuel-water mixtures in all environmental conditions; whereas, 1018 steel coupons exposed in ULSD fuel-water mixtures exposed in all environmental conditions revealed dominant corrosion products lepidocrocite, magnetite, and goethite.

Table 26. Summary of corrosion product found on 1018 steel coupons via Raman and XRD exposed in all environmental conditions for 6 months and 1 year.

Anaerobic		
Fuel	**Raman**	**XRD**
B100	Lepidocrocite	Iron Formate Hydrate
B100 Filtered	Lepidocrocite	Lepidocrocite, Iron Formate Hydrate
B20	Lepidocrocite, Magnetite	Lepidocrocite, Magnetite, Iron Formate Hydrate
B20 Filtered	Lepidocrocite, Magnetite	Lepidocrocite, Magnetite
ULSD	Lepidocrocite, Magnetite	Lepidocrocite, Magnetite
ULSD Filtered	Lepidocrocite, Magnetite	Lepidocrocite, Magnetite
Aerobic		
Fuel	**Raman**	**XRD**
B100	Lepidocrocite	Iron Formate Hydrate
B100 Filtered	Lepidocrocite	Iron Formate Hydrate
B20	N/A	N/A
B20 Filtered	N/A	N/A
ULSD	Lepidocrocite, Goethite, Maghemite	Lepidocrocite, Goethite
ULSD Filtered	Lepidocrocite, Goethite	Hematite, Goethite, Magnetite
Selective Aerobic		
Fuel	**Raman**	**XRD**
B100	Lepidocrocite	Iron Formate Hydrate
B100 Filtered	Lepidocrocite	Lepidocrocite, Hematite
B20	Lepidocrocite	Iron Formate Hydrate
B20 Filtered	Lepidocrocite, Magnetite	Lepidocrocite, Magnetite, Iron Formate Hydrate
ULSD	Lepidocrocite, Goethite	Lepidocrocite, Goethite, Iron Oxide Hydroxide
ULSD Filtered	Lepidocrocite, Goethite	Lepidocrocite, Goethite, Iron Oxide Hydroxide

The results obtained from the pH and TAN experiments revealed that pH values of the fuel and water layers are more indicative of the severity of corrosion for the 1018 steel coupons exposed in the ULSD fuel-water mixtures as depicted below by Figures 84 and 85; whereas, TAN values are more indicative of the severity of corrosion for the 1018 steel coupons exposed in B100 fuel-water mixtures (Figure 80). This disparity is clearly shown by pH value results of Tables 9, 10, 11, 13, 14, and 15, and TAN value results of Tables 17 and 18, where the pH of ULSD fuels are very acidic, with values < 4 in contrast to respectively very low TAN values

ranging from 0 to < 1. This indicates the fuels are not acidic. Hence, the pH and TAN values are inconsistent. When compared to the mass loss data tabulated in Tables 22 through 25, 1018 steel coupons exposed in the ULSD fuel-water mixtures are reported to have high mass loss values and high penetration rates that directly correspond with low pH values. Hence, TAN values do not correlate as well as pH values with respect to 1018 steel coupons exposed in ULSD fuel-water mixtures as depicted below by Figure 86. The exact opposite trend is seen in the case of 1018 steel coupons exposed in B100 fuel-water mixtures. For the case of 1018 steel coupons exposed in the B100 fuel-water mixtures, pH values from Tables 9, 10, 11, 13, 14, and 15 reveal less acidic values, often > 4, but TAN values from Tables 17 and 18 reveal high values often reaching the maximum value of 2. This indicates the fuels are very acidic. Hence, the pH and TAN values are inconsistent. Again, when compared to the mass loss data tabulated in Tables 22 through 25, 1018 steel coupons exposed in the B100 fuel-water mixtures are reported to have high mass loss values and high penetration rates that directly correspond with high TAN values. Therefore, in this case, pH values do not correlate as well as TAN values with respect to 1018 steel coupons exposed in B100 fuel-water mixtures as depicted below by Figures 78 and 79. Due to the fact that B20 fuel contains 80% ULSD fuel, corrosion of 1018 steel coupons exposed in B20 fuel-water mixtures appear to correlate with both pH and TAN values as depicted below by Figures 81 through 83. Again, as explained earlier, it is important to note that the disparity between pH and TAN values seen in the data is not atypical. pH is known to be an apparent representation on how corrosive the fuel may be, but does not indicate the acidic or alkaline constituents [23]. TAN measures the acidic or alkaline constituents but gives less of a representation on how corrosive the fuel may be [23]. In comparison to pH, TAN has a better

ability to detect weak acids, which do not readily dissociate in water [23]. Thus, pH and TAN measure different aspects of the fuel's acidic or alkaline character.

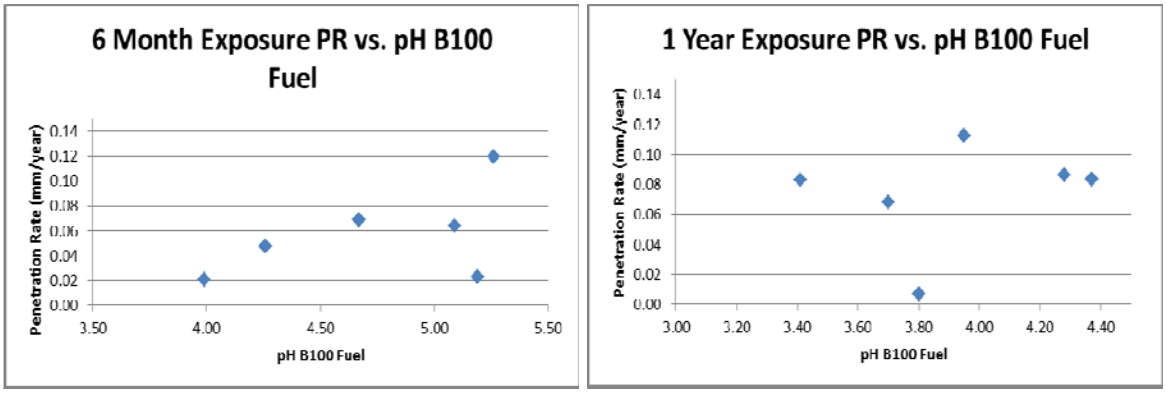

Figure 78. Penetration rate vs. pH (fuel layer) of 1018 steel exposed in all environmental conditions for 6 months/1 year in filtered/unfiltered B100 fuel-water mixtures.

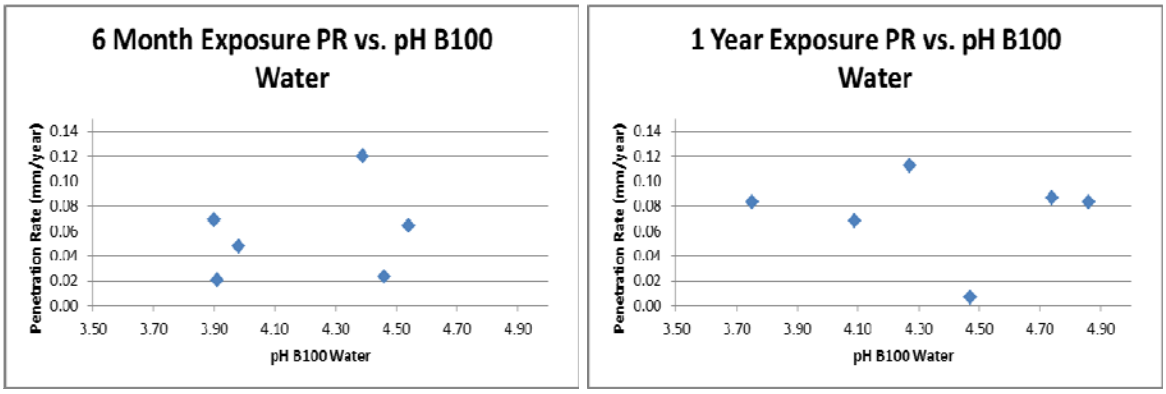

Figure 79. Penetration rate vs. pH (water layer) of 1018 steel exposed in all environmental conditions for 6 months/1 year in filtered/unfiltered B100 fuel-water mixtures.

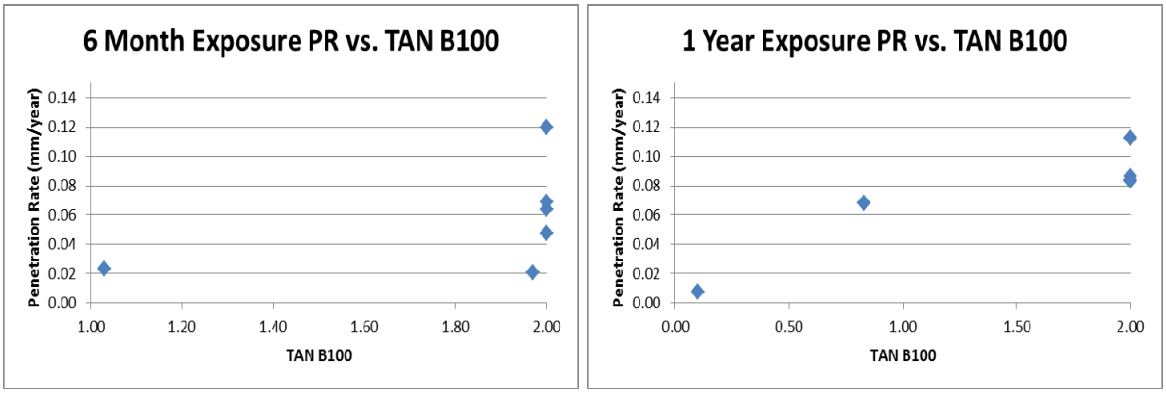

Figure 80. Penetration rate vs. TAN of 1018 steel exposed in all environmental conditions for 6 months/1 year in filtered/unfiltered B100 fuel-water mixtures.

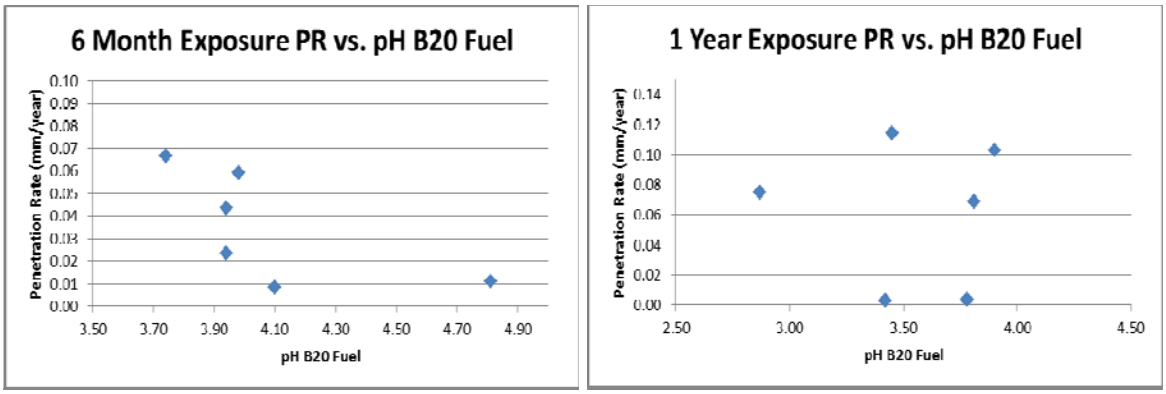

Figure 81. Penetration rate vs. pH (fuel layer) of 1018 steel exposed in all environmental conditions for 6 months/1 year in filtered/unfiltered B20 fuel-water mixtures.

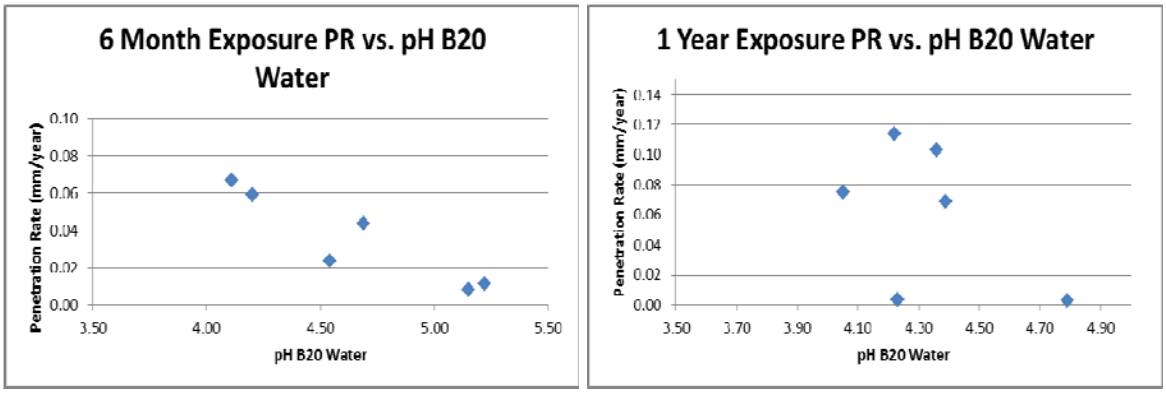

Figure 82. Penetration rate vs. pH (water layer) of 1018 steel exposed in all environmental conditions for 6 months/1 year in filtered/unfiltered B20 fuel-water mixtures.

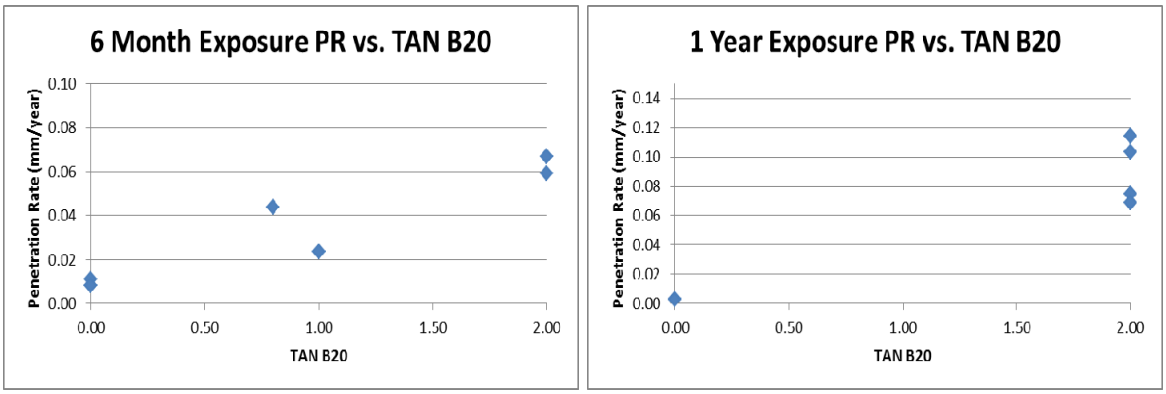

Figure 83. Penetration rate vs. TAN of 1018 steel exposed in all environmental conditions for 6 months/1 year in filtered/unfiltered B20 fuel-water mixtures.

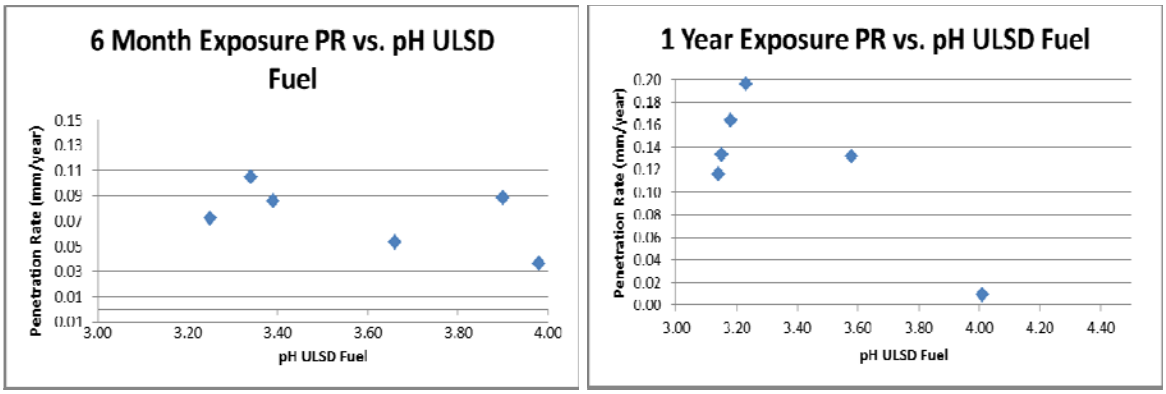

Figure 84. Penetration rate vs. pH (fuel layer) of 1018 steel exposed in all environmental conditions for 6 months/1 year in filtered/unfiltered ULSD fuel-water mixtures.

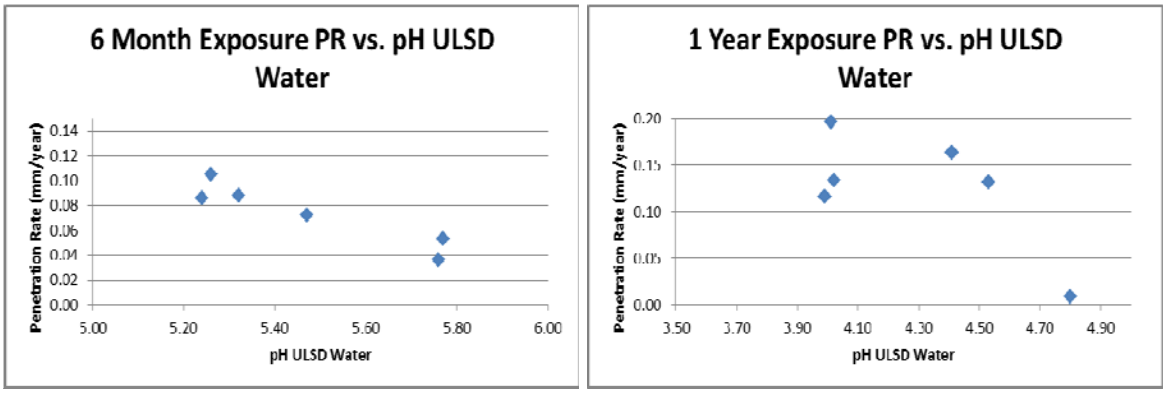

Figure 85. Penetration rate vs. pH (water layer) of 1018 steel exposed in all environmental conditions for 6 months/1 year in filtered/unfiltered ULSD fuel-water mixtures.

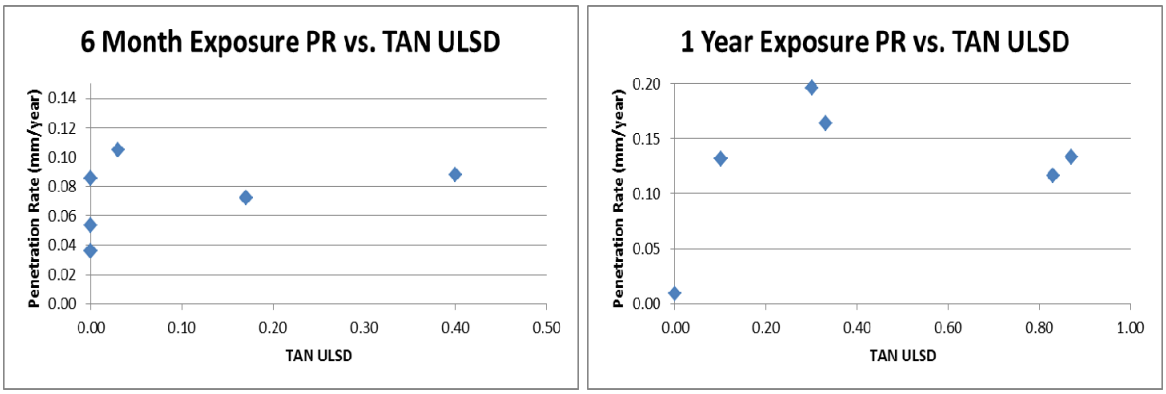

Figure 86. Penetration rate vs. TAN of 1018 steel exposed in all environmental conditions for 6 months/1 year in filtered/unfiltered ULSD fuel-water mixtures.

Due to the fact that only two microorganism were isolated from the 6 month and 1 year exposures, correlations between MIC within biodiesels and ULSD are difficult to make. Hence, future work involves incubating sterile fuel-water mixtures with the two microorganisms isolated

to determine their MIC on 1018 plain carbon steel. An additional, short-term corrosion test (e.g., one month exposure) should be performed on fresh diesel, and progressively older stored diesel to study the possibility of microbial die-off on corrosion rates.

References

1. McCarthy, P., M.G. Rasul, and S. Moazzem, *Analysis and Comparison of Performance and Emissions of an Internal Combustion Engine Fuelled with Petroleum Diesel and Different Bio-Diesels.* Fuel, 2011. **90**: p. 2147-2157.

2. Beech, I.B. and J. Sunner, *Biocorrosion: Towards Understanding Interactions between Biofilms and Metals.* Current Opinion in Biotechnology, 2004. **15**: p. 181-186.

3. Rajasekar, A., et al., *Characterization of Corrosive Bacterial Consortia Isolated from Petroleum-Product-Transporting Pipelines.* Applied Microbiology and Biotechnology, 2010. **85**: p. 1175-1188.

4. Hamilton, W.A., *Microbially Influenced Corrosion as a Model System for the Study of Metal Microbe Interactions: A Unifying Electron Transfer Hypothesis.* Biofouling: The Journal of Bioadhesion and Biofilm Research, 2003. **19**(1): p. 65-76.

5. Klofutar, B. and J. Golob, *Microorganisms in Diesel and in Biodiesel Fuels.* Acta Chimica Slovenica, 2007. **54**: p. 744-748.

6. Characklis, W.G. and K.C. Marshall, *Biofilms*. 1990, Wiley. p. 796.

7. Haseeb, A.S.M.A., et al., *Compatibility of Automotive Materials in Biodiesel: A Review.* Fuel, 2011. **90**: p. 922-931.

8. Maru, M.M., et al., *Biodiesel Compatibility with Carbon Steel and Hdpe Parts.* Fuel Processing Technology, 2009. **90**: p. 1175-1182.

9. Kaul, S., et al., *Corrosion Behavior of Biodiesel from Seed Oils of Indian Origin on Diesel Engine Parts.* Fuel Processing Technology, 2007. **88**: p. 303-307.

10. Qiang, L., Z. Jian, and Z. Xifeng, *Corrosion Properties of Bio-Oil and Its Emulsions with Diesel.* Chinese Science Bulletin, 2008. **53**(23): p. 3726-3734.

11. Haseeb, A.S.M.A., et al., *Corrosion Characteristics of Copper and Leaded Bronze in Palm Biodiesel.* Fuel Processing Technology, 2010. **91**: p. 329-334.

12. Fazal, M.A., A.S.M.A. Haseeb, and H.H. Masjuki, *Comparative Corrosive Characteristics of Petroleum Diesel and Palm Biodiesel for Automotive Materials.* Fuel Processing Technology, 2010. **91**: p. 1308-1315.

13. Fazal, M.A., A.S.M.A. Haseeb, and H.H. Masjuki, *Degradation of Automotive Materials in Palm Biodiesel.* Energy, 2012. **40**: p. 76-83.

14. Fregolente, P.B.L., L.V. Fregolente, and M.R.W. Maciel, *Water Content in Biodiesel, Diesel, and Biodiesel–Diesel Blends.* Journal of Chemical and Engineering Data, 2012.

15. Costerton, J.W., G.G. Geesey, and K.-J. Cheng, *How Bacteria Stick.* Scientific American, 1978. **238**: p. 86-95.

16. Beech, I.B., *Corrosion of Technical Materials in the Presence of Biofilms-Current Understanding and State-of-the Art Methods of Study.* International Biodeterioration & Biodegradation, 2004. **53**: p. 177-183.

17. Aktas, D.F., et al., *Anaerobic Metabolism of Biodiesel and Its Impact on Metal Corrosion.* Energy Fuels, 2010. **24**: p. 2924-2928.

18. Lee, J.S., R.I. Ray, and B.J. Little, *An Assessment of Alternative Diesel Fuels: Microbiological Contamination and Corrosion under Storage Conditions.* Biofouling: The Journal of Bioadhesion and Biofilm Research, 2010. **26**(4): p. 623-635.

19. Meredith, W., S.-J. Kelland, and D.M. Jones, *Influence of Biodegradation on Crude Oil Acidity and Carboxylic Acid Composition.* Organic Geochemistry, 2000. **31**: p. 1059-1073.

20. Garcia, L.S., *Clinical Microbiology Procedures Handbook*. 2010: ASM Press. 2540.

21. Suzuki, M.T. and S.J. Giovannoni, *Bias Caused by Template Annealing in the Amplification of Mixtures of 16s Rrna Genes by Pcr.* Applied and Environmental Microbiology, 1996. **62**(2): p. 625-630.

22. Li, S. and L.H. Hihara, *In Situ Raman Spectroscopic Study of Nacl Particle-Induced Marine Atmospheric Corrosion of Carbon Steel.* Journal of The Electrochemical Society, 2012. **159**(4): p. C1-C8.

23. Noria Corporation, *A Comprehensive Look at the Acid Number Test.* Machinery Lubrication, 2007: p. 1-8.

24. Houbraken, J., et al., *Identification of Paecilomyces Variotii in Clinical Samples and Settings.* Journal of Clinical Microbiology, 2010. **48**(8): p. 2754-2761.

25. Samson, R.A., et al., *Polyphasic Taxonomy of the Heat Resistant Ascomycete Genus Byssochlamys and Its Paecilomyces Anamorphs.* Persoonia, 2009. **22**: p. 14-27.

26. Fujie, M., et al., *Monitoring Growth and Movement of Ralstonia Solanacearum Cells Harboring Plasmid Prss12 Derived from Bacteriophage Rss1.* Journal of Bioscience and Bioengineering, 2010. **109**(2): p. 153-158.

27. Bastida, F., et al., *Tracing Changes in the Microbial Community of a Hydrocarbon-Polluted Soil by Culture-Dependent Proteomics.* Pedosphere, 2010. **20**(4): p. 479-485.

28. Oliver, J.D., *The Viable but Nonculturable State in Bacteria.* The Journal of Microbiology, 2005. **43**(S): p. 93-100.

29. Kolter, R., D.A. Siegele, and A. Tormo, *The Stationary Phase of the Bacterial Life Cycle.* Annual Reviews: Annual Review of Microbiology, 1993. **47**: p. 855-874.

30. Gaylarde, C.C., F.M. Bento, and J. Kelley, *Microbial Contamination of Stored Hydrocarbon Fuels and Its Control.* Revista de Microbiologia, 1999. **30**: p. 1-10.

31. Rauch, M.E., et al., *Characterization of Microbial Contamination in United States Air Force Aviation Fuel Tanks.* Journal of Industrial Microbiology & Biotechnology, 2006. **33**: p. 29-36.

Appendix

The following figures depict the complete SEM/EDXA analysis of the 1018 steel coupons for both 6 month and 1 year exposures.

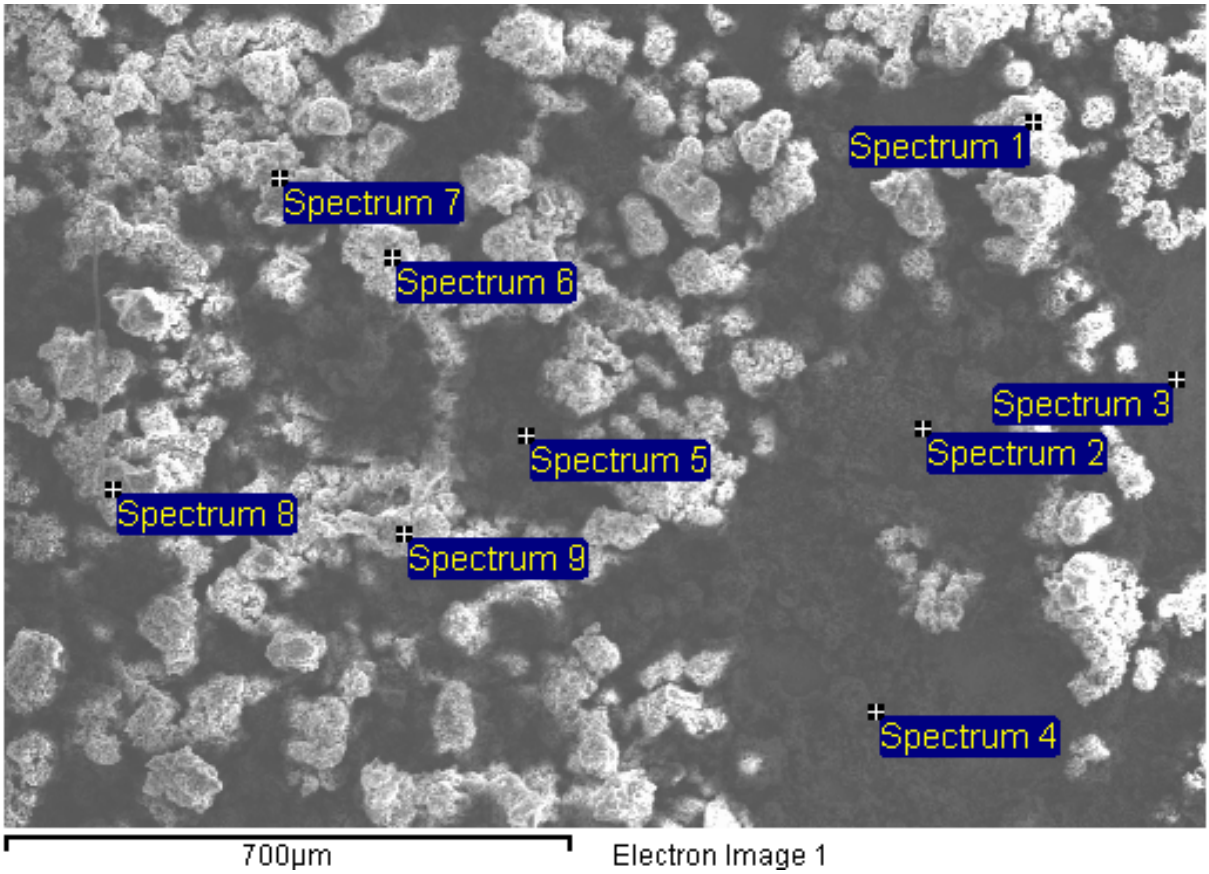

Processing option : All elements analysed

Spectrum	In stats.	C	O	Mn	Fe
Spectrum 1	Yes	38.69	33.78		27.53
Spectrum 2	Yes	31.00	52.92	0.15	15.93
Spectrum 3	Yes	41.58			58.42
Spectrum 4	Yes	27.81	41.68		30.52
Spectrum 5	Yes	34.09	50.69		15.22
Spectrum 6	Yes	28.01	64.98		7.01
Spectrum 7	Yes	37.30	53.24		9.46
Spectrum 8	Yes	34.61	57.32		8.07
Spectrum 9	Yes	27.63	66.01		6.36
Max.		41.58	66.01	0.15	58.42
Min.		27.63	33.78	0.15	6.36

All results in atomic%

Figure A1. SEM analysis of 1018 steel coupon (1UC61) exposed in unfiltered B100 fuel-water mixture exposed in an anaerobic environment.

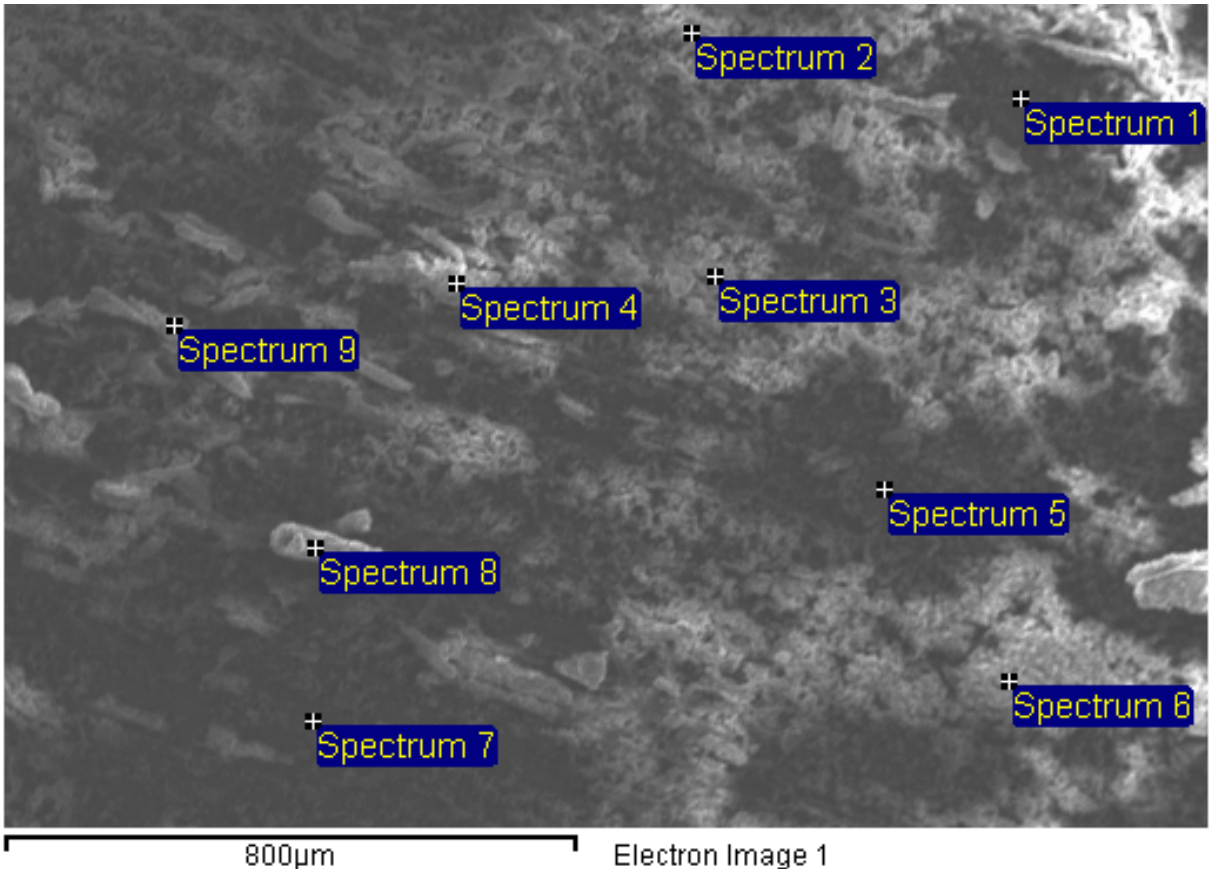

Processing option : All elements analysed

Spectrum	In stats.	C	O	Fe
Spectrum 1	Yes	40.08	51.88	8.04
Spectrum 2	Yes	59.87	27.98	12.15
Spectrum 3	Yes	43.74	35.30	20.97
Spectrum 4	Yes	35.18	33.60	31.22
Spectrum 5	Yes	46.32	45.32	8.36
Spectrum 6	Yes	46.59	47.33	6.08
Spectrum 7	Yes	50.66	41.11	8.23
Spectrum 8	Yes			100.00
Spectrum 9	Yes	43.72	50.81	5.47
Max.		59.87	51.88	100.00
Min.		35.18	27.98	5.47

All results in atomic%

Figure A2. SEM analysis of 1018 steel coupon (1UO61) exposed in unfiltered B100 fuel-water mixture exposed in an aerobic environment.

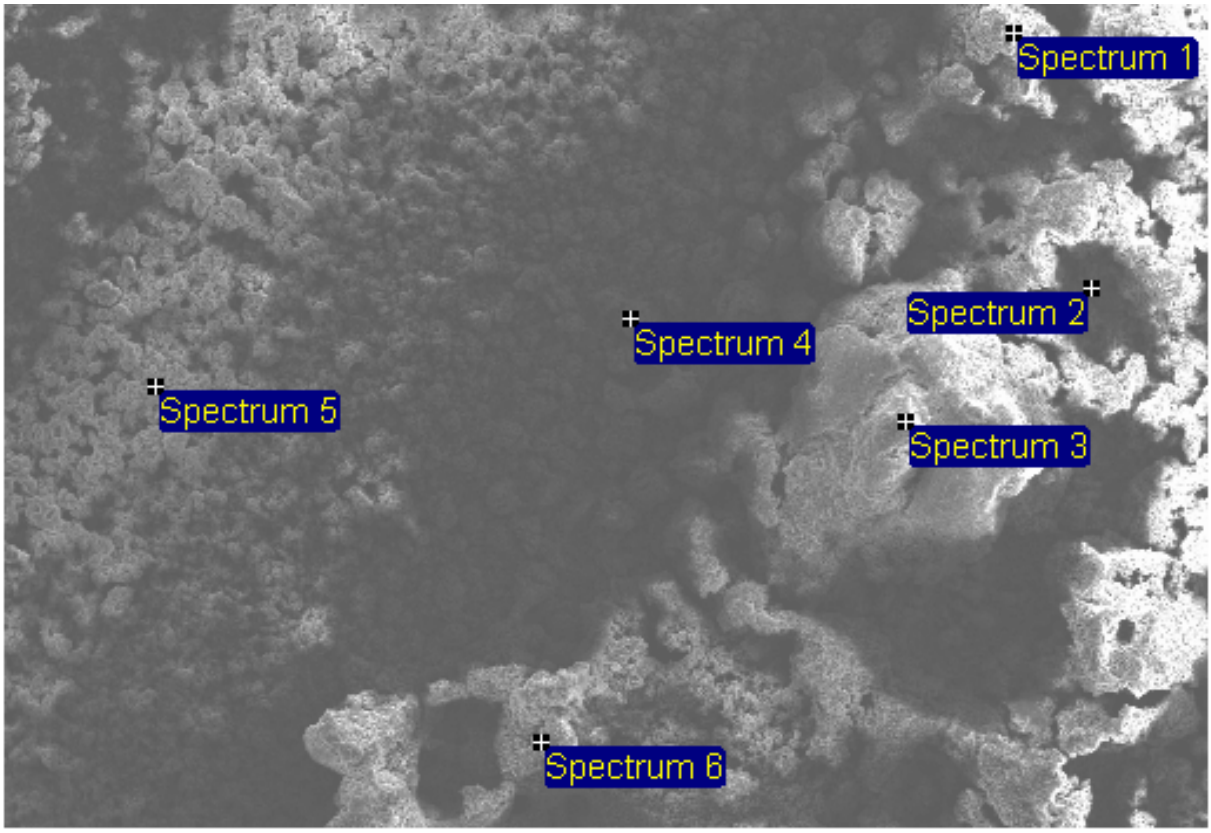

Processing option : All elements analysed

Spectrum	In stats.	C	O	Mn	Fe
Spectrum 1	Yes	30.52	59.77		9.71
Spectrum 2	Yes	24.00	16.60		59.40
Spectrum 3	Yes	42.40	54.35	0.09	3.16
Spectrum 4	Yes	39.47	54.58	0.13	5.82
Spectrum 5	Yes	39.51	23.92		36.57
Spectrum 6	Yes	30.28	56.00		13.73
Max.		42.40	59.77	0.13	59.40
Min.		24.00	16.60	0.09	3.16

All results in atomic%

Figure A3. SEM analysis of 1018 steel coupon (1UM63) exposed in unfiltered B100 fuel-water mixture exposed in a selective aerobic environment.

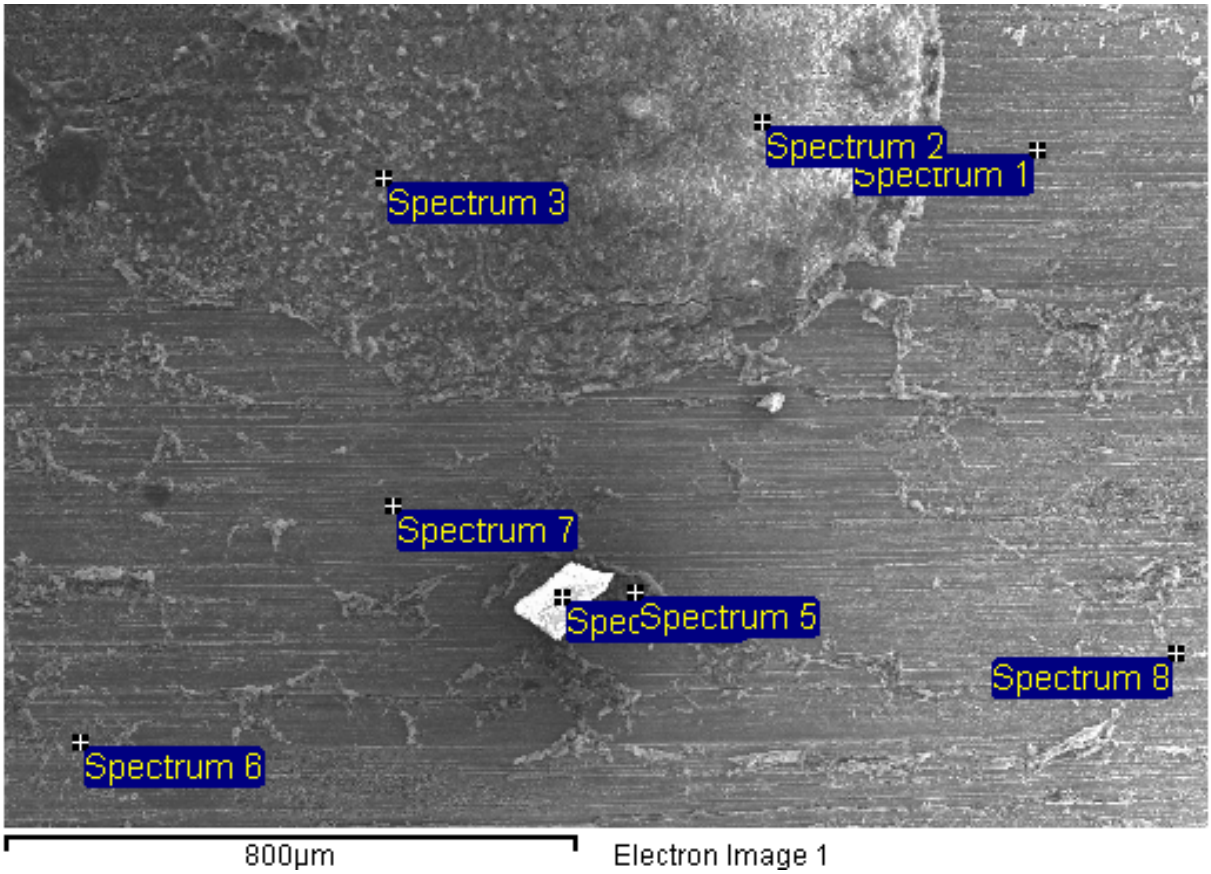

Processing option : All elements analysed

Spectrum	In stats.	C	O	Al	Mn	Fe
Spectrum 1	Yes	28.43			0.68	70.88
Spectrum 2	Yes	21.47	60.43			18.10
Spectrum 3	Yes	23.48				76.52
Spectrum 4	Yes	16.75	51.09			32.16
Spectrum 5	Yes	34.16	42.29			23.55
Spectrum 6	Yes	17.60	19.49	1.58		61.33
Spectrum 7	Yes					100.00
Spectrum 8	Yes	34.66				65.34
Max.		34.66	60.43	1.58	0.68	100.00
Min.		16.75	19.49	1.58	0.68	18.10

All results in atomic%

Figure A4. SEM analysis of 1018 steel coupon (1FC63) exposed in filtered B100 fuel-water mixture exposed in an anaerobic environment.

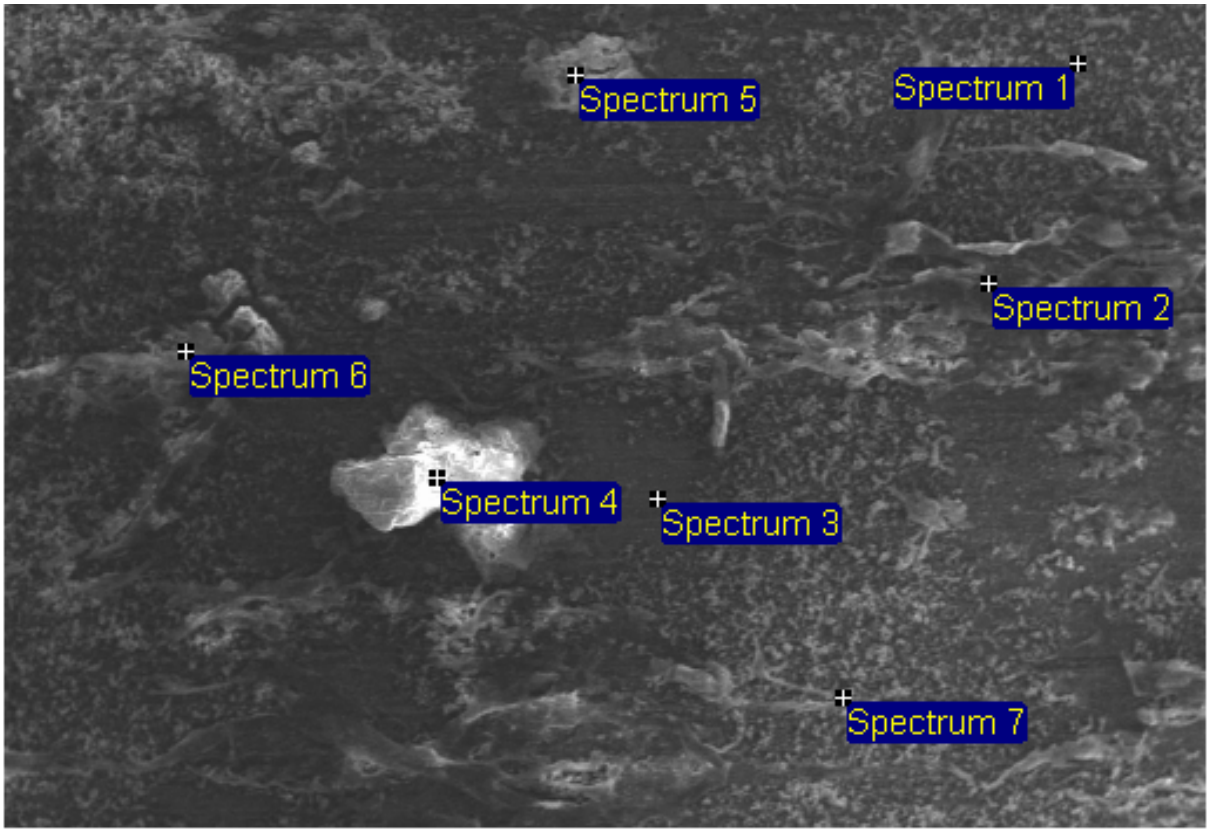

Processing option : All elements analysed

Spectrum	In stats.	C	O	Fe
Spectrum 1	Yes	54.11	28.46	17.44
Spectrum 2	Yes	70.56	21.64	7.80
Spectrum 3	Yes	42.92	32.37	24.71
Spectrum 4	Yes	46.62	41.77	11.61
Spectrum 5	Yes	47.21	45.08	7.71
Spectrum 6	Yes	64.52	29.21	6.28
Spectrum 7	Yes	62.11	21.65	16.24
Mean		55.43	31.45	13.11
Std. deviation		10.49	9.12	6.70
Max.		70.56	45.08	24.71
Min.		42.92	21.64	6.28

All results in atomic%

Figure A5. SEM analysis of 1018 steel coupon (1FO62) exposed in filtered B100 fuel-water mixture exposed in an aerobic environment.

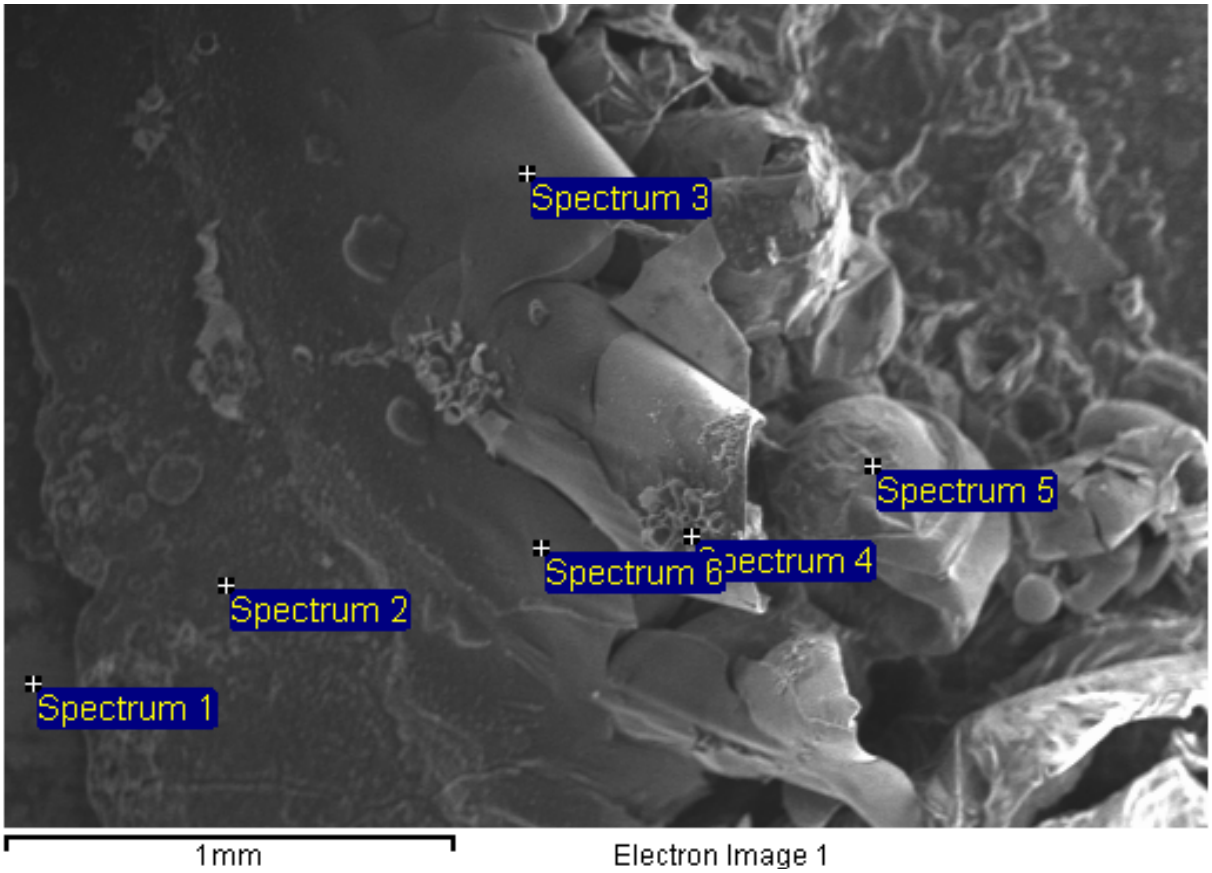

Processing option : All elements analysed

Spectrum	In stats.	C	O	Na	Fe
Spectrum 1	Yes	72.04	12.02		15.94
Spectrum 2	Yes	73.69	21.90		4.41
Spectrum 3	Yes	66.69	25.42		7.88
Spectrum 4	Yes	68.02	28.86		3.12
Spectrum 5	Yes	66.96	31.18	0.16	1.70
Spectrum 6	Yes	71.23	20.20		8.57
Max.		73.69	31.18	0.16	15.94
Min.		66.69	12.02	0.16	1.70

All results in atomic%

Figure A6. SEM analysis of 1018 steel coupon (1FM63) exposed in filtered B100 fuel-water mixture exposed in a selective aerobic environment.

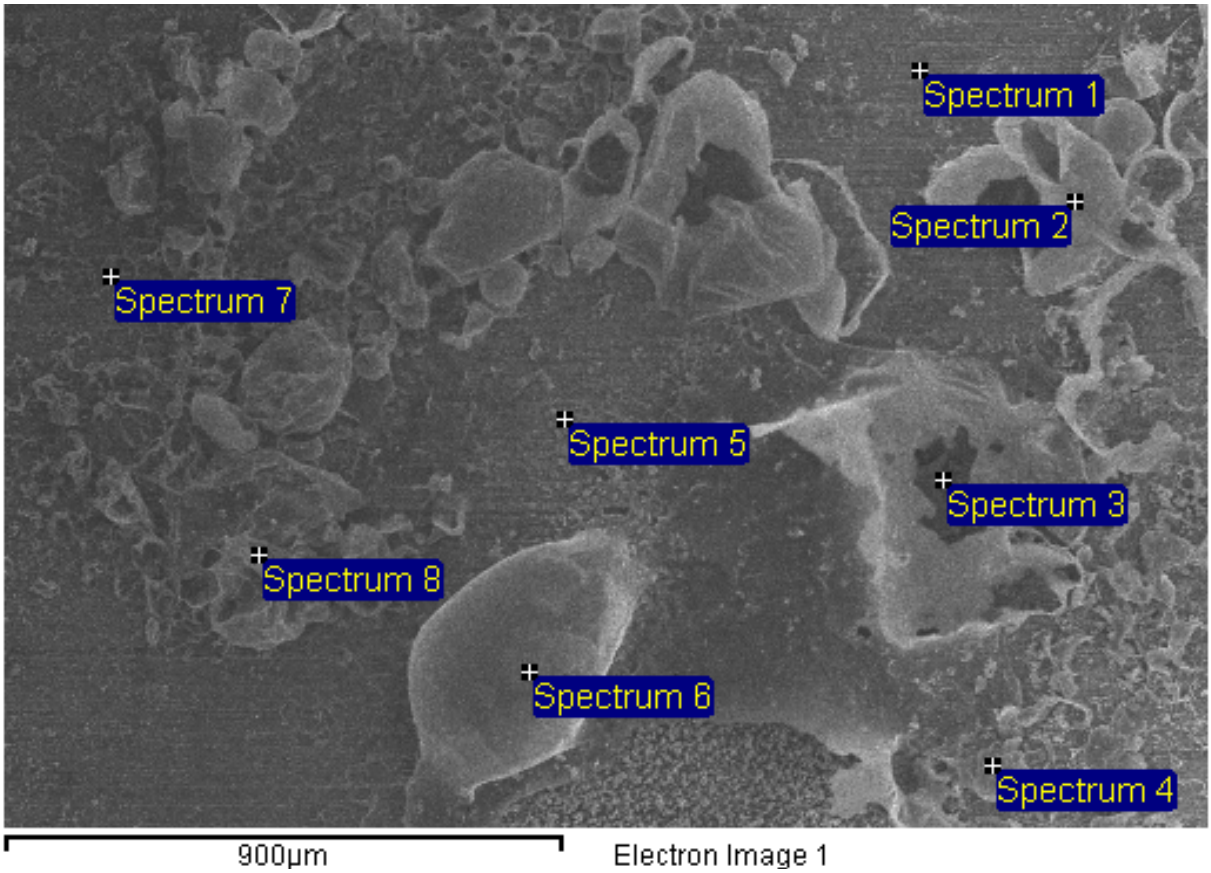

Processing option : All elements analysed

Spectrum	In stats.	C	O	Mn	Fe
Spectrum 1	Yes	62.53	21.78		15.69
Spectrum 2	Yes	45.40	39.68		14.91
Spectrum 3	Yes		40.27	4.05	55.69
Spectrum 4	Yes	32.56	55.35		12.09
Spectrum 5	Yes	57.17	32.49		10.34
Spectrum 6	Yes	39.91	45.87		14.22
Spectrum 7	Yes	46.82	35.85		17.33
Spectrum 8	Yes	42.36	48.86		8.78
Max.		62.53	55.35	4.05	55.69
Min.		32.56	21.78	4.05	8.78

All results in atomic%

Figure A7. SEM analysis of 1018 steel coupon (2UC62) exposed in unfiltered B20 fuel-water mixture exposed in an anaerobic environment.

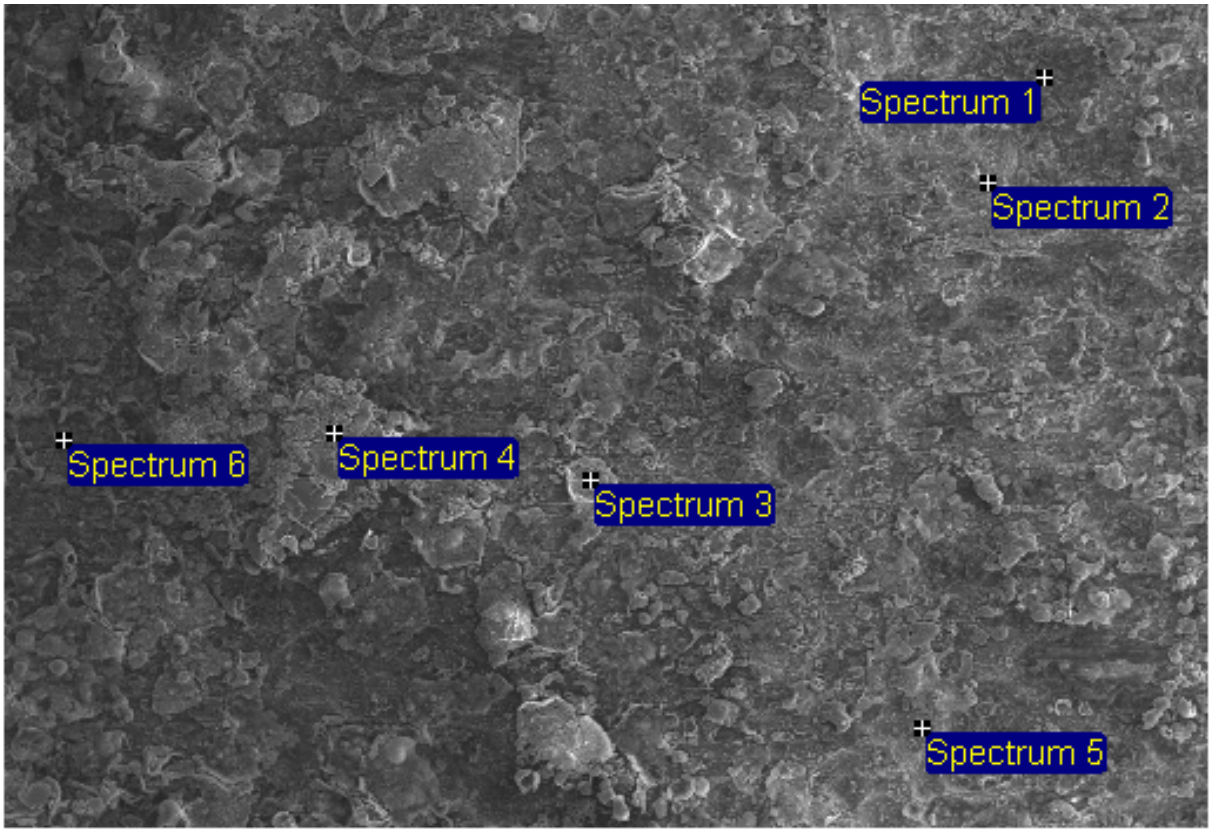

Processing option : All elements analysed

Spectrum	In stats.	C	O	Cr	Mn	Fe
Spectrum 1	Yes	57.06	28.39	0.35	0.20	14.01
Spectrum 2	Yes	52.33			0.60	47.07
Spectrum 3	Yes	19.57	64.90		0.35	15.18
Spectrum 4	Yes	20.34	50.10			29.56
Spectrum 5	Yes	41.92	11.10			46.98
Spectrum 6	Yes	57.02	22.50			20.48
Max.		57.06	64.90	0.35	0.60	47.07
Min.		19.57	11.10	0.35	0.20	14.01

All results in atomic%

Figure A8. SEM analysis of 1018 steel coupon (2UM63) exposed in unfiltered B20 fuel-water mixture exposed in a selective aerobic environment.

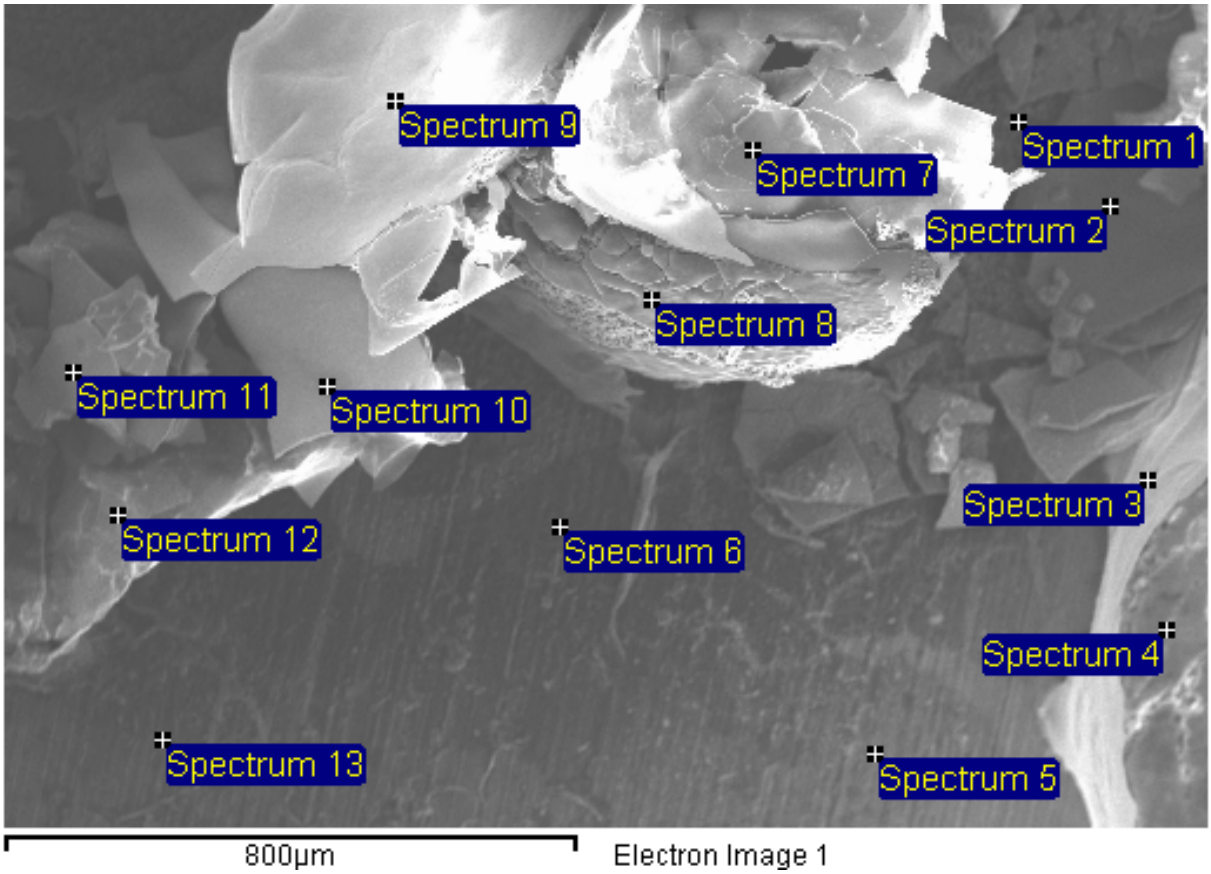

Processing option : All elements analysed

Spectrum	In stats.	C	O	Mn	Fe
Spectrum 1	Yes	18.93	2.86		78.21
Spectrum 2	Yes	26.29	56.38	0.17	17.17
Spectrum 3	Yes	58.24	36.34	0.10	5.32
Spectrum 4	Yes	40.71	12.44		46.84
Spectrum 5	Yes	28.99	3.02		67.98
Spectrum 6	Yes				100.00
Spectrum 7	Yes		3.98		96.02
Spectrum 8	Yes	62.38	21.47		16.15
Spectrum 9	Yes	52.05	17.39		30.55
Spectrum 10	Yes	24.21	4.73		71.06
Spectrum 11	Yes				100.00
Spectrum 12	Yes				100.00
Spectrum 13	Yes				100.00
Max.		62.38	56.38	0.17	100.00
Min.		18.93	2.86	0.10	5.32

All results in atomic%

Figure A9. SEM analysis of 1018 steel coupon (2FC63) exposed in filtered B20 fuel-water mixture exposed in an anaerobic environment.

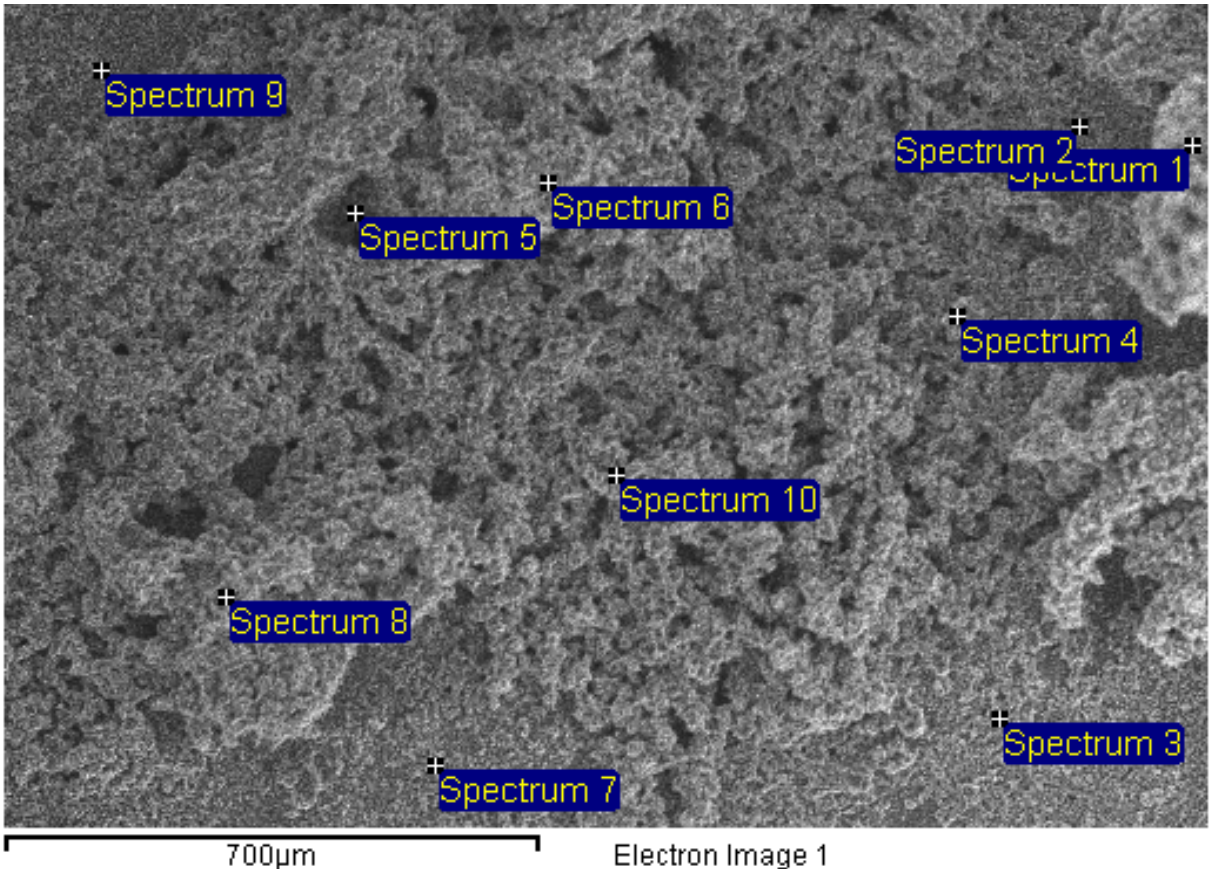

Processing option : All elements analysed

Spectrum	In stats.	C	O	Fe
Spectrum 1	Yes	45.80	30.92	23.28
Spectrum 2	Yes	26.48	6.64	66.88
Spectrum 3	Yes	59.32	6.00	34.68
Spectrum 4	Yes	73.05	18.43	8.52
Spectrum 5	Yes	37.26		62.74
Spectrum 6	Yes	23.39	2.51	74.10
Spectrum 7	Yes	50.98	12.49	36.54
Spectrum 8	Yes	53.42	36.75	9.83
Spectrum 9	Yes	71.53	18.14	10.33
Spectrum 10	Yes	70.03	22.28	7.69
Max.		73.05	36.75	74.10
Min.		23.39	2.51	7.69

All results in atomic%

Figure A10. SEM analysis of 1018 steel coupon (2FM61) exposed in filtered B20 fuel-water mixture exposed in a selective aerobic environment.

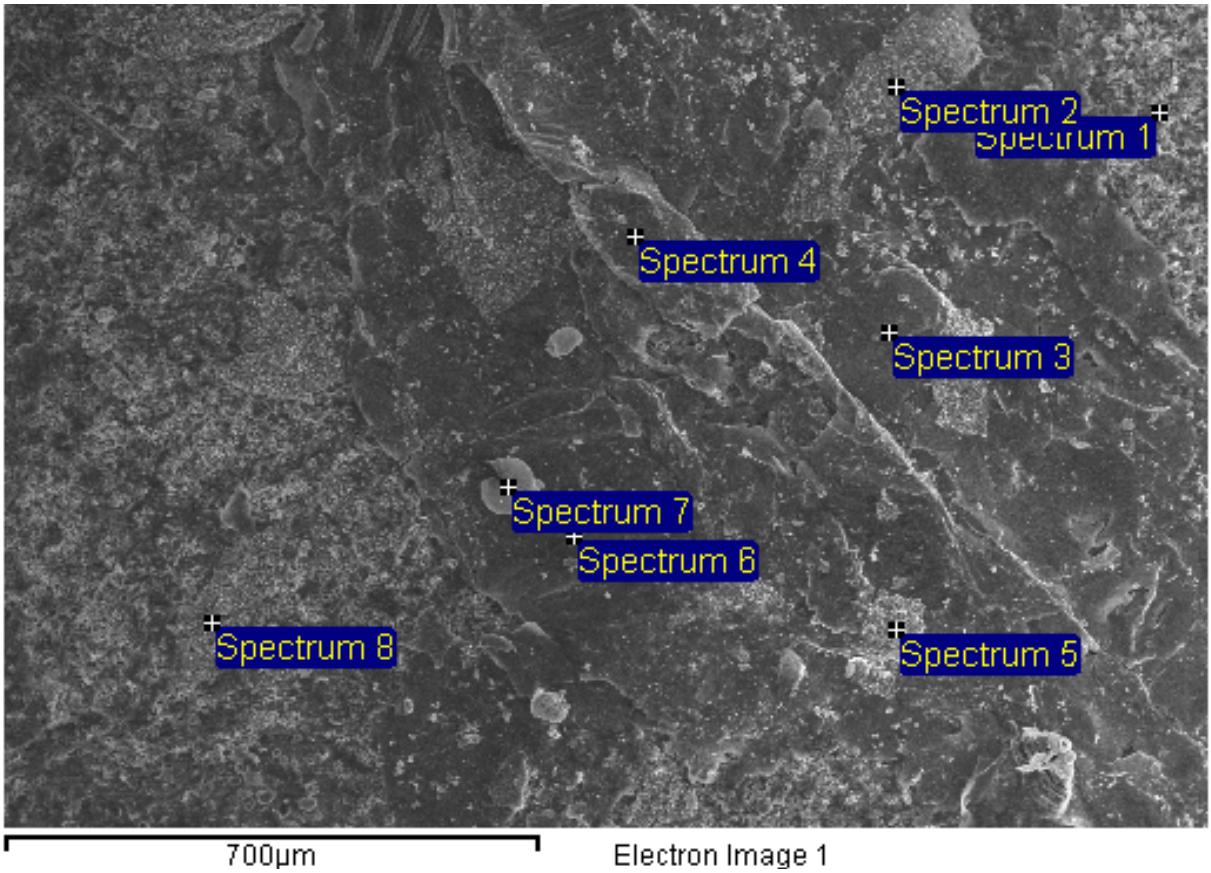

Processing option : All elements analysed

Spectrum	In stats.	C	O	Fe
Spectrum 1	Yes	70.51	15.19	14.30
Spectrum 2	Yes	61.54	29.02	9.44
Spectrum 3	Yes	57.51	23.62	18.88
Spectrum 4	Yes	83.51	11.98	4.51
Spectrum 5	Yes	54.56	34.58	10.86
Spectrum 6	Yes	61.07	26.16	12.77
Spectrum 7	Yes	57.30	30.79	11.91
Spectrum 8	Yes	44.00	27.07	28.93
Mean		61.25	24.80	13.95
Std. deviation		11.67	7.70	7.30
Max.		83.51	34.58	28.93
Min.		44.00	11.98	4.51

All results in atomic%

Figure A11. SEM analysis of 1018 steel coupon (3UC61) exposed in unfiltered ULSD fuel-water mixture exposed in an anaerobic environment.

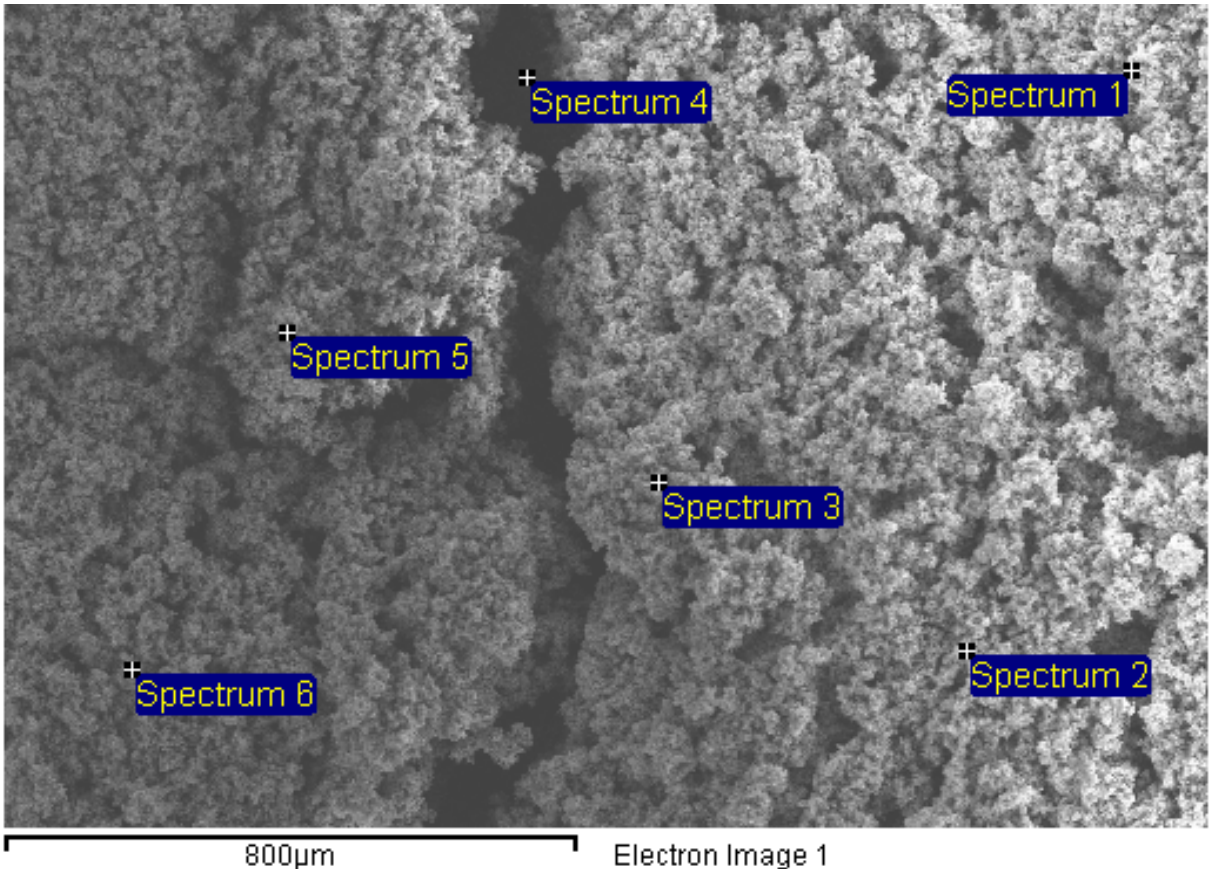

Processing option : All elements analysed

Spectrum	In stats.	C	O	Fe
Spectrum 1	Yes	37.81	33.42	28.77
Spectrum 2	Yes	34.43	52.10	13.47
Spectrum 3	Yes	37.76	43.85	18.39
Spectrum 4	Yes	39.03	49.86	11.11
Spectrum 5	Yes	35.14	42.96	21.90
Spectrum 6	Yes	35.16	56.20	8.64
Mean		36.56	46.40	17.05
Std. deviation		1.88	8.09	7.50
Max.		39.03	56.20	28.77
Min.		34.43	33.42	8.64

All results in atomic%

Figure A12. SEM analysis of 1018 steel coupon (3UO61) exposed in unfiltered ULSD fuel-water mixture exposed in an aerobic environment.

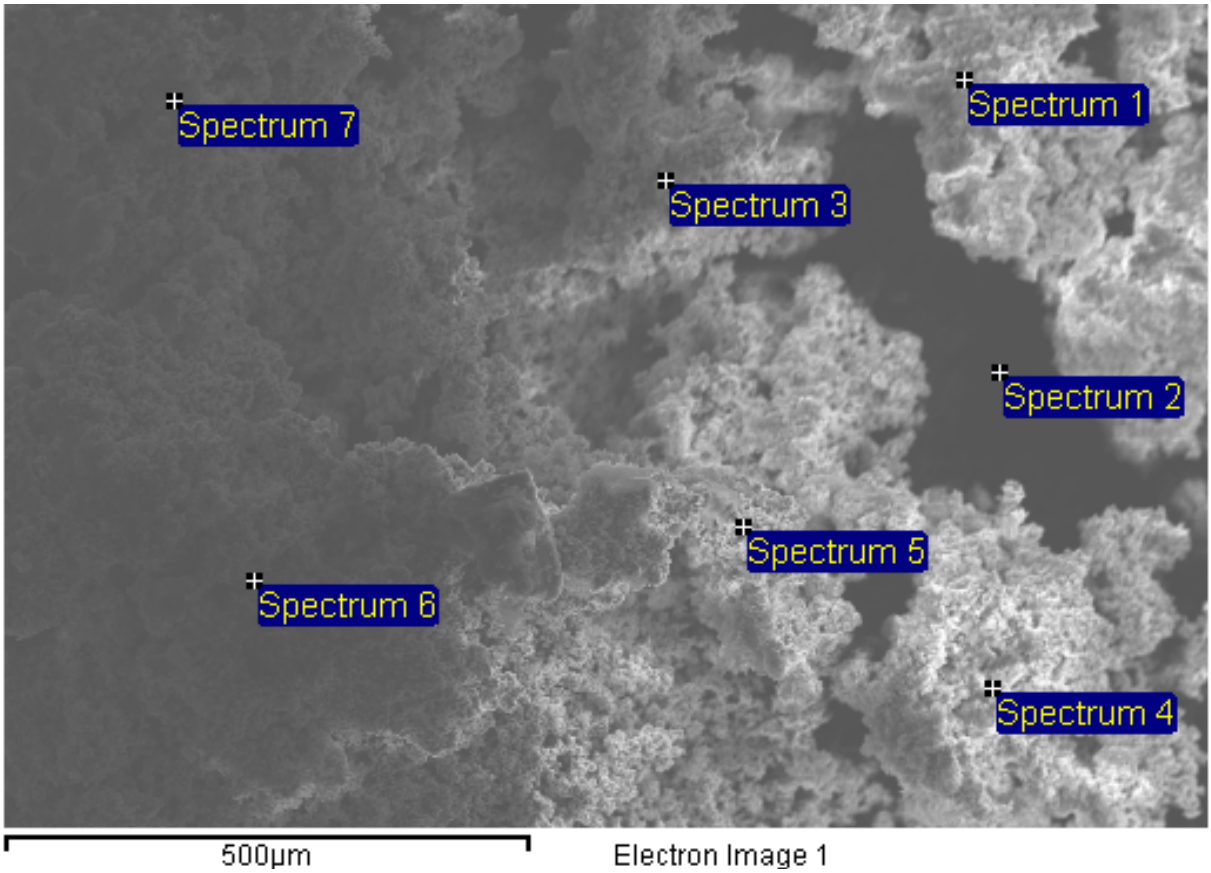

Processing option : All elements analysed

Spectrum	In stats.	C	O	Fe
Spectrum 1	Yes	26.74	60.11	13.15
Spectrum 2	Yes		2.90	97.10
Spectrum 3	Yes	23.66	61.48	14.86
Spectrum 4	Yes	20.20	61.49	18.31
Spectrum 5	Yes	17.17	62.55	20.29
Spectrum 6	Yes	32.17	51.52	16.31
Spectrum 7	Yes	25.62	60.95	13.43
Max.		32.17	62.55	97.10
Min.		17.17	2.90	13.15

All results in atomic%

Figure A13. SEM analysis of 1018 steel coupon (3UM61) exposed in unfiltered ULSD fuel-water mixture exposed in a selective aerobic environment.

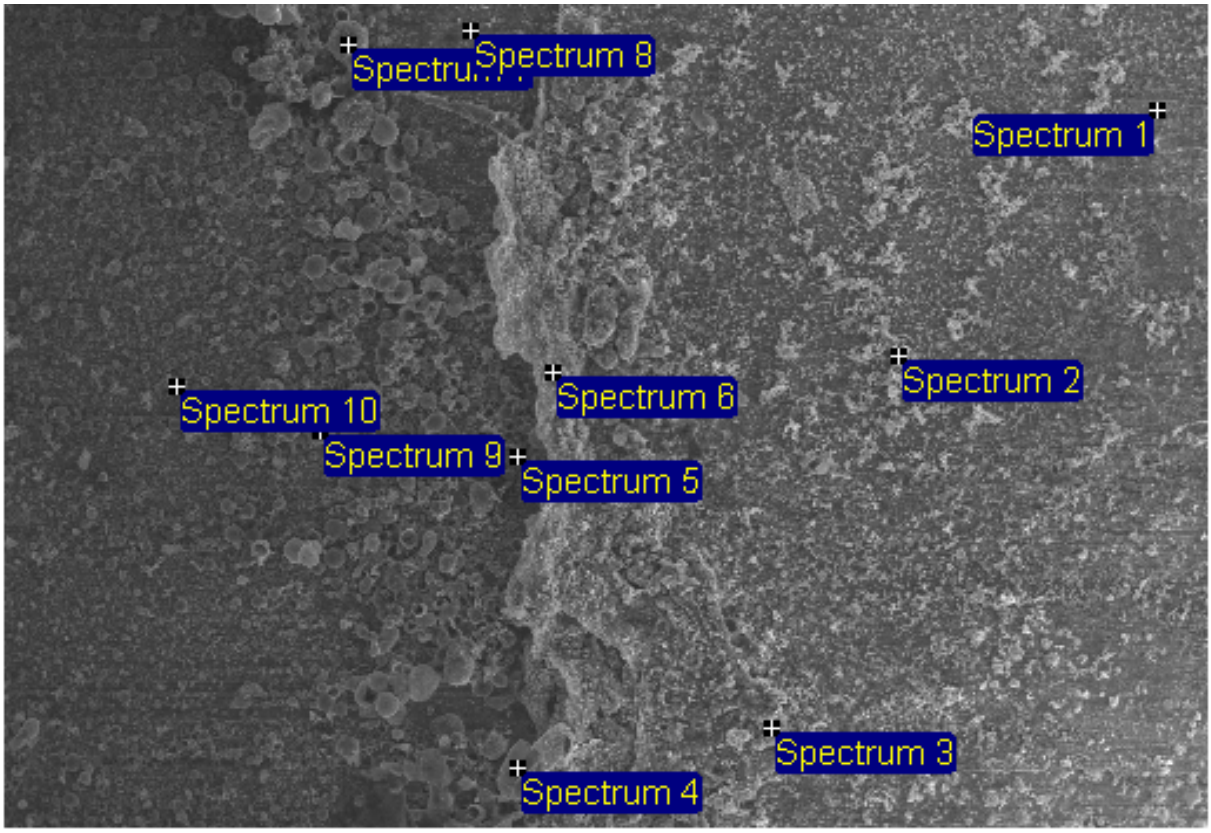

Processing option : All elements analysed

Spectrum	In stats.	C	O	Mn	Fe
Spectrum 1	Yes	43.11			56.89
Spectrum 2	Yes	33.36	38.68		27.97
Spectrum 3	Yes	66.92	17.49		15.59
Spectrum 4	Yes	53.30	38.36		8.34
Spectrum 5	Yes	38.81	13.10	1.57	46.53
Spectrum 6	Yes	64.17	28.92	0.16	6.75
Spectrum 7	Yes	53.85	28.78		17.37
Spectrum 8	Yes	60.84			39.16
Spectrum 9	Yes	40.26	48.52		11.22
Spectrum 10	Yes	59.69	25.05	0.74	14.52
Max.		66.92	48.52	1.57	56.89
Min.		33.36	13.10	0.16	6.75

All results in atomic%

Figure A14. SEM analysis of 1018 steel coupon (3FC61) exposed in filtered ULSD fuel-water mixture exposed in an anaerobic environment.

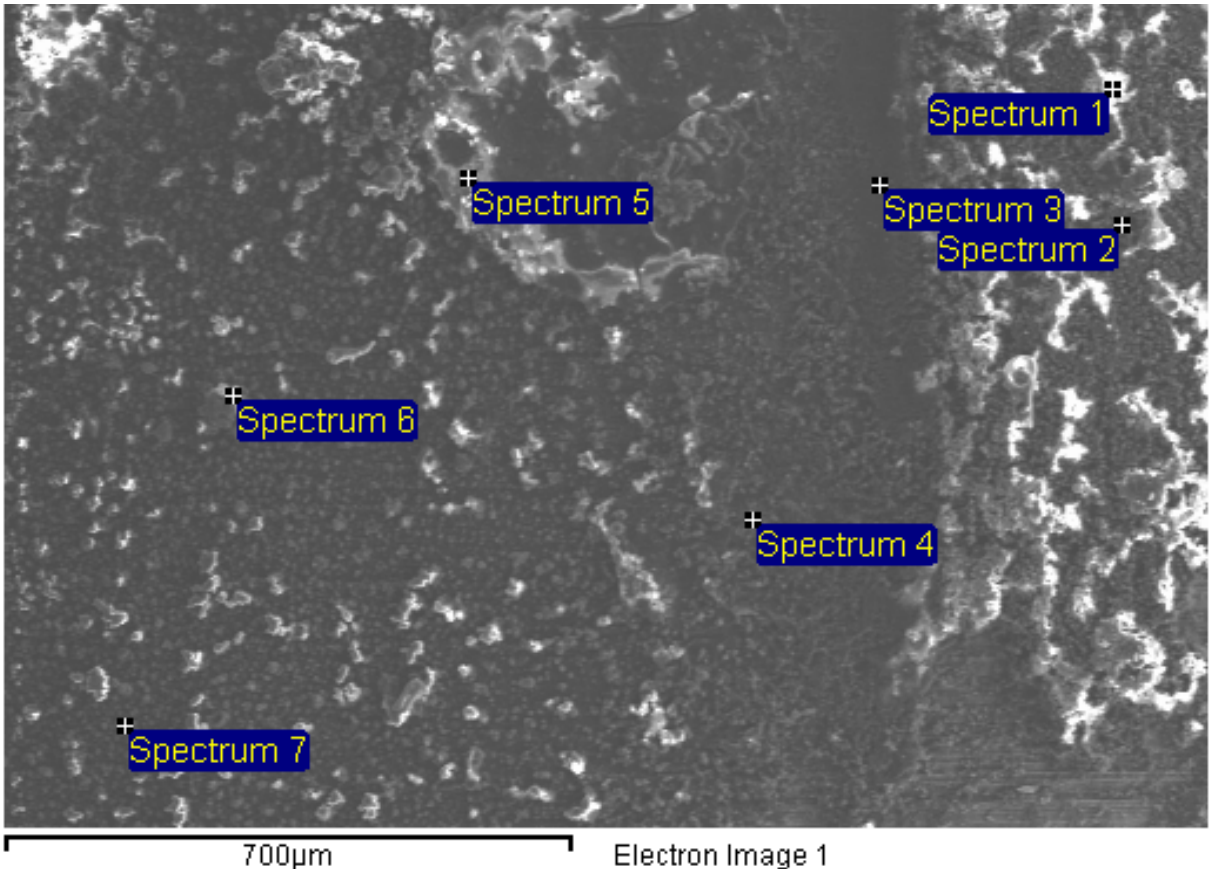

Processing option : All elements analysed

Spectrum	In stats.	C	O	Na	Mg	S	Cl	Ca	Fe
Spectrum 1	Yes	81.08	18.72	0.10					0.11
Spectrum 2	Yes	85.19	9.80	0.45					4.56
Spectrum 3	Yes	86.06	13.61	0.14					0.19
Spectrum 4	Yes	83.23	16.10				0.05		0.62
Spectrum 5	Yes	72.15	24.84	1.56	0.36	0.16	0.59	0.04	0.30
Spectrum 6	Yes	79.68	20.12	0.11			0.03		0.06
Spectrum 7	Yes	77.10	22.77	0.09					0.05
Max.		86.06	24.84	1.56	0.36	0.16	0.59	0.04	4.56
Min.		72.15	9.80	0.09	0.36	0.16	0.03	0.04	0.05

All results in atomic%

Figure A15. SEM analysis of 1018 steel coupon (3FO63) exposed in filtered ULSD fuel-water mixture exposed in an aerobic environment.

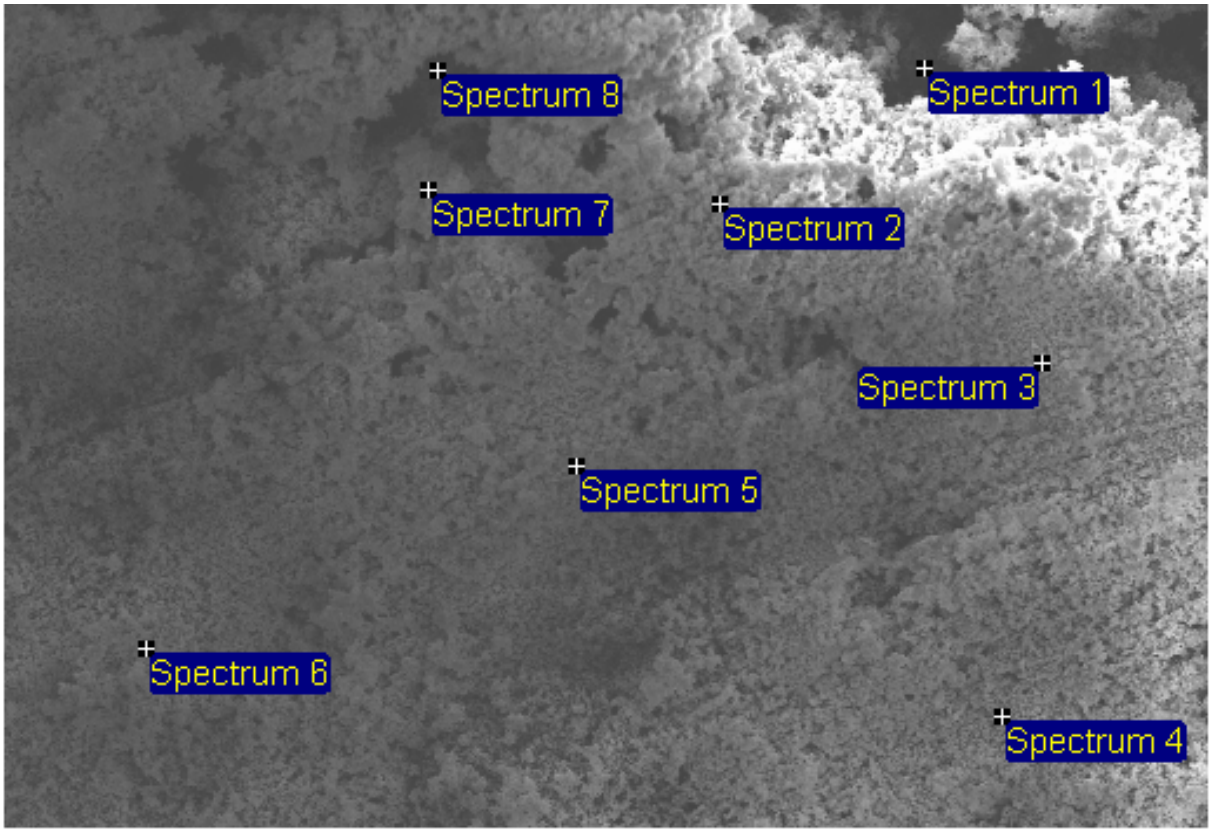

Processing option : All elements analysed

Spectrum	In stats.	C	O	Fe	Tb
Spectrum 1	Yes			100.00	
Spectrum 2	Yes	20.81	61.49	17.69	
Spectrum 3	Yes	20.55	52.59	26.86	
Spectrum 4	Yes	25.64	58.88	15.48	
Spectrum 5	Yes	18.41	59.86	21.73	
Spectrum 6	Yes	7.80	1.17	89.74	1.29
Spectrum 7	Yes	12.98	44.00	43.02	
Spectrum 8	Yes	5.33	2.63	92.03	
Max.		25.64	61.49	100.00	1.29
Min.		5.33	1.17	15.48	1.29

All results in atomic%

Figure A16. SEM analysis of 1018 steel coupon (3FM63) exposed in filtered ULSD fuel-water mixture exposed in a selective aerobic environment.

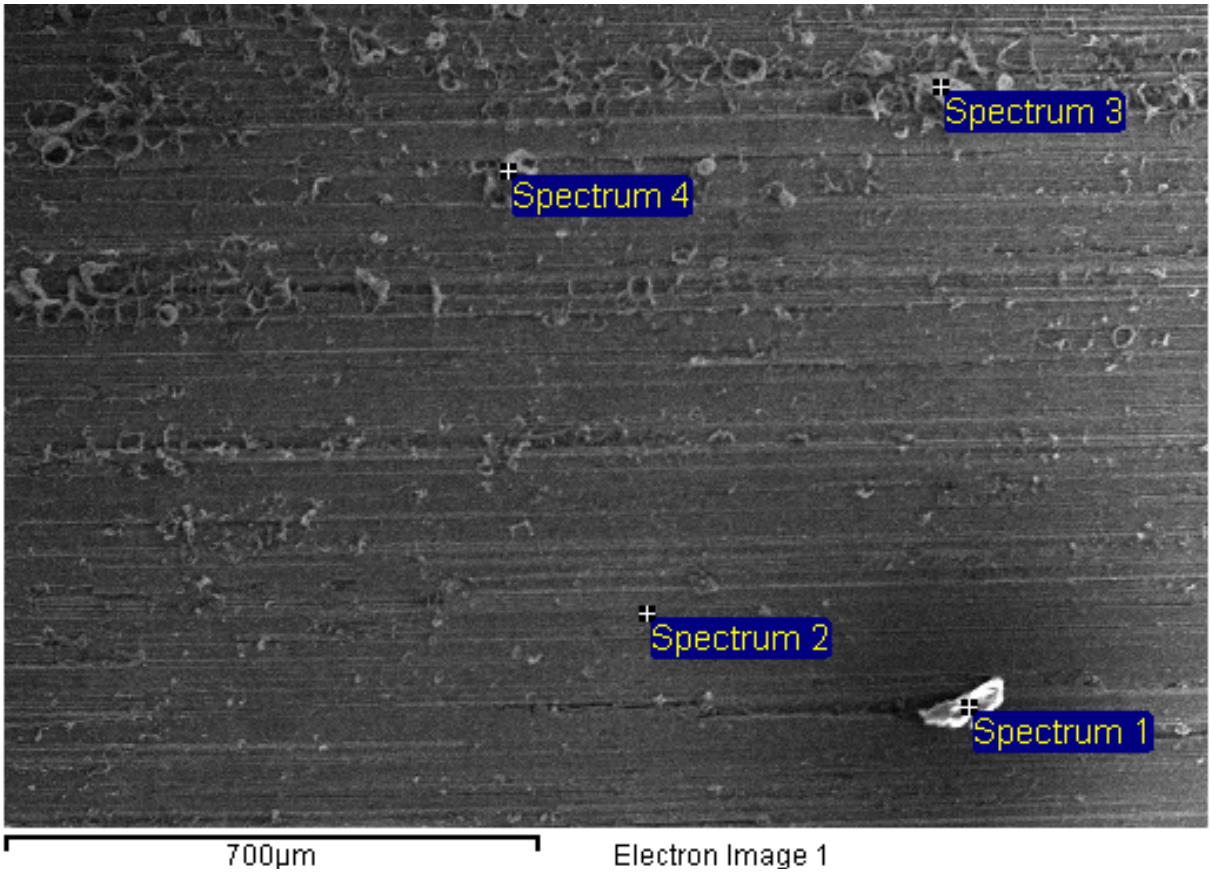

Processing option : All elements analysed

Spectrum	In stats.	C	O	S	Fe
Spectrum 1	Yes	78.43	20.82	0.49	0.26
Spectrum 2	Yes	40.06			59.94
Spectrum 3	Yes	35.70	52.68		11.62
Spectrum 4	Yes	32.98	39.16		27.86
Max.		78.43	52.68	0.49	59.94
Min.		32.98	20.82	0.49	0.26

All results in atomic%

Figure A17. SEM analysis of 1018 steel coupon (1UC12) exposed in unfiltered B100 fuel-water mixture exposed in an anaerobic environment.

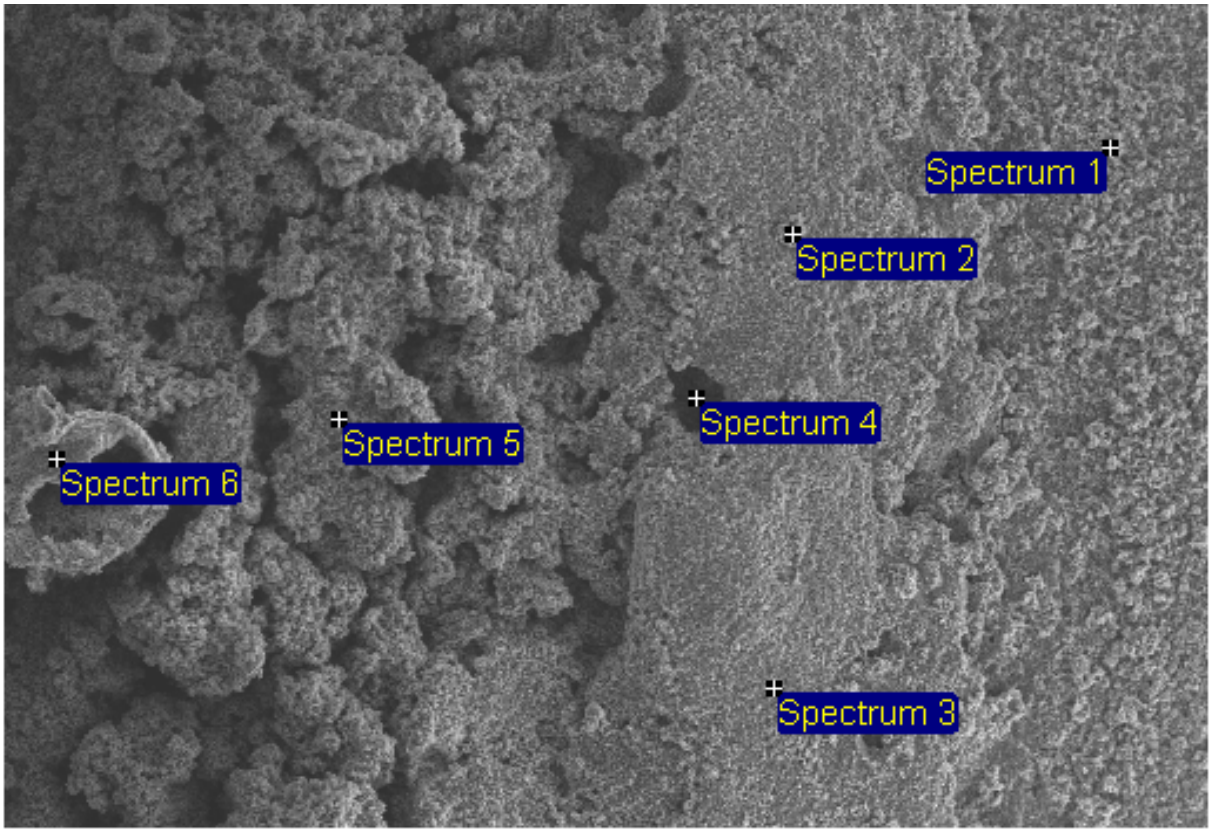

Processing option : All elements analysed

Spectrum	In stats.	C	O	Fe
Spectrum 1	Yes	39.61	55.79	4.59
Spectrum 2	Yes	28.18	63.82	7.99
Spectrum 3	Yes	37.83	55.10	7.07
Spectrum 4	Yes			100.00
Spectrum 5	Yes	35.58	55.53	8.89
Spectrum 6	Yes	36.33	47.20	16.47
Max.		39.61	63.82	100.00
Min.		28.18	47.20	4.59

All results in atomic%

Figure A18. SEM analysis of 1018 steel coupon (1UO12) exposed in unfiltered B100 fuel-water mixture exposed in an aerobic environment.

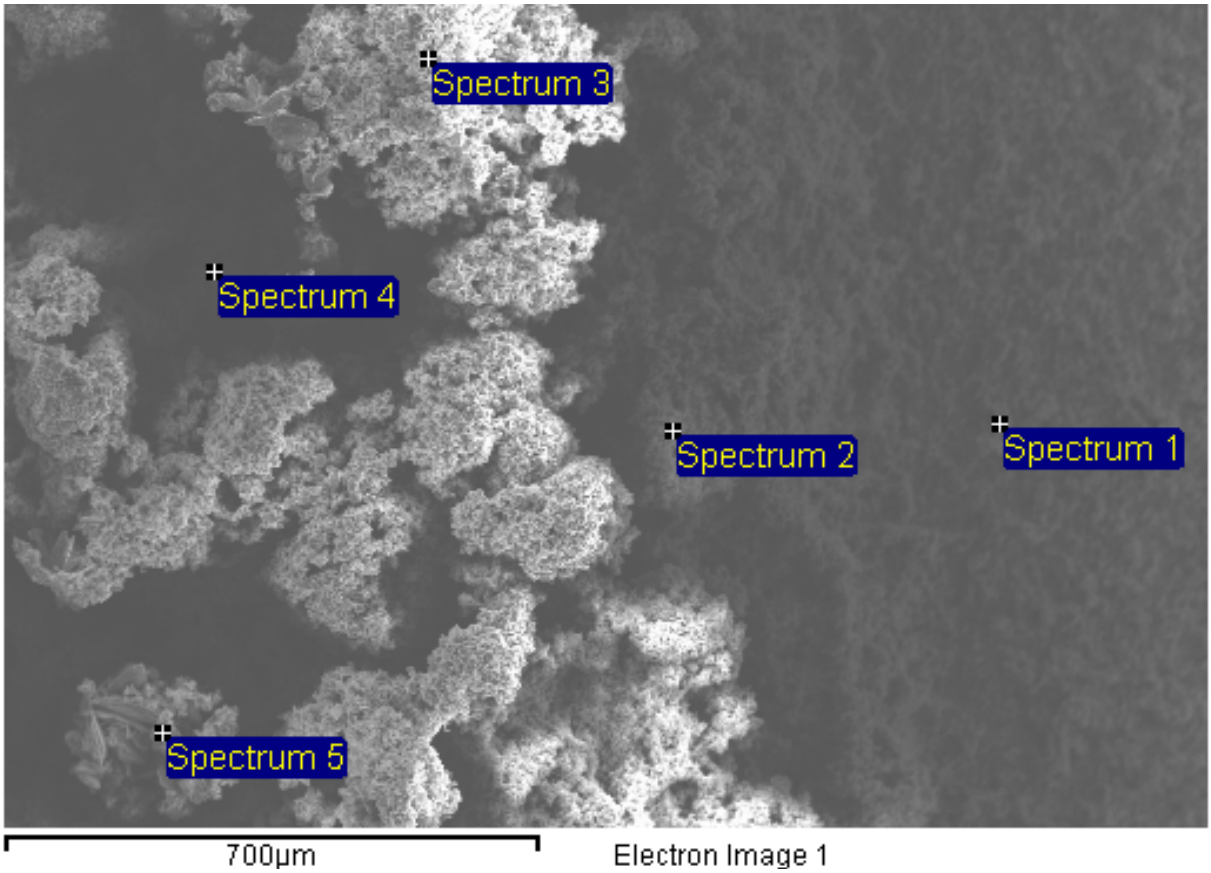

Processing option : All elements analysed

Spectrum	In stats.	C	O	Mn	Fe
Spectrum 1	Yes	37.83	55.47	0.13	6.57
Spectrum 2	Yes	29.82	60.11		10.07
Spectrum 3	Yes	29.94	57.79		12.27
Spectrum 4	Yes	30.27	55.50		14.23
Spectrum 5	Yes	32.33	65.01		2.66
Max.		37.83	65.01	0.13	14.23
Min.		29.82	55.47	0.13	2.66

All results in atomic%

Figure A19. SEM analysis of 1018 steel coupon (1UM11) exposed in unfiltered B100 fuel-water mixture exposed in a selective aerobic environment.

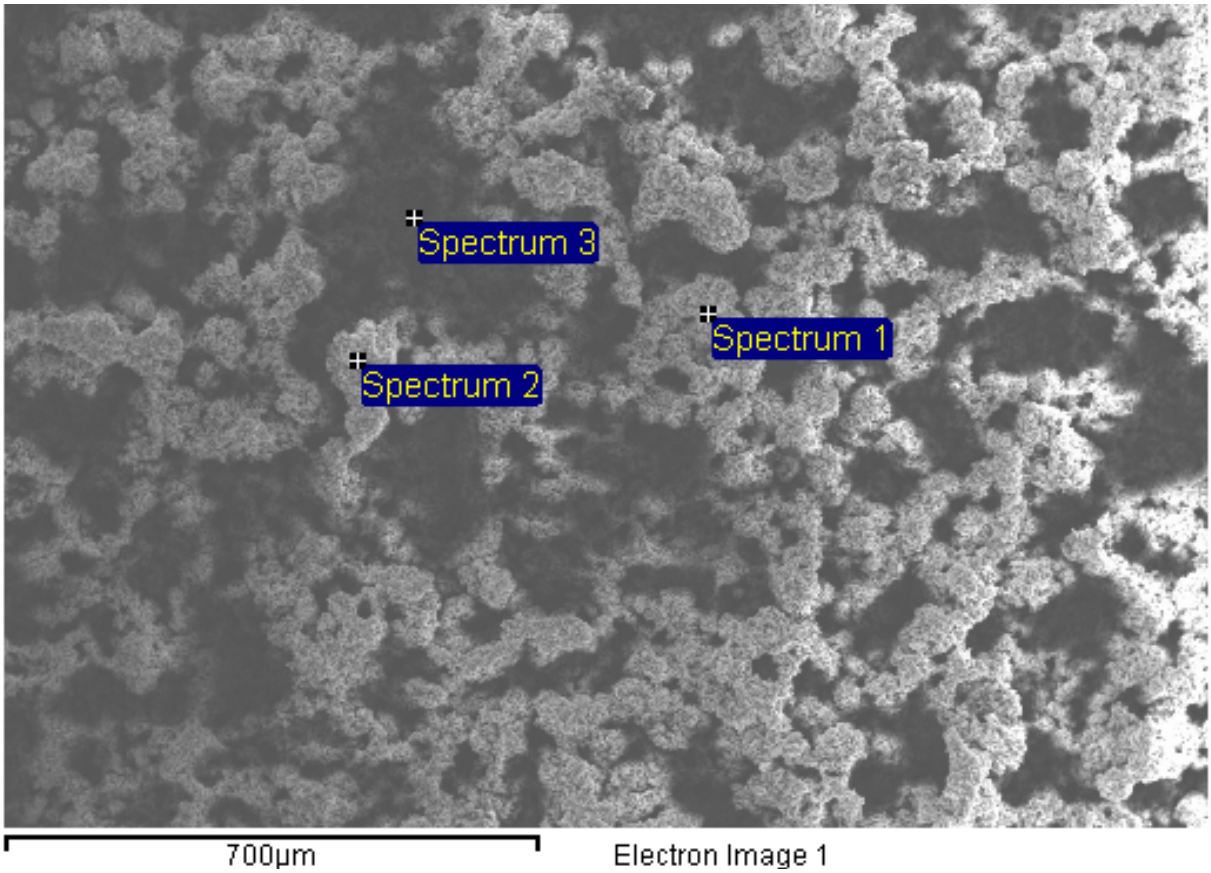

Processing option : All elements analysed

Spectrum	In stats.	C	O	Na	Al	Si	Mn	Fe
Spectrum 1	Yes	27.78	55.24				0.32	16.66
Spectrum 2	Yes	24.47	64.08	1.90	2.05	2.17		5.33
Spectrum 3	Yes	26.76	67.11					6.12
Max.		27.78	67.11	1.90	2.05	2.17	0.32	16.66
Min.		24.47	55.24	1.90	2.05	2.17	0.32	5.33

All results in atomic%

Figure A20. SEM analysis of 1018 steel coupon (1FC13) exposed in filtered B100 fuel-water mixture exposed in an anaerobic environment.

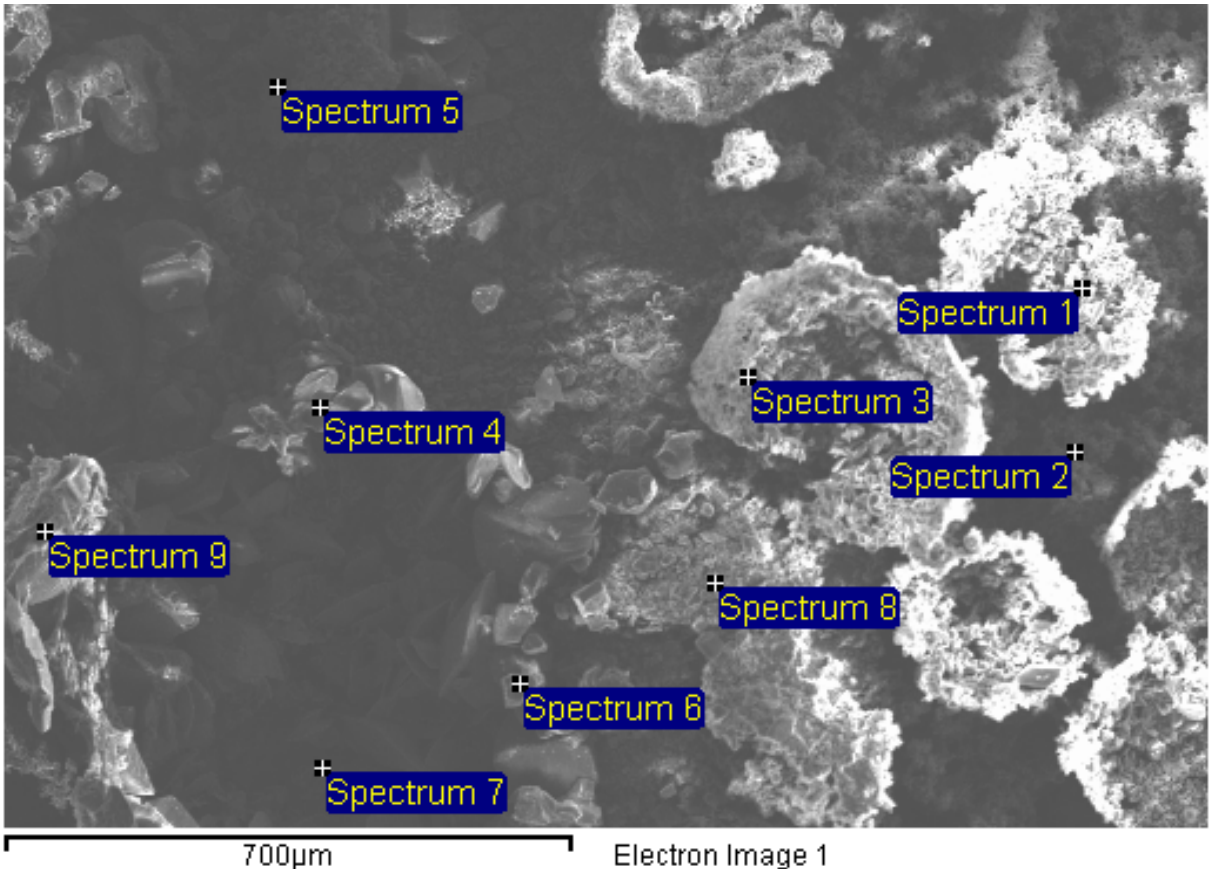

Processing option : All elements analysed

Spectrum	In stats.	C	O	Fe
Spectrum 1	Yes	29.40	66.17	4.42
Spectrum 2	Yes	28.98	50.70	20.32
Spectrum 3	Yes	30.51	29.85	39.64
Spectrum 4	Yes	28.90	68.23	2.87
Spectrum 5	Yes	27.66	67.30	5.04
Spectrum 6	Yes	33.09	62.95	3.96
Spectrum 7	Yes		9.70	90.30
Spectrum 8	Yes	30.58	61.61	7.81
Spectrum 9	Yes	56.72	38.57	4.70
Max.		56.72	68.23	90.30
Min.		27.66	9.70	2.87

All results in atomic%

Figure A21. SEM analysis of 1018 steel coupon (1FO12) exposed in filtered B100 fuel-water mixture exposed in an aerobic environment.

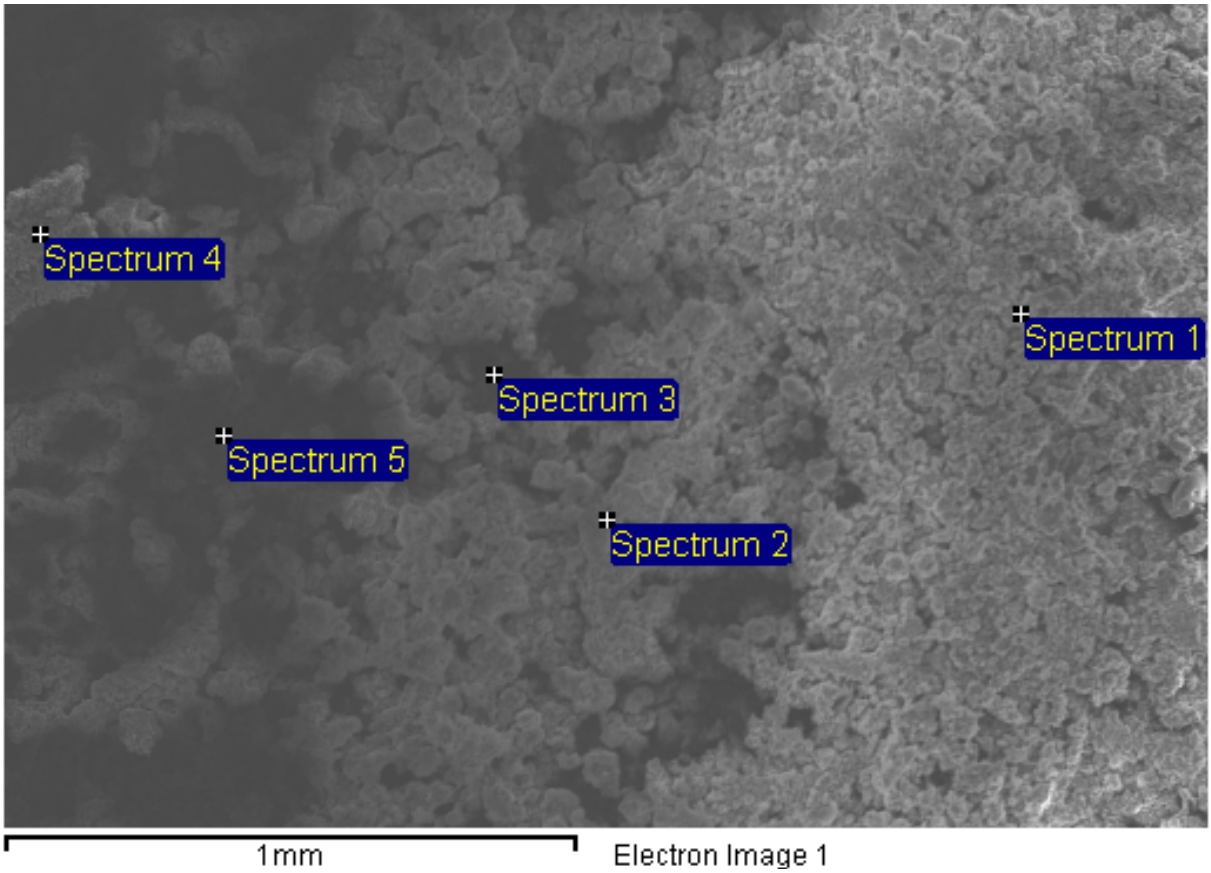

Processing option : All elements analysed

Spectrum	In stats.	C	O	Fe
Spectrum 1	Yes	35.89	49.10	15.02
Spectrum 2	Yes	35.56	49.24	15.21
Spectrum 3	Yes		7.08	92.92
Spectrum 4	Yes	40.15	48.89	10.96
Spectrum 5	Yes		7.12	92.88
Max.		40.15	49.24	92.92
Min.		35.56	7.08	10.96

All results in atomic%

Figure A22. SEM analysis of 1018 steel coupon (1FM12) exposed in filtered B100 fuel-water mixture exposed in a selective aerobic environment.

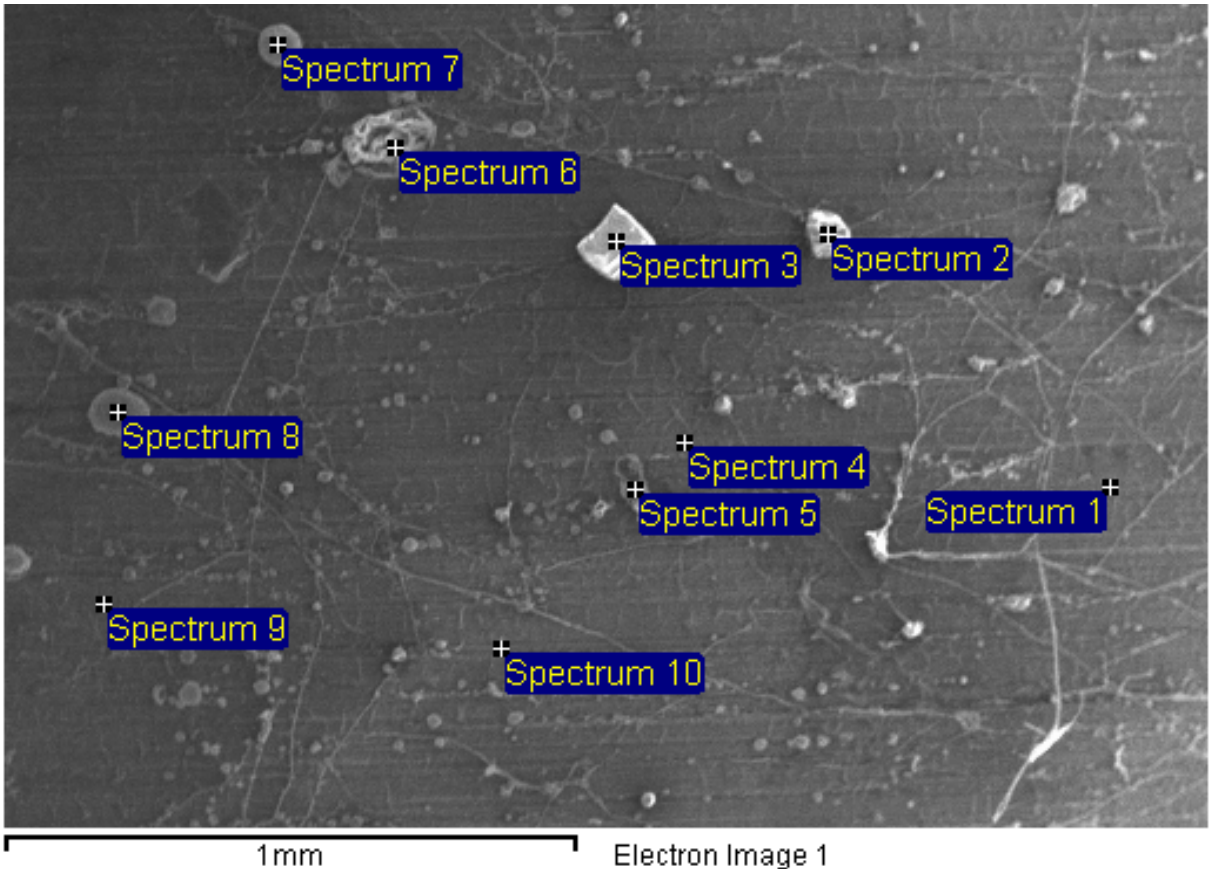

Processing option : All elements analysed

Spectrum	In stats.	C	O	Fe
Spectrum 1	Yes	67.84	10.43	21.73
Spectrum 2	Yes	34.42	53.40	12.18
Spectrum 3	Yes	12.95	68.31	18.74
Spectrum 4	Yes	59.56	17.38	23.06
Spectrum 5	Yes	64.83	13.03	22.14
Spectrum 6	Yes	37.13	51.46	11.41
Spectrum 7	Yes	41.17	47.94	10.89
Spectrum 8	Yes	44.52	40.70	14.78
Spectrum 9	Yes	82.16		17.84
Spectrum 10	Yes	65.00	17.19	17.80
Max.		82.16	68.31	23.06
Min.		12.95	10.43	10.89

All results in atomic%

Figure A23. SEM analysis of 1018 steel coupon (2UC12) exposed in unfiltered B20 fuel-water mixture exposed in an anaerobic environment.

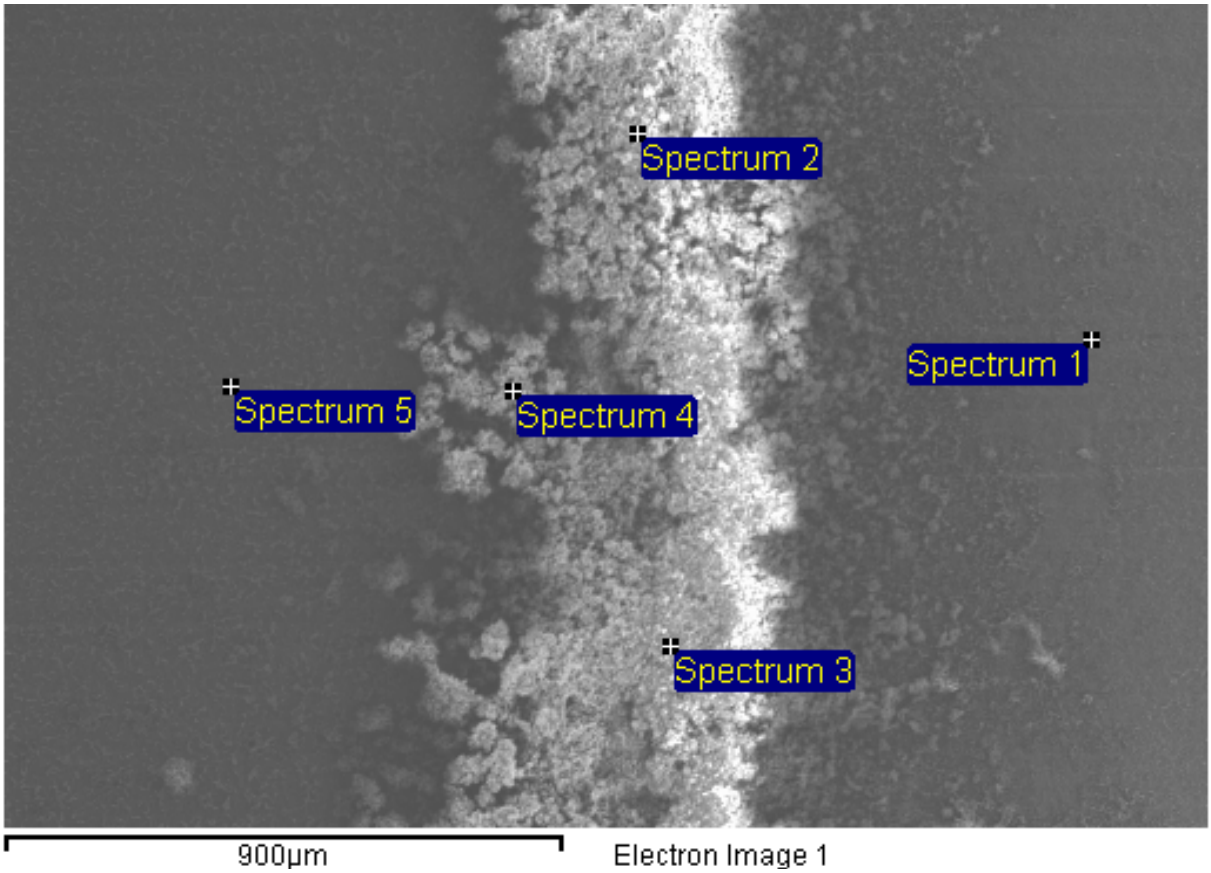

Processing option : All elements analysed

Spectrum	In stats.	C	O	Fe
Spectrum 1	Yes	25.14	60.27	14.60
Spectrum 2	Yes	27.47	64.30	8.23
Spectrum 3	Yes	26.96	56.87	16.17
Spectrum 4	Yes	26.96	64.33	8.72
Spectrum 5	Yes			100.00
Max.		27.47	64.33	100.00
Min.		25.14	56.87	8.23

All results in atomic%

Figure A24. SEM analysis of 1018 steel coupon (2UM11) exposed in unfiltered B20 fuel-water mixture exposed in a selective aerobic environment.

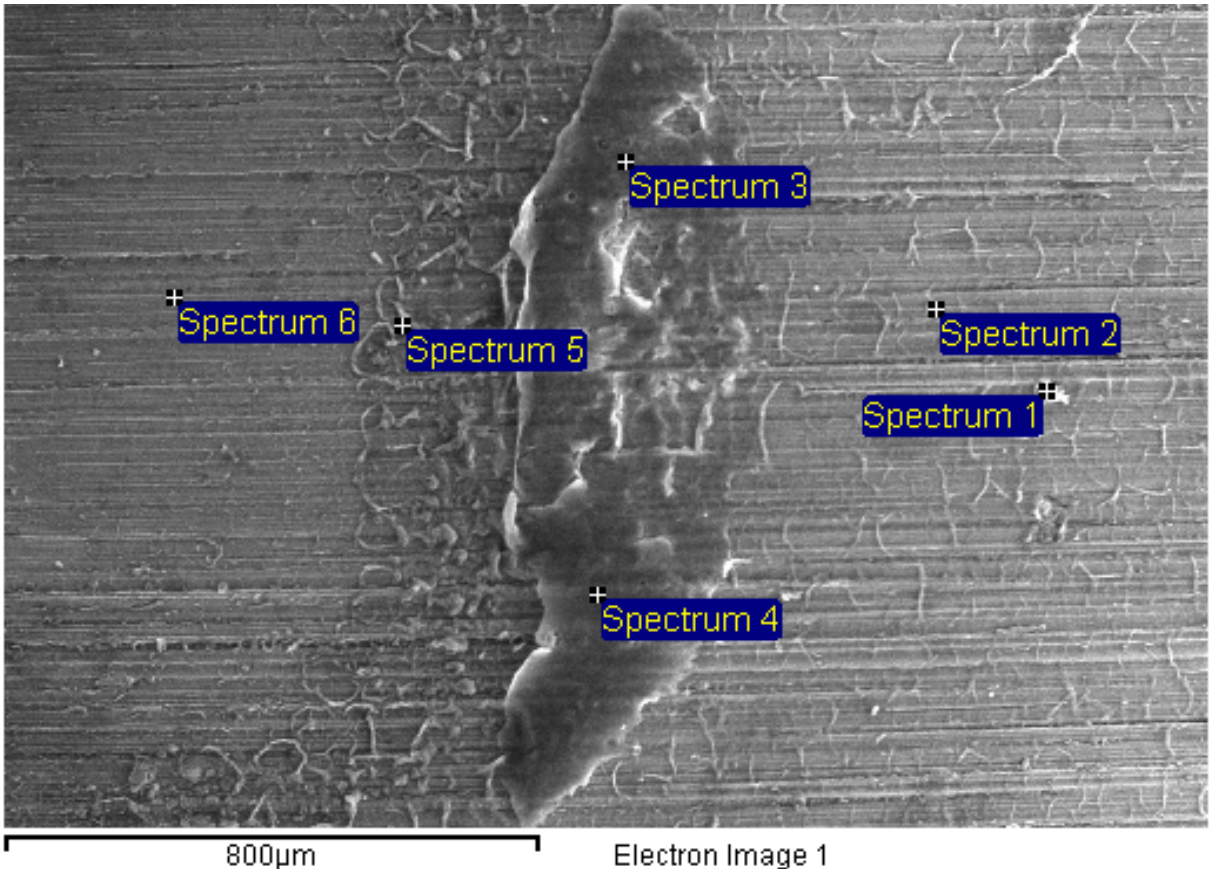

Processing option : All elements analysed

Spectrum	In stats.	C	O	Cr	Fe
Spectrum 1	Yes	67.57	10.94		21.49
Spectrum 2	Yes	67.18	5.57		27.24
Spectrum 3	Yes	49.97	30.10		19.93
Spectrum 4	Yes	51.38	28.21		20.40
Spectrum 5	Yes	60.70	22.36	0.28	16.67
Spectrum 6	Yes	34.83	13.67		51.50
Max.		67.57	30.10	0.28	51.50
Min.		34.83	5.57	0.28	16.67

All results in atomic%

Figure A25. SEM analysis of 1018 steel coupon (2FC13) exposed in filtered B20 fuel-water mixture exposed in an anaerobic environment.

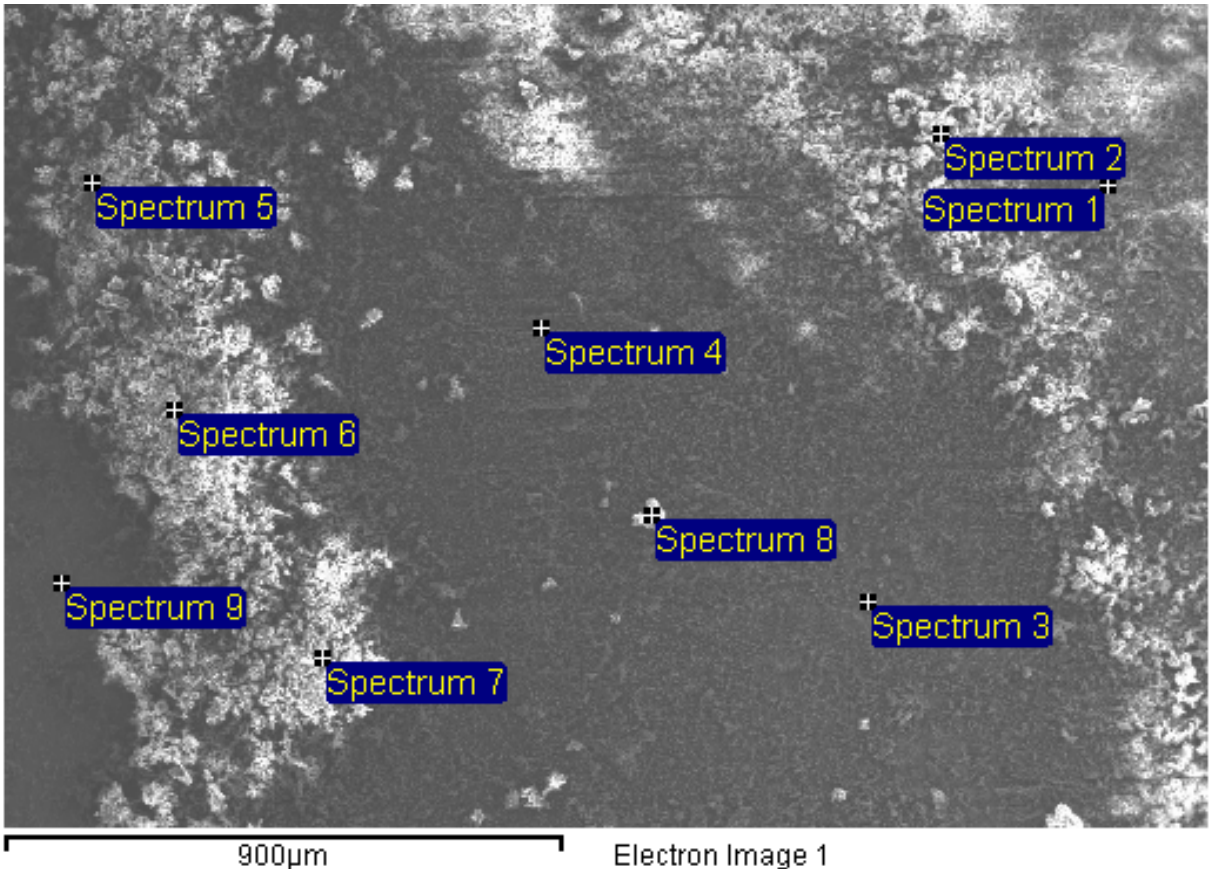

Processing option : All elements analysed

Spectrum	In stats.	C	O	Mn	Fe
Spectrum 1	Yes	24.78	57.58		17.64
Spectrum 2	Yes	27.33	60.11		12.56
Spectrum 3	Yes	27.84	50.04	0.19	21.93
Spectrum 4	Yes	24.41	39.81	0.80	34.98
Spectrum 5	Yes	31.46	63.00		5.54
Spectrum 6	Yes	29.25	59.34		11.41
Spectrum 7	Yes	30.24	62.45		7.31
Spectrum 8	Yes	28.88	65.13		5.98
Spectrum 9	Yes	25.75	63.00		11.24
Max.		31.46	65.13	0.80	34.98
Min.		24.41	39.81	0.19	5.54

All results in atomic%

Figure A26. SEM analysis of 1018 steel coupon (2FM13) exposed in filtered B20 fuel-water mixture exposed in a selective aerobic environment.

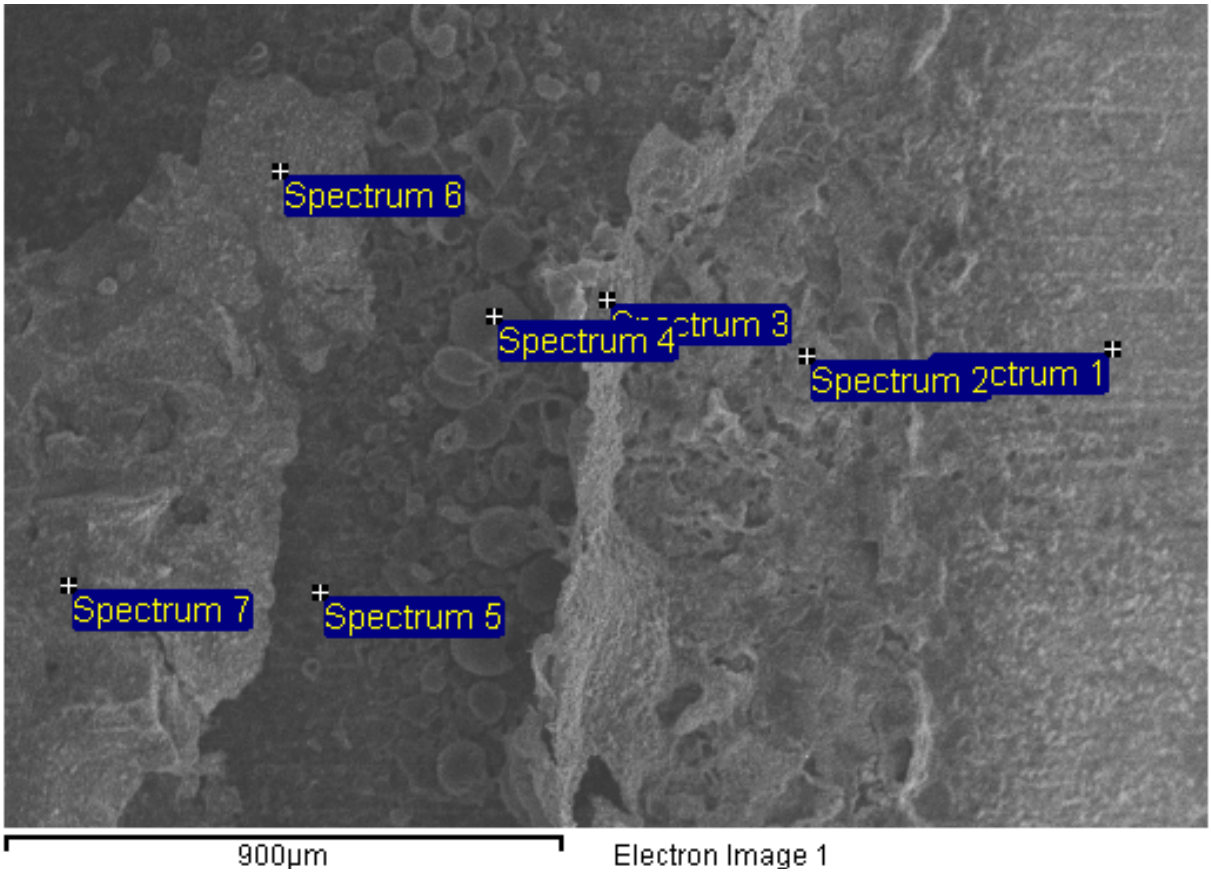

Processing option : All elements analysed

Spectrum	In stats.	C	O	Fe
Spectrum 1	Yes	54.09	27.33	18.58
Spectrum 2	Yes	45.75	33.63	20.62
Spectrum 3	Yes	75.06	15.73	9.22
Spectrum 4	Yes	36.15	51.37	12.48
Spectrum 5	Yes	53.00	35.29	11.71
Spectrum 6	Yes	49.56	36.05	14.39
Spectrum 7	Yes	40.31	43.37	16.32
Mean		50.56	34.68	14.76
Std. deviation		12.62	11.33	4.01
Max.		75.06	51.37	20.62
Min.		36.15	15.73	9.22

All results in atomic%

Figure A27. SEM analysis of 1018 steel coupon (3UC11) exposed in unfiltered ULSD fuel-water mixture exposed in an anaerobic environment.

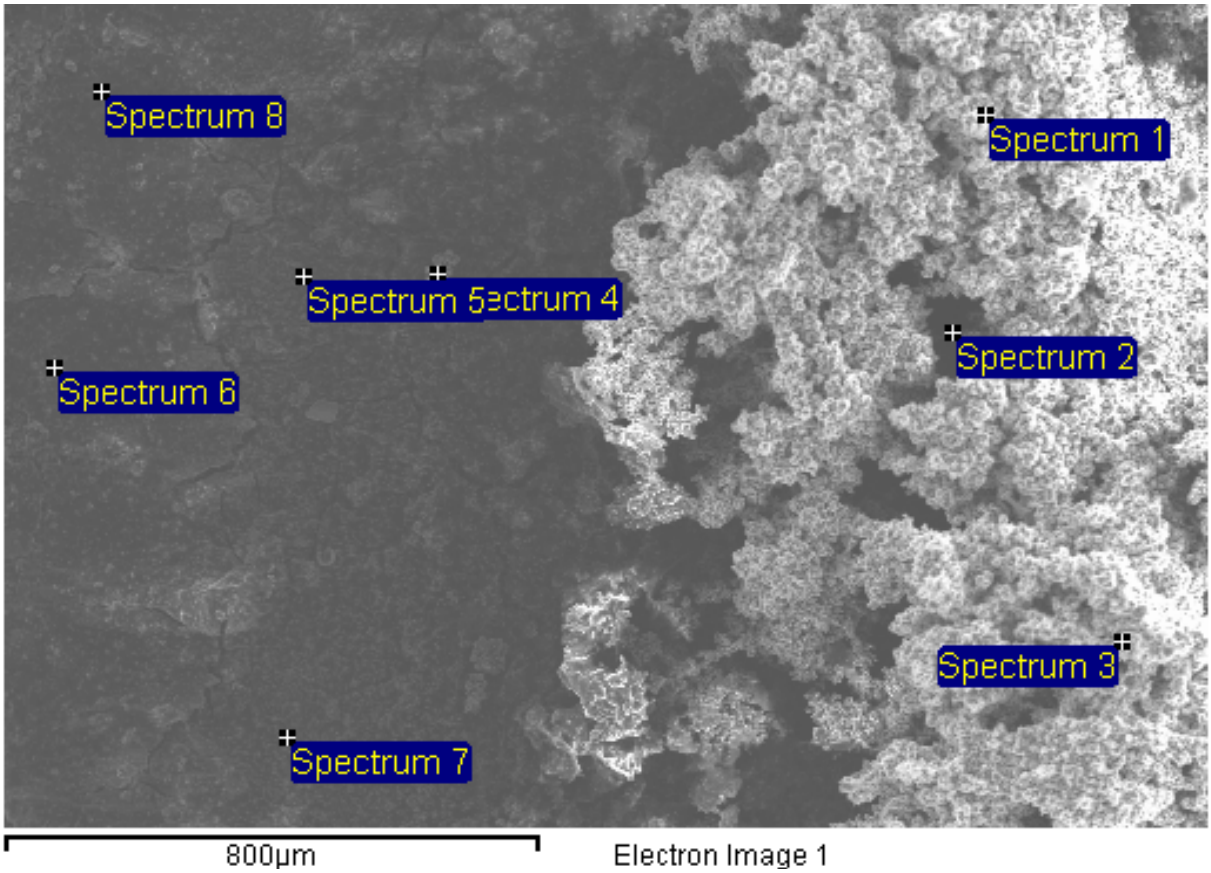

Processing option : All elements analysed

Spectrum	In stats.	C	O	Fe
Spectrum 1	Yes	77.25	19.94	2.80
Spectrum 2	Yes	47.59	10.62	41.79
Spectrum 3	Yes	72.87	22.24	4.89
Spectrum 4	Yes	74.27	22.96	2.77
Spectrum 5	Yes	78.08	19.12	2.80
Spectrum 6	Yes	75.76	19.55	4.70
Spectrum 7	Yes	85.80	12.01	2.19
Spectrum 8	Yes	79.84	14.39	5.77
Mean		73.93	17.60	8.46
Std. deviation		11.35	4.66	13.53
Max.		85.80	22.96	41.79
Min.		47.59	10.62	2.19

All results in atomic%

Figure A28. SEM analysis of 1018 steel coupon (3UO11) exposed in unfiltered ULSD fuel-water mixture exposed in an aerobic environment.

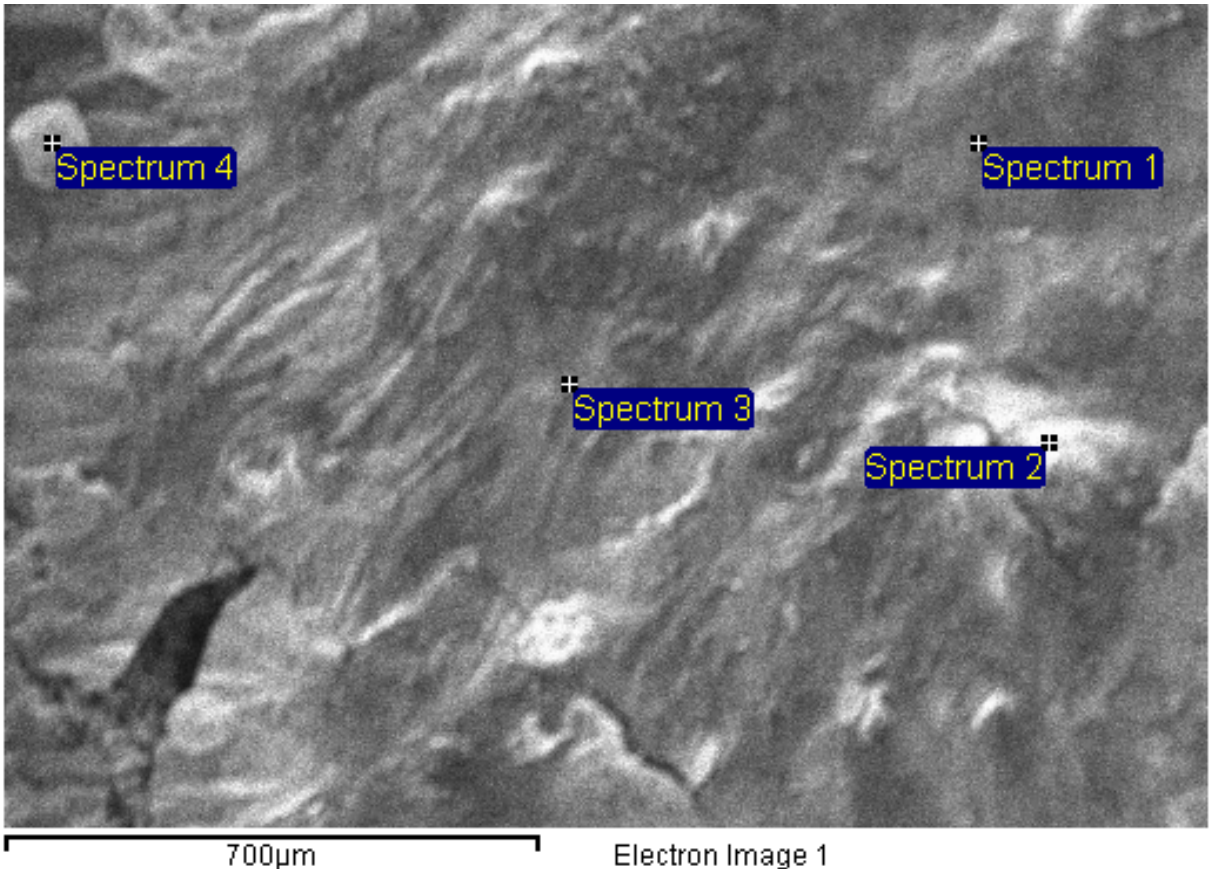

Processing option : All elements analysed

Spectrum	In stats.	C	O	Fe
Spectrum 1	Yes	74.78	14.89	10.33
Spectrum 2	Yes	76.04	16.68	7.29
Spectrum 3	Yes	73.58	20.03	6.39
Spectrum 4	Yes	61.99	28.15	9.86
Mean		71.60	19.94	8.47
Std. deviation		6.48	5.88	1.93
Max.		76.04	28.15	10.33
Min.		61.99	14.89	6.39

All results in atomic%

Figure A29. SEM analysis of 1018 steel coupon (3UM11) exposed in unfiltered ULSD fuel-water mixture exposed in a selective aerobic environment.

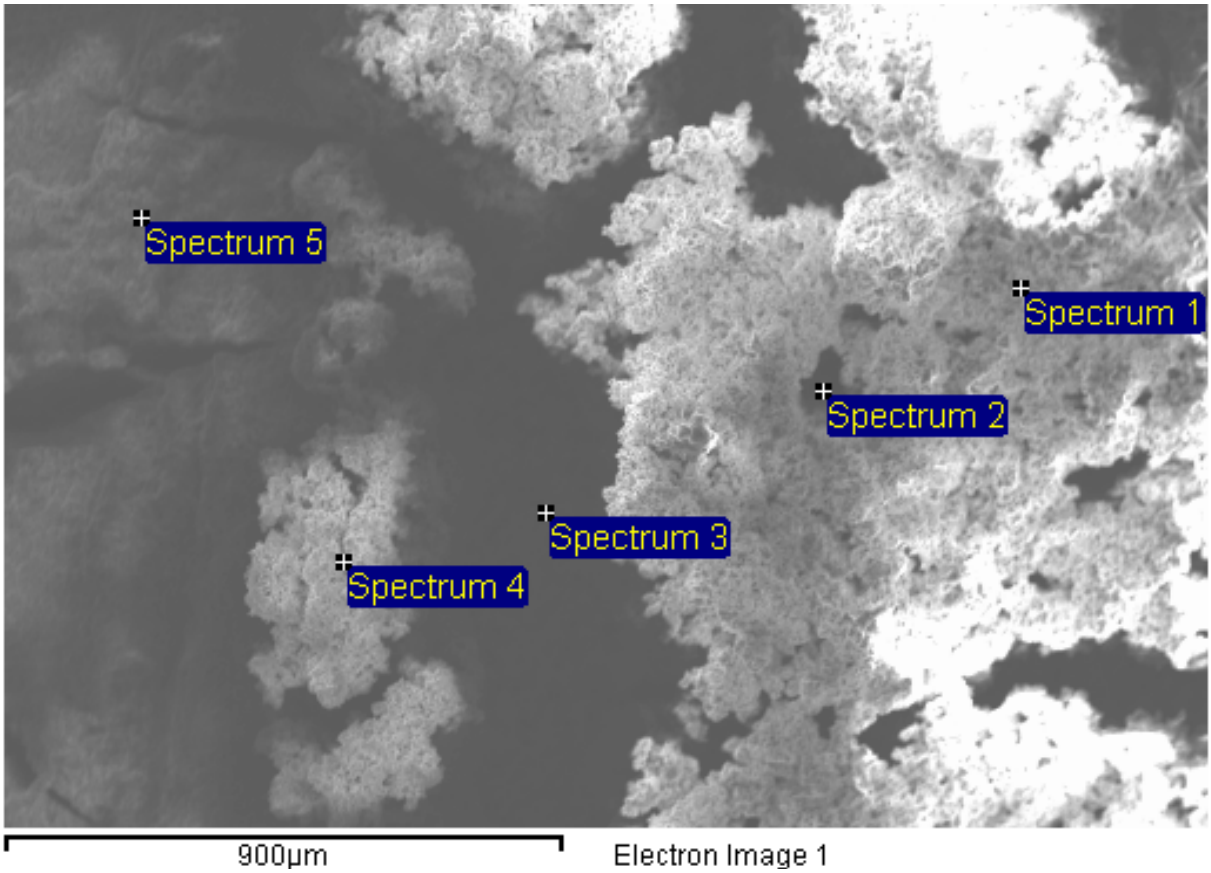

Processing option : All elements analysed

Spectrum	In stats.	C	O	Fe
Spectrum 1	Yes	71.32	25.60	3.08
Spectrum 2	Yes	32.95	2.24	64.82
Spectrum 3	Yes	27.67	7.12	65.21
Spectrum 4	Yes	65.03	23.09	11.89
Spectrum 5	Yes	64.89	18.16	16.96
Mean		52.37	15.24	32.39
Std. deviation		20.39	10.15	30.19
Max.		71.32	25.60	65.21
Min.		27.67	2.24	3.08

All results in atomic%

Figure A30. SEM analysis of 1018 steel coupon (3FC13) exposed in filtered ULSD fuel-water mixture exposed in an anaerobic environment.

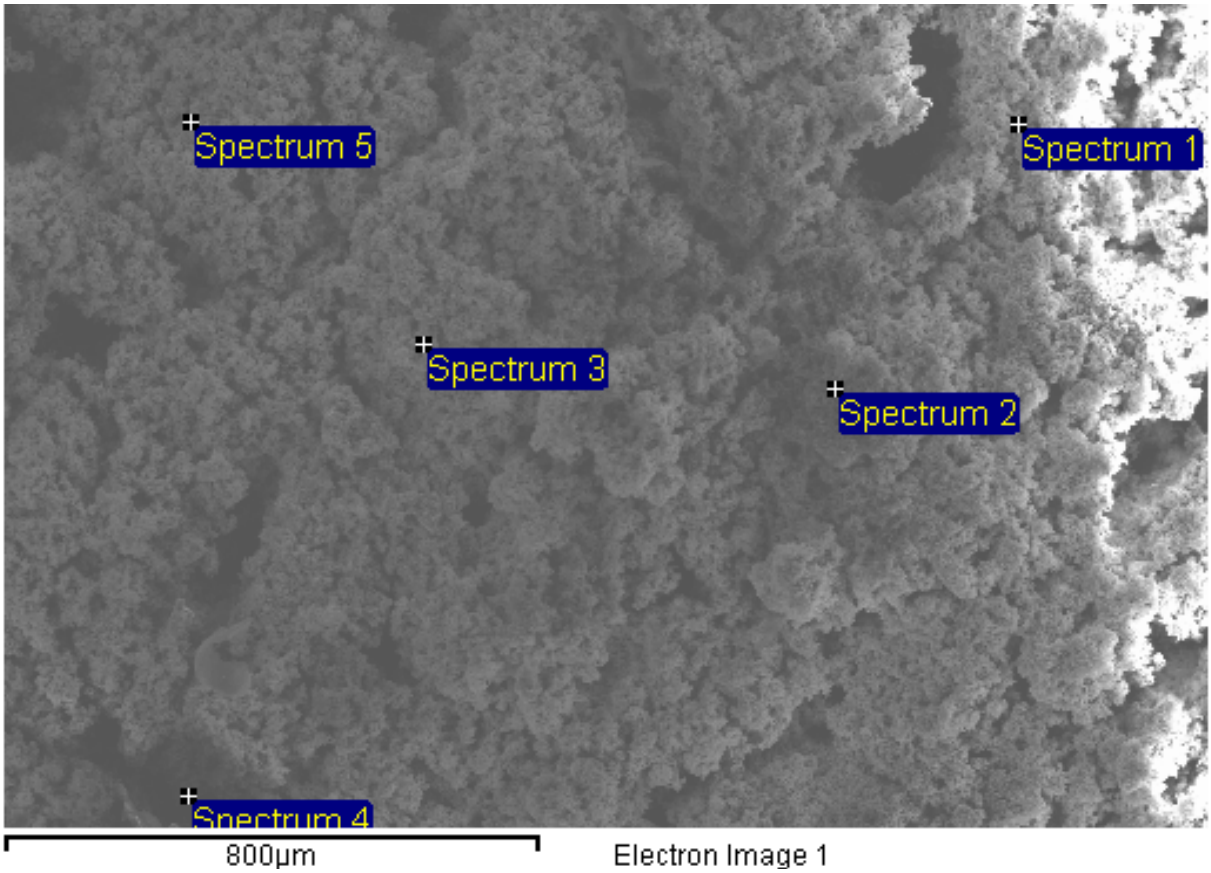

Processing option : All elements analysed

Spectrum	In stats.	C	O	Fe
Spectrum 1	Yes	51.02	40.89	8.09
Spectrum 2	Yes	52.81	27.17	20.02
Spectrum 3	Yes	41.00	26.42	32.58
Spectrum 4	Yes	14.29	4.34	81.37
Spectrum 5	Yes	56.99	34.73	8.28
Mean		43.22	26.71	30.07
Std. deviation		17.21	13.84	30.40
Max.		56.99	40.89	81.37
Min.		14.29	4.34	8.09

All results in atomic%

Figure A31. SEM analysis of 1018 steel coupon (3FO12) exposed in filtered ULSD fuel-water mixture exposed in an aerobic environment.

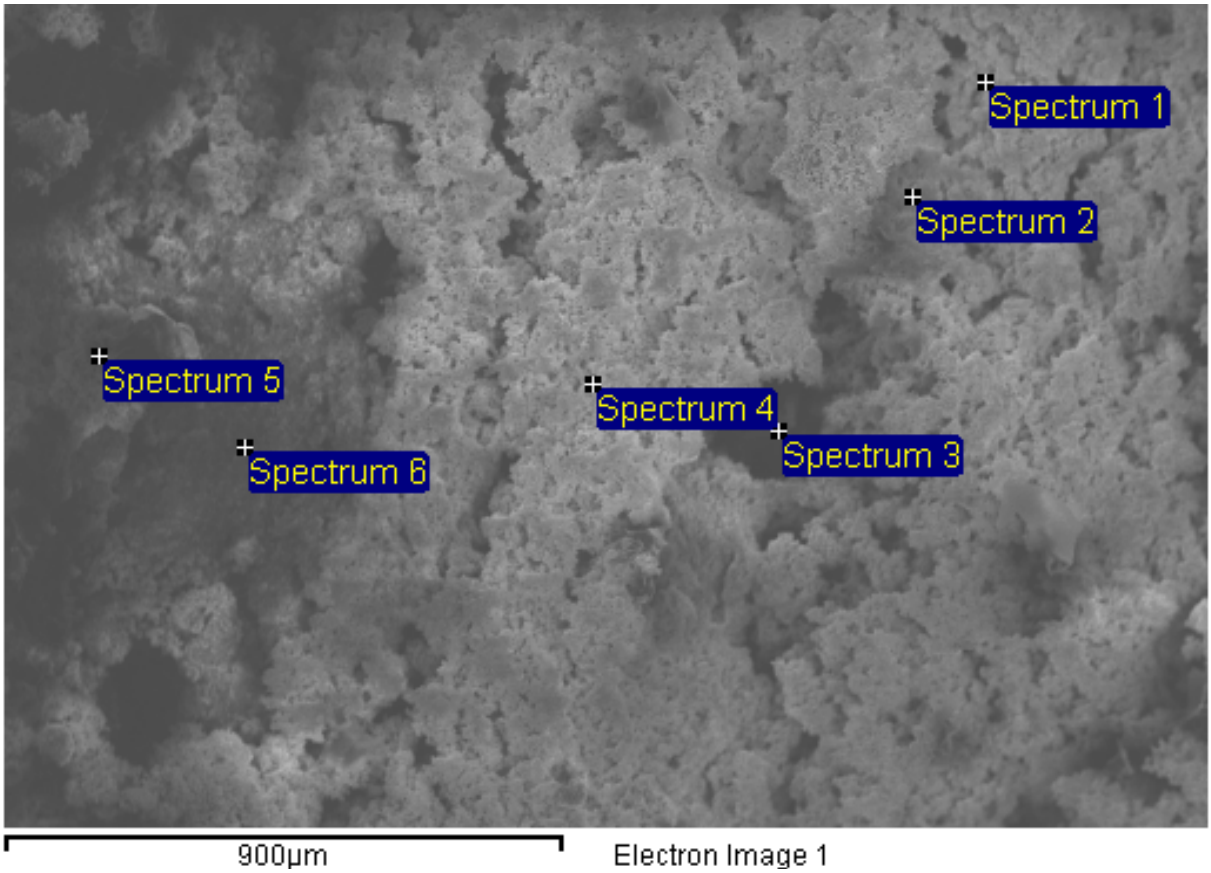

Processing option : All elements analysed

Spectrum	In stats.	C	O	Fe	Pd
Spectrum 1	Yes	38.64	27.39	33.98	
Spectrum 2	Yes		8.78	90.79	0.43
Spectrum 3	Yes			100.00	
Spectrum 4	Yes			100.00	
Spectrum 5	Yes	68.35	25.15	6.50	
Spectrum 6	Yes	61.84	32.93	5.23	
Max.		68.35	32.93	100.00	0.43
Min.		38.64	8.78	5.23	0.43

All results in atomic%

Figure A32. SEM analysis of 1018 steel coupon (3FM13) exposed in filtered ULSD fuel-water mixture exposed in a selective aerobic environment.